Towards Patient-Specific Brain Networks Using Functional Magnetic Resonance Imaging

Michael Hütel

A dissertation submitted in partial fulfillment
of the requirements for the degree of
Doctor of Philosophy
of
University College London.

Department of Medical Physics and Biomedical Engineering
University College London

May 20, 2020

I, Michael Hütel, confirm that the work presented in this thesis is my own. Where information has been derived from other sources, I confirm that this has been indicated in the work.

Abstract

fMRI applications are rare in translational medicine and clinical practice. What can be inferred from a single fMRI scan is often unreliable due to the relative low signal-to-noise ratio compared to other neuroimaging modalities. However, the potential of fMRI is promising. It is one of the few neuroimaging modalities to obtain functional brain organisation of an individual during task engagement and rest. This work extends on current fMRI image processing approaches to obtain robust estimates of functional brain organisation in two resting-state fMRI cohorts. The first cohort comprises of young adults who were born at extremely low gestations and age-matched healthy controls. Group analysis between term- and preterm-born adults revealed differences in functional organisation, which were discovered to be predominantly caused by underlying structural and physiological differences. The second cohort comprises of elderly adults with young onset Alzheimer's disease and age-matched controls. Their corresponding resting-state fMRI scans are short in scanning time resulting in unreliable spatial estimates with conventional dual regression analysis. This problem was addressed by the development of an ensemble averaging of matrix factorisations approach to compute single subject spatial maps characterised by improved spatial reproducibility compared to maps obtained by dual regression. The approach was extended with a haemodynamic forward model to obtain surrogate neural activations to examine the subject's task behaviour. This approach applied to two task-fMRI cohorts showed that these surrogate neural activations matched with original task timings in most of the examined fMRI scans but also revealed subjects with task behaviour different than intended by the researcher. It is hoped that both the findings in this work and the novel matrix factorisation approach itself will benefit the fMRI community. To this end, the derived tools are made available online to aid development and validation of methods for resting-state and task fMRI experiments.

Impact Statement

fMRI has provided the neuroscience community with great insights about brain organisation and functioning on a population level. However, spatial and temporal estimates derived on a patient level are not reliable and thus prevent widely clinical use of fMRI.

fMRI scanning is commonly accompanied by several other functional and structural modalities. As a result, fMRI scans are often short because of the competition for scanning time among various modalities. The analysis of such fMRI scans is challenging because of the inherent noisy nature of the data. Therefore, the derivation of spatial mappings of brain function in individual patients from such fMRI data requires novel image analysis tools that can cope with this scenario and produce reliable biomarkers. This work presents an ensemble of matrix factorisations approach that led to improved longitudinal reproducibility of spatial mappings of brain function in individuals suffering from Alzheimer's disease. Therefore, this approach is a step towards reliable patient-specific biomarkers derived from fMRI. This will have an immediate impact on existing cohorts, which can be analysed retrospectively with this tool in the search for novel fMRI-driven biomarkers, but will also help in the analysis of prospective cohorts in the future.

Functional brain configuration can be altered by letting subjects perform task experiments during scanning. These experiments are conducted to localise brain function but correct localisation depends on the subject following the exact experiment instructions. This work proposes a blind source separation technique that localises brain function without the need for timing information of the task experiment. The wider impact of this work is that fMRI task experiments can be scrutinised with respect to group studies but also patient-specific analysis for surgical planning. The former might be important when conducting task experiments in disease subjects and healthy controls and comparing their spatial map estimates. Occurring differences might be only due to one group consistently not complying with task instructions. The same issue relates to single subject analysis for surgical planning and might have prevented the wider adoption of fMRI in this setting because of erroneous and unreliable spatial mappings of brain function.

Therefore, the proposed technique will have an impact on validating subject performance and will help improve fMRI task experiment designs.

Acknowledgements

Over the past five years I have received support and encouragement from a great number of individuals. Prof. Sebastien Ourselin has been a mentor. His guidance has made this a thoughtful and rewarding journey. My gratitude also goes to Andrew who gave me valuable guidance and support over the course of my thesis.

I especially thank Michela: she has been generous with her time, input, and has always gone out of her way in helping me build my career.

I spent some time in Stanford, for which I thank Seb (again), Andre Altmann, Mike Greicious, and Valerio Napolioni. I learned a lot, and the work was rewarding.

I am also grateful to my clinical collaborators at the Dementia Research Centre. I would especially like to thank Prof. John Schott and Prof. Frederik Barkhof whose collaboration was pivotal for providing me with patient imaging data and spending hours on discussing results of my analysis techniques.

I would like to thank all my lab colleagues and friends, especially Nicolas Toussaint, Ivor Simpson, Catherine Scott, David Owen, Marco Lorenzi, Maria A. Zuluaga, Ninon Burgos, Sjoerd Vos, Miklos Espak and Pankaj Daga, who made our group a fun place to work. A special thanks goes to Amina for her enduring support and love!

This thesis would not have finished without the support of my family. I would like to thank my mother and my grandparents for the sacrifices they have made so that I could pursue my dreams. This will be as much as a reward for them than it is for me. Lastly, this thesis is dedicated to my father. It has been three years but not a day goes by when we do not miss you.

Contents

List of Figures

List of Tables

Abbreviations & Acronyms

AD: Alzheimer's disease

ASN: Anterior salience network

BOLD: Blood oxygen-level dependent

BR: Back-reconstruction

BSS: Blind source separation

BW: Birth weight

CAMR: Cardiac artefact motion removal

CBF: Cerebral blood flow

CEN: Central executive network

CRF: Cardiac response function

CSF: Cerebrospinal fluid

DAN: Dorsal attention network

dHCP: Developing Human Connectome Project

DMN: Default mode network

DR: Dual regression

dWMRI: diffusion weighted MRI

ECG: Electrocardiogram

EMF: Ensemble average of matrix factorisations

EPI: Echo planar imaging

FD: Frontotemporal dementia

FIR: Finite impulse response

FIX: FMRIB's ICA-based Xnoiseifier

FSL: FMRI utility of the Brain Software Library

GLM: General Linear Model

GA: Gestational age

GM: Grey matter

GPCARE: Gaussian process cardio estimation

GSR: Global signal regression

HCP: Human Connectome Project

HMF: Haemodynamic Matrix Factorisation

HR: Haemodynamic response

HRF: Haemodynamic response function

HRV: Heart rate variability

IC: Independent component

ICA: Independent component analysis

INU: Intensity non-uniformity

IRF: Impulse response function

ISI: Inter-stimulus interval

LASSO: Least absolute selection and shrinkage operator

LOAD: Late-onset Alzheimer's disease

LPA: Logopenic aphasia

LTI: Linear time-invariant

L-BFGS limited memory Broyden-–Fletcher-–Goldfarb-–Shanno

MAD: Median absolute deviation

MB: Multi-band

MCI: Mild cognitive impairment

MELODIC: Multivariate exploratory linear decomposition into independent components

MNI: Montreal Neurological Institute

MR: Magnetic resonance

MRI: Magnetic resonance imaging

MSC: Midnight Scan Club

MTGP: Multi-task gaussian process

NLML: Negative log marginal likelihood

NMF: Non-negative matrix factorisation

NNDSVD: Non-negative double singular value initialisation

PCA: Posterior cortical atrophy

PET: Positron emission tomography

PMA: Postmenstrual age

PN: Precuneus network

PPG: Photoplethysmogram

PRV: Pulse rate variability

PREC: Precuneus network

RETROICOR: Retrospective correction of physiological motion effects in fMRI

RF: Electromagnetic radio frequency

RRF: Respiratory response function

RVT: Respiratory volume change per time

SE: Squared-exponential

SMN: Sensory motor network

SN: Salient network

SNR: Signal-to-noise ratio

SPM: Spatial parametric mapping

SVD: Singular value decomposition

SVM: Support vector machine

SWFT: Short-window Fourier transform

SWS: Slice-wise signal

TA: Total Activation

TCS: Total correlation score

TFCE: Threshold-free cluster enhancement

TR: Repetition time

VN: Visual network

VSN: Visuospatial network

WM: White matter

YOAD: Young-onset Alzheimer's disease

Chapter 1

Introduction

The past decades were shaped by a revolution in cognitive and systems neuroscience by looking at the human brain in vivo using either metabolic, haemodynamic or electro-physiological imaging modalities. Magnetic resonance imaging (MRI) is one of these neuroimaging techniques which is widely used for brain studies.

MRI builds on the phenomenal effect of magnetic resonance (MR) that was first described in 1946 by Felix Bloch and Edward Purcell. Research teams led by these two discovered almost simultaneously that the magnetic moment of an atom's nuclei is modified when placed into a magnetic field. The nuclei of atoms become magnetic dipoles, which change the orientation of their rotational axis to precess about this magnetic field at a certain frequency, called Larmor frequency. If these dipoles are simultaneously exposed to an electromagnetic radio frequency (RF) field of a frequency matching the Larmor frequency, these nuclei will absorb energy from the RF field and change their nuclear state.

In neuroimaging, MRI is most commonly used to acquire structural images of the human brain. However, one can exploit magnetic characteristics of blood to visualise perfusion of the brain during task and rest.

1.1 Functional magnetic resonance imaging

A high level of blood oxygenation is generally associated with increased cerebral blood flow (CBF), which in turn is associated with elevated neuronal activity [Iadecola, 2017, Buxton et al., 2004, Kim and Ogawa, 2012, Ogawa et al., 1990b, Ogawa and Lee, 1990, Ogawa et al., 1990a].

The blood oxygen level dependent (BOLD) measures this process of oxygenation by which oxygen is reversibly bound to the ferrous ion of haemoglobin in red blood cells. The magnetic susceptibility of blood haemoglobin changes as a function of whether it is bound to oxygen or not. Therefore, changes in neuronal activity can be indirectly detected by changes in the level of blood oxygenation. The use of MR to detect changes in BOLD is referred to as functional magnetic resonance imaging (fMRI), or more specifically BOLD-fMRI [Bandettini, 2012, Bandettini et al., 1993, Friston et al., 1995]. The following briefly discusses how position can be encoded into MR signal to localise areas of the brain with blood perfusion change.

1.2 Echo planar imaging

The interaction between RF and the static magnetic field allows for the encoding of spatial position of the MR signal. This process is constantly repeated with a predefined repetition time (TR). Accordingly, fMRI can be used to obtain a time-dependent, spatial indirect measure of neuronal activation.

Although fMRI scans are presented in common software tools as volumes of voxels that are acquired every TR, each of these volumes is actually acquired in a slice-wise fashion. An individual slice is acquired with a sequence called single-shot 2D echo planar imaging (EPI). This sequence utilises just one excitation pulse to acquire a whole slice and is thus very fast compared to other MR sequences. A bipolar gradient is triggered during the readout, which produces a series of rising and falling gradient echoes with alternating sign. Between these extreme short gradient echoes, a phase encoding gradient is triggered to switch between rows in the k-space. This is a space encoding phase and frequency information of the acquired MR signal. Therefore, it only takes a small percentage of the entire TR to acquire an individual slice. An individual volume in a TR is acquired in several slices in either interleaved or continuous order with a time offset.

The fast traversal of the k-space in EPI enables great spatial and temporal resolution in fMRI. An example of series of volumes acquired during a motor localisation experiment is depicted in Figure 1.1. Each voxel in this series of volumes changes its MR signal intensity as time progresses. A voxel from the 3D volume in the left image of Figure 1.1 has a corresponding point on the y-axis in the right image showing the time course of that voxel. The x-axis shows the corresponding change of the BOLD-weighted MR signal as time progresses.

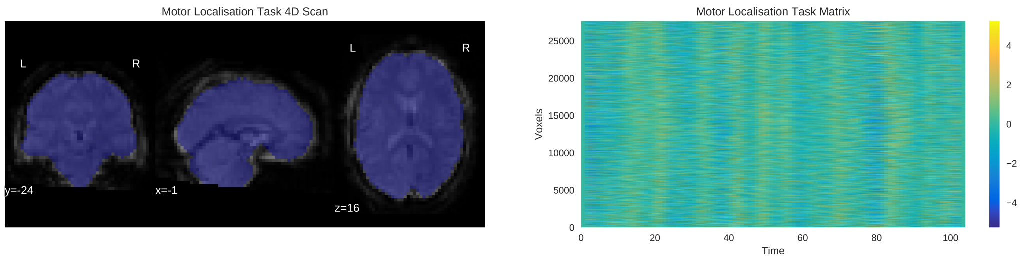

Figure 1.1: A motor localisation task fMRI scan (of the MSC cohort [Gordon et al., 2017]) in 4D form (left) and reshaped into a 2D matrix (right). The time courses in the 2D matrix are bandpass-filtered and normalised to zero mean and unit variance to emphasise spatially co-varying patterns.

1.3 The task and resting-state experiment

The introduced physical principles and techniques allow to observe change in blood perfusion across the brain. However, an experiment setting is required in which the researcher is able to alter blood perfusion in a controlled manner to allow for the desired brain function of interest to be studied.

Areas of the human brain are specialised for individual functions. For example, the sensory-motor cortex does distinct processing from the cortices for auditory or visual processing. Localised neuronal populations are thus more involved in the processing of a particular cortex-recruiting task, demanding more energy locally, which subsequently increases regional blood flow and changes the ratio between oxygenated and deoxygenated haemoglobin. The change in this ratio ultimately effects the MRI signal as discussed earlier.

The following illustrates the fMRI experiment setup on an example of a simple fMRI motor task. The subject lies inside the MRI scanner while being exposed to a presentation of task stimuli on a screen observed through a mirror fixed to the head coil.

The instructions on the screen require the subject to move body parts for a certain amount of time. These periods of task execution are interleaved with periods of rest as depicted in Figure 1.2. In addition to the functional scan, a structural MRI scan is acquired, which is used for the anatomical mapping of areas of blood perfusion change.

The general concept of a fMRI task experiment is to design a perceivable stimulus that locates cortical areas of increased neural activation specific to a particular function. A common task design consists of one or more binary time courses that resemble stimulus presentation timings. Each time course corresponds to a certain class of stimulus types, for example foot or hand in the motor task depicted in Figure 1.2. The binary time courses are convolved with smooth filters to obtain a model of the expected BOLD time course.

For each voxel of the 3D volume of the brain, the recorded MRI signal change is correlated with the expected BOLD time course. The resulting scores are aggregated into statistical activations maps. These inform the researcher with the areas of the brain that show increased activation while processing a task stimuli. The described task experiment, also called a task paradigm, comes in different forms in which timing, duration and magnitude of the stimulus are varied in a controlled manner. The time between two stimuli is hereby referred to as inter-stimulus interval (ISI). The most commonly used task paradigms are block design and event-related design.

Block designs consist of alternating periods (15-30 seconds) of task and rest conditions, for example as depicted in the motor task in Figure 1.2.

In contrast to block designs, event-related task designs present stimuli only for a few seconds with varying ISIs. A common approach is to use mixed block and event-related designs in

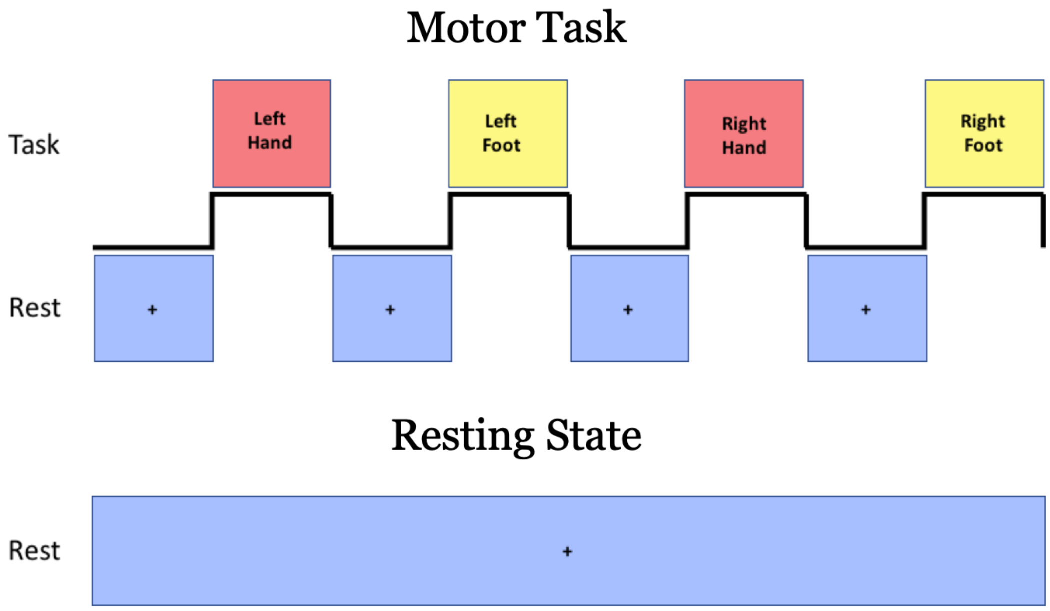

Figure 1.2: A common task paradigm for a fMRI motor task (first row). The researcher instructs the subject via a screen to move individual body parts. These periods of task activity are interleaved with periods of rest, in which the subject focuses on a crosshair (top row). The resting-state experiment requires the subject to watch the cross hair during the entire experiment. This is usually required to prevent head motion (bottom row).

which individual stimuli trains are encapsulated in task blocks. Other less common task designs are free-behaviour designs, in which a subject, for example, views short film clips before scanning and is asked to recall these clips during scanning.

Lastly, the resting-state experiment is a paradigm in which the subject is not exposed to any external stimuli. In contrast, the resting-state experiment is engaging the subject in uncontrolled intrinsic brain activity such as envisioning the future, remembering the past or mind wandering.

1.4 Image realignment and normalisation

One problem with fMRI is the signal-to-noise ratio (SNR) tends to be relatively low, hence single fMRI scans contain a significant amount of noise. Therefore, multiple subjects are aggregated in a cohort to examine activated areas engaged in a task experiment. Given that the structure of individual brains is unique, spatial normalisation is required to align brains of individual subjects into a shared analysis space. This process is outlined in Figure 1.3. The most commonly used space in fMRI is the Montreal Neurological Institute (MNI) space. The required registration processing pipeline comprises of several registration steps. Firstly, all volumes of an acquired fMRI scan are realigned to one volume of the scan, which is required because of potential head movement during the acquisition. Secondly, the realigned volumes are registered to an anatomical scan that is acquired in addition to the fMRI scan.

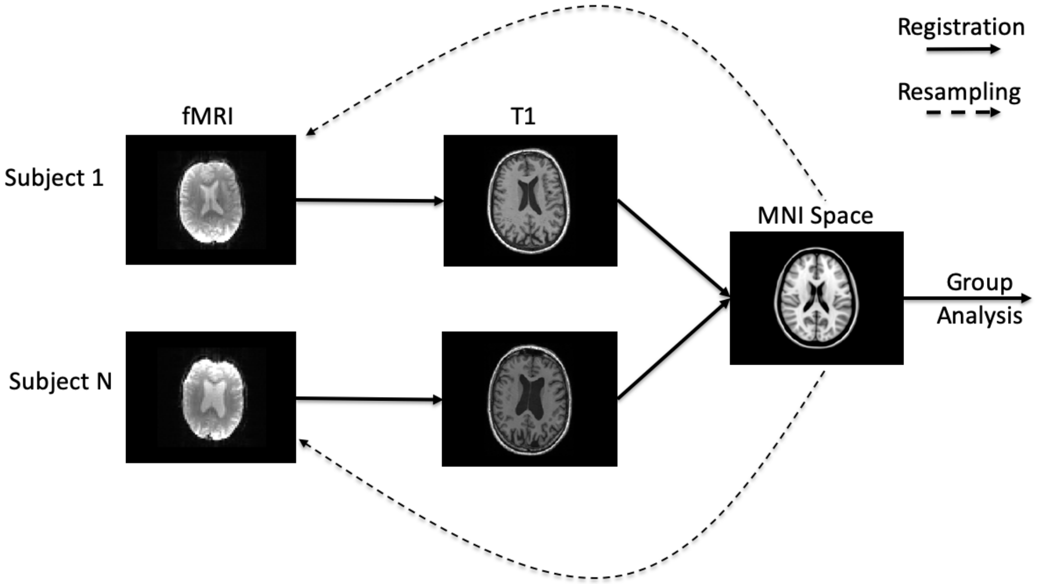

Figure 1.3: The common registration pipeline for fMRI group analysis. All volumes of a fMRI scan are realigned to a reference volume of the same scan, for example, the mean of all volumes. The reference volume is aligned with the corresponding structural scan of the subject with an affine registration. The structural scan is registered to the MNI template with a non-linear registration. The individual registrations are combined to resample each fMRI volume with only one interpolation in the MNI space.

This anatomical scan is registered to the anatomical template of the MNI space. Lastly, all volumes of an individual fMRI scan are resampled in MNI space by using the combined transformations that map each fMRI volume to the MNI space.

1.5 Image analysis

The actual analysis of areas engaged by the task experiment begins after all fMRI scans are aligned in MNI space as outlined in the previous section. The applied registration establishes imperfect but approximate spatial comparability between individual voxels of distinct subjects.

For task fMRI experiments, the “activity” in a voxel is defined as how closely the measured time course in that voxel follows the expected time course of the original task experiment. The “activity” is tested with a statistical framework provided by the General Linear Model (GLM). This approach results in a test statistic for each individual voxel in each subject. These aggregated test statistics for voxels are usually referred to as spatial mapping. The spatial mappings for subjects of an entire cohort are aggregated themselves and tested in a group model that comprises of another GLM. Depending on the hypothesis of the task experiment, contrasts between individual stimuli can be computed, for example vertical versus horizontally flickering pattern, to localise areas specific to the corresponding stimuli. Moreover, a task experiment can be performed by two different groups of subjects to ultimately compare where their statistical mappings differ in functional activation.

In contrast to task experiments, there is no hypothesised generative model of how the fMRI signal should behave during resting-state scanning. Instead, a compression of the fMRI data into an ambiguous number of components is obtained by approaches such as independent component analysis (ICA). The "activity" in a voxel of such an independent component (IC) is defined as the similarity of the time course of that voxel to the overall time course of the entire IC.

1.6 Thesis contributions

This thesis aims to develop image processing tools that improve various parts of the fMRI analysis pipeline starting at the pre-processing and ending with novel image decomposition techniques of fMRI scans. The development of these tools resulted in an open source set of software packages that will benefit the fMRI neuroimaging community.

These tools were motivated and developed for specific challenges faced in two fMRI cohorts. The first cohort comprises of preterm- and term-born adults (EPICure cohort). The resting-state fMRI data of the EPICure cohort were acquired with a TR of 3 seconds. The low TR caused physiological motion artefacts due to aliasing effects of the cardiac cycle contributing to signal variations of these fMRI time courses.

The second cohort comprises of elderly patients with forms of young-onset Alzheimer's disease (YOAD). The resting-state experiment for this cohort lasted only for 5 minutes, which created a challenge for the computation of robust single subject spatial maps and their subsequent comparison between groups in this cohort.

Although these tools were motivated by challenges faced in these two cohorts and will therefore benefit their analysis in particular, they are general enough and can be applied to a broad range of fMRI data. This will be shown on three open access cohorts publicly available, which can be used to independently reproduce the presented results.

The first part of this thesis is concerned with the removal of physiological motion artefacts from fMRI scans of the EPICure cohort using physiological recordings that were partially corrupted.

The fMRI signal is a mixture of BOLD-related and BOLD-unrelated signal change. BOLD-unrelated signal change results in structural artefacts shaped by the way the fMRI signal is acquired with EPI. The most prominent kind of BOLD-unrelated signal change is caused by head motion, which can even result in greater signal change than caused by the actual BOLD effect [Murphy et al., 2013]. Nevertheless, head motion can be controlled by subject foam padding or bite bars. Whereas the second most prominent source of structural noise patterns, physiological motion, is an inevitable contributing factor to fMRI time courses. Physiological motion is especially challenging because of the variability of cardiac and respiratory cycle unique in each subject. Physiological motion is a mechanical effect causing change in voxel tissue composition during acquisition, which ultimately results in time dependent slice artefacts.

Therefore, physiological recordings have a great importance in the removal of such physiological motion artefacts. However, physiological recordings have their own shortcomings with respect to robustness and practicality. For example, pulse plethysmography sensors are susceptible to motion, which can cause substantial periods of signal dropout. As a consequence, many fMRI cohorts are acquired without or partially corrupted physiological recordings, which ultimately prevents the use of physiological recordings for the effective removal of physiological motion artefacts.

To address corrupted physiological recordings in the EPICure cohort, a multi-task gaussian process (MTGP) model was proposed, which learned the correlation between a fMRI-derived and a physiological-derived heart rate variability estimate. The fMRI-derived heart rate is obtained from the fMRI scan by exploiting that fMRI volumes are acquired in a slice-wise manner with EPI. Therefore, a slice-wise signal (SWS) was obtained from areas of high time course variation in an acquired fMRI scan. The power spectrum of this SWS resembled the power spectrum of the recording from pulse plethysmography. This SWS underwent signal processing to extract the relevant frequency band of the cardiac cycle, and a heart rate variability was subsequently obtained from peak to peak distances.

A second heart rate was derived from peak to peak distances in the signal of the physiological recording. The MTGP model was trained on both of these heart rate variability estimates and ultimately used to predict heart rates in periods of signal corruption in the physiological recording.

This was followed by the development of two pre-processing pipelines called cardiac artefact motion removal (CAMR) and cardiac artefact motion removal with support vector machines (CAMR-SVM).

CAMR applied spatial ICA to individual fMRI scans to find physiological motion artefacts among obtained ICs. Manual artefact classification of such ICs is subjective and dependent on the decision of an expert given that the ground truth about these components is unknown. In contrast, CAMR exploited the intrinsic link between heart rate and corresponding aliasing frequencies in time courses of ICs to automate this otherwise manual classification and removal process. An open access cohort of 22 subjects acquired on a 7T scanner at the Max Planck Institute in Leipzig (MPI7T) was utilised to test the CAMR pipeline and provided data for the subsequent training of the CAMR-SVM model.

The CAMR model comprised of labelling ICs as physiological motion if their SWS explained a significant amount of variance in the physiological recording. These labelled ICs were subsequently used for training the CAMR-SVM model on temporal features of time courses of such ICs before CAMR-SVM was tested on the fMRI data of the EPICure cohort.

CAMR and CAMR-SVM resulted in a substantial reduction of cardiac aliasing frequencies in fMRI time courses in the EPICure and MPI7T cohort, respectively.

The second part of this thesis was concerned with group comparisons of brain networks between healthy and pathological individuals with distinct anatomical features. For example, comparing “activity” estimates in each voxel between subject groups can be biased by underlying anatomical characteristics, which are not fully accounted for by inter-subject registration.

Comparing groups of subjects with distinct anatomical features in MNI space, for example, normal versus atrophied brains, can translate into significant differences in the comparison of their corresponding fMRI mappings. In consequence, brain networks derived on fMRI data mapped into MNI space will likely result in artificial differences [Ji et al., 2019, Anticevic et al., 2008] in such cohorts. This phenomenon was observed in the EPICure cohort in which the comparison of individual subject maps between pre-term and term-born adults in MNI space resulted in significant differences in a dorsal attention network. On the contrary, the comparison of these spatial maps in subject-specific atlases resulted in no significant spatial differences.

The third part of this thesis was concerned with the derivation of robust spatial estimates of brain networks in individual subject scans of the YOAD cohort.

One problem with the short fMRI data of the YOAD cohort is that the SNR tends to be relatively low, hence individual fMRI images contain a significant amount of noise. In principle this noise problem could be addressed by lengthening the exposure time. However, it is difficult, as well as expensive, in practice for an elderly subject to spend a very long period in a MRI scanner.

Furthermore, noise patterns similar to the ones depicted in Figure 1.4 were found in the fMRI data of the YOAD cohort. An ensemble of many matrix factorisations (EMF) were used to address these challenges by obtaining robust spatial maps of individual brain networks despite intrinsic noise and short acquisition period of the fMRI scans. The comparison of obtained spatial map estimates between YOAD subjects and healthy elderly controls re-

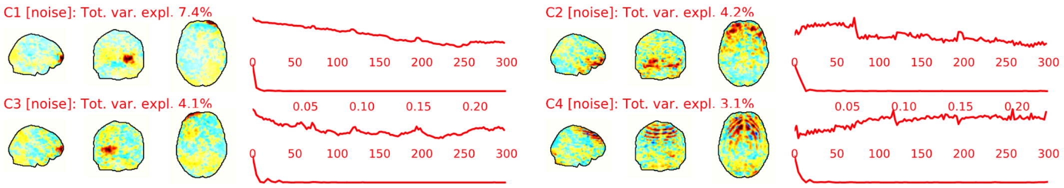

Figure 1.4: Four noise components determined in a fMRI scan with AROMA, an ICA-based denoising technique [Pruim et al., 2015].

sulted in differences in the default mode network (DMN) in the area of the precuneus cortex but also in a small regional cluster in the left and right hippocampus. These group differences obtained with EMF were compared to group differences obtained with ICA and Dual Regression (DR). The group comparison with ICA+DR resulted in similar differences in the precuneus cortex of the DMN. However, only EMF revealed these small but significant clusters in left and right hippocampus.

The last part of this thesis was concerned with the analysis of various fMRI task experiments of two publicly available cohorts, namely the Midnight Scan Cohort (MSC) and the Brainomics cohort. The EMF model was extended with a haemodynamic response filter (HRF). This so called Haemodynamic Matrix Factorisation (HMF) produced modes by using auto-encoding with convolutional kernels. Each obtained mode comprised of a spatial map and a neural activation time course. HMF was applied to the fMRI data of MSC and Brainomics cohort without knowing stimulus timings of their corresponding task designs. Modes were found whose neural activation time course matched with original stimulus timings in each of the examined tasks. In the MSC motor task, these modes showed that individual subjects confused experiment instructions, for example, moving left hand when actually right hand movement was given as experiment instruction.

The replacement of a canonical HRF with a subject-specific HRF in HMF resulted in a better temporal alignment between neural activation time course and corresponding task timings in MSC and Brainomics tasks.

1.7 Thesis organisation

The following will discuss the structure of the remaining chapters.

Chapter 2 presents a short review of the current hypothesis-driven and data-driven models for the analysis of task and resting-state fMRI with focus on the advantages and limitations of their most prominent models, GLM and ICA, respectively. In addition, a review of approaches for pre-processing of fMRI scans is provided.

Chapter 3 shows the derivation and application of the MTGP model, which is used to obtain robust heart rate estimates in periods of corrupted signal of the pulse plethysmography recording accompanying the fMRI scans of the EPICure cohort.

Chapter 4 introduces the pre-processing pipelines CAMR and CAMR-SVM, which are evaluated with respect to their ability to remove physiological motion artefacts from fMRI scans of the MPI7T and EPICure cohort.

Chapter 5 provides a comprehensive analysis of the EPICure cohort including the comparison of functional mappings and connectivity between preterm- and term-born adults.

Chapter 6 introduces the EMF model, evaluates short- and long-term reproducibility of derived single subject mappings with EMF from the YOAD cohort, and compares these spatial mappings to corresponding estimates derived with ICA and DR.

Chapter 7 presents the HMF model, the results of applying HMF to two publicly available task fMRI cohorts revealing some subjects did not comply with task instructions, and compares obtained modes to corresponding ICA estimates.

Chapter 8 concludes the thesis and outlines future research directions.

Derived Publications.

The work discussed in this thesis resulted in several conference and journal papers accepted or currently under review.

- **Hütel**, M., Melbourne, A., and Ourselin, S. Separating physiological motion artefacts from BOLD signal change with independent component analysis. Submitted for peer-review.

- **Hütel**, M., Antonelli, M., Melbourne, A. and Ourselin, S., 2021. Functional differences in the hippocampus in young-onset alzheimer's disease patients revealed by ensemble averaging of matrix factorizations. Submitted for peer-review to NeuroImage Clinical.

- Irzan, H., Molteni, E., **Hütel**, M., Ourselin, S., Marlow, N. and Melbourne, A., 2021. White matter analysis of the extremely preterm born adult brain. NeuroImage, 237, p.118112.

- Schirmer, M.D., Venkataraman, A., Rekik, I., Kim, M., Mostofsky, S.H., Nebel, M.B., Rosch, K., Seymour, K., Crocetti, D., Irzan, H. and **Hütel**, M., 2021. Neuropsychiatric disease classification using functional connectomics-results of the connectomics in neuroimaging transfer learning challenge. Medical image analysis, 70, p.101972.

- **Hütel**, M., Antonelli, M., Melbourne, A. and Ourselin, S., 2021. Hemodynamic matrix factorization for functional magnetic resonance imaging. NeuroImage, 231, p.117814.

- Raison, N., **Hütel**, M., Brunckhorst, O., Aydin, A., Ahmed, K., Ourselin, S. and Dasgupta, P., 2020. MP34-17 Assessment of mental imagery by neuroimaging for surgical development: the mind trial. The Journal of Urology, 203(Supplement 4), pp.e509-e510.

- Irzan, H., **Hütel**, M., Semedo, C., O'Reilly, H., Sahota, M., Ourselin, S., Marlow, N. and Melbourne, A., 2020. A network-based analysis of the preterm adolescent brain using PCA and graph theory. In Computational Diffusion MRI (pp. 173-181). Springer, Cham.

- **Hütel**, M., Antonelli, M., Ekanayake, J., Ourselin, S. and Melbourne, A., 2019, October. Haemodynamic Matrix factorisation for functional magnetic resonance imaging.

In Connectomics in NeuroImaging: Third International Workshop, CNI 2019, Held in Conjunction with MICCAI 2019, Shenzhen, China, October 13, 2019, Proceedings (Vol. 11848, p. 117). Springer Nature.

- **Hütel**, M., Melbourne, A. and Ourselin, S., 2018, September. Neural activation estimation in brain networks during task and rest using BOLD-fMRI. In International conference on medical image computing and computer-assisted intervention (pp. 215-222). Springer, Cham.

- **Hütel**, M., Melbourne, A., Thomas, D.L. and Ourselin, S., 2018, September. Cardiac cycle estimation for bold-fmri. In International Conference on Medical Image Computing and Computer-Assisted Intervention (pp. 267-274). Springer, Cham.

- Georgiadis, K., Young, A.L., **Hütel**, M., Razi, A., Semedo, C., Schott, J., Ourselin, S., Warren, J.D. and Modat, M., 2018, September. Computational modelling of pathogenic protein behaviour-governing mechanisms in the brain. In International Conference on Medical Image Computing and Computer-Assisted Intervention (pp. 532-539). Springer, Cham.

- **Hütel**, M., Melbourne, A., Beckmann, J., Rohrer, J., Marlow, N., and Ourselin, S., Resting-state network patterns in extremely preterm born young adults. Accepted for ISMRM, 2017.

- **Hütel**, M., Melbourne, A., Thomas, D., Rohrer, J., and Ourselin, S., Sparse networks analysis of individual resting-state bold-fmri. Accepted for ISMRM, 2017.

- Lane, C.A., Parker, T.D., Cash, D.M., Macpherson, K., Donnachie, E., Murray-Smith, H., Barnes, A., Barker, S., Beasley, D.G., Bras, J. and Brown, D., (**Hütel**, M. among et al.) 2017. Study protocol: Insight 46–a neuroscience sub-study of the MRC National Survey of Health and Development. BMC neurology, 17(1), pp.1-25.

- Bocchetta M, Toussaint N, **Hütel** M, Modat M, Cardoso MJ, Gordon E, Dick KM, Cash DM, van Swieten J, Borroni B, Galimberti D, Masellis M, Graff C, Tagliavini F, Frisoni GB, Laforce Jr R, Finger E, de Mendonca A, Sorbi S, Warren JD, Ourselin S, Rohrer JD, on behalf of the Genetic FTD Initiative (GENFI). Multimodal imaging analysis of C9orf72-associated FTD in the Genetic Frontotemporal dementia Initiative (GENFI) study. Journal of Neurochemistry. 2016; 138 (Supplement S1):245.

- **Hütel**, M., Melbourne, A., Rohrer, J., and Ourselin, S., The hidden heart rate in the slice-wise BOLD-fMRI global signal. Accepted for ISMRM, 2016.

- **Hütel**, M., Melbourne, A., Thomas, D.L. and Ourselin, S., An over-complete and efficient ICA for BOLD-fMRI. Accepted for ISMRM, 2016.

Chapter 2

Literature review

This chapter begins by describing important characteristics of BOLD-weighted MRI signal behaviour. This lays the foundation for the subsequently discussed fMRI analysis models for task and resting-state experiment. Lastly, fMRI pre-processing approaches for the removal of head and physiological motion are reviewed. The chapter concludes with summarising the most common analysis pipelines for task and resting-state fMRI experiment.

2.1 Characteristics of the BOLD-weighted MR signal

The following briefly introduces the MR physics behind the BOLD-weighted signal generation. Change in BOLD-weighted signal is observed due to blood perfusion changes indirectly caused by change in neural activation in activated brain areas. The second part discusses properties of linear time-invariant systems and their relation to BOLD signal characteristics.

2.1.1 The MR signal compartment model

The volume captured by a voxel of a few millimetres in fMRI comprises of blood and extravascular tissue including white matter (WM), grey matter (GM) and cerebrospinal fluid (CSF). Thus, the MR signal contribution in one voxel is a sum of individual signal contributions of compartments as described by the following equation:

$$S(t) = \sum_i \rho_i(t) * V_i(t) * M_{ss,i}(t) * e^{R^*_{2,i}(t)TE}, \tag{2.1}$$

where ρ is the water proton density, V is the volume fraction,

$$M_{ss} = (1 - e^{-R^*_1(t)TR}) \sin\theta (1 - \cos\theta e^{-R^*_1(t)TR}) \tag{2.2}$$

is the steady-state magnetisation with repetition time TR, echo time TE, flip angle θ, longitudinal and transverse relaxation rate $R^*_1(t) = \frac{1}{T^*_1(t)}$ and $R^*_2(t) = \frac{1}{T^*_2(t)}$ with longitudinal and transverse relaxation time $T^*_1(t)$ and $T^*_2(t)$, of the i-th compartment as described by Kim and Ogawa [2012]. The parameter TE is optimised to make the MR signal in Equation 2.1

most sensitive to the BOLD effect for a given field strength. However, this theoretical model is not used in practice. Instead, a simplified equation for the MR signal $S(t)$ is used as described by Liu [2016]:

$$\begin{aligned}
\Delta S(t) &\approx \Delta S_0(t) \cdot \left.\frac{\partial S}{\partial S_0}\right|_{t=0} + \Delta R_2^*(t) \cdot \left.\frac{\partial S}{\partial R_2^*}\right|_{t=0} + \Delta n(t) \\
&= \Delta S_0(t) \cdot \exp\left(-R_2^*(0) \cdot \mathrm{TE}\right) - \Delta R_2^*(t) \cdot S_0(0) \cdot \exp\left(-R_2^*(0) \cdot TE\right) \cdot TE + \Delta n(t) \\
&\approx S(0) \cdot \frac{\Delta S_0(t)}{S_0(0)} - S(0) \cdot \mathrm{TE} \cdot \Delta R_2^*(t) + \Delta n(t) \\
\frac{\Delta S(t)}{S(0)} &\approx \frac{\Delta S_0(t)}{S_0(0)} - \mathrm{TE} \cdot \Delta R_2^*(t) + \frac{\Delta n(t)}{S(0)}
\end{aligned} \tag{2.3}$$

where $\frac{\Delta S_0(t)}{S_0(0)}$ is the relative change in magnetisation at zero echo time, $TE \cdot \Delta R_2^*(t)$ is the relative change in the transversal relaxation rate multiplied with the echo time and $\frac{\Delta n(t)}{S(0)}$ is the relative change in the background noise [Liu, 2016]. The MR signal in Equation 2.3 has its highest BOLD-sensitivity at TE equal to $1/R_2^*$ and is almost independent to the BOLD effect at TE zero. The acquisition of the MR signal at multiple echo times instead of acquiring the MR signal at only one optimised TE is called multi-echo fMRI. The change in the relaxation rate $\Delta R_2^*(t)$ reflects changes in blood oxygenation, flow and volume. It is therefore referred to as BOLD-related MR signal change. In contrast, change in the magnetisation rate $\frac{\Delta S_0(t)}{S_0(0)}$ is referred to as BOLD-unrelated MR signal change.

2.1.2 Motion confounds altering the MR signal

The previous section described the physical origin of the BOLD signal. However, the MR signal contributions are not only determined by the BOLD effect. Head and physiological motion alter the MR signal and introduce artificial correlations and activations in subsequent fMRI analysis. The following will discuss the impact of head and physiological motion on the BOLD-weighted MR signal.

2.1.2.1 Head motion

Participant head movement during scanning can cause large signal fluctuations in the MR signal. Firstly, the change of position of the head changes the tissue composition in each voxel. The resulting change in the magnetisation rate $\frac{\Delta S_0(t)}{S_0(0)}$ can cause a substantial change in the MR signal amplitude. The spatial locations of these signal changes are most pronounced at tissue borders between grey and white matter or at the air tissue border of the brain (see Murphy et al. [2013] or Maknojia et al. [2019] for a review).

Secondly, there are inhomogeneities in the magnetic field that require shimming of the field, a process that makes the magnetic field more homogenous. Before the actual fMRI scan is acquired, the magnetic field is shimmed for the participant's head position. Any head movement is changing the locations of distortions and signal dropout, ultimately impacting the magnetisation rate $\frac{\Delta S_0(t)}{S_0(0)}$.

Lastly, any alteration in tissue composition within a voxel will lead to a change in the MR signal because the amplitude of the net magnetisation is determined by the number of spins in each voxel. Tissue movement will change the time between excitations in the portion of tissue that has moved to an adjacent slice. This relocation changes the steady state magnetisation, which will subsequently require several TRs to recover. This undesired change of the MR signal, called spin history effect, can often be up to twice the expected amplitude change caused by the BOLD effect [Murphy et al., 2013].

The discussed MR signal changes can occur due to random head motion in task or resting-state experiments and prevent the detectability of functional activation. In contrast to random head motion, head motion correlated with task stimuli can increase the false positive rate in the subsequent task analysis. For example, tasks of overt word generation cause local nonrigid movement of pharynx, tongue, and jar, which ultimately alter the magnetic field [Gopinath et al., 2009]. The largest distortion of the magnetic field due to speech occur hereby in the inferior, temporal, and frontal regions of the brain. These areas eventually present as false positive activations with similar statistical significance than areas with actual BOLD signal change [Birn et al., 1998, 2004, Johnstone et al., 2006].

The next section discusses physiological motion, an unavoidable source of noise caused by cardiac and respiratory cycle in the brain. In contrast to physiological motion, head motion can be controlled for by the researcher, for example with casts [Edward et al., 2000] or bite bars [Chang et al., 2009, Chang and Glover, 2009b,a, 2010].

2.1.2.2 Cardiac and respiratory-cycle induced motion artefacts

Physiological motion is caused by processes of the cardiac and respiratory cycle. For example, Friston et al. [1996] reported spatially altered spin history due to small head movements triggered by breathing. Cardiac pulsation and respiration cycle push the brain stem into surrounding tissue [Dagli et al., 1999], which causes tissue deformation and displacement of CSF, resulting in a great signal variability within these areas as depicted in Figure 2.4. The effect is most visible at tissue boundaries and around large vessels such as the superior sagittal and transverse sinus. Given that scans are commonly acquired with EPI, the impact of physiological bulk motion is different at each slice and depends on the phase of the corresponding physiological cycle.

Section 2.1.2 discussed artificial MR signal change due to head and physiological motion. The reader is referred to Murphy et al. [2013] for a detailed discussion of other less prevalent noise sources in fMRI.

2.2 Hypothesis-driven fMRI models

The success of approximating the haemodynamic response with linear models led to the widespread adoption of the general linear model (GLM) for the analysis of task fMRI experiments [Poline and Brett, 2012]. Task experiments are based on the hypothesis that a mapping of function to localised brain areas can be found. No other model than the GLM has reached such widespread popularity and adoption for the analysis of task fMRI experiments [Poline and Brett, 2012]. On the contrary, blind source separation (BSS) techniques are most prominent for the analysis of resting-state fMRI experiment data in which the brain is not brought into a controlled state but left to processing such as mind wandering or envisioning the future.

The following section provides a brief overview of the GLM as one of the most prominent hypothesis-driven approaches. This is followed by a review of matrix factorisation approaches, which are the most prominent data-driven approaches for the analysis of task and resting-state fMRI.

And lastly, neurophysiological approaches specifically designed for fMRI are reviewed. These approaches incorporate knowledge about characteristics of the haemodynamic response apriori in the model design and invert an assumed haemodynamic forward model to infer underlying change in neural activation.

2.2.1 Linear time-invariant systems

The majority of fMRI models rest on the assumption that neural activity translates into a BOLD signal change by following the laws of a linear time-invariant (LTI) system. Given this assumption, the translation of neural activation change into BOLD signal change is modelled as a filter operation. The impulse response function (IRF) of this linear system is referred to as haemodynamic response function (HRF) in the fMRI literature[1]. Two properties are essential in a LTI system, namely additivity and homogeneity. These characteristics are known as superposition principle. The additivity property requires the sum of BOLD responses of two separate neural activations to be equal to the BOLD response of one single neural activation of the same time duration. An example for two individual 10s boxcar activations (left column green and red) and one 20s boxcar activation (left column blue) is depicted in Figure 2.1. The sum of BOLD responses (right column blue dashed line) and their individual counterparts (right column green and red) match the BOLD response (straight blue line) of the individual neural activations. Homogeneity dictates that BOLD responses scale with the intensity of the underlying neural activity as depicted in Figure 2.2. The early days of fMRI were concerned with the question if the LTI model provides a good approximation for observed BOLD signal change; namely if the two mentioned properties

---

[1] Mind the fMRI communities' adoption of the interchangeability of HRF and IRF.

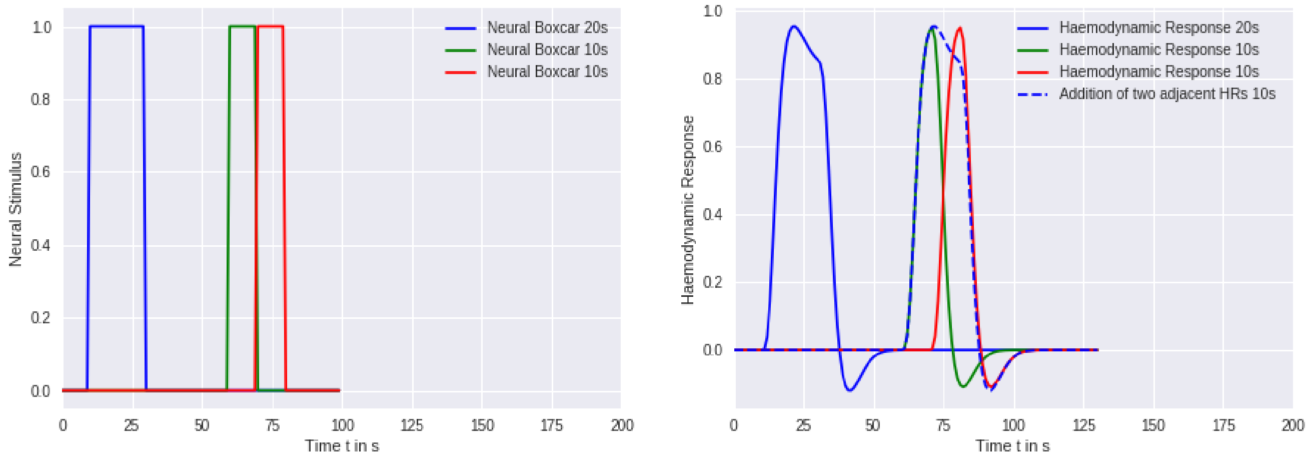

Figure 2.1: Additivity in the context of fMRI. The left plot depicts two 10 seconds idealised boxcar activations (red and green) and one 20 seconds idealised neural activation (blue). These are convolved with the HRF to obtain corresponding BOLD responses depicted in the right plot. The addition of the two BOLD responses of the 10 second neural activity equals the BOLD response of the 20 seconds neural activation.

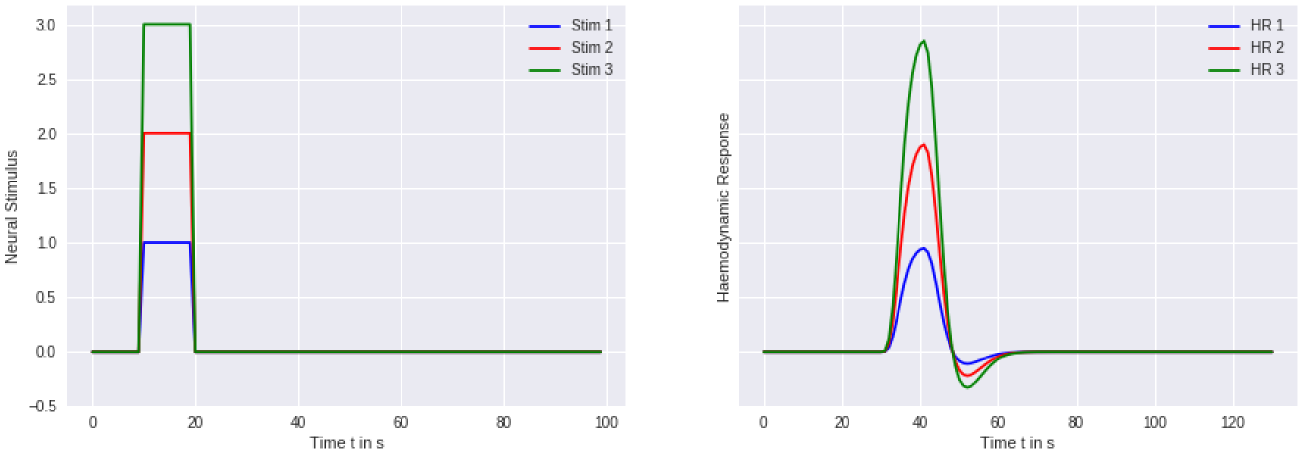

Figure 2.2: Homogeneity in the context of fMRI. The left plot shows three idealised neural activations of either intensity 1 (blue), 2 (red) and 3 (green). The right plot shows the corresponding haemodynamic response of each of these neural activations.

hold in fMRI task experiments.

The first group to put the assumed superposition principle for BOLD responses under scrutiny was Boynton et al. [1996] looking at the behaviour of the BOLD response after visual stimulation in the primary visual cortex (V1). Boynton et al. presented checker-board patterns to subjects displayed for 3, 6, 12 or 24 seconds. Boynton et al. showed that BOLD responses of 12s and 24s stimuli were closely approximated by a train of BOLD responses of individual 6s stimuli. Although, the BOLD response of 6s, 12s and 24s stimuli were less well approximated by adding BOLD responses of individual 3s stimuli.

Therefore, they concluded the additivity property may be inaccurate for stimulus exposure of 3 seconds or less. To test the homogeneity property, Boynton et al. assumed an increase in contrast of the checker-board stimulus would lead to an increase of neural activation. Their results showed that more contrast resulted in a scaled BOLD response of similar shape. Nevertheless, the BOLD response was not linearly increasing with the applied stimulus, which is expected given the assumption that the brain behaves in a highly non-linear fashion. However, evidence for the homogeneity assumption comes from animal models. For example, Albrecht and Hamilton [1982] showed that the majority of V1 neurons increase their firing rate monotonically with increased stimulus contrast.

Therefore, Boynton et al. [1996] were the first to show that induced BOLD signal change in the V1 area of the human brain approximately followed the superposition principle of a LTI system. Their work was in several ways remarkable. Not only have they provided evidence for the LTI hypothesis but also introduced a parametrised Gamma distribution model as the HRF[2] that was adapted by many subsequent studies [Boynton et al., 2012]. Their filter model was extended to a fixed parameter two gamma distribution model by groups like Glover [1999] or Friston et al. [1994] and is known today as the canonical HRF depicted in Figure 2.3.

Animal studies of the visual cortex [Logothetis et al., 2001, Logothetis and Wandell, 2004, Logothetis, 2008a] have led to the assumption in fMRI task experiments that neural activity is either on or off following the exact timing of a presented stimulus. The binary neural activity assumption in task experiments has shaped the fMRI literature for decades and constitutes the origin of hypothesis-driven models in fMRI.

2.2.2 The General Linear Model

The GLM has a lot of advantages for the analysis of task fMRI experiment data. It guarantees the best linear unbiased estimate assuming that the residual error is identically and independently distributed. Furthermore, it allows to quantify the uncertainty of individual

---

[2] The concept of modelling the HRF with a gamma distribution was borrowed from NASA scientist Watson et al. [1986], who modelled the visual perception of motion in the human eye as a LTI system using a Gamma distribution as the IRF.

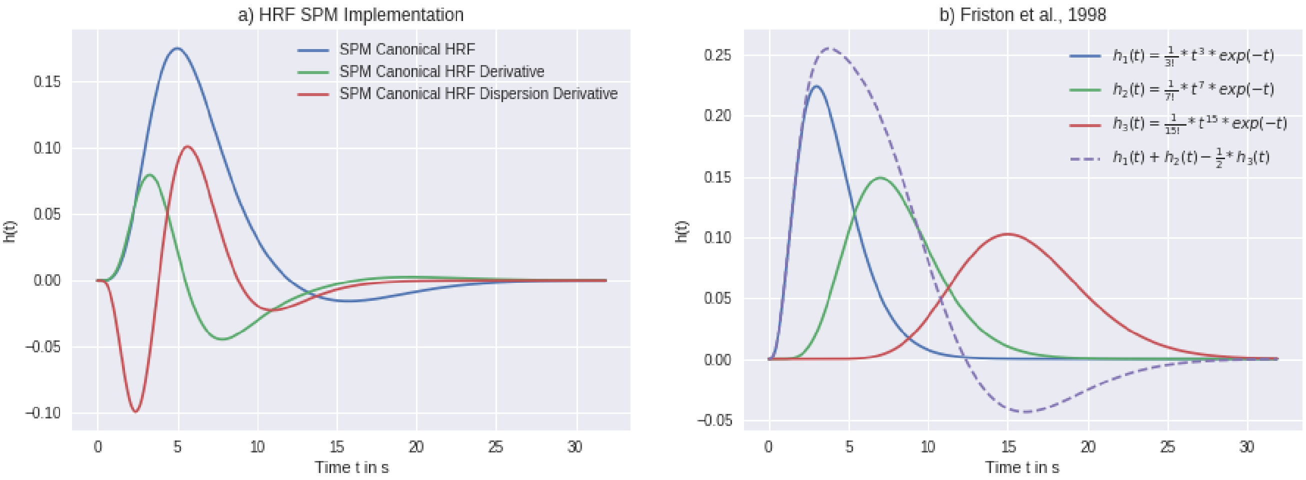

Figure 2.3: The canonical HRF and its first and second derivative are commonly used basis functions implemented in SPM $\Psi(t) = A\left(\frac{t^{\alpha_1 - 1}\beta_1^{\alpha_1}e^{-\beta_1 t}}{\Gamma(\alpha_1)} - c\frac{t^{\alpha_2 - 1}\beta_2^{\alpha_2}e^{-\beta_2 t}}{\Gamma(\alpha_2)}\right)$ with $\alpha_1 = 6$, $\alpha_2 = 16$, $\beta_1 = 1$, $\beta_2 = 1$, $c = \frac{1}{6}$. Parameter A defines the amplitude of the response. Γ represents the gamma function.

spatial estimates, and therefore, the GLM provides a rigorous statistical framework for the analysis of fMRI task experiments.

A typical model composition for the analysis of acquired fMRI time courses comprises of the hypothetical neural activation caused by the experiment stimulus convolved with a haemodynamic filter as discussed in the previous section. Early fMRI task designs [Bandettini et al., 1993, Friston et al., 1995, Boynton et al., 1996] assumed a simple constant HRF but evidence later emerged that, firstly, the shorter the stimuli the more important the correct shape of the HRF because of otherwise introduced error between modelled and actual BOLD signal, and secondly, that there was substantial variability of the HRF across subjects [Richter and Richter, 2003, Handwerker et al., 2004].

One reason why the GLM has been proven so successful in the study of fMRI task experiments is its flexibility to parameterise the HRF filter. The constant HRF can be exchanged with a HRF composed of multiple basis functions. For example, an extension to three different gamma distributions was proposed by Friston et al. [1998] depicted in Figure 2.3.

The most flexible task design is the finite impulse response (FIR) model. Hereby, the HRF is modelled by a number of finite impulse responses. However, the increase in the number of model parameters is substantial compared to designs with a limited set of basis functions. Therefore, the FIR design requires regularisation to prevent over-fitting. For example, Goutte et al. [2000] proposed placing Gaussian priors on GLM estimates to enforce smoothness in obtained HRFs.

The discussed variations of the GLM from limited basis functions to flexible FIR designs are by far the most applied approaches to localise brain function in task experiments [Poline and Brett, 2012]. This underpins the great adaptability of the GLM approach.

In contrast, other groups have proposed to use non-linear fitting techniques to estimate a parametrisation of a set of basis functions [Kruggel et al., 2000, Miezin et al., 2000, Lindquist and Wager, 2007]. However, non-linear fitting requires parameter estimation in each voxel separately and is thus impractically slow and much less applicable than using a computational efficient matrix formulation that solves the GLM for multiple voxels at the same time [Lindquist and Wager, 2007, Lindquist et al., 2009].

The GLM constitutes a mass-univariate approach for which each voxel is estimated independently and is fully specified by the explanatory covariates. Its conceptional weakness is that BOLD signal change from task processing is modelled while ongoing intrinsic brain activity is neglected. The following will introduce matrix factorisation models not requiring stimulus timings as input and therefore applicable to both, task and resting-state fMRI experiments.

2.3 Data-driven fMRI models

The GLM requires knowledge of the task experiment. The unobserved neural activation is assumed to be equal to the binary on/off task stimuli. In contrast to discussed GLM approaches, matrix factorisation models do not model each voxel independently but instead generate observed BOLD signal in each voxel from a set of compact spatial and temporal basis functions.

The estimation of these spatial and temporal basis functions is an ill-posed problem because nothing is known except the actually observed fMRI time courses. Spatial maps, time courses or both are therefore assumed to hold certain statistical properties.

Matrix factorisation approaches can broadly be separated into approaches that either derive parcellations [Schaefer et al., 2017, Eickhoff et al., 2018] or modes [Friston, 1998, Harrison et al., 2015].

Parcellation approaches find a non-overlapping clustering of the brain. More specifically, Eickhoff et al. [2018] describe an individual parcel as a ‘field that is distinguished from its neighbours by (sharp) changes in structure, function and connectivity’. Brain parcellations for fMRI analysis can originate from anatomical parcellations [Schaefer et al., 2017], clustering of fMRI time courses [Abraham et al., 2013, Ding et al., 2013, Wang et al., 2015] or clustering of characteristics from multi-modal neuroimaging [Glasser et al., 2016].

Similar to clustering, modes are inferred from voxels of similar time course behaviour. The intensity value of a voxel in a corresponding spatial map of a mode describes how well the time course of that voxel is explained by the overall time course of that mode. In contrast to parcellations, individual voxels can be part of many of such modes.

The most prominent approach to obtain modes from a given fMRI experiment is Independent Component Analysis (ICA). ICA relies on the assumption of statistical independence between individual sources. Implementations of ICA can only approximate independence by using a proxy function for statistical independence [Stone, 2004]. The most prominent ICA algorithms either operate on minimising mutual information between sources or maximising non-Gaussianity of the value distributions of sources. InfoMax [Bell and Sejnowski, 1995] and FastICA [Hyvärinen and Oja, 1997, Hyvarinen, 1999] are implementations for the mutual information and non-Gaussianity approach, respectively. However, Daubechies et al. [2009] showed that FastICA and InfoMax rather select for mutually exclusive sparse than statistically independent components. Therefore these approaches are less well suitable for fMRI but both are still widely prevalent fMRI software packages [Beckmann and Smith, 2004, Calhoun and Adali, 2012, Varoquaux et al., 2010]. Other less prominent proxy functions assume temporal complexity of any signal mixture is greater than temporal complexity of its constituent signals [Stone, 2004].

Statistical independence is either imposed on time courses, spatial maps, or on both, referred to as temporal ICA (tICA), spatial ICA (sICA) and spatial-temporal ICA (stICA), respectively [Stone, 2004]. Spatial ICA is the most widely applied approach to fMRI because the number of voxels in each scan is usually substantially larger than the number of time points [Smith et al., 2012].

Similar to GLM analysis, spatial ICA can be applied to a single fMRI scan but produces subject-dependent decompositions without a one-to-one association across spatial maps estimated for different subjects. In order to obtain a set of group spatial maps for an entire cohort, individual spatial maps can be merged in a hierarchical fashion. However, ICA computation per subject prevents comparing spatial maps across subjects because of the ambiguity of obtained ICs and the lack of means for statistical testing.

To address these issues, a two step pipeline is commonly in use shared by various approaches. Firstly, a set of group spatial maps is obtained. Therefore, fMRI scans are concatenated in time. Subsequently, a dimensionality reduction approach is applied which either comprises of one or multiple PCA reductions [Smith et al., 2014, Calhoun et al., 2015, Erhardt et al., 2011], canonical correlation analysis [Varoquaux et al., 2010] or Laplacian eigenmaps [Liu et al., 2018] dependent on memory limitations imposed by the number of time points and subjects. This is followed by spatial ICA to obtain spatial group maps.

Secondly, individual subject maps are obtained and compared with GLM analysis to retain a statistical test framework.

There are two principle approaches to reconstruct subject-specific from group spatial maps: back-reconstruction (BR) and dual regression (DR). The BR approach inverts subject loadings of the PCA reduction step(s) to obtain individual subject maps [Erhardt et al., 2011]. In contrast, DR comprises of two individual regression models. In the first regression model, spatial group maps are used to obtain subject-specific time courses. These time courses are then used in the second regression model to obtain individual subject maps [Beckmann et al., 2009]. Experiments comparing DR and BR concluded that both approaches result in similar subject-specific maps [Nickerson et al., 2017, Erhardt et al., 2011]. However, DR has the major advantage that it is not tied to the original fMRI scans used to derive group maps. Instead, DR can be used with spatial maps derived from a left-out or other fMRI cohort. This is crucial for preventing circular analysis (double dipping), which is a term for using the same data sample for exploratory and selective analysis [Kriegeskorte et al., 2009, Button, 2019].

2.3.1 Neurophysiological models

The discussed approaches for task and resting-state fMRI analysis lack unified approaches that model the entirety of BOLD signal change in an fMRI scan while maintaining the relation to underlying neural activation and spatial characteristics of the haemodynamic response.

The GLM models areas of the brain engaged in specific task processing but ignores intrinsic brain activity unrelated to these tasks. Such intrinsic brain activity was long considered noise before found to produce coherent spatial patterns of brain activity, which are referred to as resting-state networks (RSNs) [Raichle et al., 2001, Gusnard and Raichle, 2001, Fox and Raichle, 2007]. The nature of these spontaneous brain activity requires exploratory data-driven techniques such as the discussed spatial ICA approach, which are able to recover brain networks from resting-state fMRI experiments. However, these approaches do not model the association between task stimulation and BOLD signal change.

Furthermore, these generic multi-purpose matrix factorisation approaches do not incorporate spatial or temporal characteristics of fMRI data. For example, one could rearrange the order of time points of a fMRI scan without affecting the decomposition produced by spatial ICA.

Therefore, the last decade has seen developments in data-driven analysis approaches recovering experiment stimuli from task fMRI data without knowing their timings nor duration [Cole et al., 2010, Rangaprakash et al., 2018]. These models usually entail a haemodynamic forward model but, in contrast to the aforementioned GLM, belong to the class of data-driven approaches. For example, models were proposed that either use a fix impulse function, such as an estimated subject-specific HRF [Glover, 1999] or a canonical HRF [Gaudes et al., 2011], or non-linear models of the haemodynamic response [Karahanoğlu et al., 2013a].

Similar to the challenge of number of components ambiguity in matrix factorisation models, two different neural activation time courses can cause the exact same BOLD response because mapping between neural activation and haemodynamic response is not bijective [Rangaprakash et al., 2018].

Therefore, neural activation time courses of these models are optimised for certain statistical characteristics, for example, temporal sparsity or smoothness.

One of the first papers concerned with estimating neural activation proposed Wiener deconvolution filtering [Glover, 1999] but does not constrain shape of estimated neural activation. Zarahn et al. estimates neural activation in the time domain instead of the frequency domain using a set of limited basis functions [Zarahn, 2000]. These two contributions were generalised by others [Gitelman et al., 2003, McLaren et al., 2012] to a more general framework for the estimation of neural activation time courses using gaussian priors.

Most commonly, recent deconvolution approaches use some form of sparsity to regularise neural activation time courses. Approaches based on linear regression use Tikhonov regularisation [Gaudes et al., 2011] or the Least Absolute Selection and Shrinkage Operator (LASSO) [Hernandez-Garcia and Ulfarsson, 2011, Caballero Gaudes et al., 2013]. Other approaches use sparsity regularisation in the Wavelet domain with custom wavelet basis functions tailored to the characteristics of the HRF [Khalidov et al., 2011]. All aforementioned deconvolution approaches are applied to individual BOLD time courses without leveraging similar behaviour of adjacent voxels.

In addition to sparsity regularisation of the neural activation estimates in each voxel, the approach Total Activation (TA) [Karahanoğlu et al., 2013a, Farouj et al., 2017, Zöller et al., 2019] uses spatial priors enforcing temporal similarity within spatial regions.

TA constitutes a parcellation-based approach in which each voxel is assigned to only one cluster. Similar to Abraham et al. [2013], the assignment of each voxel is achieved by minimising spatial total variation in addition to inverting the haemodynamic forward model.

In contrast, mode-based approaches allow for overlapping clusters with one voxel being part of multiple clusters. One recent approach has been proposed by Harrison et al. [Harrison et al., 2015, 2019], which decomposes a cohort of fMRI subjects into group and single subject spatial maps modelling the intrinsic auto-correlation in BOLD time courses and spatial correlation among adjacent voxels.

The past sections have provided a brief overview of the most common approaches to analyse task and resting-state fMRI experiments. The following section will complement this overview with how these models are combined with approaches to remove various noise sources from fMRI data.

2.4 fMRI pre-processing

Physiological and head motion artefacts manifest as spatially structured noise patterns in fMRI scans as previously discussed in Section 2.2. The following discusses pre-processing techniques for the removal of such noise contributions.

2.4.1 Pre-processing with physiological recordings

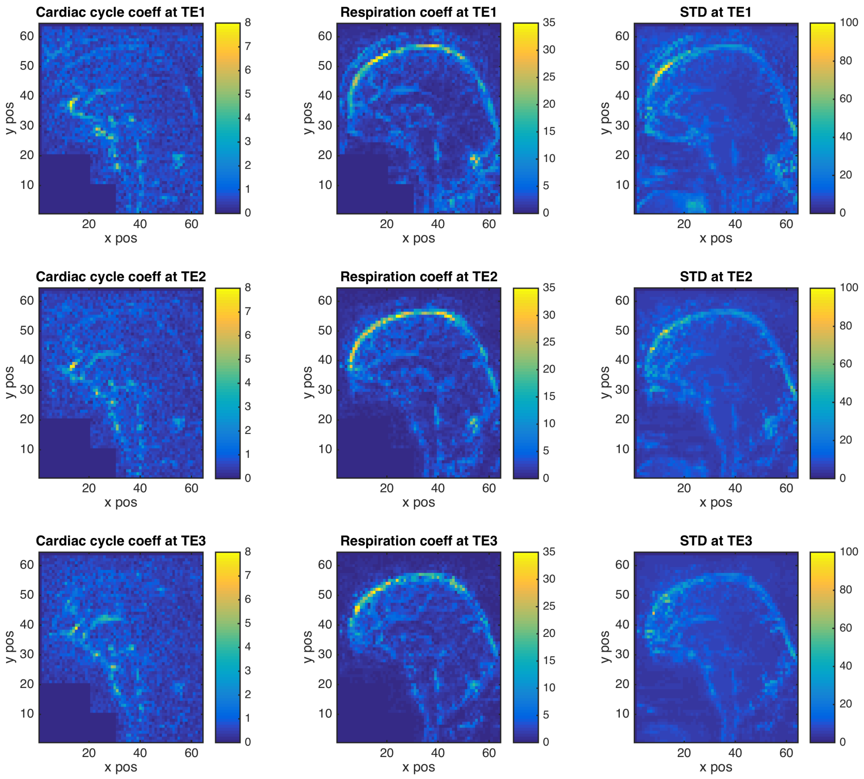

Figure 2.4: The mapping of cardiac (first row) and respiratory (second row) coefficients from RETROICOR onto the middle sagittal slice of the acquired fMRI scan depicts the large influence of physiological cycles in the vicinity of large blood vessels. Regions influenced by physiology also show high similarity to regions with the greatest standard deviation of BOLD time course fluctuations (third row).

The recording of physiological cycles using breathing belts and pulse oximeters to correct for the slice dependent signal artefacts caused by physiological motion is becoming more common.

The most prominent technique for such retrospective correction of physiological motion effects in fMRI (RETROICOR) [Glover et al., 2000] calculates the phase of cardiac and respiratory signals with reference to corresponding slice acquisition times. Physiological motion from respiration and cardiac cycle components are approximated by their low-frequency Fourier series expansion given by

$$y_\delta = \sum_{m=1}^{M} a_m^c cos(m\phi_c) + b_m^c sin(m\phi_c) + a_m^r cos(m\phi_r) + b_m^r sin(m\phi_r) \ , \qquad (2.4)$$

where a_m^c, b_m^c and a_m^r, b_m^r are corresponding coefficients for cardiac and respiratory function respectively, and $\phi_c(t)$ and $\phi_r(t)$ are the phases in the respective cardiac and respiratory cycles at time t.

Figure 2.4 depicts cardiac and respiratory coefficient mappings estimated with the RETROICOR model for a sagittal slice of *my brain* acquired with high temporal resolution using a multi-echo BOLD-weighted EPI sequence with echo times 8.3ms, 21.4ms and 34ms and TR 300ms on a Siemens Trio scanner. The first column shows sum of first and second order cardiac coefficients at distinct TEs. The second column shows the corresponding respiratory coefficients and the third column shows standard deviation across time courses calculated in each voxel.

The RETROICOR model has been extended with additional regressors such as respiratory volume change per time (RVT) [Birn et al., 2006, 2008] or heart rate variability (HRV) [Chang et al., 2009, Shmueli et al., 2007]. Other groups proposed to use the down-sampled pulse oximetry recording as regressor because its exhibited power in frequencies matched those found in independently recorded cardiac and respiration signals [Verstynen and Deshpande, 2011].

Recordings from pulse oximetry sensors may exhibit poor signal quality due to subject motion, lack synchronisation information to scanner triggers, or are regarded as a time-consuming setup before fMRI acquisition within a clinical setting [Gray et al., 2009].

The discovery of the overlap between high standard deviation and physiological model coefficients has therefore led to approaches in which noise covariates are derived from fMRI scans itself. These approaches are discussed in the following.

2.4.2 Data-driven pre-processing

Many data-driven pre-processing approaches have been proposed for when physiological recordings are not available or impractical (see [Murphy et al., 2013] for a review). The following provides a brief overview.

Many approaches extract noise time courses from fMRI data and include these as additional covariates in the single-subject GLM analysis used for task fMRI experiments (or linear pre-processing models used for resting-state fMRI).

These approaches assume MR signal change in non grey matter tissue is only affected by brain motion, hardware-related noise or physiological motion [Weissenbacher et al., 2009, Jo et al., 2010]. Therefore, noise covariates are obtained by using one or more average time courses from locations of WM or CSF voxels determined by a tissue probability mask [Weissenbacher et al., 2009, Anderson et al., 2011, Jo et al., 2010].

To address head motion explicitly, 6 rigid body realignment parameters are most commonly included as additional covariates [Power et al., 2012, Van Dijk et al., 2012, Friston et al., 1996, Lund et al., 2005, 2006], but the regression of up to 36 realignment covariates and spike regressors (including mean CSF, WM and global average BOLD signal) has also been proposed to effectively remove head motion artefacts [Satterthwaite et al., 2012, 2013]. However, the major disadvantage of including many realignment parameters and their derivatives is that these covariates capture motion in scans affected by head motion while randomly removing variance in scans with no motion. As an alternative, Satterthwaite et al. thus suggested the inclusion of head motion severity measures while testing differences among subject groups [Satterthwaite et al., 2013].

Other fMRI pre-processing approaches leverage the dead-time in the EPI pulse sequence to acquire the MR signal at multiple TEs [Bright and Murphy, 2013]. Therefore, a less commonly applied dual-echo spiral EPI sequence is used to acquire fMRI scans at TE 3.3ms and 35ms. The longer the TE the more BOLD-sensitive is the MR signal. Physiological motion affects the MR signal at each TE equally. Ultimately, the short TE time courses are regressed from their long TE equivalents to remove physiological motion effects. Hereby, required scanning time and temporal resolution are not elongated, which is a tremendous advantage of this approach.

Another set of fMRI pre-processing approaches comprises of matrix factorisation approaches. Although, spatial [Thomas et al., 2002] or temporal PCA-based [Behzadi et al., 2007] de-noising approaches have been proposed, the most effective and commonly used data-driven approach for noise removal is spatial ICA. Hereby, spatial ICA is directly applied to each single fMRI scan to remove ICs with spatial characteristics of head or physiological motion. There are two types of such pre-processing pipelines. In the first type, ICs of a set of subjects are manually labelled as noise [Kelly Jr et al., 2010, Griffanti et al., 2017, Sochat et al., 2014, Salimi-Khorshidi et al., 2014, Griffanti et al., 2014]. The labelled ICs are subsequently used to train a classifier, which is ultimately applied to unseen subject cohorts.

In the second type of pipeline, only a few explicit and interpretable features are used to identify noise ICs [Tohka et al., 2008, Bhaganagarapu et al., 2013, Pruim et al., 2015, Kundu et al., 2012].

The most prominent among IC de-noising techniques are FMRIB's ICA-based Xnoiseifier (FIX) [Salimi-Khorshidi et al., 2014, Griffanti et al., 2014] and ICA-based Automatic Removal Of Motion Artefacts (ICA-AROMA) [Pruim et al., 2015].

There are two key disadvantages of such spatial ICA classification pipelines. Firstly, the classification only reflects the opinion of experts because the underlying ground truth of spatial maps is ultimately unknown. Therefore, actual brain network spatial maps may be mistaken as noise and are removed from the fMRI data. Secondly, the classification process is likely to overfit to a specific cohort [Pruim et al., 2015]. A labor-intensive labelling of ICs is thus required for new data cohorts, for example, on fMRI data acquired on a new

MRI scanner or when using fMRI data with TRs not present in the current training cohort. However, a great strength of such ICA de-noising techniques is their adaptiveness to the amount of noise present in each subject. More specifically, the fewer head motion occurs during scanning the fewer ICs are removed from the individual fMRI scan.

2.5 Summary

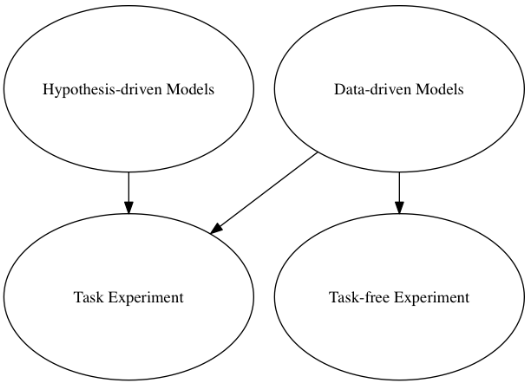

Figure 2.5: There are hypothesis- and data-driven models for the analysis of fMRI data. Hypothesis-driven models are used for the analysis of task experiments. Data-driven models are primarily used on task-free experiments but are also applicable to task experiments.

There are two classes of models to analyse task and resting-state experiments as depicted in Figure 2.5. Hypothesis-driven models mainly evolved around the GLM and have been used to study task experiments. Hypothesis-driven models explicitly provide a model of how stimuli are translated into a haemodynamic response. The assumption of linear behaviour in most of these models rests on the observation that BOLD signal behaviour were approximately found to behave linear given the ISI is above 2s [Boynton et al., 1996, 2012]. Nevertheless, models addressing non-linearities [Friston et al., 1998] or use a more neurophysiological plausible model [Buxton et al., 2004] exist but are less prevalent in practice.
The shared hypothesis across these models is that stimulus presentation causes an immediate increase in neural activation. Evidence from animal studies supports this hypothesis in the eloquent cortex [Logothetis et al., 2001]. For example, the pioneering work by Logothetis and colleagues [Logothetis et al., 2001, Logothetis and Wandell, 2004, Logothetis, 2008a] examined the relationship between BOLD and neural activation change in animal models. In these experiments, monkeys were viewing checker-board patterns in a MRI scanner while measurements of neuronal activity and BOLD signal change in their visual cortex were recorded simultaneously. Their work provided evidence about the intrinsic link between increased neural activity and BOLD signal increase[3]. Measured electric signal increases are

---

[3] Similarly, a negative BOLD response was reported in monkeys [Shmuel et al., 2006] linked to a decrease in neural activity.

local field potentials, which are the summation of post-synaptic electric potentials from adjacent neuron populations [Logothetis, 2008a].

Hypothesis-driven models have been mainly used to localise specialised areas of the brain recruited during a specific task. The advantage of hypothesis-driven models is their straightforward comparison of spatial map estimates across subjects. The disadvantage of hypothesis-driven models is neural activation change due to task stimuli can be modelled but neural activation change driven by intrinsic brain activity is neglected.

In contrast to hypothesis-driven models, data-driven approaches find decompositions of the fMRI data into components with certain assumed statistical characteristics. Two of the most prevalent characteristics are statistical independence and sparsity [Daubechies et al., 2009]. The advantage of data-driven models is their ability to reveal spatially coherent patterns of BOLD signal change due to spontaneous intrinsic neural activation.

However, their disadvantage is that spatial maps derived from a single fMRI scan can not be compared instantly because of the ambiguity of decompositions across subjects. For example, a spatial map may be found in one component in one subject whereas it may split into two components in another subject. Therefore, an intermediate step of computing a set of shared group components is always required, which are then used to obtain a corresponding spatial estimates in the individual subject. The comparison of components across subjects is thus always dependent on the chosen set of group components.

Task and task-free experiments provide complementary insights into the functional organisation of the brain but evolved into separate communities in the literature because the origin of observed spontaneous low-frequency BOLD fluctuations was debated before animal or craniotomy studies provided substantial evidence for their neurophysiological origin [He et al., 2008, Leopold and Maier, 2012, Hacker et al., 2017, Kucyi et al., 2018].

However, the recent years have seen a coalescence of task and resting-state fMRI analysis approaches. For example, Smith et al. examined the similarity between extracted brain networks from resting-state fMRI and from a meta-analysis of several fMRI task experiment data [Smith et al., 2009]. Since then, a growing body of research found similarities in the spatial boundaries in brain networks obtained from task and resting-state fMRI [Mennes et al., 2010, Cole et al., 2014, 2016, Tavor et al., 2016, Gratton et al., 2018].

Chapter 3

Improving heart rate variability estimation for the EPICure cohort

3.1 Introduction

During fMRI scanning without task engagement, spontaneous neural activation due to intrinsic task processing can be observed in form of spatial co-activation patterns in the brain. However, the BOLD effect is only an indirect measure of neural activation and is driven by hemodynamic changes in blood perfusion. These hemodynamic changes are not only driven by neural activation change but respiratory and cardiac cycle.

Therefore, a strong link exists between neural activation processing and physiological states of the human body. Homeostasis, a mechanism of maintaining consistency of the internal body state, is an essential process in the regulation of motivational states and emotions, cognitive representation, maturational social and cultural development [Critchley and Seth, 2012, Critchley et al., 2013, Fotopoulou and Tsakiris, 2017, Park et al., 2014, Mulcahy et al., 2019].

Therefore, the field is moving towards studying brain responses in the context of whole-body physiological processes [Chang et al., 2016].

One complementary measure to functional brain responses is heart rate variability (HRV), which refers to fluctuations in the beat-to-beat interval of the cardiac cycle. HRV arises due to the interaction between parasympathetic (vagal) and sympathetic nervous system influences on the sinoatrial node [Berntson et al., 1997, Chang et al., 2013].

HRV is a measure of autonomic activity, which is crucial to quickly adapt to environmental changes, and therefore directly impacts regional changes in neural activation during task and resting-state fMRI experiments [Chang et al., 2013, McCraty and Shaffer, 2015]. The high frequency components in HRV ($0.15 - 0.4$Hz) are primarily attributed to modulation of the heart rate by the respiratory cycle. The lower frequency components in HRV ($0.05 - 0.15$Hz) are believed to reflect a mixture of sympathetic and parasympathetic processes [Chang et al., 2013, Mulcahy et al., 2019].

Co-variations of BOLD responses and heart rate have been found across the entire cortex but are most pronounced in cortical and sub-cortical areas involved in autonomic representation and control such as anterior cingulate cortex (ACC), prefrontal cortex (PFC), insular cortices, and amygdala [Shmueli et al., 2007, Chang et al., 2013, Thayer et al., 2012, Jennings et al., 2016, Sakaki et al., 2016, Schulz, 2016, de la Cruz et al., 2017, 2019]. These specific nodes of the brain are usually referred to as central autonomic network (CAN) [Chang et al., 2013, Durantin et al., 2014, Chang et al., 2016, Mandrick et al., 2016, Maier and Hare, 2017, Mulcahy et al., 2019].

Higher resting HRV in individuals is associated with enhanced cognitive performance on tasks of working memory, attention, and inhibitory control [Hansen et al., 2009, Elliot et al., 2011, Gillie et al., 2014, Mandrick et al., 2016, Maier and Hare, 2017, Mulcahy et al., 2019]. Therefore, HRV is considered a proxy measure of healthy cardiac function, of central autonomic control of internal bodily state, and of the capacity for adaptive inhibition and emotion regulation [Williams et al., 2015, Mulcahy et al., 2019].

The development of the autonomic nervous system, for example, the myelination of the vagus nerve, occurs during the third trimester and is interrupted at preterm birth. The development of the autonomic nervous system is likely to have an impact on autonomic control [Karvonen et al., 2019] and is also associated with an increased rate of heart diseases in adulthood [Crump et al., 2019, 2021].

In preterm birth, an infant is delivered at less than 37 completed weeks of gestation instead of 40 weeks for a full-term birth. Infants born at 32 weeks or less are significantly more likely to suffer from cerebral palsy, cognitive deficits, loss of neuro-motor function and can have long-term difficulties in education [White et al., 2014]. Due to medical advances, infants are increasingly likely to survive preterm birth, but it remains the leading cause of neonatal mortality, and associated morbidity often persists into adulthood.

Several psychological deficits cannot be measured until school age, and for this reason intervention cannot be performed in the perinatal period, or infancy. If medical imaging could be used to assess children at an early developmental stage, intervention could be recommended and tested with greater success.

Neuroimaging studies allow to investigate the underlying tissue substrate of the broader neuropsychological differences observed in preterm cohorts; but the long-term neuroimaging phenotype of extremely-preterm adolescents is relatively unknown.

3.1.1 Motivation

In addition to neuroimaging, measures of the heart rate are required to study the relation between HRV and brain nodes of the CAN. Therefore, physiological recordings can be acquired

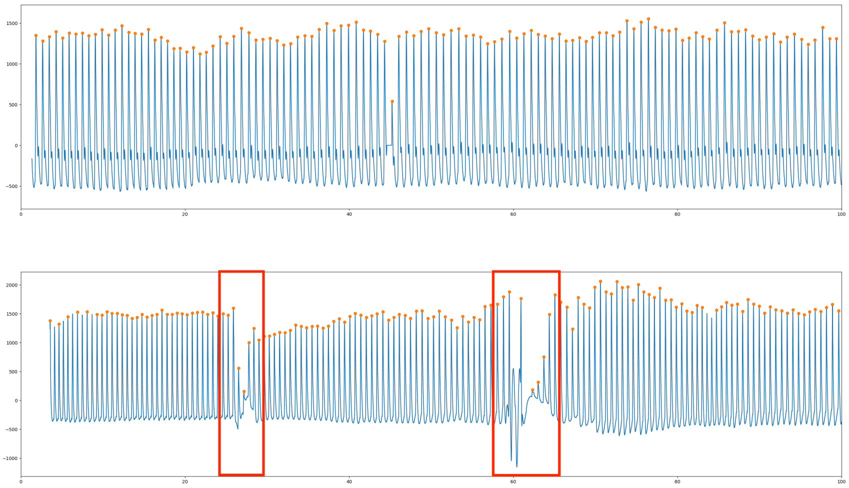

Figure 3.1: A train of detected heart rate peaks from a good (top) and a corrupted (bottom) physiological recording of the EPICure cohort.

simultaneously during fMRI scanning. The following briefly describes the most prominent techniques for recording the heart rate in the fMRI setting (see Mulcahy et al. [2019] for a review).

The most prominent way to measure heart rate during fMRI scanning is either an electrocardiogram (ECG) or an optically obtained photoplethysmogram (PPG). Both of these approaches have advantages and disadvantages in the fMRI setting.

ECG is susceptible to radio-frequency (RF) pulses, switching of gradients during fMRI acquisition, displacement of the ECG sensors within the magnetic field of the MR scanner, muscle movement or other electrical equipment [Oster and Clifford, 2017].

In contrast, an optically-driven PPG is commonly obtained by using a pulse oximeter. Hereby, the pulse oximeter illuminates the skin and measures changes in light absorption associated with changes in blood perfusion. Pulse oximetry is easier to deploy in a MRI environment and has proven successful for calculating HRV under the assumption of a stationary heart rate [Chang and Glover, 2009b, Schäfer and Vagedes, 2013]. In contrast to ECG, the pulse oximeter recording is delayed by the time between contraction of the heart and the measure of blood at the peripheral recording point. This so called pulse transit time is dependent on beat to beat blood pressure and vascular compliance. The resulting pulse rate variability (PRV) can therefore only be considered as a proxy measure for HRV [Mulcahy et al., 2019]. The delay between ECG and photoplethysmograph is approximately 120ms ± 25 (courtesy of Karin Shmueli from her response to reviewers in Shmueli et al. [2007]).

Pulse oximetry is not susceptible to electrical interference as ECG but comes with challenges of its own in the MRI environment, e.g. subject motion. Figure 3.1 shows a train of cardiac cycle peaks for a small period of time in a good quality and a corrupted physiological recording acquired with a pulse oximetry. The interval of signal dropout (red squares) is caused by subject motion. This creates a challenge for the extraction of PRV from such physiological recordings and corrupts the subsequent analysis of the interaction between PRV and BOLD signal change in the brain.

3.1.2 Previous work

The cardiac cycle causes pulsatile arterial blood flow. This pulsation is translated into brain tissue and fluids bound by the cranial cavity. The resulting physiological motion ultimately interferes with the MR signal [Wagshul et al., 2011].

Pulse oximetry provides a means to record cardiac cycles during scanning. Hereby, the cardiac physiological recording is processed to match slice acquisition timings of the corresponding fMRI scan. A linear model is built to measure how much variance these physiological covariates explain in fMRI time courses [Glover et al., 2000].

Such models showed that slow variations in the cardiac cycle are coupled with signal variations in BOLD time courses [Shmueli et al., 2007, Chang and Glover, 2009b]. Physiological recordings synchronised to slice acquisition times can be used to delineate fMRI time courses from cardiac and other physiological fluctuations [Chang and Glover, 2009b].

However, an ideal research setup is most commonly only found in a controlled research setting whereas patient throughput is traded for diligence in a clinical setup. Recordings from pulse plethysmography sensors can thus exhibit poor signal quality due to subject motion, often lack synchronisation to scanner triggers, or are neglected entirely to shorten experiment setup.

Therefore, data-driven approaches increased in relevance, in which physiological signals are directly extracted from fMRI data.

Temporal ICA has been utilised [Beall and Lowe, 2014, Beall, 2010] in which temporal ICs are either extracted using spatial prior masks or matched with available physiological recordings.

The approach by Ash et al. [2013] uses a multi-class support vector machine (SVM) to predict cardiac and respiratory phase estimates, which showed comparable performance to RETROICOR regressors from corresponding physiological recordings.

Aslan et al. [2019] deploys convolutional neural networks to obtain HRV at the slice-level. Similar approaches for respiratory cycle extraction and processing exploit characteristics of specific fMRI acquisition schemes to obtain respiratory signals from the fMRI scan [Salas et al., 2021, Hocke and Frederick, 2021].

This chapter is concerned with the correction of signal failures in physiological recordings acquired with pulse oximetry, which accompanied the resting-state fMRI scanning of a cohort of term- and preterm-born adults.

3.1.3 Proposed solution

The physiological recordings of the examined cohort were not synchronised to scanner triggers of the fMRI acquisition. Additionally, recordings comprised of corrupted signal periods of varying length due to subject motion.

This chapter shows how the pulsality effect, which causes minimal change in tissue composition of fMRI volumes in each slice, is exploited to extract heart rate and ultimately PRV estimates.

Therefore, an average slice-wise signal (SWS) is obtained from areas of high time course variation in each slice of the fMRI scans. The power spectrum of the average SWS resembled the power spectrum of the physiological recording from pulse plethysmography. Similarly to obtaining the heart rate from physiological recordings, a peak extraction algorithm was applied to the filtered SWS to extract PRV.

The degree of correlation between SWS-derived PRV and PRV derived from the pulse oximeter recording was learned with a Multi-Task Gaussian Process (MTGP) model. The MTGP model also incorporated a time shift parameter to account for the potential lag between PRV derived from SWS and from physiological recoding of the pulse oximeter.

The proposed Gaussian Process CARdio Estimation (GPCARE) model produced a joint estimate of the PRV compensating for missing signal periods in physiological recordings.

3.2 Materials and methods

The following introduces imaging data and required signal processing of the fMRI time courses before obtaining PRV estimates from these scans. This is followed by the introduction of Gaussian processes and their extension to Multi-task Gaussian Processes.

3.2.1 Imaging data

The examined fMRI data was taken from a cohort of adults either term-born or born at a preterm gestational age (EPICure).

The EPICure study group is a consortium of clinicians and scientists who authored a study of all the infants born extremely preterm in the UK during 1995. This cohort has been followed since birth, with a wide-ranging and thorough set of psychological and physical examinations. It is only now, at 19 years of age, that the group have had MRI scans. This cohort was important in establishing the difficulties of growing up after extremely preterm birth, through early childhood and into adulthood.

Recruitment was open to all infants born extremely preterm in the UK and Ireland from March to December, 1995. This study was continued to collect psychological, physiological and other markers of subject health and development, including at 6, 11, 16 and 19 years of age. These measurements were compared with a matched cohort recruited from school classmates. EPICure is the source of the MRI scans examined in this work, performing MRI on this cohort for the first time at age 19.

Individuals are imaged using a Philips 3T Achieva. The 3D T1-weighted volume is acquired at $1 \times 1 \times 1\text{mm}^3$ isotropic resolution (TR/TE = 6.78/3.06 ms). Each fMRI scan comprises of 200 volumes acquired with TR 3000ms, TE 30ms, flip angle 80°, voxel size $2.5 \times 2.5 \times 3\text{mm}^3$, field of view (FoV) 240mm^2, 50 oblique transverse slices, slice order descending.

The preterm born young adults show large dilated ventricles compared to their term-born peers as depicted in Figure 3.2.

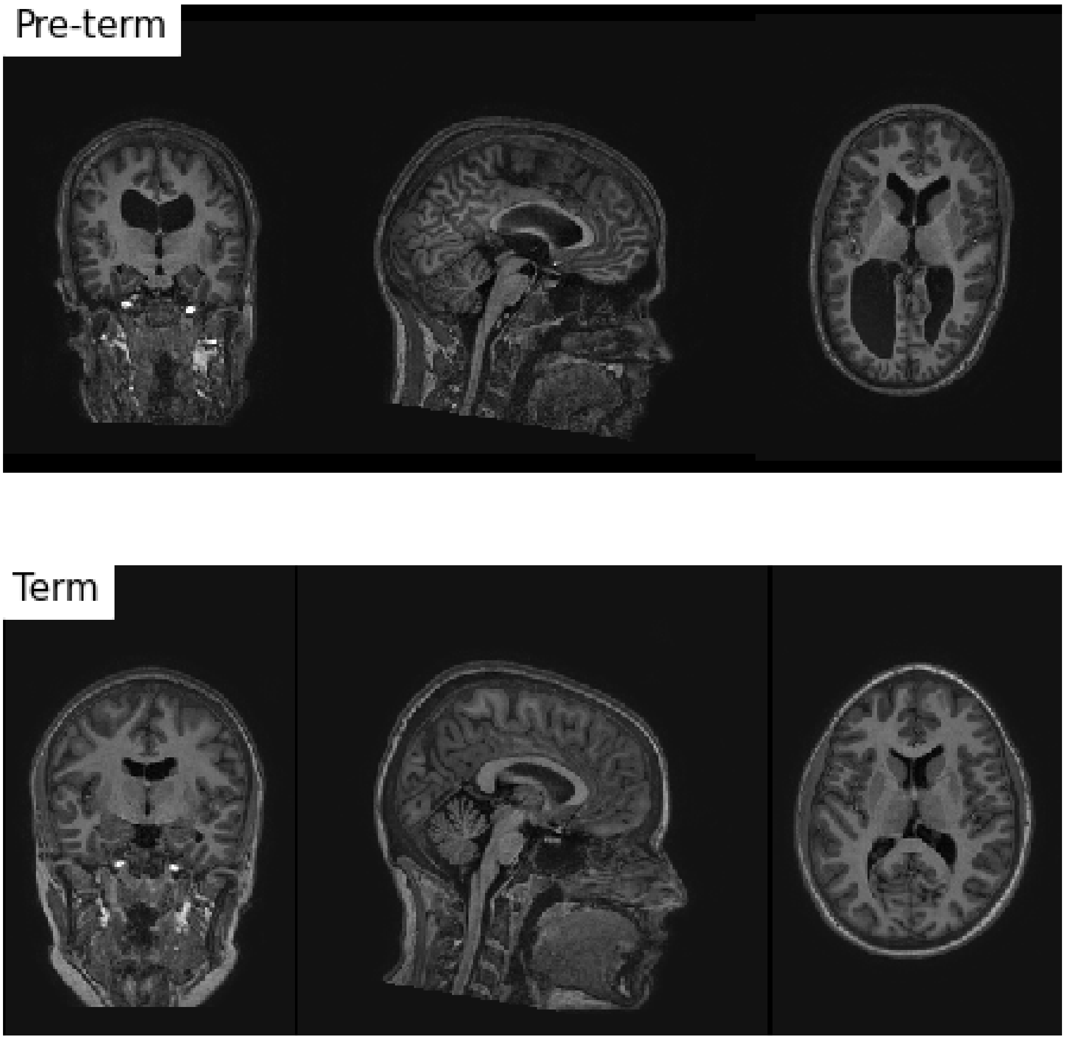

Figure 3.2: Juxtaposition of a T1 scan of a preterm- (top row) versus a term-born subject (bottom row). A characteristic feature of preterm born subjects are large ventricles extending into posterior region of the brain.

3.2.2 Image and signal pre-processing

fMRI volumes were corrected for head motion by realigning volumes to the first volume of the scan. The frame-wise displacement from the motion realignment parameters of the rigid-body registration was obtained for each subject scan.

fMRI time courses were corrected for polynomial trends and normalised to zero mean and unit variance. Slices were reordered with respect to their slice acquisition timing. The sagittal FoV was cropped to have an approximate equal contribution of brain tissue and cerebral fluids for each slice. The SWS was obtained by computing the STD-weighted average in each slice, which resulted in a signal sampled every TR divided by the number of slices. The obtained signal was very noisy due to averaging from slices with different tissue compositions. A bandpass filter ($0.6-2.0$Hz) was applied to isolate desired cardiac frequencies. The frequency with the greatest power in this band was peak filtered (gaussian filter) with a bandwidth of 0.5Hz. The same signal processing was applied to pulse plethysmography recordings acquired with a Philips physiological monitoring unit. An example of the power spectrum of SWS and a corresponding physiological recording from pulse plethysmography is depicted in Figure 3.3 (first row). Peak to peak distances were extracted of SWS and pulse plethysmography recording to obtain PRV estimates.

3.2.3 Gaussian process regression models

The outlined pre-processing resulted in a set of training data points $D = \{(x_i, y_i | i = 1, \cdots, n)\}$ with time points x_i, PRV measurements y_i and number of measurements n. Given this set of training data points, an input-output mapping is required between x and y.

There are many approaches of learning functions f that describe the mapping between x and y.

One wants to make predictions for new inputs x^* not part of the observed training data. More specifically, the periods of measurement failures in the considered physiological recordings. One hopes to find a function f that generalises beyond the finite training data to make predictions for all possible input values. Assumptions about the characteristics of such a function f are required because otherwise any function which is consistent with the training data would be equally valid. These assumed characteristics can be expressed as prior information, for example, a preference for smoother functions [Rasmussen and Williams, 2006].

An elegant mathematical framework to evaluate many of such hypotheses is a Gaussian process (GP). The following is a brief introduction of GPs based on Rasmussen and Williams [2006], Duvenaud [2014], and Dürichen et al. [2014].

A GP is a generalisation of the gaussian probability distribution. In contrast to probability distributions that describe random variables, a stochastic process governs the properties of functions.

More specifically, a GP given by $f \sim GP(\mu, \Sigma)$ is any distribution over functions such that any finite set of function values $f(x_1), f(x_2), \cdots f(x_N)$ have a joint Gaussian distribution. Before conditioning on training data, a GP is completely specified by its mean function μ and its covariance function $\Sigma = k(x, x')$.

The mean function is assumed to be zero everywhere, since uncertainty about the mean function can be modelled by adding an extra term to the kernel. Therefore, the kind of structure captured by a GP model is entirely determined by its kernel Σ and specifies how the model generalises to unseen data.

Modifying Σ allows to encode prior knowledge about the concerned covariance function. Various kernels are available to describe the behaviour of f. The squared exponential (SE), one among the most prominent covariance functions, is given by

$$k_{\mathrm{SE}}(r) = \theta_A^2 \exp\left[-\frac{r^2}{2\theta_L^2}\right] \tag{3.1}$$

where θ_A and θ_L are hyper-parameters modelling amplitude and time scaling. Hereby, the Euclidian distance between two indices is denoted by $r = ||x - x'||_2$.

The proposed single GP model for PRV estimates used a constant mean function $\mu(x) = c$ and SE covariance function $k_{\mathrm{SE}}(r)$ assuming heart rate to fluctuate slowly around a mean with STD determined by hyper-parameter θ_A and an autocorrelation determined by hyper-parameter θ_L.

The individual elements of the covariance matrix Σ for input vector $x \in \mathbb{R}^n$ were given by evaluating the covariance at $k_{\mathrm{SE}}(r)$. Prediction on test time points x^* were made by averaging over all possible parameter values weighted by their posterior probability. The predictive distribution for $f^* \doteq f(x^*)$ at x^* was computed using the posterior distribution

$$p(y^*|x^*, x, y) \sim \mathcal{N}(m(y^*), var(y^*)) \tag{3.2}$$

with mean $m(y^*) = \mu(x^*) + \Sigma(x, x^*)^T \Sigma(x, x)^{-1}(y - \mu(x))$ and variance $var(y^*) = \Sigma(x^*, x^*) - \Sigma(x, x^*)^T \Sigma(x, x)^{-1} \Sigma(x, x^*)$. The hyper-parameters were optimised by minimising the negative log marginal likelihood (NLML) given by

$$-\log p(y|x, \theta) = \frac{1}{2}\log|\Sigma| + \frac{1}{2} y^T \Sigma^{-1} y + \frac{n}{2}\log 2\pi \ . \tag{3.3}$$

As discussed in Dürichen et al. [2014], the first term of Equation 3.3 penalises model complexity whereas the second term penalises low data likelihood. The optimisation with gradient descent is thus an intrinsic bias variance trade-off.

3.2.4 Multi-task Gaussian Process regression models

The implementation of the Multi-task Gaussian Process (MTGP) model was adopted from Dürichen et al. [2014] to learn a joint estimate of PRV from SWS and pulse plethysmography recording. The following overview is a brief summary of the detailed description of this model in Dürichen et al. [2014].

In the MTGP model, a single GP model is extended to m physiological recordings. The training data comprises of time points $X = \{x_i^j | i = 1,...,n^j\}$ and $Y = \{y_i^j | i = 1,...,n^j\}$, in which physiological recording j was acquired at n^j time points. To link time points x_j^i and PRV estimates y_j^i to task j, a label l_j is added to the model with $l_j = j$.

Dürichen et al. [2014] assumes independence between covariance functions $k_{CORR}(l,l')$ and $k_{TIME}(x,x')$, which determine the correlation between and temporal covariance within individual GPs, respectively. The combined covariance function is given by

$$k_{MTGP}(x,x',l,l') = k_{CORR}(l,l') \times k_{TIME}(x,x') \ . \tag{3.4}$$

According to Dürichen et al. [2014], this covariance function $k_{MTGP}(x,x',l,l')$ can be expressed in matrix notation as the Kronecker product of Σ_{CORR} and Σ_{TIME} assuming $n^j = n$ for $j = 1,...,m$ such that

$$\Sigma_{MTGP}(X,l,\theta_{CORR},\theta_{TIME}) = \Sigma_{CORR}(l,\theta_{CORR}) \otimes \Sigma_{TIME}(X,\theta_{TIME}) \ . \tag{3.5}$$

Similarly to the single GP model, hyper-parameters of the MTGP model were optimised by minimising NLML.

3.3 Experiments and results

Individual GPs (covariance function k_{TIME}) and the MTGP model (covariance function k_{MTGP}) were learned on time points and PRV estimates of SWS and plethysmography recording. An example is depicted in Figure 3.3 for individual GP and MTGP model in second and third row, respectively. The MTGP model coped with missing data using the learned information from the covariance matrix Σ_{CORR}. The PRV estimate of the GP associated with the plethysmography recording followed the PRV of the GP associated with the SWS in periods of missing data (fifth row) whereas the individual GP model only returned to the signal mean (fourth row). Cardiac pulsation effects were mostly pronounced at the ventricle borders and in large vasculature, for example, the transversal sinus depicted in the statistical parametric mapping of the GP associated with SWS (sixth row).

The difference between the frequency with the greatest power in the SWS and plethysmography recording was computed. The difference between both PRV estimates was low in all

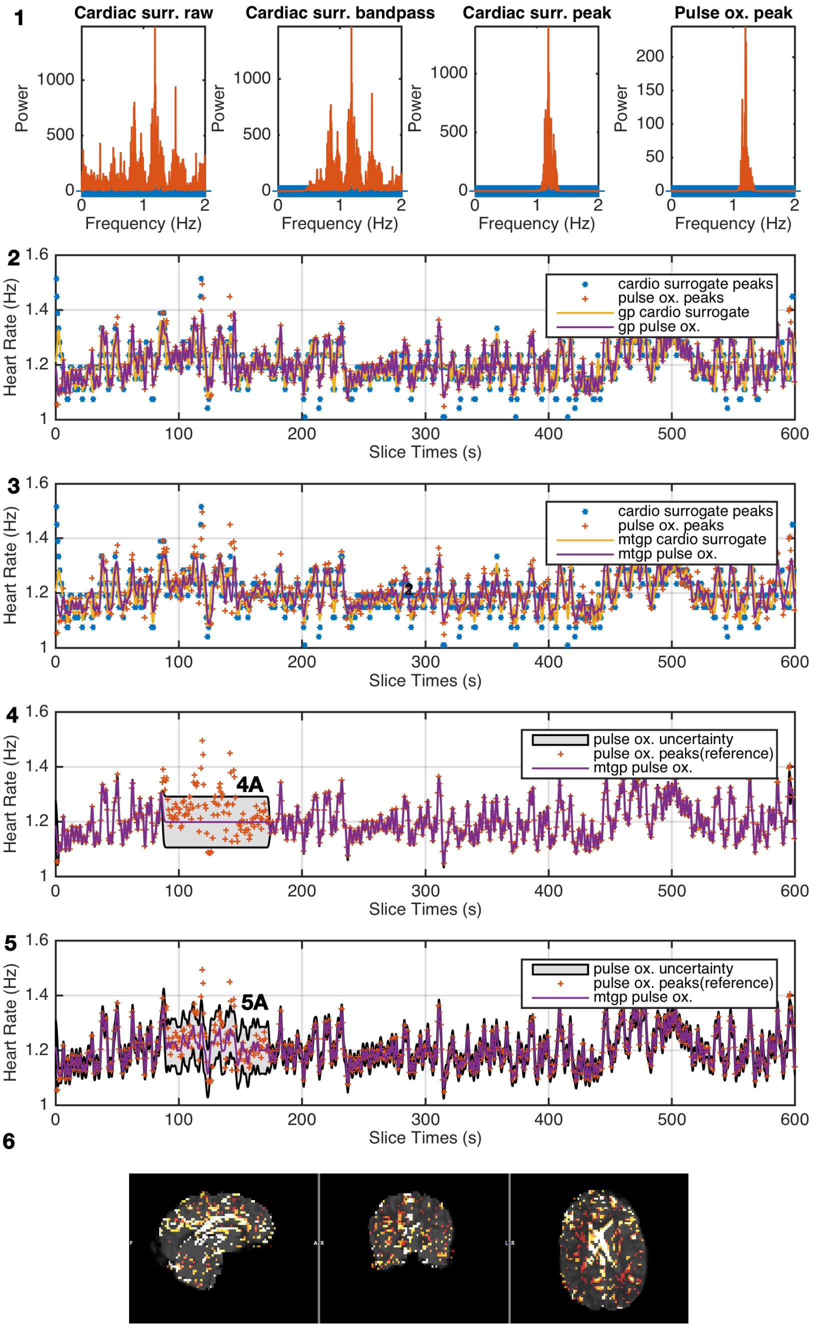

Figure 3.3: The applied signal processing on SWS (original power spectrum, after bandpass filtering, and after peak filtering from left to right) and the corresponding bandpass and peak filtered power spectrum of the plethysmography recording of subject 19 (1). Individual GPs (2) and MTGP model GPs (3) trained on time point peaks of average slice signal and plethysmography signal. Individual GPs (4) and MTGP model GPs (5) with simulated measurement failure in interval (84 s, 164 s). The uncertainty of the GP processes in the period of missing measurements (4A and 5A). The statistical parametric mapping (uncorrected p-value ≤ 0.05) for variance explained by the PRV estimates obtained from the MTGP model with coefficients displayed in red (low) to white (high) (6).

subjects (median 0.01, 25^{th} percentile 0.008, 75^{th} percentile 0.078, outliers 4). The difference distributions between both PRVs within the individual GP framework and the MTGP framework are depicted in Figure 3.4. Subjects were sorted by quality of their plethysmography signal from good quality (left) to noisy (right).

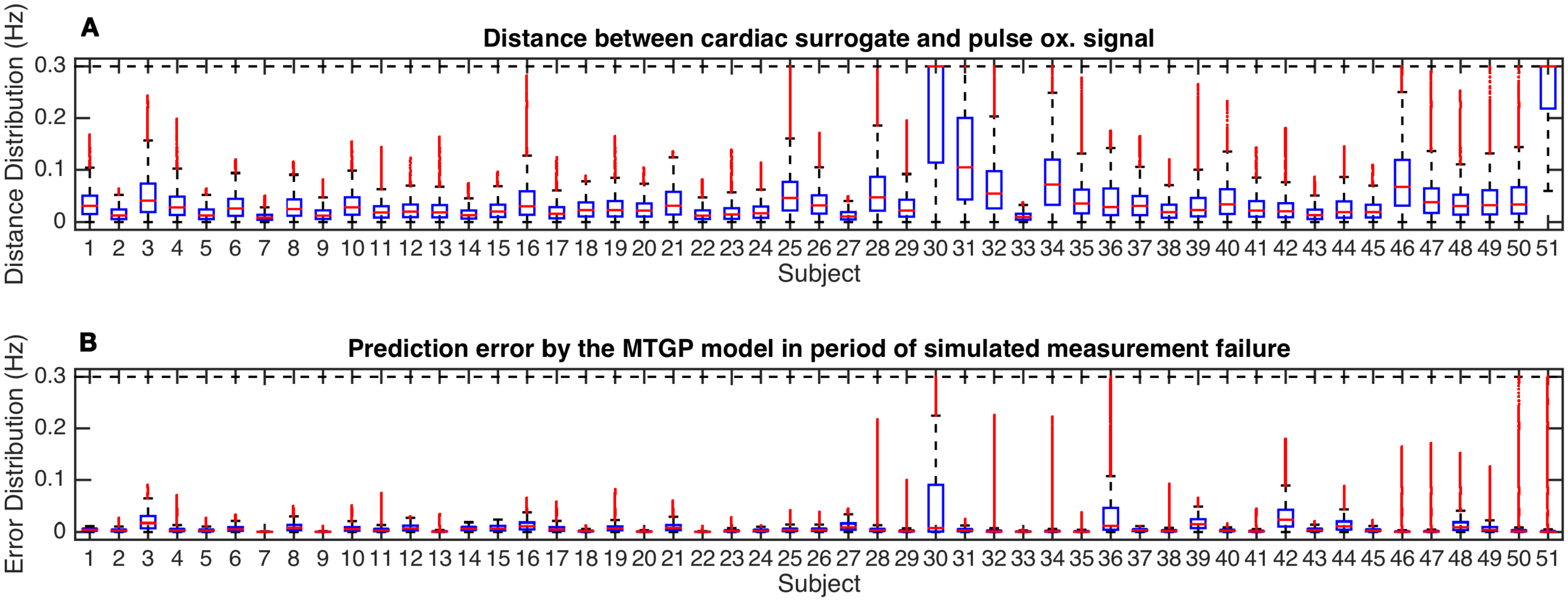

Figure 3.4: The boxplots show differences of PRV estimates obtained from SWS and the plethysmography recording at slice acquisition times of the fMRI scan for the individual GP model (A) and for the MTGP model (B). The blue frames are the 25^{th} percentile to 75^{th} percentile. Outliers are indicated by red dots.

3.4 Discussion and Conclusions

An image processing pipeline was presented to directly extract PRV estimates from fMRI scans.

This was followed by a MTGP model used to learn a robust joint estimate of PRV from two noisy PRV estimates extracted from SWS and pulse plethysmography recording. Hereby, the MTGP model leveraged covariance functions proposed by Dürichen et al. [2014] to model correlation and time shift between these two PRVs.

Multiple periods of signal were corrupted in the plethysmography recordings. These corrupted periods were likely the result of motion but potentially also occurred from poor sensor connection or detachment. The heart rate of some subjects showed ranges of large variability. Such large heart rate variability is unusual during rest and might have been caused by subjects falling asleep during scanning.

The application of the MTGP model resulted in robust joint estimate of the PRV compared to estimates from an individual GP model of the physiological recording.

The proposed MTGP model can incorporate information from more than one physiological recording such as electrocardiogram or breathing belt, and is able to learn the temporal interdependence of individual physiological recordings. Therefore, it has broad use for the improvement of fMRI pre-processing approaches that rely on physiological recordings.

The following chapter will leverage these improved heart rate estimates for the identification of physiological motion ICs and their removal from fMRI scans.

Chapter 4

Separating physiological motion artefacts from BOLD signal change with Independent Component Analysis

4.1 Introduction

The haemodynamic response is caused by a mixture of neurophysiological changes influenced by respiratory and cardiac cycle [Chang et al., 2016]. BOLD-unrelated signal may arise from hardware instabilities, head motion but also from physiological motion [Murphy et al., 2013, Caballero-Gaudes and Reynolds, 2017, Liu, 2016]. However, one must differentiate BOLD-related from BOLD-unrelated physiological influences on the fMRI signal. The former are coupled to neurophysiological processes whereas the later alter the MR signal due to a change in voxel tissue composition caused by cardiac pulsation or respiratory bulk motion as discussed in the literature review and in previous Chapter 3. This chapter introduces a pipeline for the removal of such physiological motion artefacts present in the resting-state fMRI data of the EPICure cohort and a publicly available 7T fMRI cohort.

4.1.1 Motivation

The detection of neurophysiological haemodynamic changes driven by neuronal activity is hampered by physiological motion. The cardiac cycle causes pulsatile arterial blood flow and this pulsation is translated into brain tissue and fluids bounded by the cranial cavity. fMRI volumes are commonly acquired slice-wise with EPI as discussed earlier in the literature review. The cardiac and respiratory cycles may affect these slices differently causing various structural patterns of noise artefacts in the fMRI data.

More specifically, the measurement of the BOLD effect is hampered by two types of motion: head motion and physiological motion. Whereas head motion causes severe signal drop-out, physiological motion causes subtle signal change pronounced at tissue boundaries of vascular dilation and contraction. Head motion can be controlled with proper head padding or bite bars but physiological motion is an intrinsic source of signal variation in fMRI scans, which thus can only be addressed retrospectively through image processing.

4.1.2 Previous work

The most prominent model for the removal of such physiological motion artefacts is RETROICOR (Image-based method for retrospective correction of physiological motion effects in fMRI [Glover et al., 2000]). RETROICOR calculates the phase of cardiac and respiratory recordings with reference to recorded slice triggers and uses a Fourier series expansion to produce physiological noise covariates. These are subsequently used in a linear model to remove physiological variations from fMRI time courses. In the past years, the RETROICOR model was extended with additional covariates such as respiratory volume change per time (RVT) [Birn et al., 2006, 2008] and heart rate variability (HRV) [Chang et al., 2009]. These covariates are built by convolution with respiratory and cardiac response functions, respectively, estimated from reference fMRI cohorts [Chang et al., 2009, Birn et al., 2008]. Others found an association between low-frequency heart rate fluctuations and fMRI time courses in a substantial number of voxels [Shmueli et al., 2007].

Despite the importance and need for such retrospective image processing, difficulties arise in the process of acquiring these physiological recordings.

Firstly, recordings from pulse plethysmography sensors can exhibit poor signal quality due to subject motion (hand or foot) because the subject does not remain still over entire periods of long scanning time. Secondly, physiological recordings are often not synchronised to the timings of the fMRI acquisition sequence. Lastly, physiological recordings require a time-consuming setup before scanning and might therefore be neglected entirely in the clinical setting.

Therefore, many noise covariates are directly derived from the fMRI scan when physiological recordings are not available [Murphy et al., 2013]. Tissue-based covariates are extracted from white matter (WM) and cerebrospinal fluid (CSF) probability masks assuming their signal consists entirely of noise fluctuations. Others used atlas regions to locate ventricles or draining vessels [Jo et al., 2010] from which average time courses are extracted. These approaches can be combined with temporal principal component analysis (tPCA) to extract multiple covariates from CSF and WM locations [Behzadi et al., 2007].

However, ICA is currently the most prominent approach to separate spatial patterns of noise from BOLD fluctuations [Thomas et al., 2002, Griffanti et al., 2014, Salimi-Khorshidi et al., 2014, Pruim et al., 2015]. Two of these approaches, CORSICA and PESTICA, explicitly target physiological motion. CORSICA applies ICA to obtain temporal ICs with characteristics of physiological motion [Perlbarg et al., 2007]. PESTICA constitutes a slice-wise ICA approach, which selects temporal ICs with similarity to RETROICOR regressors [Beall and Lowe, 2007].

A more recent work [Aslan et al., 2019] extracts cardiac signals directly from reordering fMRI slices with respect to their acquisition time, followed by signal processing and application of a neural network.

4.1.3 Proposed solution

This chapter proposes two pre-processing pipelines called cardiac artefact motion removal (CAMR) and cardiac artefact motion removal with support vector machines (CAMR-SVM). CAMR applies spatial ICA to individual fMRI scans and finds physiological motion among the obtained ICs in each scan. The component classification utilises the SWS introduced in Chapter 3 to label an IC as physiological motion. Therefore, a SWS is computed using time course and spatial map of an IC so that a new signal is obtained which comprises of an average slice value per slice acquisition time. This SWS of an IC is compared to the pulse plethysmography recording accompanying the fMRI scan to classify if the IC is a physiological motion component.

The CAMR pre-processing model was applied to a publicly available cohort of 22 subjects acquired on a 7T scanner at the Max Planck Institute for Human Cognitive and Brain Sciences (MPI7T). Each subject was scanned in 4 sessions resulting in a total of 88 fMRI scans. These scans were used as a training cohort for the second proposed pre-processing model CAMR-SVM. Therefore, a SVM was trained on a large set of signal features of time courses of ICs that were identified as physiological motion by CAMR.

CAMR-SVM was subsequently applied to the EPICure cohort for which pulse plethysmography recordings were available but lacked synchronisation to slice acquisition times of the fMRI scans.

Lastly, pre-processing with CAMR and CAMR-SVM resulted in a greater reduction of cardiac aliasing frequencies in fMRI time courses than pre-processing with RETROICOR in MPI7T and EPICure cohort, respectively.

4.2 Methods

Figure 4.1 depicts an overview of proposed approaches CAMR and CAMR-SVM. For each fMRI scan, common pre-processing was applied including rigid body realignment and high pass filtering to remove linear trends from fMRI time courses.

For the CAMR model, pre-processing was followed by spatial ICA to obtain a set of 40 ICs. For each of these ICs, the product of time course vector and spatial map vector resulted in a matrix. The average over the spatial dimension of this matrix resulted in a corresponding SWS for each IC. These SWSs were used as explanatory variables in a linear regression

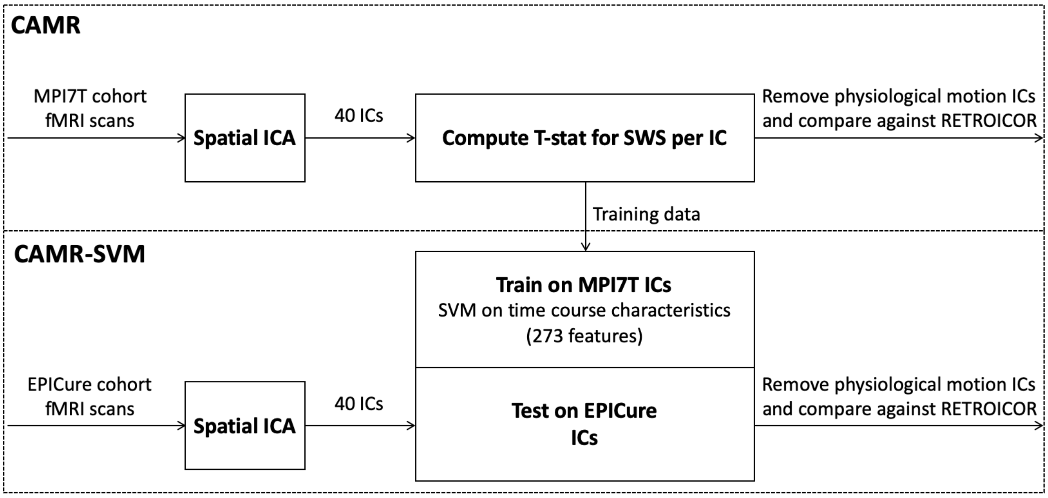

Figure 4.1: Overview of individual processing steps for CAMR and CAMR-SVM.

model with the dependent variable being the time course of the physiological recording. A SWS for which the t-statistic of the regression model showed a significant association to the physiological recording was classified as physiological motion.

For the CAMR-SVM model, a support vector machine (SVM) was trained on signal features of time courses of ICs obtained from the fMRI data of the MPI7T cohort. The trained CAMR-SVM model was subsequently tested on ICs obtained from the EPICure cohort. These models and RETROICOR were compared in their ability to reduce cardiac aliasing frequencies.

4.2.1 CAMR

4.2.1.1 Spatial ICA

The proposed model was applied to BOLD time courses of length T measured in 3D voxel space (X,Y,Z). This 4D tensor was reshaped into a matrix $\mathbf{Y} \in \mathbb{R}^{T \times V}$ with $V = X * Y * Z$[1]. A spatial ICA was computed for each subject fMRI matrix using Multivariate Exploratory Linear Decomposition into Independent Components (MELODIC part of FMRIB Software Library FSL v5.0) [Smith et al., 2004, Woolrich et al., 2009, Jenkinson et al., 2012] resulting in a set of C spatial maps $\mathbf{S} \in \mathbb{R}^{C \times V}$ and corresponding time courses $\mathbf{W} \in \mathbb{R}^{T \times C}$.

4.2.1.2 Slice-wise signal computation

The matrix product of the time course vector $w \in \mathbb{R}^{T \times 1}$ and spatial map vector $s \in \mathbb{R}^{1 \times V}$ was computed and produced a new matrix $V \in \mathbb{R}^{T \times V}$. This matrix was reshaped into $V \in \mathbb{R}^{(T*Z) \times (X*Y)}$. The average across the second dimension resulted in a SWS vector $v \in \mathbb{R}^{(T*Z) \times 1}$ measured at every slice acquisition time $\frac{\mathrm{TR}}{\mathbf{Z}}$ as depicted in Figure 4.2.

---

[1] The influence of a 3D mask on the approach is neglected for the purpose of illustration.

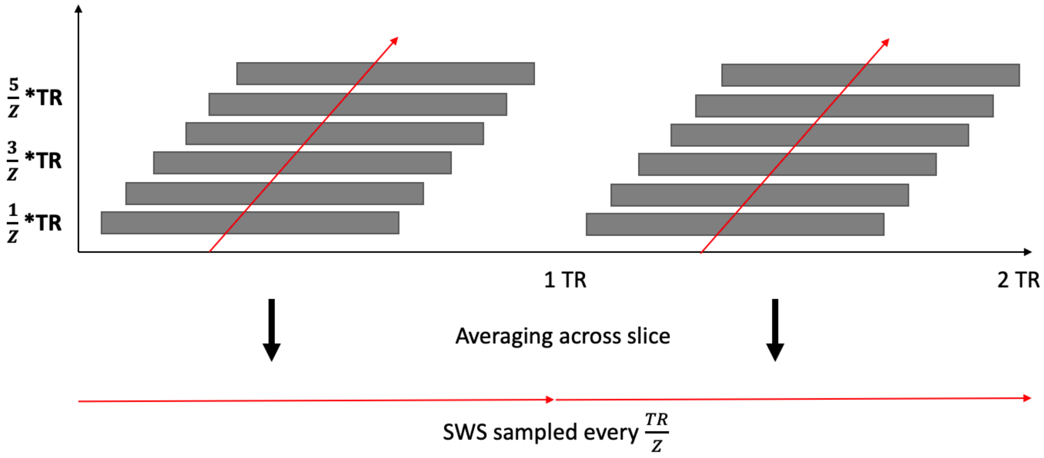

Figure 4.2: Overview of the slice-wise signal (SWS) computation for each IC.

4.2.1.3 Slice-wise signal classification

The following describes how physiological motion ICs were determined in each scan.

A linear regression was performed in which the explanatory variables comprised of the SWS vectors and the dependent variable comprised of the pulse plethysmography recording. Hereby, the plethysmography recording was resampled to the slice acquisition times of the fMRI scan.

The test statistic of obtained regression coefficients was used for classifying each SWS vector. The SWS was considered physiological motion if the p-value of the corresponding test statistic was less than 0.01. An example of four time courses of such ICs among time courses of the entire ICs of a decomposition into 40 components is depicted in Figure 4.3.

For each scan, a weighted average of SWSs identified as physiological motion was computed. To visually compare frequency contributions in physiological recording and this weighted average signal, a short-window Fourier Transform (SWFT) with a window length of 64 seconds was computed. An example of the SWFT plot of this weighted average signal is depicted in Figure 4.4. The corresponding heart rate extracted from time distances between signal peaks in the physiological recording was superimposed on the SWFT as red dashed line. The dashed yellow lines correspond to frequencies in other Nyquist zones caused by aliasing in the lower frequency band.

4.2.1.4 Physiological motion removal

Similarly as in Pruim et al. [2015], the last step of the CAMR model comprised of removal of ICs classified as physiological motion. Therefore, linear regression was performed using the full set of IC time courses as a explanatory variables. Both the time courses of ICs and the matrix of parameter estimates were partitioned into a physiological motion and signal part, according to the t-statistic of regression model. The variance associated with

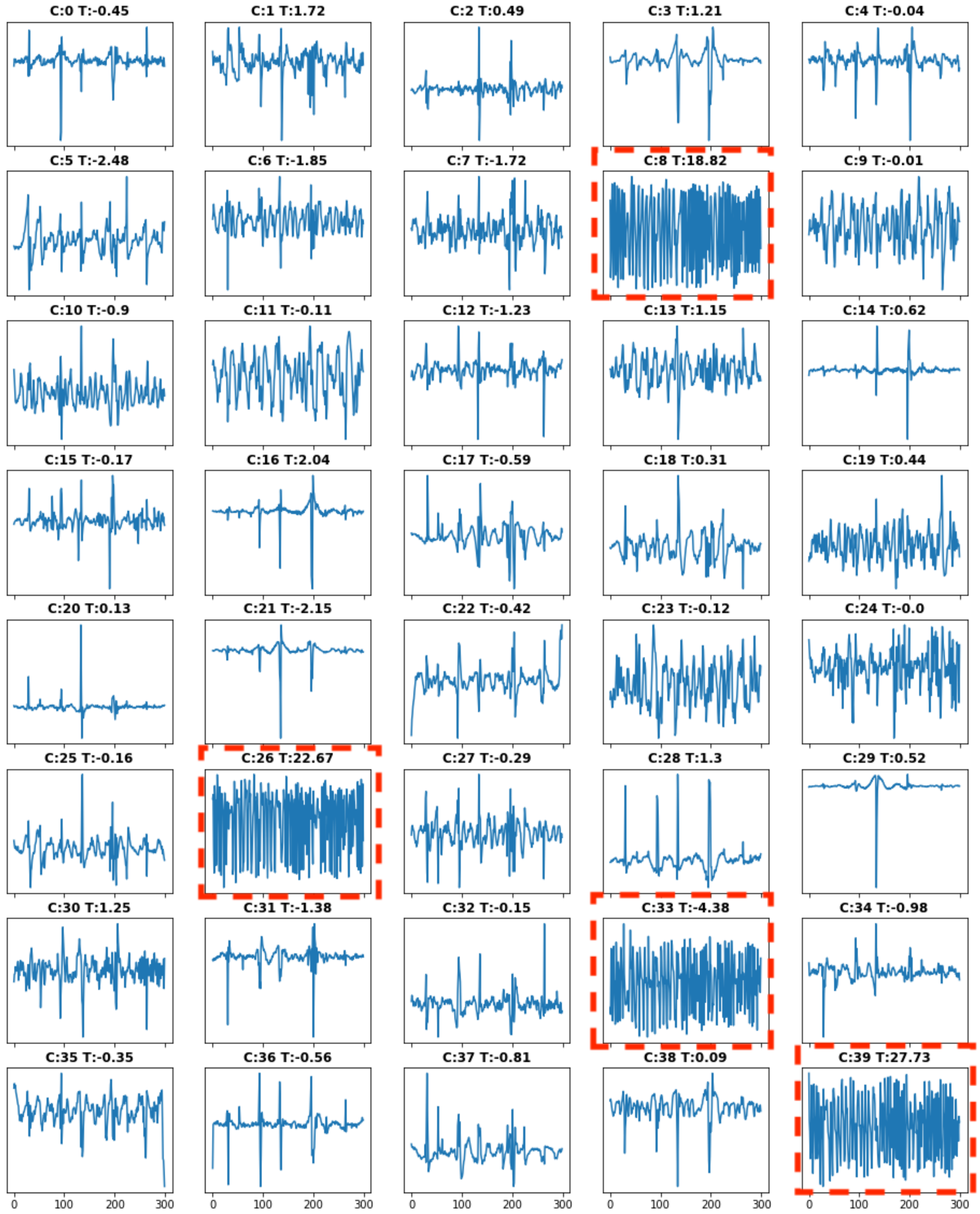

Figure 4.3: Time courses of ICs of a decomposition into 40 components. Their corresponding test statistic was obtained with a linear regression model whose explanatory variables comprised of the SWSs of these 40 ICs. The dependent variable comprised of the physiological recording from pulse plethysmography resampled at $\frac{\mathrm{TR}}{\mathbf{Z}}$.

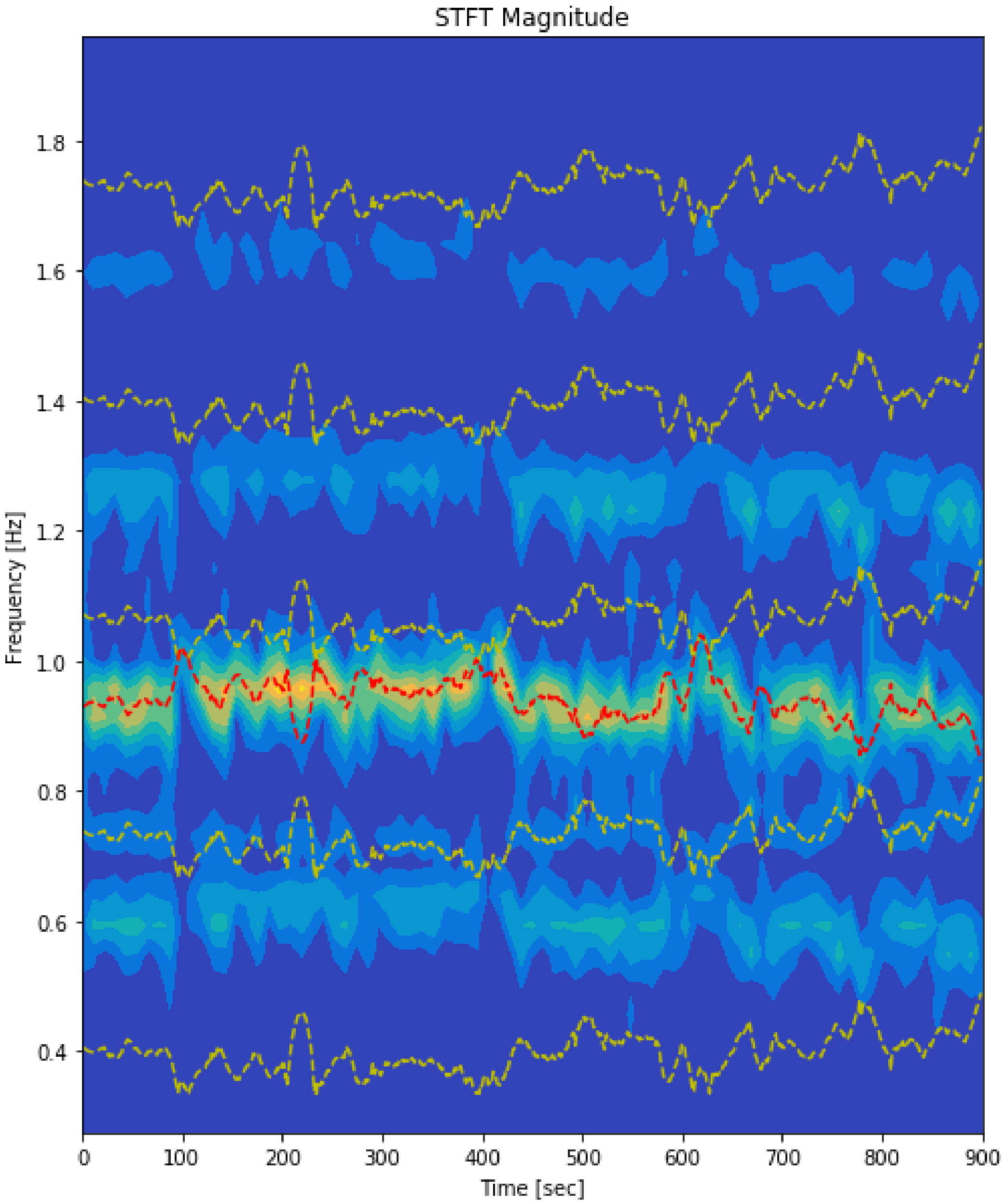

Figure 4.4: The SWFT plot of the weighted average of four SWSs that were identified as physiological motion by the linear regression model for scan 001-01. The dashed red line depicts the heart rate extracted from time differences between signal peaks in the corresponding physiological recording. The dashed yellow lines correspond to frequencies in other Nyquist zones caused by aliasing in the lower frequency band.

the physiological motion ICs was subsequently subtracted from the fMRI data.

4.2.1.5 Cardiac aliasing frequencies

The sampling frequency of fMRI scans of both cohorts $\mathbf{f_{Volume}}$ ($\frac{\mathbf{1}}{3\mathrm{s}}$) was less than twice the maximum frequency of occurring frequencies in the heart rate extracted from physiological recordings.

Therefore, heart rate frequency contributions in the acquired fMRI time courses cannot be removed by low-pass filtering but manifest as aliasing frequencies in fMRI time courses, which overlap with low frequency fluctuations of the haemodynamic response.

However, heart rate frequencies $\mathbf{f}_{\text{heart rate}}$ observed in the physiological recording were used to calculate heart rate aliasing frequencies $\mathbf{f}_{\text{cardiac aliasing}}$:

$$\mathbf{f}_{\text{cardiac aliasing}} = \begin{cases} \mathbf{f}_{\text{heart rate}} \bmod \mathbf{f}_{\text{nyq}}, & \text{if } \frac{\mathbf{f}_{\text{heart rate}}}{\mathbf{f}_{\text{nyq}}} \bmod \mathbf{2} = \mathbf{0} \\ \mathbf{f}_{\text{nyq}} - (\mathbf{f}_{\text{heart rate}} \bmod \mathbf{f}_{\text{nyq}}), & \text{otherwise} \end{cases} \tag{4.1}$$

where $\mathbf{f_{nyq}} = \frac{\mathbf{f_{Volume}}}{\mathbf{2}}$ is the Nyquist frequency. Accordingly, frequencies $f_{\text{cardiac source aliasing}}$ in higher Nyquist zones were obtained with the following equation:

$$\mathbf{f}_{\text{source cardiac aliasing}} = \mathbf{f_{Volume}} * \mathbf{n} \pm \mathbf{f}_{\text{cardiac aliasing}} \tag{4.2}$$

An example of these aliasing frequencies is depicted in Figure 4.4 as yellow dashed lines for corresponding heart rate frequencies (red dashed line).

The relation between $f_{\text{cardiac source aliasing}}$ and $f_{\text{cardiac source aliasing}}$ is non-deterministic. Many frequencies can cause corresponding aliasing frequencies in lower frequency bands. However, the change in heart rate frequencies over time leaves a unique fingerprint in the data.

4.2.2 CAMR-SVM

The above pipeline can only be applied if physiological recordings are available and in exact synchrony with acquisition timings of the fMRI sequence. To provide a physiological motion removal tool when physiological recordings are not available, a support vector machine was trained on signal features of time courses of ICs classified as physiological motion by CAMR.

4.2.2.1 Time course feature extraction

The open source library tsfresh [Christ et al., 2016] was used to automatically extract features of time courses. The feature extraction pipeline comprised of feature extraction and feature filtering[2] to obtain a set of features used for training the SVM.

Firstly, the entire set of available features in tsfresh was applied to time courses of ICs of

---

[2] The process is described in detail at `https://tsfresh.readthedocs.io/en/latest/text/feature_filtering.html`

a training data set. Secondly, each of the aggregated features was independently evaluated with respect to predicting the correct class of the training data set of ICs.

4.2.2.2 SVM-based classification training

These time course features were used for training a SVM with a liner kernel ($C = 0.005$). The performance of the CAMR-SVM model was tested on a hold-out data set.

4.3 Experiments and results

The proposed CAMR model was tested on simulated data and fMRI data of the MPI7T cohort. This was followed by testing the CAMR-SVM model on the EPICure cohort, respectively. The following describes conducted experiments on simulated and real fMRI data in detail.

4.3.1 Imaging data

The MPI7T cohort is a previously published open source data set of 22 subjects with an average age of 23 years [Gorgolewski et al., 2015][3]. Imaging data were acquired on a 7T Siemens MAGNETOM. Structural images were acquired using a 3D MP2RAGE sequence (TR/TE=5s/2.45ms) with 0.7mm^3 isotropic voxel size. fMRI scans were acquired with TR 3s, TE 17ms, flip angle 70°, 1.5mm^3 isotropic voxel size, FoV 192mm^2, 70 oblique transverse slices, and interleaved slice order. Subjects were instructed to stay awake, keep their eyes open and focus on a cross. The fMRI scans were accompanied by physiological recordings that comprised of pulse plethysmography recording, respiration belt recording and slice acquisition timestamps.

The second cohort comprised of 107 subjects of the EPICure cohort, which was introduced at the beginning of Chapter 3. The resting-state fMRI scans comprised of 200 volumes acquired with TR 3000ms, TE 30ms, flip angle 80°, voxel size $2.5 \times 2.5 \times 3$mm^3, field of view (FoV) 240mm^2, 50 oblique transverse slices, slice order descending. Pulse oximetry recordings were available for each fMRI scan but came without the recording of slice acquisition timestamps. In both cohorts, fMRI volumes were realigned to correct for head motion and high-pass filtered (100s) to remove linear and quadratic trends from these time courses.

The CAMR and CAMR-SVM model were applied to MPI7T cohort and EPICure cohort, respectively. For the MPI7T and EPICure cohort, recordings from pulse plethysmography were used to build 4 cardiac RETROICOR covariates [Glover et al., 2000] and one heart rate variability (HRV) covariate [Chang et al., 2009]. For the EPICure cohort, RETROICOR covariates were built by assuming a synchronous start of physiological recording and image acquisition due to missing slice acquisition timestamps. In addition to these pre-processing models, global signal regression (GSR) was applied to both cohorts.

---

[3] `http://openscience.cbs.mpg.de/7t_trt/`

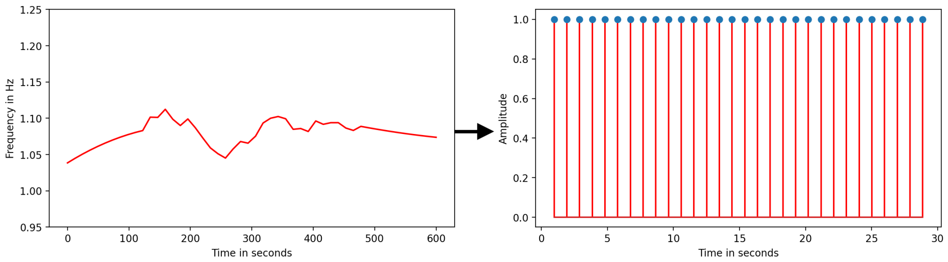

Figure 4.5: An average heart rate (h_{avg}) was randomly drawn from a normal distribution with $\mu = 1.1$ and $\sigma^2 = 0.2$, which was followed by drawing 50 heart rates from a uniform distribution $[h_{avg} - 0.15, h_{avg} + 0.15]$ for corresponding 50 time points across interval $[0, 600]$. A Savitzky-Golay filter with window length 21 and order 2 was used to fit a smooth function to these 50 data points (left). A pulse train was generated from this simulated heart rate (right).

4.3.2 Simulated data

To evaluate the proposed CAMR and CAMR-SVM pipeline, simulated data was obtained with the generative model:

$$Y = WS + C \otimes F + M \otimes 1 + E, \tag{4.3}$$

where $Y \in \mathbb{R}^{T\times V}$ was the fMRI time courses, T was the number of time points, V was the number of voxels in the brain mask, $W \in \mathbb{R}^{T\times 3}$ and $S \in \mathbb{R}^{3\times V}$ were time courses and spatial maps of the simulated resting-state networks, $F \in \mathbb{R}_+^{1\times V}$ was a spatial map of tissue probabilities of CSF, $C \in \mathbb{R}^{T\times 1}$ was simulated physiological motion, $M \in \mathbb{R}^{T\times 1}$ was simulated head motion, $\otimes$ was the Kronecker product, and E was added Gaussian noise.

Three commonly observed brain networks including the default-mode network (DMN), salient network (SN) and dorsal attention network (DAN) were taken from the spatial maps published by Shirer et al. [2012]. The spatial maps S were resampled to voxel size $4 \times 4 \times 4\text{mm}^3$ to reduce computational complexity.

The corresponding time courses W were randomly generated events drawn from a half-normal distribution and convolved with the canonical HRF. These time courses were sampled at 50Hz for 600s to match the acquisition length of the EPICure data. The physiological motion signal C was generated by the following random process. Firstly, an average heart rate (h_{avg}) was randomly drawn from a normal distribution with $\mu = 1.1$ and $\sigma^2 = 0.2$. This was followed by drawing 50 heart rates from a uniform distribution $[h_{avg} - 0.15, h_{avg} + 0.15]$ for corresponding 50 time points across interval $[0, 600]$. A Savitzky-Golay filter with window length 21 and order 2 was used to fit a smooth function to these 50 data points. This guaranteed a realistic smoothly changing heart rate across the 600s time interval. Secondly, a pulse train was generated from this simulated heart rate as depicted in Figure 4.5. Head motion M was simulated by using random rigid body rotations and translations drawn from

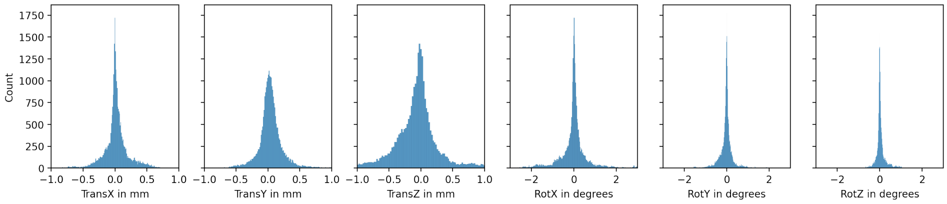

Figure 4.6: The distribution of 3 translations and 3 rotations estimated in the realignment process of fMRI volumes of the EPICure data.

motion parameters estimated in the realignment of volumes of the resting-state fMRI data of the EPICure cohort. The corresponding distributions for the three translations (mm) and rotations (degrees) are depicted in Figure 4.6. Six time courses were drawn from these distributions. The final head motion time course M was obtained by applying temporal principal component analysis (tPCA) to these six to extract the first principal temporal component.

Ten simulated fMRI scans were obtained with the presented simulation model. Furthermore, slice-wise EPI acquisition was simulated by sampling the simulated fMRI time courses Y at slice acquisition times $T_{sl} = \frac{3\text{s}}{50}, \frac{2*3\text{s}}{50}, \cdots, 600\text{s}$.

For CAMR, 9 ICs were estimated and results were compared to pre-processing with RETROICOR using the 5 covariate model described in Section 4.3.1.

4.3.2.1 Simulation 1

In the first experiment, the head motion term in Equation 4.3 was neglected. CAMR was evaluated on data simulated with only using brain networks, physiological motion and Gaussian noise. The percentage of frequency contributions in the aliasing window were compared before and after preprocessing with CAMR and RETROICOR.

4.3.2.2 Simulation 2

The second experiment comprised of the complete simulation model in Equation 4.3. Aliasing frequency contributions in the fMRI time courses were compared before and after preprocessing with CAMR and RETROICOR.

4.3.3 Results from simulated data

A scan of simulation 1 is shown before and after pre-processing with CAMR in Figure 4.7. The SWFT of the SWS of the simulated scan showed the change in cardiac frequency contributions resembled the simulated heart rate (A). Spatial ICA resulted in 3 ICs whose spatial maps resembled the simulated brain networks and 6 ICs whose spatial maps resembled slice artefacts due to simulated physiological motion (B). The linear regression model correctly identified these ICs as physiological motions. After removing these ICs from the simulated scan, cardiac frequency contributions substantially decreased in power.

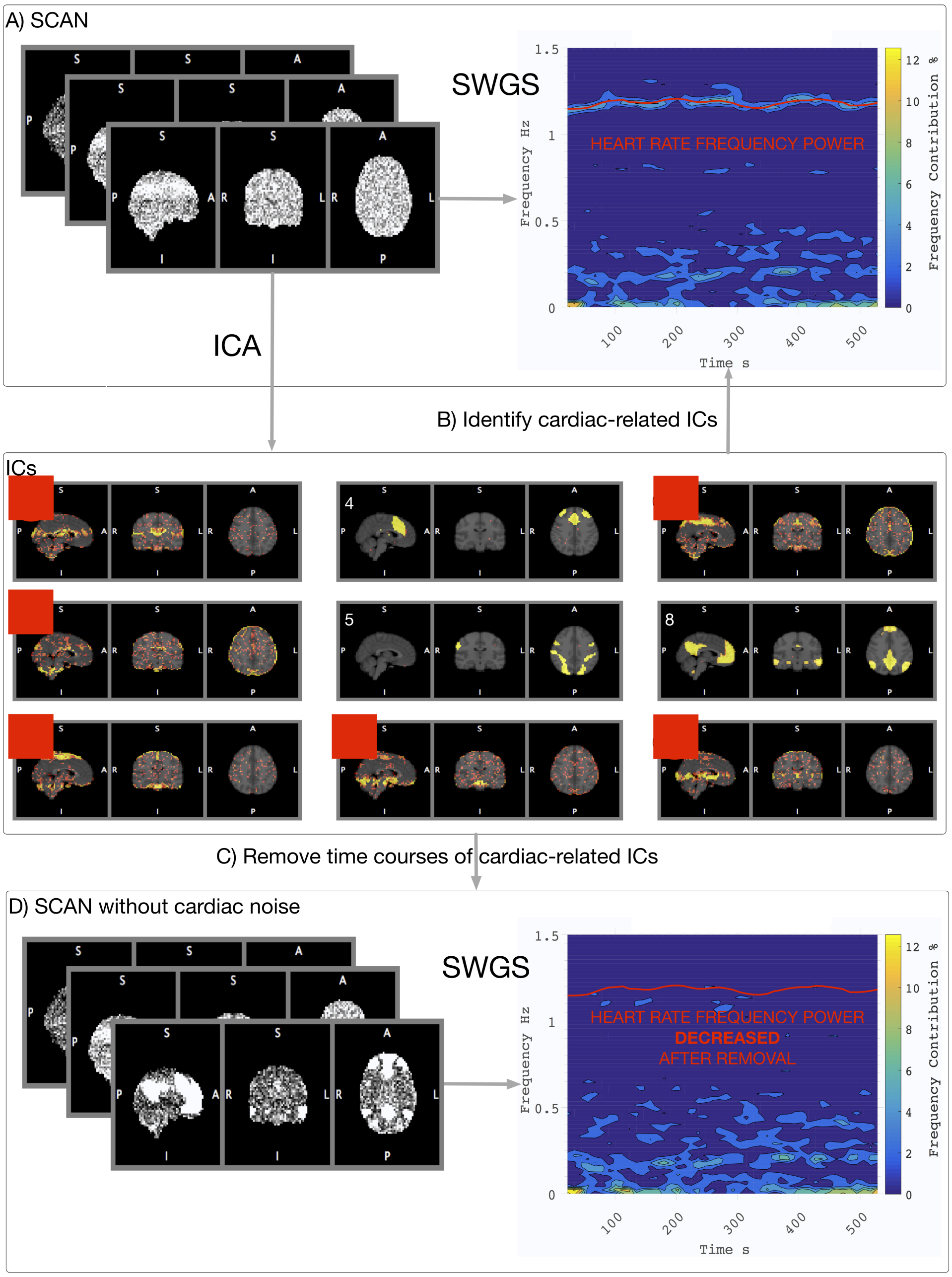

Figure 4.7: A) A simulated scan before pre-processing with CAMR. The red line depicts the simulated heart rate. CAMR comprised of spatial ICA composing each simulated scan into 9 ICs. Each IC consisted of a spatial map and time course. B) A linear regression was used to measure how much the SWS of each IC correlated with the physiological recording. C) All physiological motion ICs identified by the linear regression model (here marked with the red square sign) were removed from the original scan. D). The frequency contributions in the SWFT plot of the SWS of the scan in the proximity of the heart rate were substantially reduced in power after removing physiological motion ICs.

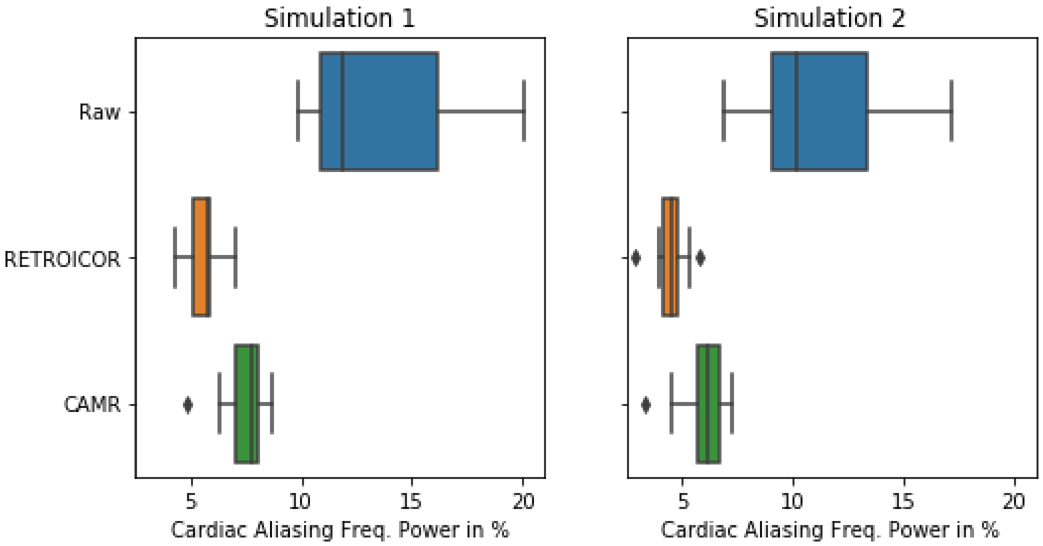

Figure 4.8: Results from simulated data. The cardiac aliasing frequency contribution for simulation 1 (left) and simulation 2 (right) in raw and pre-processed fMRI data with CAMR and RETROICOR.

4.3.3.1 Simulation 1

The average power of aliasing heart rate frequencies in simulation data 1 was 13.5% ($\sigma = 3.5$). Aliasing frequency power was 7.3% ($\sigma = 1.1$) after pre-processing with CAMR and 5.6% ($\sigma = 0.8$) after pre-processing with RETROICOR as depicted in Figure 4.8 (left). The power of aliasing frequencies was on average greater reduced with RETROICOR than CAMR.

4.3.3.2 Simulation 2

The average power of aliasing heart rate frequencies in simulation data 2 was 11.2% ($\sigma =$ 3.5). The average frequency power was 5.9% ($\sigma = 1.1$) after RICERCAR pre-processing and 4.5% ($\sigma = 0.8$) after RETROICOR pre-processing as depicted in Figure 4.8 (right). Table 4.1 shows the outcome of a paired t-test comparing RETROICOR and CAMR. CAMR performed significantly less well than RETROICOR in reducing cardiac aliasing frequencies in simulated data.

4.3.4 Results from imaging data

4.3.4.1 CAMR

Figure 4.9 shows a SWFT plot of the weighted average of SWSs of ICs identified as physiological motion for the four scans of subject 002. The original heart rate extracted from the corresponding physiological recordings (red dashed line) and corresponding frequencies in other Nyquist zones (yellow dashed lines) are superimposed on the corresponding SWFT plot. The average aliasing frequency power in unprocessed fMRI data was 7.5% ($\sigma = 1.9$) in the MPI7T cohort as depicted in Figure 4.10. Aliasing frequency power reduced to 6.6%

Data	A	B	t-val	p-unc	p-corr
Sim1	CAMR	RETROICOR	5.63	0.000320	
Sim2	CAMR	RETROICOR	4.31	0.001948	
EPICure	CAMR-SVM	GSR	-23.81	≤ 0.0001	≤ 0.0001
EPICure	CAMR-SVM	RETROICOR	-18.09	≤ 0.0001	≤ 0.0001
EPICure	CAMR-SVM	Raw	-18.41	≤ 0.0001	≤ 0.0001
EPICure	GSR	RETROICOR	25.73	≤ 0.0001	≤ 0.0001
EPICure	GSR	Raw	25.01	≤ 0.0001	≤ 0.0001
EPICure	RETROICOR	Raw	-6.87	≤ 0.0001	≤ 0.0001
MPI7T	CAMR	GSR	-25.70	≤ 0.0001	≤ 0.0001
MPI7T	CAMR	RETROICOR	-10.64	≤ 0.0001	≤ 0.0001
MPI7T	CAMR	Raw	-17.51	≤ 0.0001	≤ 0.0001
MPI7T	GSR	RETROICOR	24.95	≤ 0.0001	≤ 0.0001
MPI7T	GSR	Raw	32.09	≤ 0.0001	≤ 0.0001
MPI7T	RETROICOR	Raw	-10.95	≤ 0.0001	≤ 0.0001

Table 4.1: The outcome of a paired t-test comparing RETROICOR to CAMR in simulated data. Similarly, this t-test was applied to pairs of CAMR, RETROICOR, and GS, in the EPICure; and to pairs of CAMR-SVM, RETROICOR, and GS in the MPI7T cohort. CAMR performed statistically less well in the reduction of cardiac frequency contributions in simulated data than RETROICOR. CAMR and CAMR-SVM significantly outperformed RETROICOR and GSR in the reduction of cardiac frequency contributions in real imaging data.

($\sigma = 1.7$) after RETROICOR and 5.6% ($\sigma = 1.2$) after CAMR pre-processing. Aliasing frequency power increased to 9.3% ($\sigma = 2.3$) after GSR pre-processing.

Table 4.1 shows outcomes of a pair-wise applied paired t-test comparing RETROICOR, GS and CAMR. CAMR significantly outperformed RETROICOR and GS in the reduction of cardiac frequency contributions.

4.3.4.2 CAMR-SVM

The SWFT plot of the SWS of ICs classified as physiological motion is depicted in Figure 4.11 for four scans of the EPICure cohort. The original heart rate extracted from the physiological recording (red dashed line) and corresponding frequencies in other Nyquist zones (yellow dashed lines) are superimposed on the individual SWFT plot. The average aliasing frequency contribution before pre-processing was 5.8% ($\sigma = 2.3$) in the EPICure cohort as depicted in Figure 4.12, which is lower than in the MPI7T cohort. RETROICOR reduced aliasing frequency contributions to 5.7% ($\sigma = 2.2$) and CAMR reduced aliasing frequency contributions to 4.1% ($\sigma = 1.8$). Aliasing frequency contribution increased to 6.9% ($\sigma = 2.6$) with GSR pre-processing.

Table 4.1 shows outcomes of a pair-wise applied paired t-test comparing RETROICOR, GS and CAMR-SVM. CAMR-SVM significantly outperformed RETROICOR and GS in the reduction of cardiac frequency contributions.

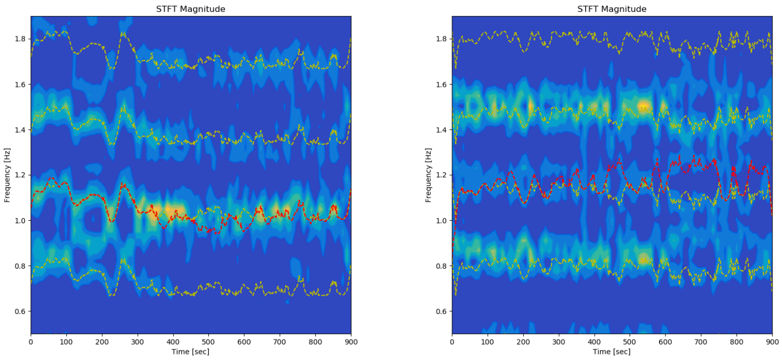

(a) 002-01 **(b)** 002-02

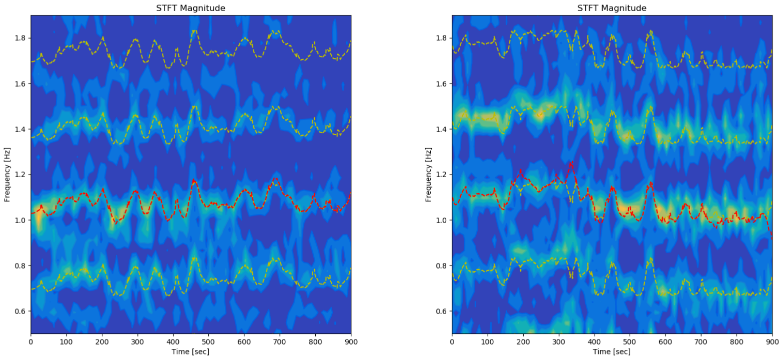

(c) 002-11 **(d)** 002-12

Figure 4.9: The SWFT of the weighted average of SWSs of ICs identified as physiological motion for the four scans of subject 002 of the MPI7T cohort. The original heart rate extracted from physiological recordings (red dashed lines) and corresponding frequencies in other Nyquist zones (yellow dashed lines) are superimposed on the corresponding SWFT plot.

4.4 Discussion

A novel pre-processing pipeline was proposed to remove physiological motion artefacts caused by the cardiac cycle. Two versions of this pipeline, CAMR and CAMR-SVM, are proposed, which either work with or without additional physiological recordings. CAMR classifies ICs as physiological motion depending on the amount of variance such ICs explain in the physiological recording.

In contrast to CAMR, CAMR-SVM can be used without physiological recordings but requires training on a set of already classified ICs. This training data were ICs of the MPI7T cohort classified by CAMR. Hereby, CAMR-SVM trained a SVM on temporal features of time courses of these ICs. Ultimately, the performance of CAMR-SVM was evaluated on the EPICure cohort. The application of both, CAMR and CAMR-SVM, resulted in a reduction of aliasing frequency contributions caused by physiological motion.

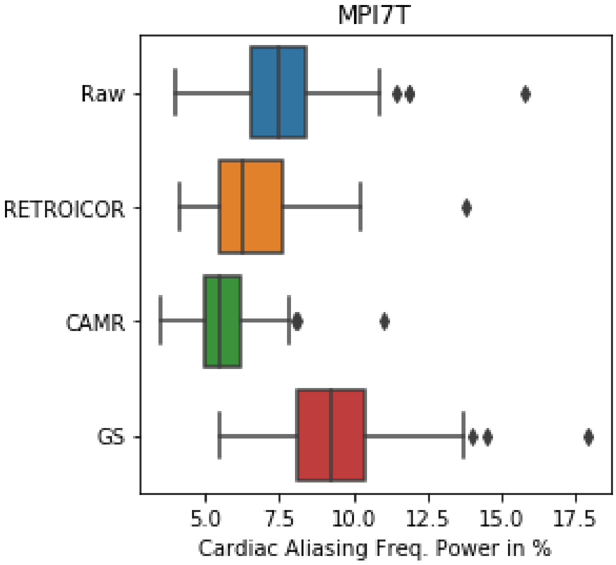

Figure 4.10: Overview of cardiac aliasing frequency contributions in raw fMRI data and after pre-processing with CAMR, RETROICOR and GSR in the MPI7T cohort. CAMR outperformed RETROICOR in reducing aliasing frequency contributions. Strikingly, GSR left cardiac aliasing frequencies unchanged or even increased their power.

The CAMR and CAMR-SVM model were compared to RETROICOR. RETROICOR outperformed CAMR on simulated data but was outperformed by CAMR and CAMR-SVM in the two examined imaging cohorts. Head motion potentially explains the discrepancy in performance between results obtained with RETROICOR on the simulated data and on the MPI7T cohort. RETROICOR outperformed CAMR in simulated data but the simulated fMRI data was perfectly temporal aligned with simulated the simulated pulse signal. However, RETROICOR performed less well on real data.

This is likely due to head motion creating a mismatch between assumed and actual slice positions along the time axis. For example, Jones et al. [2008] showed that performing volume realignment without slice-time correction before applying RETROICOR resulted in the best reduction in temporal noise. This supports our finding that physiological motion artefacts presented in a slice-dependent manner in the analysed fMRI cohorts. However, studies analysing physiological motion in fMRI data vary substantially with respect to the number of influenced voxels [Birn et al., 2006, 2008, Chang et al., 2009, Chang and Glover, 2009a, Bianciardi et al., 2009, Jo et al., 2010]. Chang et al. [Chang et al., 2009, Chang and Glover, 2009b,a, 2010] found many voxels of the brain affected by physiological motion. However, all fMRI scans in these studies were acquired with subjects using bite bars to rigorously prevent head motion. With no head motion, physiological motion becomes the most prevalent noise source in the fMRI scans.

In contrast, RETROICOR covariates were found to explain a relatively low amount of vari-

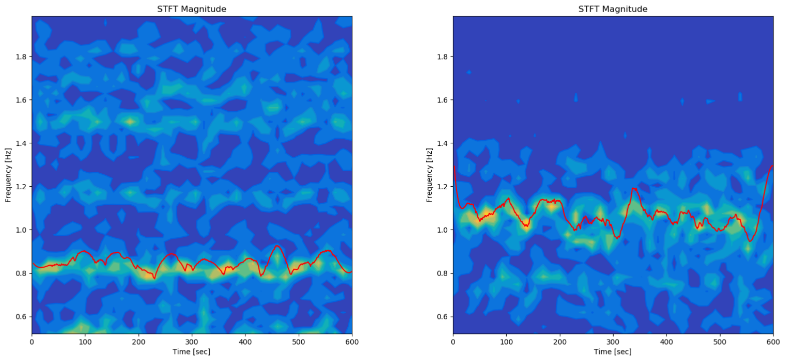

(a) Subj13620 **(b)** Subj14416

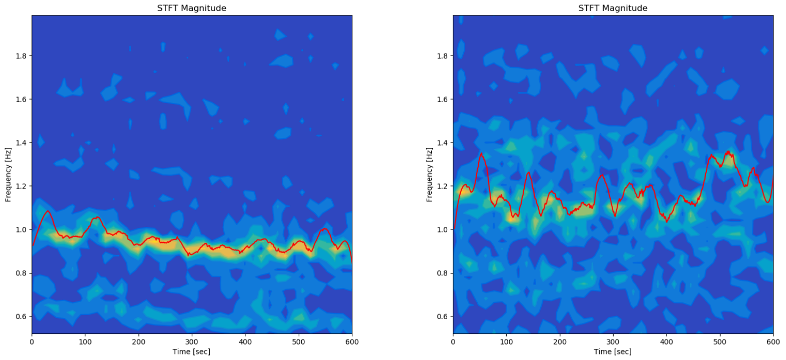

(c) Subj14121 **(d)** Subj15516

Figure 4.11: The SWFT of the weighted average of SWSs of ICs classified as physiological motion for four different subject scans of the EPICure cohort. The original heart rate (red dashed line) extracted from the physiological recording and corresponding frequencies in other Nyquist zones (yellow dashed lines) are superimposed on the corresponding SWFT plot.

ance in studies using only foam padding to prevent head motion [Bianciardi et al., 2009]. Our findings showed that low head motion fMRI scans had more pronounced aliasing frequency contributions of the heart rate.

Furthermore, GSR had not proven to be effective in the reduction physiological motion frequencies but actually resulted in an increase in power of cardiac aliasing frequencies. This is expected because physiological motion will cause distinct structural noise patterns in fMRI volumes acquired in a slice-wise fashion with EPI.

Another limitation of RETROICOR covariates is there strong reliance on good quality physiological recordings. In a laboratory setting, there is sufficient time to prepare proper physiological monitoring. For example, in Chang et al. [2009], physiological recordings were acquired with electrocardiography (ECG) known to produce more precise heart rate estimates.

However, in a clinical setting, physiological recordings are often acquired with pulse plethys-

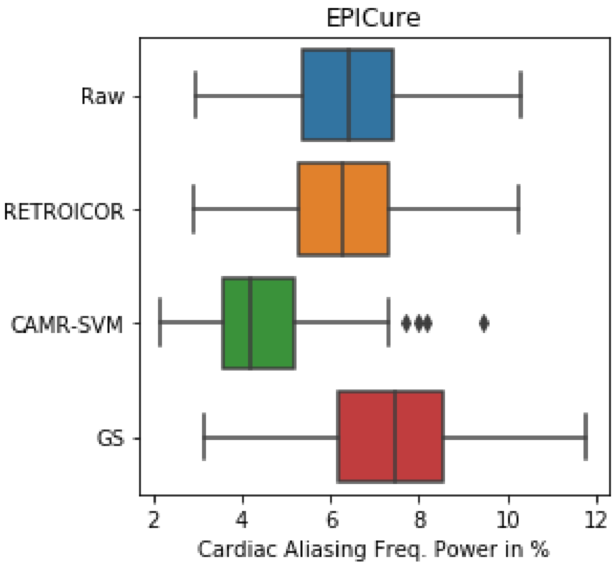

Figure 4.12: Overview of cardiac aliasing frequency contributions before and after pre-processing with CAMR-SVM, RETROICOR and GSR in the EPICure cohort. CAMR-SVM outperformed RETROICOR in reducing aliasing frequency contributions of the heart rate. Similar to the result with GSR on the MPI7T cohort, GSR left cardiac aliasing frequencies unchanged or increased their frequency contributions.

mography. This type of signal acquisition is sensitive to motion. The sensor can slip from its initial position creating signal drop-out or noise in the recording. The error builds up in peak to peak extraction and ultimately corrupts RETROICOR covariates.

Furthermore, RETROICOR does not account for a phase difference between cardiac cycles in hand and the brain. For example, the delay between ECG and photoplethysmograph measurements is approximately 120ms ± 25 (courtesy of Karin Shmueli).

Another limiting factor might be that a pulse photoplethysmograph recording unit often only outputs heart rate peak timings without providing the entire raw physiological recording.

These shortcomings in the acquisition of physiological recordings render RETROICOR covariates less effective. The proposed CAMR and CAMR-SVM model are less sensitive to these error sources. CAMR only requires the physiological recording of the cardiac cycle for the classification of ICs and can potentially be extended to work with only heart rate traces instead of the raw physiological recording. CAMR-SVM circumvents the requirement for physiological recordings entirely but requires pre-training on a cohort with physiological recordings. The obtained time course features are likely TR dependent and therefore the SVM pipeline might require re-training when used on fMRI data with substantially different TRs.

Furthermore, CAMR and CAMR-SVM were proposed to address physiological motion artefacts. However, physiological motion and physiological interactions in haemodynamic response can not always be fully disentangled. The former creates slice-dependent artefacts due to interaction of pulsatile motion with slice acquisition of EPI, whereas the latter are low-frequency interactions between cardiac cycle and haemodynamic response [Shmueli et al., 2007, Chang et al., 2009, Birn et al., 2008, Chang et al., 2013, Thayer et al., 2012]. For instance, Chang et al. [2013] showed a significant influence of elevated heart rate variability on functional connections between dorsal anterior cingulate cortex and amygdala to brain regions in the prefrontal cortex.

Similar observation are made for the respiratory cycle. For example, brain regions strongly correlating with respiratory fluctuations were found to overlap with spatial clusters of the DMN [Birn et al., 2008, Murphy et al., 2013].

Lastly, the effect of the cardiac cycle on the brain might be intensified by other hidden physiological parameters such as body weight, arterial blood pressure or vascular resistance [Murphy et al., 2013]. These hidden factors thus deserve a more rigorous examination with respect to their influence on the haemodynamic response, which constitutes an exciting area for future research.

4.5 Conclusion

Neuroimaging such as with fMRI has been used to determine localised functional differences between healthy and disease cohorts. However, these spatial differences might not be conclusive at the individual subject level. It thus remains a great challenge to obtain reliable functional connectivity estimates at subject level so that diagnostic decisions can be made solely on a subject's brain scan.

This chapter showed that heart rate variability can be found by exploiting the unique way in which fMRI volumes are acquired with EPI. Two spatial ICA-based frameworks, CAMR and CAMR-SVM, were presented which allowed the identification of physiological motion artefacts and their removal, showing an effective reduction of cardiac aliasing frequency contributions in fMRI scans.

Chapter 5

Resting-state network patterns in extremely-preterm born young adults

5.1 Introduction

The prevalence of extreme-prematurity is increasing across the globe. Neuroimaging studies allow to investigate the underlying tissue substrate of the broader neuropsychological differences observed in preterm cohorts; but the long-term neuroimaging phenotype of extremely-preterm adolescents is relatively unknown.

This chapter examines if there is a variability in the pattern of functional networks in extremely-preterm born 19 year-olds relative to a group of their term-born peers using resting-state fMRI.

5.1.1 Motivation

Infants born at 32 weeks or less are significantly more likely to suffer from cerebral palsy, cognitive deficits, loss of motor function and can have long-term difficulties in education [White et al., 2014]. Extreme prematurity is a global health concern. Rates of prematurity are increasing worldwide and the long-term impacts of extreme prematurity are only recently beginning to be understood. Although several studies have been carried out analysing structural data [Nosarti et al., 2014], less is known about the long term neurophysiological functional differences.

One way to non-invasively examine functional brain differences in preterm- and term-born individuals is fMRI. Hereby, the blood-oxygen–level-dependent (BOLD) contrast, which measures the ratio between oxygenated and deoxygenated haemoglobin, is used as proxy measure for neural activation. Spontaneously occurring neural activations while being scanned during rest have been found to organise in spatiotemporal patterns, so called resting-state brain networks (RSN) [Biswal et al., 1995, Beckmann et al., 2009, Varoquaux et al., 2010, Damoiseaux et al., 2012].

For the healthy adult brain, these RSNs have been extensively studied by large neuroimaging initiatives such as the Young Adult Human Connectome Project (HCP) [Van Essen et al., 2012, 2013, Glasser et al., 2013].

Similarly, large open source neuroimaging initiatives are dedicated to determine disruptions in the development of functional and structural connectivity in the brain in individuals affected by premature birth. For example, the Developing Human Connectome Project (dHCP) is a large cohort that seeks to establish the functional and structural connectome at 20 to 44 weeks of gestational age (GA). The long-term objective of this cohort is to gain insights about human brain development and early intervention to prevent neurological and psychological disorders [Makropoulos et al., 2018, Bastiani et al., 2019, Fitzgibbon et al., 2020, Eyre et al., 2020].

Analysis by Eyre et al. [2020] of the fMRI scans acquired at this early age provided a detailed characterisation about the functional connectivity, showing that preterm birth caused significant early and widespread disruption of the formation of functional RSN in infants.

5.1.2 Previous work

Spatial patterns of RSNs of the eloquent cortex (sensori-motor, auditory, visual and language) are present in infants from as early as 26 weeks postmenstrual age (PMA) [Doria et al., 2010, Smyser et al., 2010, Thomason et al., 2017]. In contrast, it is still debated if RSNs associated with higher cognitive function evolve as early in life (reviewed in Gilmore et al. [2018]). For example, the work by Gao et al. provided evidence that spatial maps of DMN and DAN are already seen in adults within the first year after birth, whereas spatial maps of salience and fronto-parietal networks converge to their characteristic shape within the second year after birth [Gao et al., 2015b,a].

In contrast, results by the dHCP show spatial enlargement and increase in within-network connectivity with age in all examined RSNs including posterior parietal, fronto-parietal, prefrontal and visual association RSNs [Eyre et al., 2020].

These observed functional developments are supported by rapid structural changes during the first year of brain development including myelination of white matter and gyrification of the cerebral cortex (reviewed in Dubois et al. [2014]).

The disruption of functional integrity in infants might relate to widely observed neuropsychological and visual processing differences seen later in life in extremely preterm born cohorts [Marlow et al., 2005, Blencowe et al., 2013].

5.1.3 Proposed solution

This chapter investigates if widespread functional differences [Eyre et al., 2020] in infancy will also be present at early adulthood. Therefore, a cohort of 19 year-old preterm born individuals and age-matched peers (EPICure) underwent resting-state fMRI scanning.

The fMRI scans of these EPICure subjects were used to compare functional differences in spatial maps of established RSNs.

Therefore, Multivariate Exploratory Linear Decomposition into Independent Components (MELODIC), a popular approach to establish group-level RSNs was applied to the EPICure cohort [Smith et al., 2004, Woolrich et al., 2009, Jenkinson et al., 2012]. MELODIC implements spatial ICA, a dimensionality reduction approach with the objective to produce statistically independent components. MELODIC was applied to 138 resting-state fMRI scans of the EPICURE cohort. Therefore, fMRI scans were pre-processed and mapped into MNI space.

Group-level spatial maps were derived from a normative subset of the resting-state fMRI scans of the term-born adults. This was followed by Dual Regression to obtain spatial maps of RSNs in the remaining term-born adults and in all preterm-born adults. Subsequently, these spatial maps were compared voxel-wise between the preterm- and term-born group in MNI space.

This comparison showed differences in the dorsal attention network (DAN). These differences were located in a small cluster in the right anterior intra-parietal sulcus. Additionally, preterm-born subjects presented with less within-network functional connectivity across several RSNs.

Furthermore, functional connectivity between pairs of brain atlas regions was compared in the EPICure cohort.

In contrast to the analysis in MNI space, this analysis examined functional connectivity in native subject space by deriving an atlas from structural imaging for each subject [Cardoso et al., 2015]. The functional connectivity between pairs of regions in these atlases was computed using partial correlation.

The atlas-based group comparison revealed differences in functional connectivity between nodes in the basal ganglia and areas in the frontal cortex. However, these differences were less significant when using average heart rate, gender, head motion, and total intracranial volume (TIV) as noise covariates in this group comparison of functional connectivity.

5.2 Materials and Methods

5.2.1 Data acquisition

One hundred and thirty-eight participants are recruited from the EPICure study of infants born extremely preterm at 26 completed weeks of gestation or less between March and December 1995 in the United Kingdom and the Republic of Ireland. The cohort includes a group of 53 full-term (FT) born who are socio-economically matched with 85 extremely preterm (EP) born [O'Reilly et al., 2020]. Table 5.1 reports the details of the EPICure co-

Participants characteristics	EP	FT
Number of subjects N	85	53
Gender (female/male)	49/36	32/21
Completed Weeks of gestation		
$23 := 22-23$ W (female/male)	7/2	−/−
$24 := 24$ W (female/male)	14/8	−/−
$25 := 25$ W (female/male)	28/26	−/−
$40 :=$ from 37 W (female/male)	−/−	32/21

Table 5.1: Participant characteristics of the EPICure project including number of subjects in each group, gender, and completed weeks of gestation (Copy from Irzan et al. [2021]).

hort. T1-weighted MRI and diffusion weighted MRI (dWMRI) acquisitions were performed on a 3T Philips Achieva system at subjects' 19th birthday. MPRAGE T1-weighted MRI images were acquired at TR of 6.93ms, TE of 3.14ms with 1mm isotropic resolution.

Diffusion-weighted MRI were acquired at $(2.5 \times 2.5 \times 3\text{mm})$ resolution across b-values of $(0, 300, 700, 2000\frac{\text{s}}{\text{ms}^2})$, and $\text{n} = 4, 8, 16, 32$ directions. The acquisitions are performed at TE 70ms, TR 3500ms, with field of view $(240 \times 240 \times 150\text{mm})$, flip angle 90 degrees, and SENSE factor of one. The corresponding analysis of the diffusion data can be found in Irzan et al. [2021].

The resting-state fMRI scans comprised of 200 volumes acquired with TR 3000ms, TE 30 ms, flip angle 80°, voxel size $2.5 \times 2.5 \times 3\text{mm}^3$, field of view (FoV) 240mm^2, 50 oblique transverse slices, slice order descending.

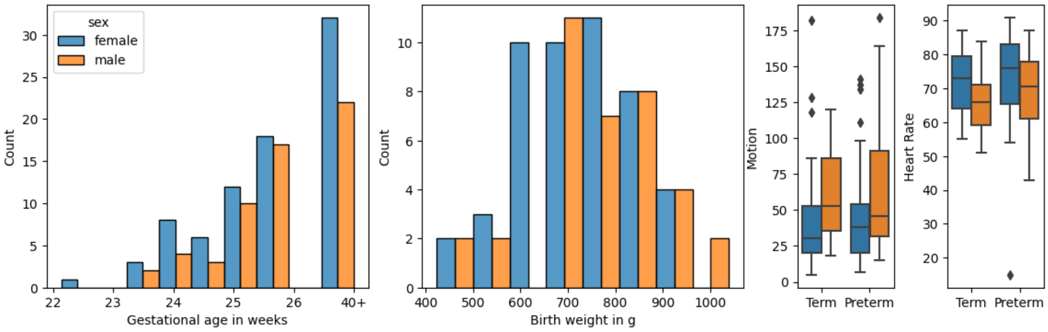

Figure 5.1: Distribution of gestational age (ga), birth weight (bw) for the preterm born subjects, number of motion outlier volumes identified by the pre-processing pipeline of the fMRI data, and the average heart rate from the pulse oximeter recording acquired during fMRI scanning.

5.2.2 Data preparation

Pre-processing was performed using FMRIPREP version 1.4 ([Esteban et al., 2019], RRID:SCR_016216), a Nipype ([Gorgolewski et al., 2011], RRID:SCR_002502) based tool.

5.2.2.1 Pre-processing of anatomical data

Each T1w (T1-weighted) volume is corrected for intensity non-uniformity (INU) using N4BiasFieldCorrection (v2.1.0) [Tustison et al., 2010] and skull-stripped using antsBrainExtraction.sh (v2.1.0) using the OASIS template. Spatial normalisation to the ICBM 152 Nonlinear Asymmetrical template version 2009c (RRID:SCR_008796) [Fonov et al., 2009] was performed through nonlinear registration with the antsRegistration tool of ANTs (v2.1.0, RRID:SCR_004757) [Avants et al., 2008], using brain-extracted versions of both T1w volume and template. Brain tissue segmentation of cerebrospinal fluid (CSF), white-matter (WM) and grey-matter (GM) was performed on the brain-extracted T1w using fast (FSL v5.0.9, RRID:SCR_002823).

5.2.2.2 Pre-processing of resting-state fMRI data

Functional data was slice time corrected using 3dTshift from AFNI v16.2.07 ([Cox, 1996], RRID:SCR_005927) and motion corrected using mcflirt (FSL v5.0.9) [Jenkinson et al., 2002]. This was followed by co-registration to the corresponding T1w using boundary-based registration [Greve and Fischl, 2009] with twelve degrees of freedom, using flirt (FSL). Motion correcting transformations, BOLD-to-T1w transformation and T1w-to-template (MNI) warp were concatenated and applied in a single step using antsApplyTransforms (ANTs v2.1.0) using Lanczos interpolation. Frame-wise displacement [Power et al., 2014] was calculated for each functional run using the implementation of Nipype. These fMRI time course were further pre-processing by regressing 18 volume realignment parameters, bandpass regressors $(0.01-0.1\text{Hz})$[Cox, 1996], and 6 anatomical region regressors. Spatial smoothing with a 5mm kernel was applied. Time courses were normalised to zero mean and unit standard deviation.

5.2.2.3 Pre-processing of pulse oximetry recordings

Pulse oximetry records were available for each individual subject of the EPICure cohort but not synchronised to the MR data acquisition times. A multi-task Gaussian process model was used to derive a pulse rate variability (PRV) measure while also correcting missing periods in the physiological recordings as presented in Chapter 3.

5.3 Experiments and results

5.3.1 Group-level networks derivation

The group maps of RSNs were obtained with sICA implemented in FSL MELODIC [Beckmann and Smith, 2004, Beckmann et al., 2009] with automatic dimensionality estimation using 22 of the healthy term-born adult group. These individuals were excluded from all subsequent DR analysis. The obtained 42 ICs were manually labelled according to the cri-

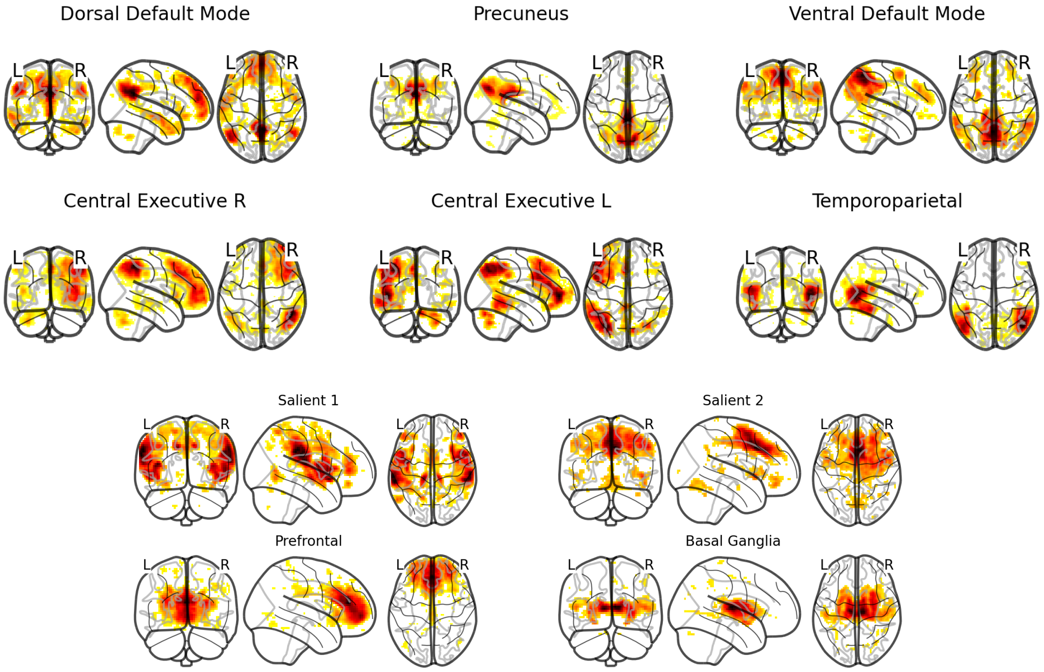

Figure 5.2: Identified group RSNs associated with higher cognitive function included the dorsal and ventral default mode network (dDMN and vDMN), precuneus network (PREC), dorsal attention network (DAN), left and right central executive network (LCEN and RCEN), temporo-parietal network (TPN), two salient networks (SN1 and SN2), prefrontal network (PFN), and basal ganglia network (BGN).

teria in Griffanti et al. [2017], resulting in 22 identified RSNs ICs and 20 noise ICs.

The identified RSNs associated with higher cognitive brain function depicted in Figure 5.2 included the dorsal and ventral default mode network (dDMN and vDMN), precuneus network (PREC), left and right central executive network (LCEN and RCEN), temporo-parietal network (TPN), dorsal attention network (DAN), two salient networks (SN1 and SN2), prefrontal network (PFN), and basal ganglia network (BGN). Furthermore, several RSNs networks mapping the eloquent cortex were found including motor, visual, auditory and language networks depicted in Figure 5.3. These RSNs included four visual (VN1-VN4), one auditory (AN), multiple sensory-motor networks (medial motor - MN, left hand - LH, right hand - RH, tongue - T), and a left and right language network (LL and LR).

5.3.2 Subject-level RSN group comparison

The total of 42 group-level ICs (22 RSNs and 20 noise ICs) were regressed from subjects for group comparison (31 FT born, 85 EP born). More specifically, DR was used to obtain spatial maps in each subject. The first regression resulted in subject-specific time courses for each of the 42 group ICs. These time courses were used in a second regression to obtain subject-specific spatial maps in MNI space.

Subsequently, a comparison to test for the effects of group (term vs. preterm birth) was

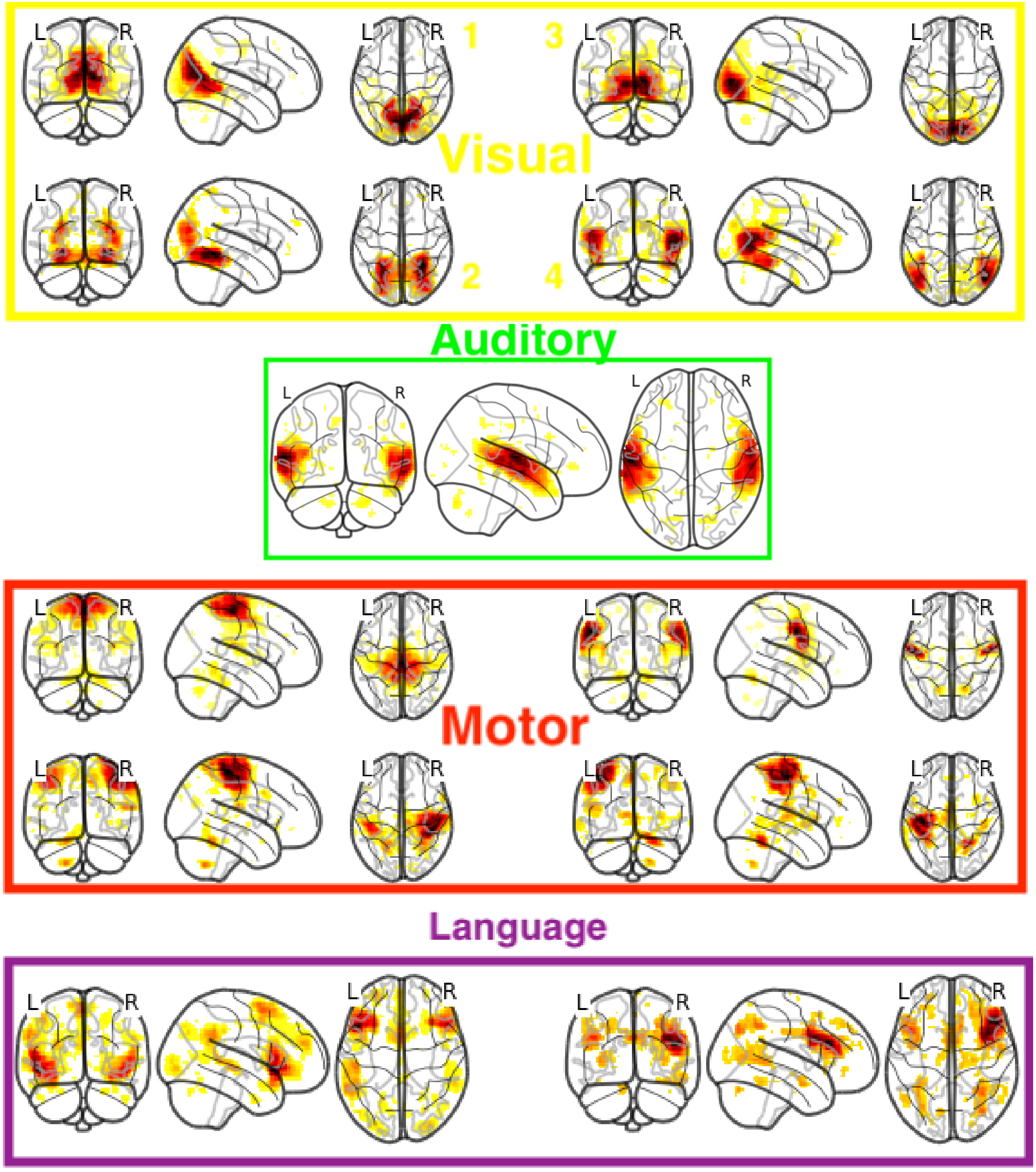

Figure 5.3: RSNs mapping the eloquent cortex included four visual (VN1-VN4), one auditory (AN), multiple sensory-motor networks (medial motor - MN, left hand - LH, right hand - RH, tongue - T), and a left and right language network (LL and LR).

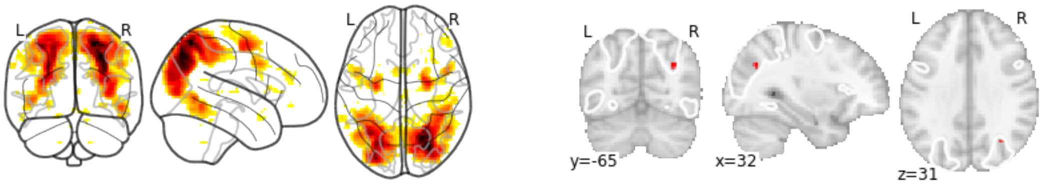

Figure 5.4: The spatial map of the dorsal attention RSN (left) and the corresponding spatial difference between term- and preterm-born subjects after multiple comparison correction with FWE (right). The red area in the DAN in the right anterior intra-parietal sulcus is significantly less connected in preterm-born subjects (p-values less than 0.05). This cluster is not significant when also correcting for the number of examined RSNs (Bonferroni correction).

performed. The number of motion outlier volumes, average heart rate, gender, and TIV were modelled as noise covariates.

Statistical tests were performed using the implementation in FSL randomise and threshold-free cluster enhancement with 5000 permutations [Beckmann et al., 2009, Nickerson et al., 2017, Winkler et al., 2014]. Multiple statistical tests across voxels were corrected for family-wise error-rate (FWE). Voxel with p-values less than 0.05 were considered as significant. Additionally, Bonferroni correction was applied to account for the number of examined RSNs.

As described in Eyre et al. [2020], the measure *core network strength* of individual RSNs was compared between preterm and term-born subjects. This measure was determined for each RSN for each subject by masking the RSN-specific spatial map by the corresponding group-level map thresholded at $Z > 3$, then calculating the mean over β parameter estimates within the masked image. Subsequently, a GLM was used to test for group differences in core network strength between term- and preterm-born adults while controlling for gender, head motion, average heart rate, and TIV[1].

The group analysis comparing spatial maps of term-born and preterm-born RSNs in MNI space resulted in a significant difference in the DAN depicted in Figure 5.4. One small cluster presented in the right anterior intra-parietal sulcus of the DAN. However, the cluster was not significant when also taking into account the number of examined RSNs (Bonferroni correction). Raw core strength (top row) and core strength using gender, head motion, average heart rate and TIV as additional covariates (bottom row) were compared in the 22 RSNs between term- and preterm-born subjects as depicted in Figure 5.5. The single star indicates p-values below 0.05 in the test statistic of a non-parametric Mann–Whitney U test. The double star indicates p-values below 0.05 corrected for multiple comparison. Raw core strength was weaker in preterm-born adults in VN3 but did not survive Bonfer-

---

[1] Implemented in statsmodels 0.12.2.

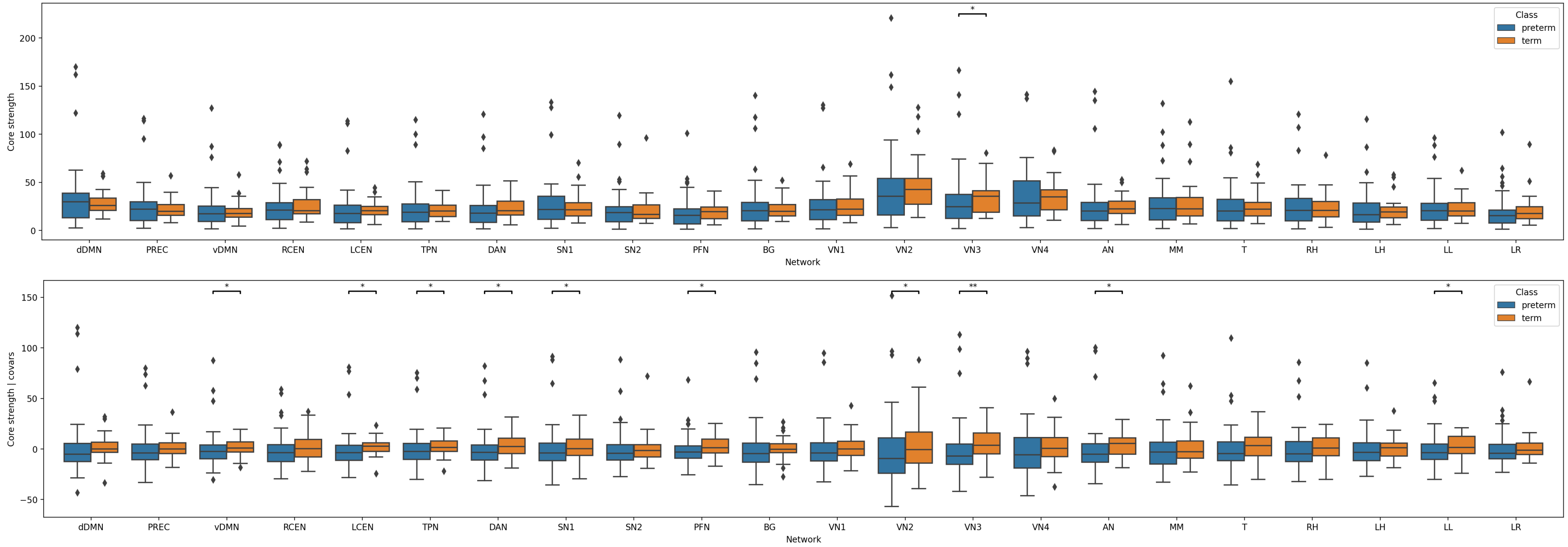

Figure 5.5: Raw core strength (top row) and core strength corrected for gender, head motion, average heart rate and TIV (bottom row) in all 22 RSNs including networks of higher cognitive function: dorsal and ventral default mode network (dDMN and vDMN), precuneus network (PREC), left and right central executive network (LCEN and RCEN), temporo-parietal network (TPN), dorsal attention network (DAN), two salient networks (SN1 and SN2), prefrontal network (PFN), and basal ganglia network (BGN); and RSNs mapping the eloquent cortex: four visual (VN1-VN4), one auditory network (AN), four sensory-motor networks (medial motor - MN, left hand - LH, right hand - RH, tongue - T), and left and right language network (LL and LR). The single star indicates p-values below 0.05 in the test statistic of a non-parametric Mann–Whitney U test. The double star indicates p-values below 0.05 corrected for multiple comparison. Raw core strength is weaker in preterm-born adults in VN3 but does not survive Bonferroni correction. In contrast, multiple RSNs showed p-values less than 0.05 comparing core strength between term- and preterm-born subjects using the additional covariates: gender, head motion, average heart rate, and TIV. These RSNs are vDMN, LCEN, TPN, DAN, SN1, PFN, VN2, VN3, AN and LL. However, only the lower core strength in VN3 in preterm-born adults remained significant after correcting for multiple comparison.

roni correction. In contrast, multiple RSNs showed p-values less than 0.05 comparing core strength between term- and preterm-born subjects using the additional covariates: gender, head motion, average heart rate, and TIV. However, only the lower core strength in VN3 remained significant after correcting for multiple comparison.

5.3.3 Functional connectivity matrices using GIF-parcellations

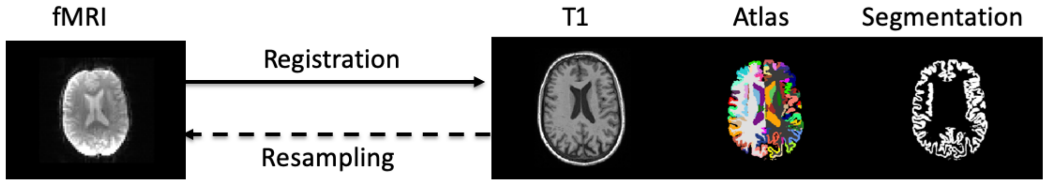

Figure 5.6: fMRI volumes were registered to the structural scan. Atlas and segmentation were resampled in fMRI space.

The second analysis compared functional connectivity estimates between pairs of atlas regions. Therefore, the geodesic information flow (GIF) algorithm [Cardoso et al., 2015] was applied to the structural T1 image of each subject to produce a subject-specific atlas. fMRI scans were registered to their corresponding T1 image and resampled in T1 space. Region-wise time courses were extracted and pair-wise partial correlation[2] was computed between all pairs of cortical atlas regions as depicted in Figure 5.6. A large number of pairs of atlas regions poses a challenge for group comparison because of the large number of tests to be conducted. Therefore, atlas regions were limited to nodes of the basal ganglia, frontal cortex, and nodes significantly modulated by low-frequency heart rate variability as described in Chang et al. [2013]. Furthermore, left and right atlas region of a brain area were merged into one cluster by taking the average of the two extracted time courses to further reduce multiple comparison in the subsequent analysis. The full list of areas used in the analysis is depicted in Figure 5.7, which displays the average functional connectivity of the term-born control group in as a connectivity matrix and a corresponding glass brain with the largest 10% of edge values visible. No significant partial correlation was observed between heart rate and any of the examined brain regions. Similarly to core strength, raw partial correlations between pairs of atlas regions were compared to partial correlations corrected for gender, head motion, average heart rate and TIV. The comparison of raw partial correlations resulted in 14 differences with p-values less than 0.01. However, of the 14 differences, 6 of these remained significant and 2 new significant differences were found after correcting for aforementioned covariates. Increased functional connectivity in preterm-born subjects was observed between pallidum and precentral gyrus, thalamus and cuneus, lingual gyrus and orbital part of the inferior frontal gyrus, opercular part of the inferior frontal gyrus

---

[2] Implemented in nilearn 0.7.0.

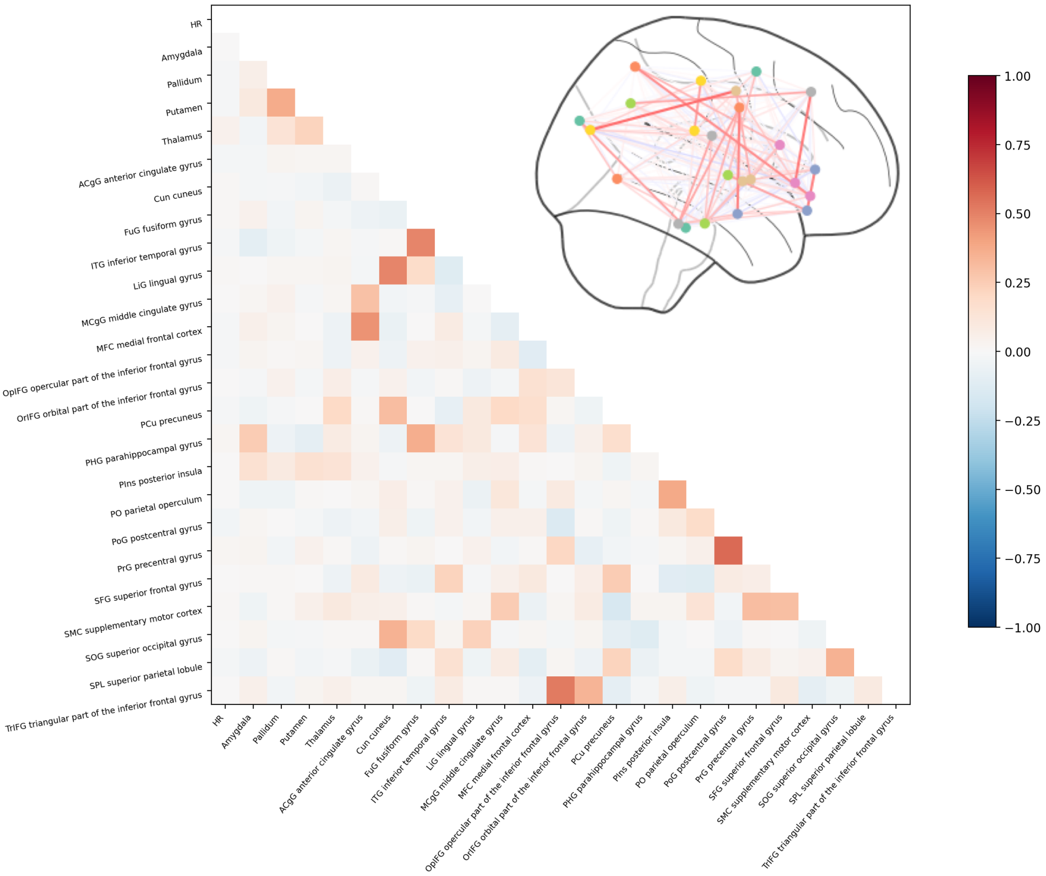

Figure 5.7: Functional connectivity (partial correlation) between pairs of GIF atlas regions in the term-born subject group. No significant partial correlation was observed between heart rate and any of the examined brain regions.

and superior parietal lobule, precuneus and triangular part of the inferior frontal gyrus, and parahippocampal gyrus and precentral gyrus.

Reduced functional connectivity in preterm-born subjects was observed between precuneus and thalamus, and triangular part of the inferior frontal gyrus and superior parietal lobule. Non of these differences remained significant after Bonferroni correction for multiple comparison. Distributions of structural volumes of atlas regions are depicted for preterm- (blue) and term-born adults (orange) in Figure 5.9. Significant differences determined by a non-parametric Mann–Whitney U test are denoted by $*$ and $**$ for uncorrected and corrected (Bonferroni) p-values < 0.01, respectively. The volume of the preterm basal ganglia was significantly less than that in the term group. Similarly, the volume of many cortical regions were also significantly lower in preterm-born adults than in their term-born peers.

5.4 Discussion

The functional mapping and connectivity was examined in a cohort of 19 year old preterm- and an age-matched control group of term-born adults. Spatial ICA and DR were applied to

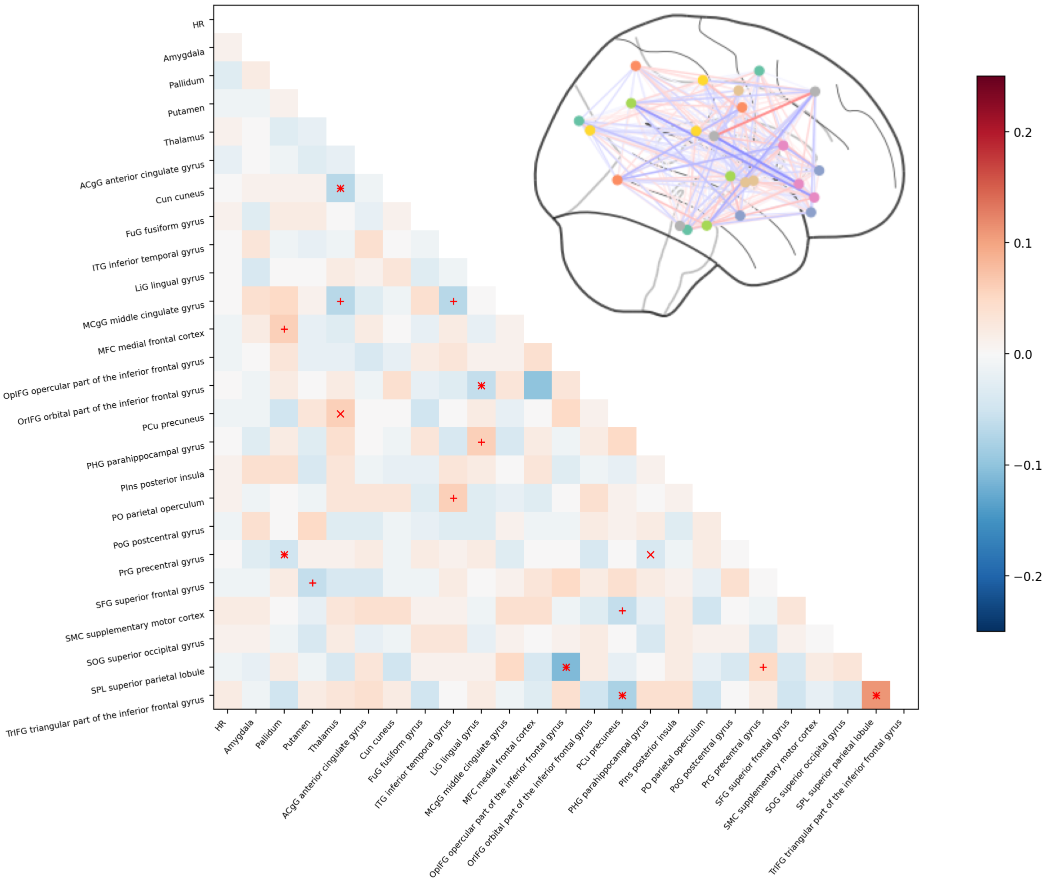

Figure 5.8: Functional connectivity of the term-born adults was compared to their preterm-born peers. Edges on the blue colour scale had less functional connectivity in the term-borns; edges on the red colour scale had greater functional connectivity in term-born. The comparison of raw partial correlations resulted in 14 differences with p-values less than 0.01 (denoted by +). However, only 6 of these 14 differences remained significant (denoted by ∗) and 2 new significant differences (denoted by ×) were found after correcting for gender, head motion, average heart rate, and TIV.

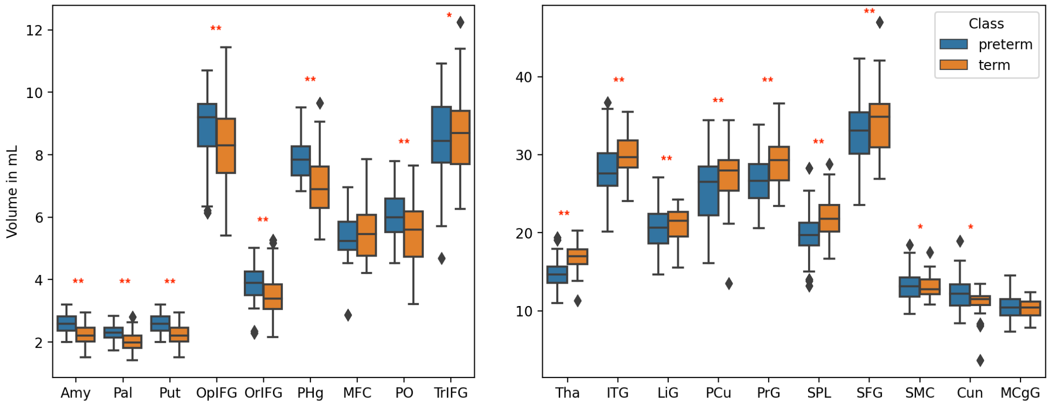

Figure 5.9: Volumes of individual subcortical and cortical brain regions obtained from the structural T1 scan in each subject.

the resting-state fMRI scans of these subjects. The comparison of spatial mappings between these two groups resulted in stronger functional connectivity in term- than preterm-born adults in a small cluster in the right anterior intra-parietal sulcus of the DAN. Greater core strength in term-born adults was found in 10 of 22 obtained RSNs. Only one significant difference in core strength remained after correcting for multiple comparison.

Secondly, a functional connectivity analysis based on subject-specific anatomical atlases was conducted and showed differences in connections between nodes of the basal ganglia and several cortical brain regions. However, none of these differences remained significant after correcting for multiple comparison.

The analysis of the EPICure cohort resulted in 22 RSNs including networks of higher cognitive function and networks mapping the eloquent cortex including visual, motor, auditory and language cortices.

Many of these obtained RSNs are found in infants and neonates. In preterm born neonates, evidence suggests that the development of default mode and attentions networks is delayed compared to areas of the eloquent cortex [Fransson et al., 2011].

The difference between term- and preterm-born adults in the small cluster in the right anterior intra-parietal sulcus of the DAN is in line with such findings. The origin of this difference might be found in the disruption of the developmental process in premature birth. However, this difference has not been reported in infants and does not survive correction for multiple comparison when taking into account the number of examined ICs. Therefore, the observed difference in the right anterior intra-parietal sulcus of the DAN might only be observed due to chance.

Greater network core strength was observed in multiple RSNs in term-born adults compared to their preterm-born peers in the EPICure cohort. This is in line with the work by Damaraju et al. [2010] or Smyser et al. [2016], which found the spatial extent of RSNs to be indistinguishable between preterm- and term-born infants but found connections between RSNs to be significantly stronger in infants born at term. Similarly, [Eyre et al., 2020] found core strength to increase in all examined RSNs with age (infants scanned at 37-43.5 weeks PMA).

RSNs mapping the eloquent cortex and RSNs associated with higher cognitive function were equally affected in the EPICure cohort. This is in alignment with findings by Eyre et al. [2020] but in contrast to results obtained by Smyser et al. [2010], which found RSNs mapping the eloquent cortex to be less impacted by prematurity than RSNs of higher cognitive function.

Others obtained more localised differences in functional connections between nodes of the basal ganglia and frontal cortex [Toulmin et al., 2015, Ball et al., 2016].

Ball et al. [2016] used spatial ICA to derive a functional parcellation followed by DR to derive subject-specific spatial maps. These spatial maps were used to select features in a machine learning pipeline that was trained to distinguish fMRI scans of term- from preterm-born subjects. Functional connectivity between nodes in the basal ganglia and frontal cortex were overrepresented among discriminatory features in this machine learning model.

Another approach was taken by Toulmin et al. [2015] that used a combination of spatial ICA and seed-based analysis to segment the thalamus. Firstly, spatial ICA was used to derive RSNs in each subject. Secondly, time courses of voxels in the thalamus were correlated with the time courses of these obtained RSNs. The RSN with the greatest correlation was then associated with the corresponding voxel in the thalamus. Their analysis revealed that more extreme prematurity was linked with increased functional connectivity between thalamus and lateral primary sensory cortex. Furthermore, they found that functional connectivity between thalamus and cortex in the prefrontal, insular and anterior cingulate regions was on average stronger in the term-born subjects.

In agreement with Toulmin et al. [2015], the thalamus of preterm born adults in the EPICure cohort showed significantly increased functional connectivity to the cuneus. In disagreement with Toulmin et al. [2015], functional connectivity to anterior cingulate gyrus, middle cingulate gyrus, and superior frontal gyrus was also increased (although not significantly).

Additionally, the analysis of the EPICure cohort showed significantly reduced functional connectivity between thalamus and precuneus.

However, most of these differences disappeared when gender, average heart rate, head motion, and TIV were used as covariates in the comparison of functional connectivity.

Chang et al. [2013] showed that slow variations in the heart rate correlate strongly with BOLD signal change in anterior cingulate cortex and amygdala [Chang et al., 2013, 2016]. Therefore, differences in functional connectivity between nodes in the basal anglia and these prefrontal areas might be due to increased resting heart rates as seen in preterm-born adults of the EPICure cohort. In contrast, differences in functional connectivity of basal ganglia nodes to cuneus and precuneus remained after the inclusion of average heart rate as covariate.

Correlations between heart rate and BOLD signal change have been found most pronounced in areas involved in autonomic representation and control such as ACC, PFC, insular cortices and amygdala [Shmueli et al., 2007, Chang et al., 2013, Thayer et al., 2012, Jennings et al., 2016, Sakaki et al., 2016, Schulz, 2016, de la Cruz et al., 2017, 2019].

Higher resting HRV in individuals was associated with enhanced cognitive performance on tasks of working memory, attention, and inhibitory control [Hansen et al., 2009, Elliot et al., 2011, Gillie et al., 2014, Mandrick et al., 2016, Maier and Hare, 2017, Mulcahy et al., 2019]. Therefore, HRV is considered a proxy measure of healthy cardiac function, of central autonomic control of internal bodily state, and of the capacity for adaptive inhibition and emotion regulation [Williams et al., 2015, Mulcahy et al., 2019].

The development of the autonomic nervous system, for example, the myelination of the vagus nerve, occurs during the third trimester and is interrupted at preterm birth. The interruption of the full development of the autonomic nervous system is likely to have an impact on autonomic control [Karvonen et al., 2019] and is also associated with an increased incidence of heart diseases in adulthood [Crump et al., 2019, 2021].

The results on the EPICure cohort showed that many differences in functional connectivity disappeared when removing cofounds such as average heart rate in the comparison. A link between brain function and altered heart function in preterm-born adults is possible but requires future research.

The visual processing system has significant connections between the posterior region of the thalamus and visual cortex. Therefore, reduced thalamic volume is consistent with the difference in core strength of VSN3 in preterm-born adult of the EPICure cohort.

However, the major limitation of this fMRI study is that it is an ill-posed problem to determine the origin of observed differences in functional connectivity and core strength because of the mixture of underlying contributing factors such as structure, physiology and actual neurophysiological brain activity. Future research with complementary neuroimaging techniques, for example using simultaneous EEG-fMRI, will help to better disentangle these factors and help to attribute changes in the haemodynamic response to actual neural activation change [Arichi et al., 2017, Roche-Labarbe et al., 2007, Milh et al., 2007].

Another limitation of this study is that functional connectivity is dependent on how parcellations are defined. Coarse parcellations with nodes of overlapping functional areas result in erroneous functional network topology [Smith et al., 2011], ultimately altering derived group comparison results. The conducted analysis on the EPICure cohort mitigates this limitation by using sICA with automatic dimensionality estimation, a technique to choose number of components supported by the fMRI data. The second analysis was conducted with subject-specific anatomical atlases to mitigate the risk for misalignment and overlapping of functionally distinct areas.

Finally, another limitation for most fMRI analyses is head motion, which has been shown to cause substantial alterations of group analysis results in developmental cohorts [Power et al., 2012]. To account for head motion in the EPICure analysis, rigid realignment motion parameters and derivatives were removed during pre-processing. However, the inclusion of head motion regressors does not result in a complete elimination of head motion artefacts [Satterthwaite et al., 2013]. Despite no significant differences in head motion between term- and preterm-born adults in this cohort (see Figure 5.1), a head motion summary statistic (number of outlier volumes affected by head motion) [Satterthwaite et al., 2013, Maknojia et al., 2019] was included as an additional covariate in the performed group analysis of the

EPICure cohort.

5.5 Conclusion

The obtained results on the EPICure cohort have established common RSNs in the extremely-preterm 19 year old brain and compared these to those present in a group of term-born peers. No striking differences in the types of pattern obtained were observed. Functional within-network connectivity was significantly lower in preterm-born adults in VN3 of the visual RSNs. It is well known that preterm cohorts are more susceptible to visual impairment, and the obtained results may represent a neuroimaging manifestation of this impairment, which is believed to be more than a retinal pathology and extends to the visual processing regions of the cortex. Future work will bridge the gap between network-based neuroimaging and objective functional impairment in this cohort by obtaining measurements in tasks assessing visual processing.

Chapter 6

Single-subject spatial map estimation for clinical fMRI acquisitions

6.1 Introduction

Functional Magnetic Resonance Imaging (fMRI) is a key neuroimaging technique in large cohort studies, allowing the analysis of healthy and pathological networks of spontaneous brain function. Dual regression (DR) is the most prominent technique to obtain single subject spatial map estimates for comparing healthy and pathological subjects. However, as in any regression approach, DR is prone to overfit a data set with only few time points, the more the number of model parameters is increased. To regularise the DR approach, one can apply spatial smoothing kernels to fMRI scans. Unfortunately, this increases the partial volume bias if the compared groups have different compositions in underlying brain tissue. This chapter analyses a cohort of young-onset Alzheimer's disease (YOAD) subjects, which only underwent very short resting-state fMRI scanning. Therefore, a novel approach is proposed that circumvents dual regression with an ensemble average of matrix factorisations (EMF) to obtain detailed spatial map estimates in healthy and pathological YOAD subjects. These single subject spatial maps obtained with the proposed EMF are compared to spatial estimates obtained with MELODIC and DR. Spatial maps obtained with EMF showed greater reproducibility than spatial maps obtained with MELODIC and DR. Furthermore, differences in results of both approaches are examined when comparing spatial map estimates between individuals diagnosed with Alzheimer's disease (AD), posterior cortical atrophy (PCA) and healthy controls. Both approaches revealed known differences in functional connectivity in the Precuneus cortex. In addition, EMF detected significant differences in small clusters matching the anatomical locations of the hippocampus.

6.1.1 Motivation

Alzheimer's disease (AD) is a progressive neurodegenerative disease comprising of a preclinical stage, an intermediate stage of mild cognitive impairment (MCI), and a final stage of dementia. Affected individuals suffer impairment of cognitive function due to the accelerated death of grey matter (see Frisoni et al. [2010] for a review).

AD is associated with the accumulation of abnormal proteins in the brain, which is accompanied by progressive synaptic, neuronal and axonal damage. These changes may begin to occur several years prior to any symptomatic effects.

Current therapeutic intervention focuses on delaying the onset of AD but requires reliable early detection before an accelerated neural deterioration occurs.

Biomarkers are required to facilitate earlier detection of AD. Among potential AD biomarkers are low cerebrospinal fluid (CSF), amyloid-β 42 levels and amyloid tracer retention on positron emission tomography (PET), and temporo-parietal patterns of reduced 18F-fluorodeoxyglucose uptake on PET (see Rathore et al. [2017], Ewers et al. [2011] or Weiner et al. [2013] for a review).

fMRI represents a key imaging technique for many large neuroimaging cohort studies. The potential of fMRI to measure changes in functional cortical networks means that it is well suited to complement the local structural information provided by other MR contrasts.

Several large dementia studies using fMRI [Greicius et al., 2004, Weiner et al., 2013, Lane et al., 2017] have found differences in functional connectivity between AD and healthy-elderly subjects among such cortical networks. One prominent among these is the default mode network (DMN). Functional differences in the spatial cluster of the DMN located in the Precuneus cortex have been consistently found in AD patients [Greicius et al., 2004, Zhou et al., 2010].

However, YOAD represents a particularly challenging form of dementia since it is currently unclear what are the neurological substrates of the highly variable clinical presentation. Therefore, the following explorative analysis of functional connectivity in the examined YOAD cohort hopes to aid current understanding of this disease.

6.1.2 Previous work

Matrix decomposition techniques that extract salient components subject to proxy functions modelling statistical independence are among the most prominent approaches to analyse and extract brain networks from resting-state fMRI data [Daubechies et al., 2009, Varoquaux et al., 2010]. The most commonly used software package (MELODIC[1]) is based on Independent Component Analysis (ICA). MELODIC comprises of two parts to obtain single-subject spatial maps. Firstly, pre-processed and spatially normalised fMRI scans are concatenated

---

[1] `https://fsl.fmrib.ox.ac.uk/fsl/fslwiki/MELODIC`

in time to obtain a set of spatial group maps with ICA. Secondly, two regression models, referred to as Dual Regression (DR), are applied: the first uses spatial group maps from ICA to obtain subject-specific time courses and the second uses these time courses to obtain subject-specific spatial maps.

However, DR likely overfits the fMRI data if scanning time is short and no regularisation is included in these regressions. Therefore, wide Gaussian spatial smoothing kernels are typically applied as a pre-processing step to increase signal to noise ratio (SNR) in fMRI data. However, spatial smoothing has a major disadvantage because of partial-volume effects at both the intra- and inter-subject level. At the intra-subject level, smoothing causes cardiac and respiratory fluctuations in cerebrospinal fluid (CSF) and white matter (WM) tissue to mix with BOLD signal fluctuations in grey matter (GM) tissue. This likely prevents the estimation of the true spatial extent and unique detail in these subject-specific brain networks. At the inter-subject level, the mixture of noise and BOLD signal is exacerbated by the anatomical heterogeneity across atrophied brains in disease cohorts as depicted in Figure 6.1. Observed functional differences across patient groups might therefore only reflect differences in underlying tissue composition in these patient groups.

Figure 6.1: An example of atrophy heterogeneity among AD subjects. (Courtesy of Carole Sudre)

Furthermore, the reproducibility of resting-state networks is often only reported at the group level [Jovicich et al., 2016]. Little is known about the reproducibility and stability of subject-specific resting-state networks derived from fMRI scanning within a clinical setting suffering from short scanning times, artefacts and often poor subject compliance.

Functional pathologies in resting-state networks have the potential to reveal much about early dementia but discovered differences are often dependent on a catalog of assumptions, for example the the kernel size of the spatial smoothing operator, and therefore suffer from poor reproducibility.

This motivated the development of a technique that is robust in the setting of short image acquisition, reduces the amount of model assumptions to be made and allows for a separation of BOLD-related signal from BOLD-unrelated signal in a similar fashion such as ICA.

6.1.3 Proposed solution

This chapter introduces a new matrix factorisation approach applied to a YOAD cohort that comprises of subjects that come with resting-state fMRI scanning of about five minutes. These subjects were scanned twice in a timeframe of approximately one week. In addition to that, some subjects received additional scanning after one year.

An ensemble average of these matrix factorisations (EMF) is obtained for each scan of the cohort in order to extract single-subject spatial maps of brain networks at multiple time points (initial or follow up scan session). This is followed by a group analysis comparing these spatial maps between AD, PCA, and healthy elderly subjects.

Furthermore, these single-subject spatial maps are compared to spatial maps obtained with MELODIC (ICA and DR).

Lastly, the group comparison results of EMF and MELODIC are juxtaposed and put in context with existing findings from literature. The comparison between EMF and MELODIC showed that spatial maps obtained with EMF resulted in more significant differences in the group analysis stage.

6.2 Materials and methods

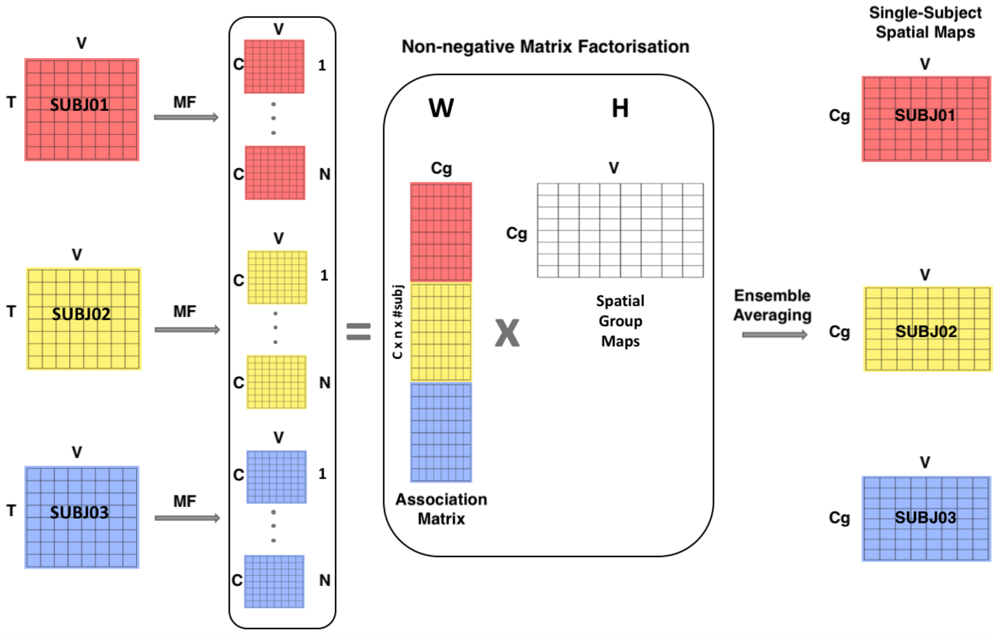

Figure 6.2: The proposed approach comprises of training individual matrix factorisations and their subsequent ensemble averaging with non-negative matrix factorisation.

The pipeline of the proposed approach consists of two parts as outlined in Figure 6.2. In the first part, N matrix factorisations (MF_1 to MF_N) are computed for a single-subject resting-state fMRI scan. Each of these matrix factorisations produces a set of time courses and spatial maps. In the second part, the spatial maps (H_1 to H_N) are fed into a non-negative matrix factorisation (NMF), which produces a set of weights and a set of group-level spatial maps. The set of weights is used to obtain a weighted ensemble average of individual spatial maps (H_1 to H_N), ultimately resulting in spatial maps for each subject that correspond to the group-level spatial maps.

Section 6.2.1 discusses the proposed matrix factorisation followed by Section 6.2.2 that describes ensemble averaging of these matrix factorisations.

6.2.1 Single-subject matrix factorisation

The proposed model is applied to BOLD time courses of length T for S subjects, measured at V voxels: $\{\mathbf{Y_s} \in \mathbb{R}^{T\times V}, s = 1\cdots S\}$. For each subject, N matrix factorisations are computed. Each of these matrix factorisations constitutes a low bias and high variance decomposition of an individual scan, which comprises of a set of time courses and spatial maps. Each matrix factorisation is computed with cost function

$$J = R + \lambda_1 R_{sparse} + \lambda_2 R_{tv}, \tag{6.1}$$

which comprises of the l2 norm R of original and reconstructed fMRI data, spatial sparsity term R_{sparse}, and spatial smoothness total variation term R_{tv}. The l2 cost function is given by

$$R = \frac{1}{2}\|\mathbf{W}\sigma(\mathbf{W}^\top\mathbf{Y}) - \mathbf{Y}\|_2^2, \tag{6.2}$$

with corresponding gradients for $\mathbf{W}$:

$$\begin{aligned}\frac{\partial R}{\partial \mathbf{W}} = &(\mathbf{W}\sigma(\mathbf{W}^\top\mathbf{Y}) - \mathbf{Y})[\sigma(\mathbf{W}^\top\mathbf{Y})]^\top + \\ &\mathbf{Y}((([\sigma(\mathbf{W}^\top\mathbf{Y})]^\top\mathbf{W}^\top - \mathbf{Y}^\top)\mathbf{W}) \odot [\sigma'(\mathbf{W}^\top\mathbf{Y})]^\top\end{aligned} \tag{6.3}$$

The spatial maps are computed with $\mathbf{H} = \sigma(\mathbf{W}^\top\mathbf{Y})$. Hereby, σ is $max(h,0)$ to ensure that spatial maps $\mathbf{H} \in \mathbb{R}_+^{C\times V}$ consist only of positive values.

Proxy functions for spatial sparsity and smoothness of the spatial maps $\mathbf{H}$ are computed with a Kullback-Leibler divergence and total variation term, respectively. The exponential distribution is used to enforce sparsity in each spatial map. The shape of this exponential distribution is determined by hyper-parameter λ_0, which ultimately controls the sparsity of spatial maps. The spatial sparsity term R_{sparse} is therefore given by the Kullback-Leibler divergence of the assumed exponential distribution determined by λ_0 and the estimated exponential distribution in each spatial map:

$$R_{sparse} = \Delta(\lambda_0\|\lambda) = \log(\lambda_0) - \log(\lambda) + \frac{\lambda}{\lambda_0} - 1, \tag{6.4}$$

with $\lambda = \frac{1}{V}\sum_{i=0}^{V} H_{ij}$. The gradient with respect to lambda is given by

$$\frac{\partial}{\partial\lambda} = \mathrm{diag}(1 \oslash \lambda) + \mathrm{diag}(1 \oslash \lambda_0), \tag{6.5}$$

with element-wise division denoted by $\oslash$.

To enforce spatial smoothness among estimated maps, an anisotropic total variation term is computed. Therefore, the spatial maps matrix $\mathbf{H}$ is reshaped into a 4D tensor $\mathbf{H}^{(\mathbf{4D})}$. The total variation regularisation cost for this tensor is given by:

$$\begin{aligned} R_{tv} = \sum_{c,i,j,k} & \left|\mathbf{H}^{(\mathbf{4D})}{}_{c,i+1,j,k} - \mathbf{H}^{(\mathbf{4D})}{}_{c,i,j,k}\right| + \\ & \left|\mathbf{H}^{(\mathbf{4D})}{}_{c,i,j+1,k} - \mathbf{H}^{(\mathbf{4D})}{}_{c,i,j,k}\right| + \\ & \left|\mathbf{H}^{(\mathbf{4D})}{}_{c,i,j,k+1} - \mathbf{H}^{(\mathbf{4D})}{}_{c,i,j,k}\right| \end{aligned} \tag{6.6}$$

The product of $\mathbf{H} = \sigma(\mathbf{W}^\top \mathbf{Y})$ can be rewritten element-wise as

$$\begin{bmatrix} \\ \sigma(\mathbf{W}^\top y_1) & \sigma(\mathbf{W}^\top y_2) & \dots & \sigma(\mathbf{W}^\top y_V) \\ \\ \end{bmatrix} \tag{6.7}$$

with $\sigma(\mathbf{W}^\top y_1)$ being a column vector for voxel v. All column vectors taken together form the spatial maps $\mathbf{H}$ as depicted in Equation 6.7. Furthermore, the original data $\mathbf{Y}$ can be reshaped into individual matrices along either dimension $V1$, $V2$ or $V3$. Equation 6.6 can then be computed by the following term

$$\begin{aligned} R_{tv} = & \sum_{i}^{V2} \sum_{j}^{V3} \|\sigma(\mathbf{W}^\top \mathbf{Y}_{\mathbf{ij}}^{(\mathbf{1})}) \mathbf{D}_{\mathbf{1}}^\top \|_1 + \\ & \sum_{i}^{V1} \sum_{j}^{V3} \|\sigma(\mathbf{W}^\top \mathbf{Y}_{\mathbf{ij}}^{(\mathbf{2})}) \mathbf{D}_{\mathbf{2}}^\top \|_1 + \\ & \sum_{i}^{V1} \sum_{j}^{V2} \|\sigma(\mathbf{W}^\top \mathbf{Y}_{\mathbf{ij}}^{(\mathbf{3})}) \mathbf{D}_{\mathbf{3}}^\top \|_1 \end{aligned} \tag{6.8}$$

with $\mathbf{Y}_{\mathbf{ij}}^{(\mathbf{1})} \in \mathbb{R}^{T \times V1}$, $\mathbf{Y}_{\mathbf{ij}}^{(\mathbf{2})} \in \mathbb{R}^{T \times V2}$, $\mathbf{Y}_{\mathbf{ij}}^{(\mathbf{3})} \in \mathbb{R}^{T \times V3}$, $\mathbf{D_1} \in \mathbb{R}^{(V1-1) \times V1}$, $\mathbf{D_2} \in \mathbb{R}^{(V2-1) \times V2}$ and $\mathbf{D_3} \in \mathbb{R}^{(V3-1) \times V3}$. The respective matrices $\mathbf{D_i}$ have the form

$$\mathbf{D_i} = \begin{pmatrix} -1 & 1 & & & & & \\ & -1 & 1 & & & & \\ & & -1 & 1 & & & \\ & & & \ddots & & & \\ & & & -1 & 1 & & \\ & & & & -1 & 1 & \end{pmatrix} \tag{6.9}$$

The gradient for regularisation term for an-isotropic total variation with respect to $\mathbf{W}$

is given by

$$
\begin{aligned}
\frac{\partial R_{tv}}{\partial \mathbf{W}} = \\
\sum_{i}^{V2}\sum_{j}^{V3}\mathbf{Y}_{\mathbf{ij}}^{(\mathbf{1})}((\mathbf{D_1}\operatorname{sign}\left(\mathbf{D_1}^{\top}\sigma(\mathbf{W}^{\top}\mathbf{Y}_{\mathbf{ij}}^{(\mathbf{1})})^{\top}\right)\odot \dots \\
\sigma'(\mathbf{W}^{\top}\mathbf{Y}_{\mathbf{ij}}^{(\mathbf{1})})^{\top}))+ \\
\sum_{i}^{V1}\sum_{j}^{V3}\mathbf{Y}_{\mathbf{ij}}^{(\mathbf{2})}((\mathbf{D_2}\operatorname{sign}\left(\mathbf{D_2}^{\top}\sigma(\mathbf{W}^{\top}\mathbf{Y}_{\mathbf{ij}}^{(\mathbf{2})})^{\top}\right)\odot \dots \\
\sigma'(\mathbf{W}^{\top}\mathbf{Y}_{\mathbf{ij}}^{(\mathbf{2})})^{\top}))+ \\
\sum_{i}^{V1}\sum_{j}^{V2}\mathbf{Y}_{\mathbf{ij}}^{(\mathbf{3})}((\mathbf{D_3}\operatorname{sign}\left(\mathbf{D_3}^{\top}\sigma(\mathbf{W}^{\top}\mathbf{Y}_{\mathbf{ij}}^{(\mathbf{3})})^{\top}\right)\odot \dots \\
\sigma'(\mathbf{W}^{\top}\mathbf{Y}_{\mathbf{ij}}^{(\mathbf{3})})^{\top}))
\end{aligned}
\tag{6.10}
$$

The gradient of cost function J is optimised with the limited memory Broyden-–Fletcher-–Goldfarb-–Shanno (L-BFGS) optimisation scheme.

6.2.2 Ensemble averaging of matrix factorisations

Firstly, spatial maps of N matrix factorisations of each subject are concatenated $\mathbf{H}_{ALL} = \{\mathbf{H}_{ns} \in \mathbb{R}^{C\times V}, s = 1\cdots S, n = 1\cdots N\}$ to compute group-level spatial maps. These are obtained with a fast coordinate descent non-negative matrix factorisation (CD-NMF) algorithm [Hsieh and Dhillon, 2011] that optimises loss function

$$\frac{1}{2}\|\mathbf{A}\mathbf{H}_{group} - \mathbf{H}_{ALL}\|_2^2. \tag{6.11}$$

The CD-NMF is initialised with a non-negative double singular value initialisation (NNDSVD) [Boutsidis and Gallopoulos, 2008] for $\mathbf{A} \in \mathbb{R}^{(C*N*S)\times C_{group}}$ and $\mathbf{H}_{group} \in \mathbb{R}^{C_{group}\times V}$ to speed up convergence and to guarantee deterministic behaviour. No regularisation term is applied in CD-NMF.

Secondly, these weights of CD-NMF are used to compute weighted ensemble averages of matrix factorisations to ultimately obtain spatial maps in each subject that correspond to the group-level spatial maps. An overview of the individual steps involved in the ensemble averaging of matrix factorisations is given in Figure 6.2.

6.2.3 Data acquisition

The YOAD cohort comprises of participants recruited prospectively from 2013 to 2015 from a specialist cognitive disorders clinic [Slattery et al., 2017, Parker et al., 2018]. None of the participants had a known mutation or family history suggestive of autosomal dominant inheritance. All participants gave written informed consent after formal approval by the National Hospital for Neurology and Neurosurgery Research Ethics Committee. The final sample included 69 participants, of which 45 met criteria for YOAD. Twenty-four participants had no history of cognitive concerns and were classified as healthy controls. Controls were matched for age and gender and are predominantly spouses of YOAD patients. From the 45 YOAD patients, 14 participants fulfilled criteria of posterior cortical atrophy (PCA), 28 of AD, 2 of logopenic progressive aphasia (LPA) and 1 of frontotemporal dementia (FD) according to published criteria [Slattery et al., 2017, Parker et al., 2018]. The LPA and FD subjects were excluded from analysis due to the low number of participants per group. The study comprised of comprehensive MRI scanning at baseline and one-year follow-up. A subgroup of participants underwent fMRI scanning one week after baseline and/or follow-up, resulting in a maximum of four resting-state fMRI sequences per participant. Anatomical T1 (standard MPRAGE) images and resting-state fMRI scans (TR = 2200ms, voxel size $3.31 \times 3.31 \times 3.3$mm, 36 oblique transverse slices, slice order interleaving, 140 volumes) were acquired on a Siemens 3T scanner. Anatomical T1 and resting-state fMRI data from 58 subjects (14 PCAs, 26 ADs and 18 HCs) were included in the baseline comparison and 41 of these 58 (8 PCAs, 17 ADs and 16 HCs) were used for follow-up comparisons.

6.2.4 Data preparation

Pre-processing was performed using FMRIPREP version 1.4 ([Esteban et al., 2019], RRID:SCR_016216), a Nipype ([Gorgolewski et al., 2011], RRID:SCR_002502) based tool.

6.2.4.1 Pre-processing of anatomical data

Each T1w (T1-weighted) volume is corrected for intensity non-uniformity (INU) using N4BiasFieldCorrection (v2.1.0) [Tustison et al., 2010] and skull-stripped using antsBrainExtraction.sh (v2.1.0) using the OASIS template. Spatial normalisation to the ICBM 152 Nonlinear Asymmetrical template version 2009c (RRID:SCR_008796) [Fonov et al., 2009] was performed through nonlinear registration with the antsRegistration tool of ANTs (v2.1.0, RRID:SCR_004757) [Avants et al., 2008], using brain-extracted versions of both T1w volume and template. Brain tissue segmentation of cerebrospinal fluid (CSF), white-matter (WM) and grey-matter (GM) was performed on the brain-extracted T1w using fast (FSL v5.0.9, RRID:SCR_002823).

6.2.4.2 Pre-processing of resting-state fMRI data

Functional data was slice time corrected using 3dTshift from AFNI v16.2.07 ([Cox, 1996], RRID:SCR_005927) and motion corrected using mcflirt (FSL v5.0.9) [Jenkinson et al., 2002]. This was followed by co-registration to the corresponding T1w using boundary-based registration [Greve and Fischl, 2009] with twelve degrees of freedom, using flirt (FSL). Motion correcting transformations, BOLD-to-T1w transformation and T1w-to-template (MNI) warp were concatenated and applied in a single step using antsApplyTransforms (ANTs v2.1.0) using Lanczos interpolation. Frame-wise displacement [Power et al., 2014] was calculated for each functional run using the implementation of Nipype. Spatial smoothing was not applied. The pre-processed fMRI time courses were bandpass-filtered $(0.01-0.1\text{Hz})$[Cox, 1996]. Time courses were normalised to zero mean and unit standard deviation.

6.3 Experiments and results

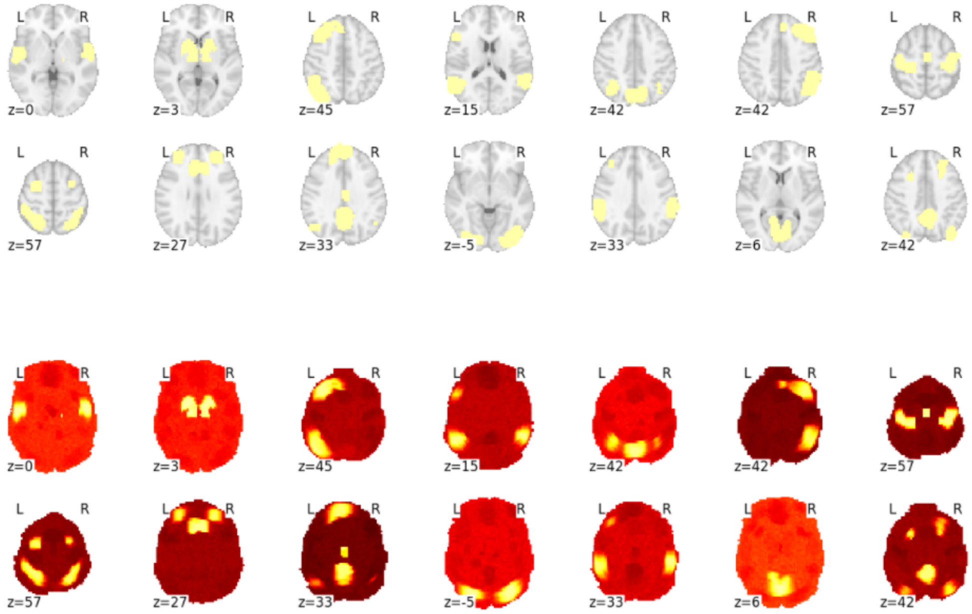

Figure 6.3: The spatial maps of the 16 simulated resting-state networks from study [Shirer et al., 2012] (top row). The corresponding estimated spatial maps from components obtained with EMF (bottom row).

EMF was applied to simulated fMRI data characterised by the same voxel resolution and TR of the real resting-state fMRI data of the YOAD cohort. Simulated data was computed from spatial networks [Shirer et al., 2012] and randomly generated BOLD time-courses [Smith et al., 2011].

Each subject is simulated by $Y = WH^T + E$ where $Y \in \mathbb{R}^{T \times V}$ is fMRI time courses of length T, measured at V voxels, $W \in \mathbb{R}^{T \times C}$ and $H \in \mathbb{R}^{C \times V}$ are C time courses and spatial maps of simulated resting-state networks, and E is added Gaussian noise.

The original 3D spatial maps used in the simulated data and their corresponding EMF estimates are depicted in Figure 6.3. The hyper-parameters λ_0, λ_1, and λ_2 were tuned to recover the spatial maps and BOLD time courses in the simulated data. These optimal hyper-parameters were used to obtain single-subject spatial maps with EMF in the YOAD cohort.

In addition to EMF, spatial group ICA and DR (ICA+DR) were applied to the resting-state data of the YOAD cohort. More specifically, spatial group maps were obtained by running ICA on all concatenated resting-state scans of both disease patients and healthy controls fMRI data combined. Subsequently, the group spatial maps were used to obtain subject-specific spatial maps of these corresponding group maps, and associated time courses, using two individual regressions.

Firstly, for each subject, the spatial group maps were regressed (as spatial regressors in a multiple regression) into the subject's 4D space-time dataset. This resulted in a set of subject-specific time courses, one per group-level spatial map. Next, those time courses were regressed (as temporal regressors, again in a multiple regression) into the same 4D dataset, resulting in a set of subject-specific spatial maps, one per group-level spatial map [Beckmann et al., 2009, Nickerson et al., 2017].

For both approaches, a set of seven networks within obtained components were visually and methodologically identified (i.e. the top seven best-fits using the template matching procedure described by Greicius et al. on the group EMF and ICA+DR results, using the networks reported in Shirer et al. as a template; [Greicius et al., 2004, Shirer et al., 2012]) as dorsal default mode network (dDMN), ventral default mode network (vDMN), Precuneus network (PREC), salient network (SN), left and right central executive network (LCEN and RCEN), and sensory motor network (SMN).

In the following, short and long-term spatial reproducibility of spatial maps of these networks are compared between EMF and ICA+DR. Subsequently, spatial map estimates of each approach are compared between disease subjects and healthy normals.

6.3.1 Spatial map estimation with EMF and ICA+DR

To determine the spatial reproducibility of single-subject maps, EMF and ICA+DR were applied to the resting-state fMRI data of the YOAD cohort. Hereby, spatial maps obtained with EMF showed greater reproducibility than their equivalents obtained with ICA+DR.

The reproducibility of spatial maps was compared for scans one week and one year apart. To account for the bias of the number of estimated components, the analysis was performed for 20, 30 and 40 estimated components with both approaches, EMF and ICA+DR.

Furthermore, single-subject spatial maps produced by EMF were compared to spatial maps produced by ICA+DR with no, 4mm or 8mm spatial smoothing applied at the end of the pre-processing pipeline of the fMRI scans.

Table 6.1 summarises reproducibility and correlation to group component for the corresponding spatial maps of resting-state networks found among either 20, 30 or 40 estimated components dependent on the kernel size of spatial smoothing applied at the end of the fMRI pre-processing pipeline.

The column "Reproducibility" shows mean and standard deviation of the intra-subject spatial reproducibility computed for resting-state networks.

Accordingly, column "Correlation to Group Component" shows mean and standard devia-

Technique	Estimated Components	Correlation to Group Component	Reproducibility
EMF	20	0.37 ± 0.07	$\mathbf{0.45 \pm 0.10}$
	30	0.37 ± 0.07	0.37 ± 0.13
	40	$\mathbf{0.38 \pm 0.07}$	0.39 ± 0.12
DR	20	$\mathbf{0.27 \pm 0.06}$	$\mathbf{0.14 \pm 0.07}$
	30	0.22 ± 0.05	0.10 ± 0.05
	40	0.17 ± 0.04	0.05 ± 0.03
DR 4.0mm	20	$\mathbf{0.41 \pm 0.20}$	$\mathbf{0.27 \pm 0.10}$
	30	0.35 ± 0.07	0.20 ± 0.09
	40	0.28 ± 0.06	0.13 ± 0.06
DR 8.0mm	20	$\mathbf{0.49 \pm 0.07}$	$\mathbf{0.42 \pm 0.11}$
	30	0.48 ± 0.07	0.31 ± 0.10
	40	0.40 ± 0.07	0.26 ± 0.10

Table 6.1: The mean and standard deviation of the intra-subject spatial reproducibility and correlation of single-subject spatial maps to their corresponding spatial group map dependent on the number of estimated components and applied spatial smoothing kernels for EMF and ICA+DR.

tion of the correlation of each single-subject map to its corresponding spatial group map. The intra-subject spatial reproducibility and correlation to group component decreased with an increase in the number of estimated components for ICA+DR.

In contrast, both of these correlations remained at a stable level when increasing the number of estimated components in the EMF approach. More intriguingly, the intra-subject spatial reproducibility for EMF was higher than the average of correlation between single-subject map and corresponding spatial group map. In contrast, the opposite effect was seen in estimates obtained with DR.

The intra-subject spatial reproducibility was found to be higher in single-subject spatial maps obtained with EMF than in their equivalents obtained with DR.

The results on spatially smooth data showed that smoothing of fMRI scans before feeding them into ICA+DR resulted in artificially improved spatial reproducibility of single-subject maps because of the removal of subject-specific details.

Larger smoothing kernels resulted in smoother single-subject and group maps. This is evident when comparing DR estimates for the two smoothing kernels, 4mm and 8mm. The larger the spatial smoothing kernel the greater intra-subject reproducibility and correlation to group spatial map. The increase in both of these measures showed increases in correlation are artificial. This is due to the effect that smoothing with larger kernels produces more blurry spatial map estimates that have a higher intra-subject correlation mainly because of the effect that single-subject maps are less detailed.

Nevertheless, the best spatial reproducibility in DR estimates was achieved for 20 estimated components and scans pre-processed with 8mm smoothing kernels. This was still lower than the best spatial reproducibility achieved with EMF for 20 estimated components and no spatial smoothing.

Therefore, the following analysis focused on resting-state networks obtained among 20 estimated components because both approaches, EMF and ICA+DR, showed the best intra-subject spatial reproducibility with this number of estimated components. The corresponding spatial group maps of dDMN, vDMN and PREC obtained with EMF and ICA+DR are depicted in Figure 6.4. Table 6.2 summarises mean and standard deviation of reproducibility across spatial maps in the seven networks (dDMN, vDMN, PREC, LCEN, RCEN, SMN, SN) for each patient group (Controls, AD and PCA) for scans one week (short-term reproducibility) or one year apart (long-term reproducibility).

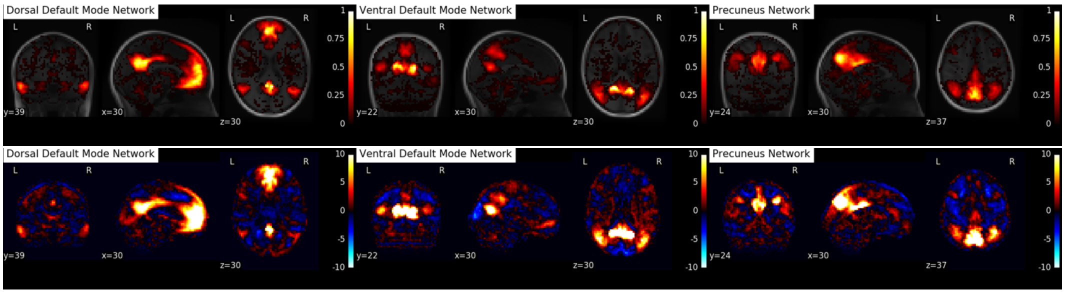

Figure 6.4: The precuneus, ventral and dorsal default mode network obtained by EMF (top) and ICA (bottom) among a decomposition into 20 components.

Method	**Group**	Long	Short
DR	**AD**	0.12 ± 0.06	0.14 ± 0.07
	Control	0.15 ± 0.08	0.18 ± 0.09
	PCA	0.12 ± 0.06	0.14 ± 0.07
EMF	**AD**	0.45 ± 0.08	0.45 ± 0.11
	Control	0.48 ± 0.09	0.53 ± 0.1
	PCA	0.36 ± 0.09	0.41 ± 0.1

Table 6.2: The mean and standard deviation of the short and long term reproducibility of spatial maps of seven networks (dDMN, vDMN, PREC, SN, LCEN, RCEN, SMN) produced by EMF and DR without spatial smoothing.

The group-specific analysis confirmed the general finding that spatial reproducibility is greater in spatial maps obtained with EMF than with ICA+DR. As expected, short-term reproducibility is greater than long-term reproducibility for both analysis approaches but the decrease from short to long term reproducibility is greater in EMF than ICA+DR. Figure 6.5 depicts single-subject spatial maps of the dDMN, vDMN and PREC in first and second scan (approximately one week follow-up) in three subjects obtained with EMF.

These single-subject maps correspond to spatial group maps of dDMN, vDMN, and PREC shown in Figure 6.4. There are unique spatial features in subjects as highlighted by pink, cyan and green dotted circles. These spatial features were not found in corresponding spatial

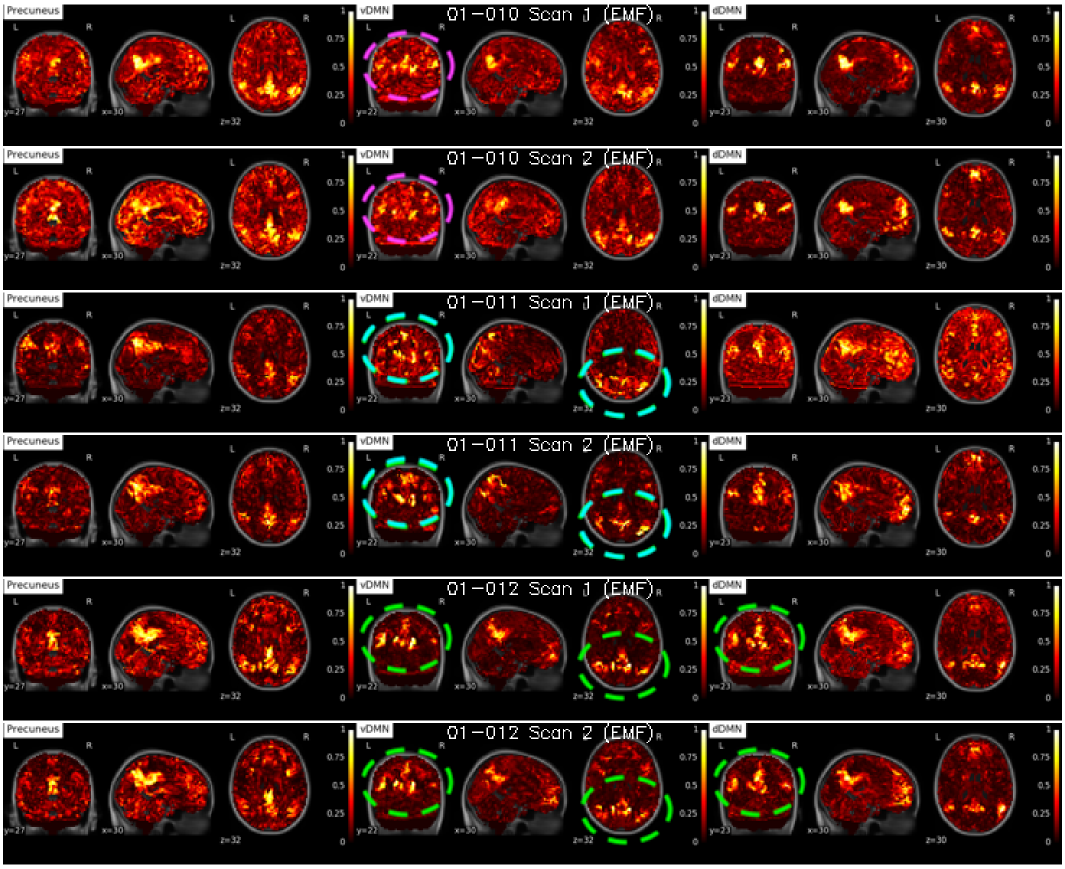

Figure 6.5: Examples of single-subject default mode networks (dDMN, vDMN, PREC) in three subjects. The depicted spatial map estimates are from their first and their second one week follow-up scan obtained with EMF. Unique spatial features in subjects are highlighted by pink, cyan and green dotted circles.

maps obtained with DR. Figure 6.6 depicts the spatial group map of the dDMN obtained with EMF (first row) and ICA (fourth row) among 20, 30, and 40 estimated components (left to right). The corresponding single-subject map of the first scan and a subsequent scan one week later of subject 1 is depicted for estimates obtained with EMF (second and third row) and DR (fifth and sixth row). The spatial group maps of the dDMN estimated with EMF and ICA are relatively similar. However, the spatial map of the dDMN for subject 1 obtained by EMF shows little variation across decompositions with varying number of estimated components whereas substantial variation is seen in the spatial maps obtained by DR. Similar observations are seen in other subjects as depicted in spatial maps obtained for subjects 01-004 to 01-007 with EMF in Figure 6.7 and with DR in Figure 6.8.

6.3.2 Group comparison of EMF and ICA+DR estimates

The single-subject spatial maps of dDMN, vDMN, PREC and SMN among a decomposition into 20 components were compared between different groups and time points. This group analysis was repeated using the spatial maps obtained by ICA+DR.

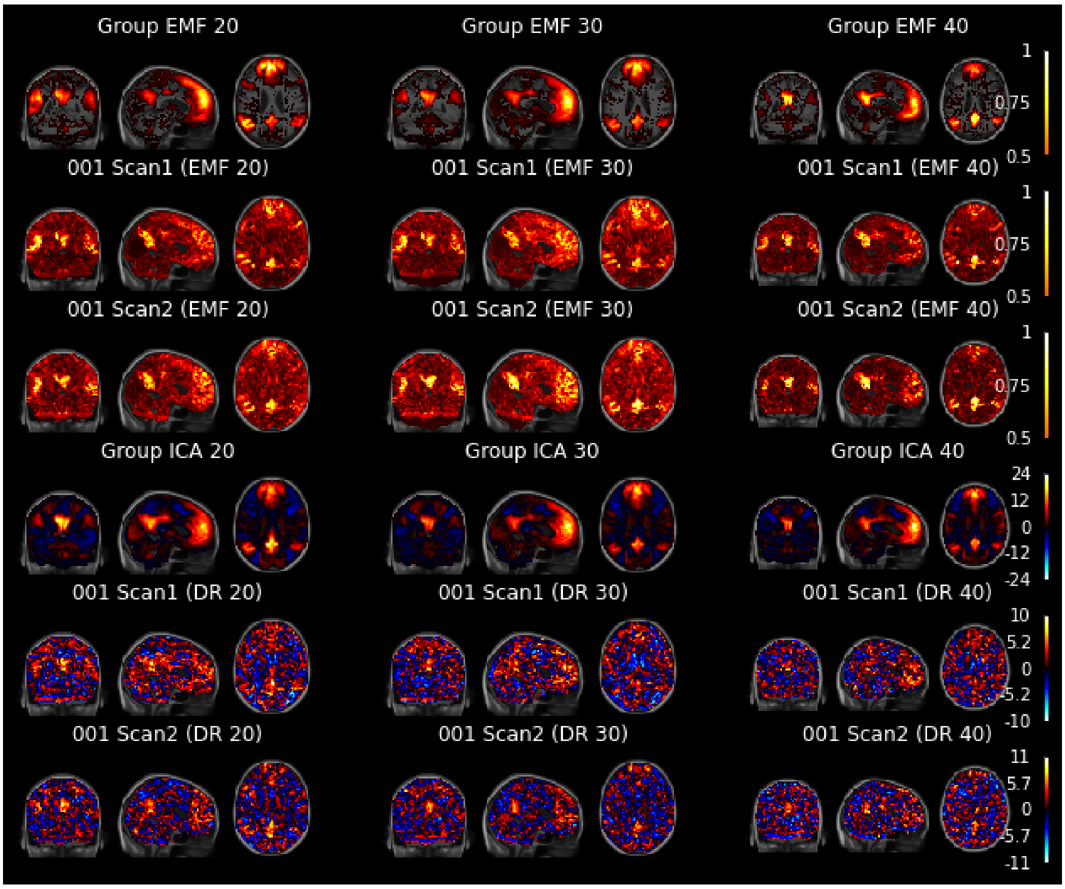

Figure 6.6: The spatial group map of the dDMN in decompositions of 20, 30, and 40 components (from left to right) obtained with EMF (row 1) and ICA (row 4). The corresponding spatial maps of the first and a subsequent one week follow-up scan in subject 1 are depicted for EMF in row 3 and 4, and for DR in row 5 and 6.

The group analysis for both approaches entailed a voxel-wise between group statistical testing on the subject-specific spatial maps using FSL's randomise permutation-testing tool [Winkler et al., 2014]. To control for differences in grey matter volume, the individual grey matter partial volume maps at baseline and follow-up were included as a voxel-wise regressor in the between-group comparison as described in [Oakes et al., 2007]. The selection for the networks to be included in the comparison was driven by prior findings by Damoiseaux et al. [2012] showing the involvement of the default mode network in AD. Therefore, the default mode networks (dDMN, vDMN, PREC) were included in the group comparison because differences among single-subject spatial maps were expected in these networks when comparing healthy elderly to AD subjects. However, similar as proposed by Damoiseaux et al. [2012], the SMN was included in the comparison as a control network in which no differences were anticipated.

The spatial maps of the seven networks for each subject scan from EMF and ICA+DR were used in six sub-analyses (baseline control vs. baseline AD; baseline control vs. baseline

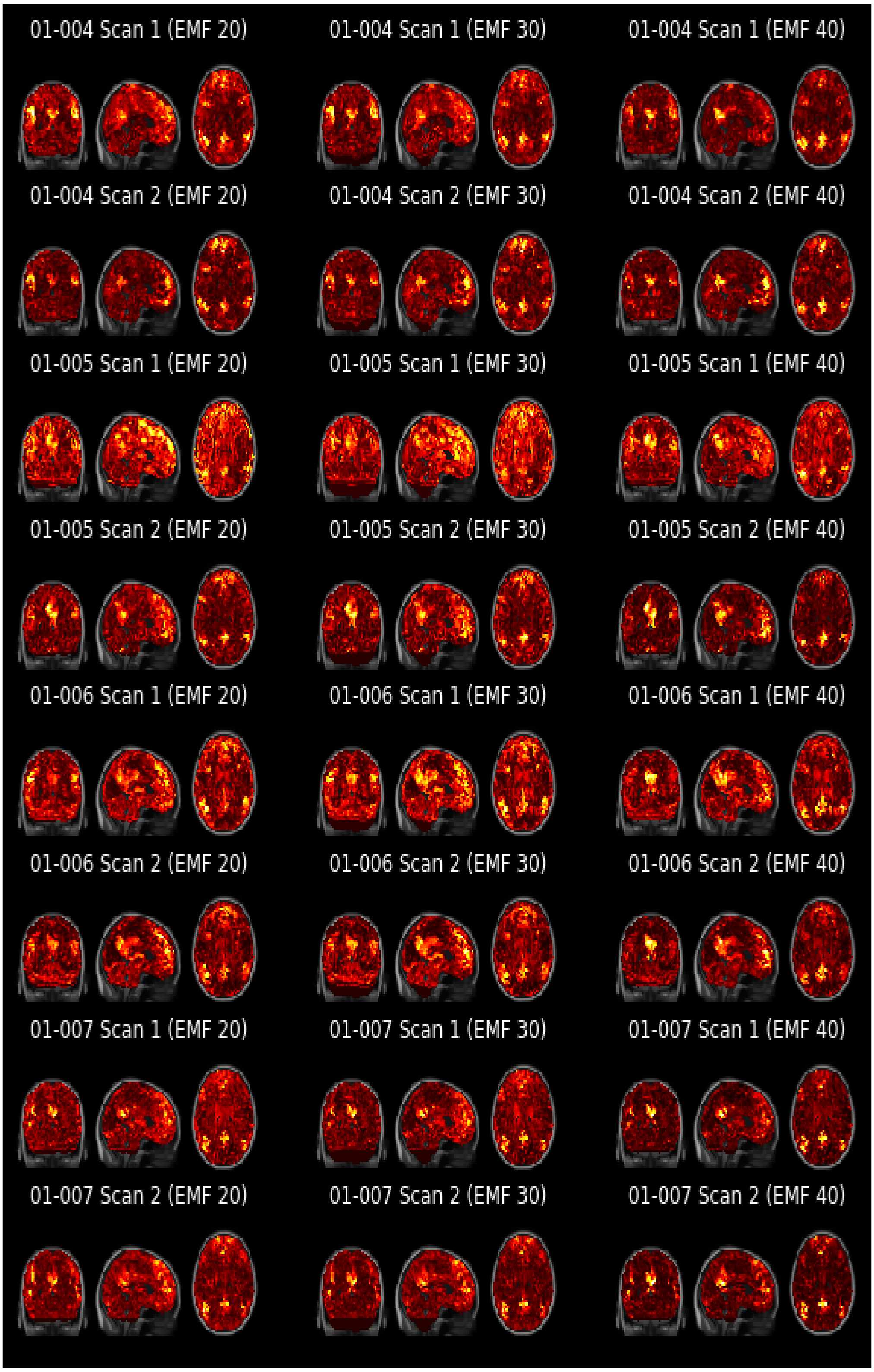

Figure 6.7: The spatial maps of dorsal DMN, ventral DMN and Precuneus network in decompositions of 20, 30, and 40 components obtained with EMF (Subject 4, 5, 6, 7, 8 from top to bottom).

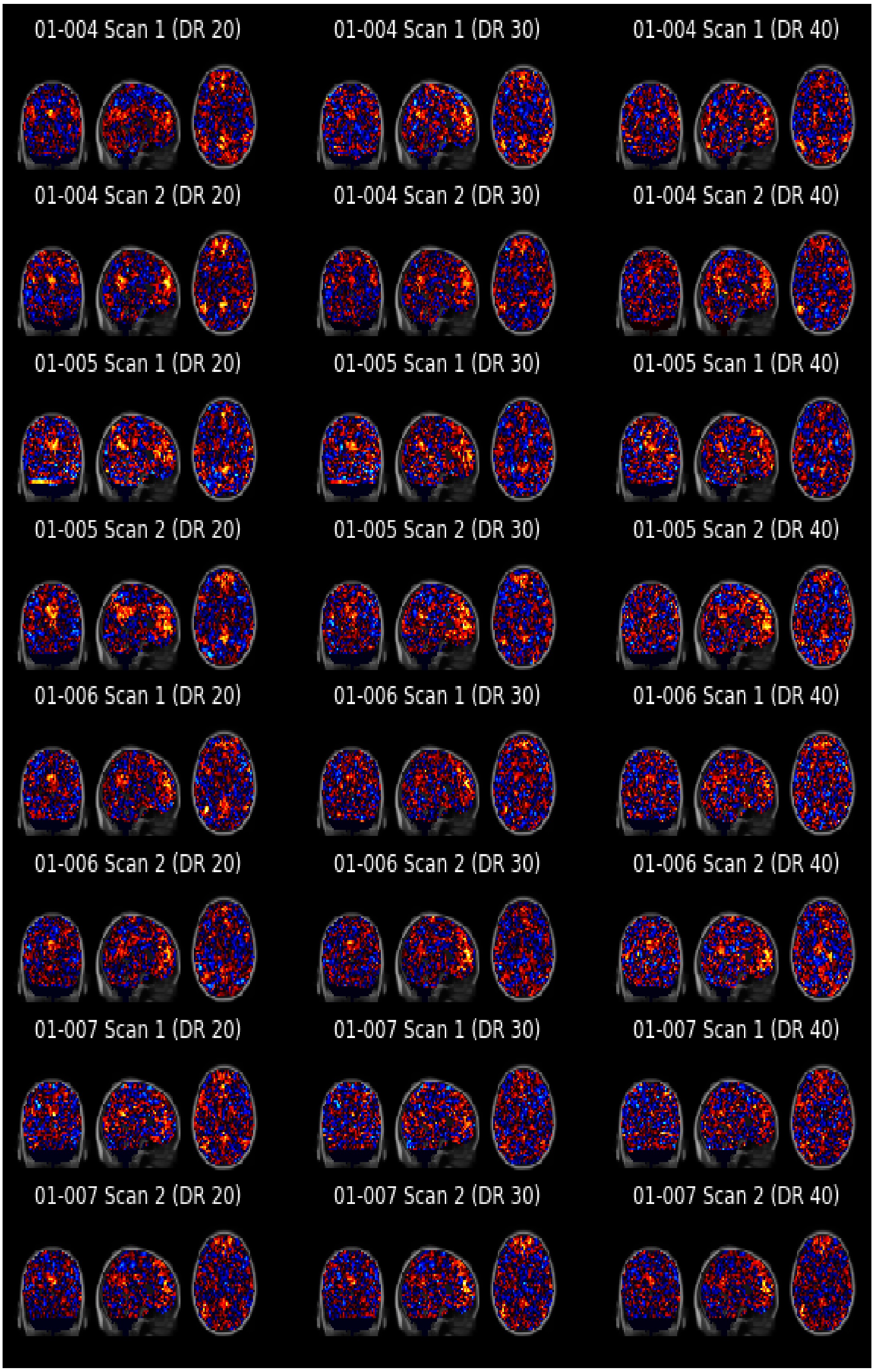

Figure 6.8: The spatial maps of dorsal DMN, ventral DMN and Precuneus network in decompositions of 20, 30, and 40 components obtained with spatial ICA (Subject 4, 5, 6, 7, 8 from top to bottom).

Technique	**Contrast**	**Network**	**Voxels**	**Region**	**Peak MNI coordinates (mm)**
EMF	Healthy > AD	Precuneus	138	Precuneus Cortex	-8,-68,25
			96	Cingulate Gyrus	4,-44,22
			13	Angular Gyrus	-35,-53,37
		dorsal DMN	345	Precuneus Cortex	-2,-62,10
			72	Lateral Occipital Cortex	-47,-62,19
			69	Middle Temporal Gyrus	46,-53,13
		ventral DMN	400	Cingulate Gyrus	1,-41,34
			397	Frontal Medial Cortex	4,49,-11
			384	Frontal Pole	-20,37,31
			278	Middle Frontal Gyrus	25,28,34
			77	Lateral Occipital Cortex	-41,-74,28
			54	Lateral Occipital Cortex	43,-71,34
	Healthy > PCA	Precuneus	104	Precuneus Cortex	-5,-74,31
		dorsal DMN	134	Paracingulate Gyrus	-8,55,1
			79	Precuneus Cortex	-2,-62,16
			12	Angular Gyrus	46,-56,19
		ventral DMN	351	Middle Frontal Gyrus	-29,10,46
			164	Precuneus Cortex	1,-44,40
			95	Lateral Occipital Cortex	-35,-83,22
			77	Middle Frontal Gyrus	25,28,37
			15	Superior Frontal Gyrus	22,1,52
			13	Lateral Occipital Cortex	37,-74,34
	AD > PCA	dorsal DMN	10	Left Putamen	-23,13,-2
ICA+DR	Healthy > AD	Precuneus	99	Precuneus Cortex	-11,-65,28
			21	Cingulate Gyrus	-5,-41,22
		dorsal DMN	208	Precuneus Cortex	1,-50,37
			85	Precuneus Cortex	-14,-62,10
			30	Lateral Occipital Cortex	-41,-71,22
			28	Precuneus Cortex	19,-62,19
	Healthy > PCA	dorsal DMN	11	Precuneus Cortex	1,-47,49
			10	Precuneus Cortex	10,-47,43
		ventral DMN	16	Paracingulate Gyrus	10,55,1

Table 6.3: Obtained spatial differences by the EMF and ICA+DR group comparison for dDMN, vDMN and PREC. Only coordinates of cluster with number of voxels greater or equal than 10 are listed in this table.

PCA; baseline AD vs. baseline PCA; baseline control vs. follow-up control; baseline AD vs. follow-up AD; and baseline PCA vs. follow-up PCA). To find significant differences between controls, AD, and PCA patients at baseline, a t-test was performed using threshold-free cluster enhancement (TFCE) with $p \leq 0.05$ family-wise error correction. For the longitudinal analysis, a repeated measures analysis was performed testing for the difference between baseline and follow-up in each group using TFCE with $p \leq 0.05$. The following describes the differences obtained at baseline between controls and AD, controls and PCA, as well as AD and PCA. Table 6.3 provides all obtained clusters showing a significant difference between healthy controls, AD, and PCA subjects for the group analysis conducted with either EMF or ICA+DR estimates. Table 6.3 shows clusters with sizes of greater or equal than 10 voxels. The comparison between controls and AD subjects resulted in positive differences

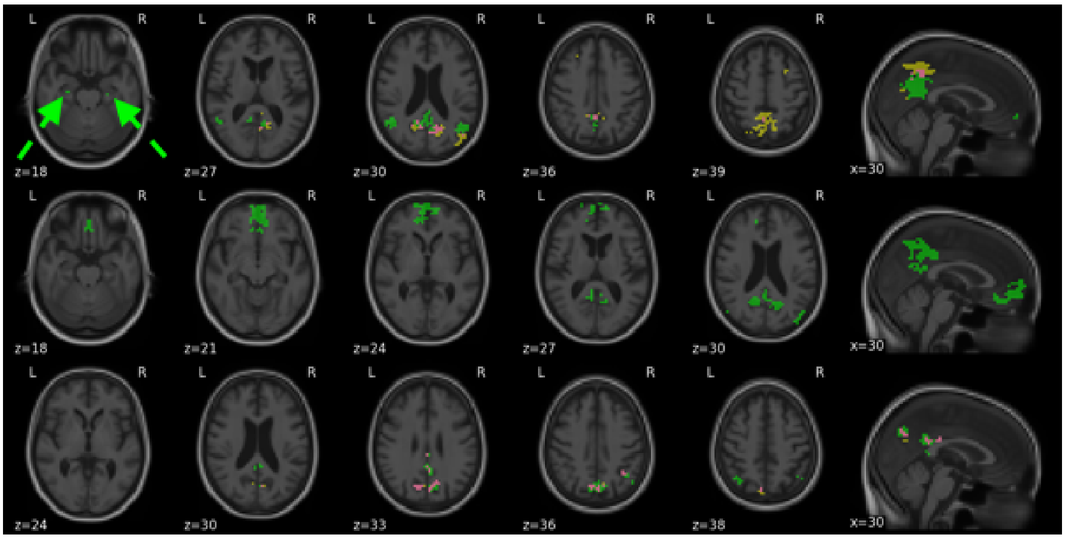

Figure 6.9: Spatial differences between AD patients and healthy elderly controls in the dDMN (top row); vDMN (middle row); and PREC (bottom row). Functional connectivity in the dDMN, vDMN and PREC is decreased in AD patients compared with controls (displayed in green for results with EMF; in yellow for results with DR; and in pink for the overlap). The green arrows highlight the subtle but significant difference in the left and right hippocampus. The statistical maps, thresholded using TFCE and $p \leq 0.05$ family-wise error correction, are overlaid on the computed anatomical average of all T1-weighted subject scans in MNI space.

(controls > AD) in the three default mode networks (dDMN, vDMN, PREC) as depicted in Figure 6.9. Areas in which functional connectivity is greater in controls than in AD patients is displayed in green for results obtained with EMF, in yellow for results obtained with ICA+DR, and in pink for the overlap of the two. The most dominant region for greater functional connectivity in controls than in AD was the Precuneus cortex found in all three of these default mode networks. The Precuneus cortex also had the largest overlap of significant areas (controls > AD) found by both analysis approaches. The least overlap was found in the vDMN, in which no results of ICA+DR were significant after multiple-comparison correction. In addition to the large differences in the Precuneus cortex, small differences were found in the left and right hippocampus in the dDMN highlighted by the dashed green arrows in Figure 6.9. The comparison between control and PCA subjects resulted in positive differences (controls > PCA) in the considered default mode networks (dDMN, vDMN, PREC) as depicted in Figure 6.10. Areas in which functional connectivity was greater in controls than in PCA patients is displayed in green for results obtained with EMF, yellow for results obtained with DR, and pink for the overlap of the two. Similarly to the comparison of healthy controls and AD patients, the most dominant region for these differences was the Precuneus cortex, which showed less functional connectivity in PCA subjects compared to controls in all three of these default mode networks. Similarly as for controls and AD group,

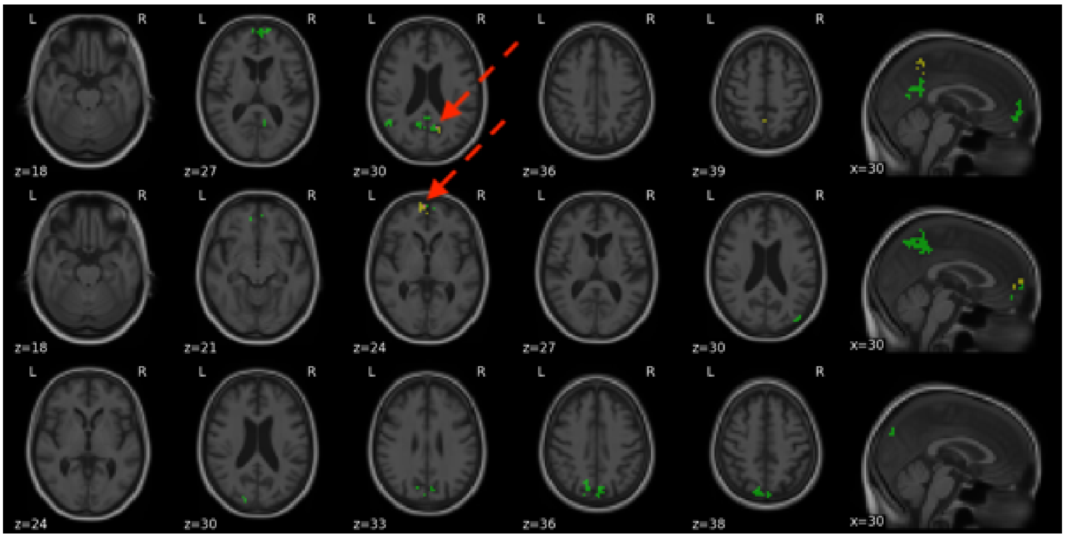

Figure 6.10: Spatial differences between PCA patients and healthy elderly controls in the dDMN (top row); vDMN (middle row); and PREC (bottom row). Similarly to the difference found for AD patients, functional connectivity in the dDMN, vDMN and PREC was decreased in PCA patients compared with controls (displayed in green for results with EMF; in yellow for results with DR; and in pink for the overlap). The red arrows highlight the small areas of overlap that matched for both approaches. The depicted statistical maps, thresholded using TFCE and $p \leq 0.05$ family-wise error correction, are overlaid on the computed anatomical average of all T1-weighted subject scans in MNI space.

the largest overlap of significant areas (controls > PCA) was found in the PREC as well. The least overlap was found in the vDMN, in which no results of DR were significant after multiple-comparison correction.

No significant differences were observed in the opposite contrasts in these default mode networks in either comparing AD or PCA patients to healthy controls. Furthermore, no significant differences were observed comparing AD to PCA patients. No significant differences were observed in the SMN. No significant differences were found in the longitudinal group comparison of baseline and follow-up in control, AD and PCA group.

6.4 Discussion

An ensemble averaging of matrix factorisations was proposed to obtain robust single-subject spatial maps in a cohort of AD, PCA, and healthy elderly subjects. This was followed by comparing these single-subject spatial maps between groups. Ultimately, the analysis of the YOAD cohort with by EMF is compared to equivalent analysis estimates obtained with ICA+DR.

The spatial reproducibility of seven networks was compared between both approaches. Higher intra-subject spatial reproducibility was observed in single-subject maps obtained by EMF than by ICA+DR. The same observation holds when increasing the number of estimated components or even when applying 4mm and 8mm smoothing kernels in the pre-processing of the fMRI scans of the ICA+DR analysis pipeline.

The single-subject spatial map of the seven analysed resting-state networks from EMF were used in an analysis comparing AD, PCA and healthy elderly group. This comparison was repeated with the corresponding spatial maps obtained with ICA+DR.

EMF and ICA+DR identified the Precuneus cortex with significantly greater functional connectivity in default mode networks in subjects of the healthy elderly control group than in subjects of AD or PCA group. However, the group comparison of spatial maps obtained by EMF resulted in more significant differences than the group comparison of spatial maps obtained by DR, and revealed small significant clusters of greater functional connectivity in the hippocampus cluster of the dDMN.

Matrix decomposition approaches are key to extracting brain networks Beckmann et al. [2009], Abraham et al. [2013] from resting-state fMRI data. The disadvantage of these techniques is their reliance on certain statistical assumptions to hold for underlying obtained sources. For example, ICA is effective at removing scanner- or physiological motion-related noise sources by maximising a proxy measure for statistical independence. The chosen proxy measure has a strong influence on the distribution of voxel intensities of these obtained spatial maps.

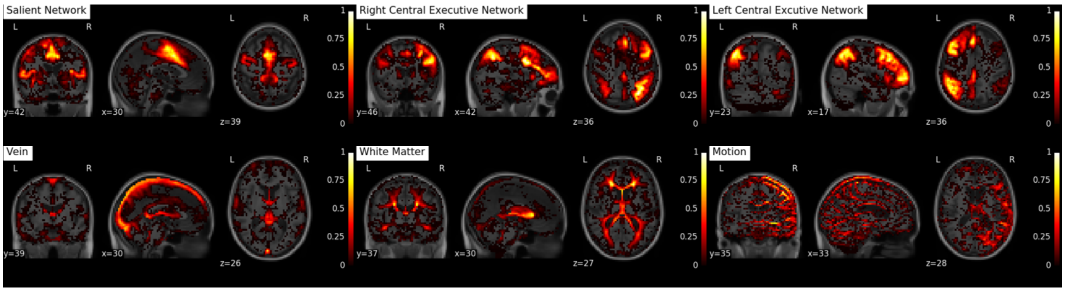

Figure 6.11: Six of the 20 group-level components. The top row depicts the Salient Network (SN), left and right Central Executive Network (LCEN and RCEN). The bottom row depicts typical BOLD-fMRI noise components including a vein, white matter and motion component. Noise components exhibit a different spatial smoothness than brain network components.

A sparsity regularisation term was chosen for EMF because of the profound observation by Daubechies et al. [2009], which showed that prominent ICA implementations, FastICA and InfoMax, tend to produce sparse rather than independent sources in various scenarios of simulated fMRI data. This finding motivated the field to derive novel ICA implementations for fMRI that optimise for both, independence and sparsity [Boukouvalas et al., 2018]. However, while ICA is still the most prominent tool for de-noising of fMRI scans, the majority of the field has moved to matrix factorisations approaches relying entirely on sparse component extraction. These approaches have shown to outperform ICA implementations in fMRI classification tasks [Dadi et al., 2020, Mensch et al., 2021, Gramfort et al., 2013, Dadi et al., 2019, Michel et al., 2011] or in finding spatial clusters of similar time course behaviour [Varoquaux et al., 2010, Abraham et al., 2013].

Current fMRI analysis approaches such as ICA+DR produce reliable functional mappings when scanning times are greater than 10 minutes [Murphy et al., 2007]. However, the fMRI scans of the YOAD cohort (approximately 5 minutes) were acquired in a very common clinical research scenario where scanning time is expensive and fMRI is only one part of a larger scanning sequence. Such short scanning times are prone to result in invalid conclusions because of noisy spatial map estimates.

This was also evident when analysing the short fMRI data of the YOAD cohort with ICA and DR. The regressions of the DR approach do not entail regularisation of the model parameters, which can lead to overfitting of individual subject time courses in the first regression, and ultimately, to unstable noisy individual spatial maps obtained by the second regression. Therefore, spatial smoothing is usually applied as a form of regularisation to reduce degrees of freedom and to prevent overfitting. However, the potential worsening of the bias introduced by anatomical differences with spatial smoothing, i.e. atrophied brains in AD and PCA patients, can cause artificial functional differences in between-subject analyses as demonstrated by Oakes et al. [2007].

Spatial smoothing can introduce partial volume effects mixing BOLD-driven grey matter signal with noise signals in adjacent white matter and CSF.

Hence, there is demand for techniques that work robustly on short fMRI scans while not being dependent on spatial smoothing for regularisation.

In addition, as a result of the hemodynamic response that has varying spatial smoothness across brain regions, it is difficult to justify a fixed spatial smoothness across the brain.

Therefore, the advantage of EMF is the removal of a reliance on spatial smoothing in the derivation of subject-specific spatial maps. Here, it has been shown how striking individual brain networks in individual subjects can be revealed by making use of ensemble averaging of many matrix factorisations regularised with spatial sparsity and total variation terms.

Although hyper-parameter tuning is required for the individual regularisation terms of EMF, it is less restrictive than spatial smoothing because it only favours spatially smooth components, but does not enforce a fixed spatial smoothness. EMF was thus able to produce not only smooth resting-state network components (first row) but also high-frequency noise components (second row) as depicted in Figure 6.11.

In contrast to AD, more specifically also referred to as late-onset AD (LOAD), YOAD represents a less well understood and particularly challenging form of dementia since it is currently unclear what are the neurological substrates of the highly variable clinical presentation. Accurate diagnosis and study of disease progression in this cohort is critical for making progress in healthcare with the development of medical treatments for early intervention and the provision of targeted support.

The decrease in functional connectivity observed in the Precuneus cortex in dDMN, vDMN and PREC in patients with AD and PCA compared to healthy elderly controls was found with both analysis pipelines, EMF and ICA+DR, and is in line with the existing literature [Lehmann et al., 2015, Agosta et al., 2012, Binnewijzend et al., 2012, Damoiseaux et al., 2012, Greicius et al., 2004] and complementary imaging results for this YOAD cohort [Parker et al., 2019, Slattery et al., 2017, Parker et al., 2018]. The Precuneus is a major hub of the DMN and is thus included in multiple of the subnetworks [Utevsky et al., 2014]. The findings put emphasis on the importance of Precuneus alterations in AD and suggest that this region may drive the changes within the DMN networks observed in previous studies [Badhwar et al., 2017, Damoiseaux et al., 2012, Klaassens et al., 2017]. Although the observed change in functional connectivity is in line with findings of previous studies [Damoiseaux et al., 2012], the observed temporal pattern of alterations goes against predictions. Whereas previous studies found decreased posterior DMN along with increased ventral and anterior DMN connectivity at baseline and decreased connectivity in all DMN networks at follow-up, the observed functional differences only showed decreased functional connectivity in AD and PCA patients compared to subjects of the healthy control group. In addition, Damoiseaux et al. [2012] found increased connectivity of the dDMN. The exact opposite observation was seen in this YOAD cohort.

The alterations in functional connectivity found in PCA patients agrees with some previous studies [Fredericks et al., 2019, Migliaccio et al., 2016], but contradicts the results of [Lehmann et al., 2015], where the dDMN presented with an increase in anterior functional connectivity along with a decrease in connectivity in the vDMN.

For both, PCA and AD group, the partial inconsistency of these results and those of previous studies might be explained by a discrepancy in disease stage in the examined disease groups. For example, Damoiseaux et al. [2012] used a general AD sample whereas this examined cohort is concerned with YOAD subjects.

In addition, results obtained with EMF showed significantly decreased functional connectivity in the left and right hippocampus in the dDMN in AD patients. Changes in the hippocampus were confirmed by a complementary imaging study for this cohort [Parker et al., 2019]. Functional alterations in the hippocampus were also found in previous studies [Badhwar et al., 2017, Binnewijzend et al., 2012] comparing AD to age-matched subjects. However, these findings were inconclusive and were only confirmed by a limited number of other studies [Allen et al., 2007, Supekar et al., 2008, Wang et al., 2006], which also reported decreased functional connectivity in the hippocampus. The clinical diagnosis of AD, and YOAD in particular, masks a spectrum of diverse conditions and pathological progression. Functional imaging and post-processing techniques such as EMF have the potential to reveal much that is currently unknown about these diseases. However, despite the mitigation of spatial smoothing effects and adding the probability of grey matter at a given voxel as a covariate when comparing pathological to healthy subjects, the possibility remains that functional differences are caused by underlying structural differences not yet detectable in underlying anatomical scanning. It is beyond the scope of this paper and remains a challenge for future research to disentangle changes in functional mappings from underlying changes in brain structure.

Nevertheless, our proposed EMF technique has broad applicability to the subject-wise analysis of resting-state fMRI data and its key contribution is the improved spatial detail and spatial reproducibility in single-subject map estimation.

6.5 Conclusion

This chapter has shown that a robust derivation of single-subject spatial maps from short resting-state fMRI data acquired within a clinical setting is possible. The estimated spatial maps showed greater reproducibility when compared to spatial estimates derived with the current state-of-art pipeline ICA+DR. Although the comparison between groups of these spatial maps obtained by EMF and DR has resulted in similar localised differences, only the group comparison of spatial maps derived by EMF showed a significant difference in the left and right hippocampus cluster in the dDMN.

The analysis of fMRI scans often focuses on the comparison of spatial features in functional brain mappings. The next chapter extends the presented EMF model with a haemodynamic kernel and thus allows computing of surrogate neural activation time courses. Furthermore, the next chapter will validate this extension on two open source task fMRI cohorts of healthy subjects and show that experiment compliance can be inferred from these surrogate neural time courses.

Chapter 7

Haemodynamic Matrix Factorisation for Functional Magnetic Resonance Imaging

7.1 Introduction

The General Linear Model (GLM) used in task-fMRI relates activated brain areas to extrinsic task conditions. The translation of resulting neural activation into a hemodynamic response is commonly approximated with a linear convolution model using a hemodynamic response function (HRF). There are two major limitations in GLM analysis. Firstly, the GLM assumes that neural activation is either on or off and matches the exact stimulus duration in the corresponding task timings. Secondly, brain networks observed in resting-state fMRI experiments present also during task experiments, but the GLM approach models these task-unrelated brain activity as noise.

This chapter proposes a novel kernel matrix factorisation approach, called hemodynamic matrix factorisation (HMF), that addresses both limitations by assuming that task-related and task-unrelated brain activity can be modelled with the same convolution model as in GLM analysis. By contrast to the GLM, the proposed HMF is a blind source separation (BSS) technique, which decomposes fMRI data into modes. Each mode comprises of a neural activation time course and a spatial mapping. Two versions of HMF are proposed in which the neural activation time course of each mode is convolved with either the canonical HRF or predetermined subject-specific HRFs.

Firstly, HMF with the canonical HRF is applied to two open-source cohorts. These cohorts comprise of several task experiments including motor, incidental memory, spatial coherence discrimination, verbal discrimination task and a very short localisation task, engaging multiple parts of the eloquent cortex. HMF modes were obtained whose neural activation time course followed original task timings and whose corresponding spatial map matched cortical areas known to be involved in the respective task processing.

Secondly, the alignment of these neural activation time courses to task timings were further improved by replacing the canonical HRF with subject-specific HRFs during HMF mode computation.

In addition to task-related modes, HMF also produced seemingly task-unrelated modes whose spatial maps matched known resting-state networks.

The validity of a fMRI task experiment relies on the assumption that the exposure to a stimulus for a given time causes an imminent increase in neural activation of equal duration. The proposed HMF is an attempt to falsify this assumption and allows to identify subject task participation that does not comply with the experiment instructions.

7.1.1 Motivation

Neural activation causes a complex change in neuro-physiological parameters of the cerebral blood flow (CBF) [Buxton et al., 2004, Kim and Ogawa, 2012]. Functional magnetic resonance imaging (fMRI) measures one of these neuro-physiological parameters, which is the blood oxygen level dependent (BOLD) response. The transition of neural activation into BOLD responses is approximated by a linear shift-invariant system (LSI) using an impulse response that is known as haemodynamic response function (HRF) [Boynton et al., 2012]. In the context of fMRI, the LSI is known as haemodynamic forward model. One of the most defining assumptions of the haemodynamic forward model is that neural activity is an idealised variable, which is either on or off following the exact timing of a presented stimulus.

The most simple haemodynamic forward model convolves a fixed neural activation time course with a fixed filter (referred to as canonical HRF) known from empirical evidence [Logothetis, 2008b]. For a given fMRI task experiment, the haemodynamic forward model results in a BOLD time course, which is compared to observed BOLD time courses in the data to identify areas of the brain that respond to the presented stimuli of the task.

However, there is substantial intra- and inter-subject variability in the BOLD response [Aguirre et al., 1998, Handwerker et al., 2004, 2012, Arichi et al., 2012], either caused by variations in neural activation, in the HRF or in both. Therefore, estimating the variables of the haemodynamic forward model is an ill-posed problem because the BOLD response is the only observed variable, whereas neural activation and HRF are unobserved latent variables. Various approaches have been proposed that either focus on estimating neural activation or HRF by assuming either one or the other to be known.

7.1.2 Previous work

The GLM is the most prominent model used by the approaches that estimate HRF while keeping neural activation fixed. The GLM uses the stimulus timing to construct a set of temporal regressors that are fitted to the time course of every voxel of a fMRI scan. Multiple basis functions can be used to estimate HRF [Henson et al., 2001], usually canonical HRF and its first and second derivative are commonly used in task experiments. In general, the more basis functions are used, the more likely the GLM will overfit the data. To solve this problem, several regularisation techniques have been proposed: constraints in form of temporal prior information [Marrelec et al., 2003, Ciuciu et al., 2003], restrictions on temporal smoothness [Goutte et al., 2000] or a rank constrain on HRF estimates for similar events [Pedregosa et al., 2015]. Other approaches address the regularisation problem by exploiting temporal similarity among adjacent voxels. Parcellation-based HRF estimation has been introduced by Makni et al. [Makni et al., 2005, 2008] and was subsequently extended in Vincent et al. [2010] or Chaari et al. [2013]. These approaches divide the brain into temporal homogeneous regions and estimate a HRF per region.

However, the above GLM based approaches rely on the assumption that evoked neural activation matches assumed neural activation in the task experiment, but it is unknown to what extent this assumption holds across the brain. More importantly, task compliance might vary greatly among subjects resulting in different neural activation patterns than intended by the experimenter. Furthermore, these approaches ignore intrinsic brain activity that operates in the background unrelated to extrinsic task processing. Such intrinsic brain activity was long considered noise before found to produce coherent spatial patterns of brain activity that are referred to as resting-state networks [Raichle et al., 2001, Gusnard and Raichle, 2001, Fox and Raichle, 2007]. All the aforementioned problems occur due to the unknown nature of neural activation in task processing. In contrast to HRF estimation, blind source separation (BSS) techniques have been proposed to obtain estimates of neural activation. These techniques are part of the realm of deconvolution techniques that estimate neural activation but constrain the haemodynamic forward model to either a fix impulse function [Glover, 1999, Gaudes et al., 2011] or a set of fix basis functions [Karahanoğlu et al., 2013a]. Similarly to HRF estimation, regularisation is required because the space of possible solutions is too large given that multiple neural activation time courses can cause the same BOLD response time course. Therefore, Zarahn [2000] proposed to estimate neural activation in the time domain instead of the frequency domain using a set of limited basis functions. This work was extended [Gitelman et al., 2003, McLaren et al., 2012] by using Gaussian priors to restrict neural activation estimates.

Other deconvolution methods force neural activation estimates to be sparse [Gaudes et al., 2011, Hernandez-Garcia and Ulfarsson, 2011, Caballero Gaudes et al., 2013]. Other approaches resemble characteristic properties of the HRF, for example, by applying sparsity regularisation in the Wavelet domain with custom Wavelet basis functions [Khalidov et al., 2011].

All aforementioned approaches for neural activation estimation have been applied voxel-wise without leveraging the similarity of BOLD signal change among adjacent voxels. On the contrary, the Total Activation (TA) approach [Karahanoğlu et al., 2013a] and its extensions [Farouj et al., 2017, Zöller et al., 2019] use spatial priors that enforce temporal similarity of neural activation time courses within a pre-defined region. These regions are defined by an anatomical atlas in which each voxel is assigned to only one region (or cluster).

In contrast to TA, voxels can belong to multiple clusters in mode-based approaches that decompose fMRI data into a set of spatial maps and corresponding time courses. Spatial independent component analysis (sICA) [Beckmann and Smith, 2004] is the most common mode-based approach, in which the decomposition is obtained by maximising a proxy function for spatial independence. The main disadvantage of sICA in fMRI is that it does not incorporate spatial or temporal characteristics of fMRI data. Indeed, the order of time points of a fMRI scan can be rearranged without affecting the sICA result.

More recent mode-based approaches have therefore been proposed that model the distinctive auto-correlation in fMRI time courses and spatial correlation among adjacent voxels [Varoquaux et al., 2011, Harrison et al., 2015, de Pierrefeu et al., 2017, Harrison et al., 2019].

The brain comprises of functionally specialised regions and task activation maps revealed by fMRI experiments were therefore found to be sparse [Friston and Price, 2001, Frost and Goebel, 2012, Cole et al., 2014, Petersen and Sporns, 2015]. These activation maps usually comprise of multiple clusters of spatially adjacent voxels. Daubechies et al. [2009] concluded that sparsity and not independence is an ideal optimisation criteria for BSS techniques in the domain of fMRI. Therefore, approaches based on sparsity and total variation regularisation emerged in the literature.

The hierarchical dictionary learning approach by Varoquaux et al. [2011] incorporates a Smooth-Lasso (SL) spatial regularisation term to obtain subject- and group-level spatial modes. De Pierrefeu et al. have proposed l1 sparsity and total variation (TV) constrains on spatial mode computation via PCA [de Pierrefeu et al., 2017].

Mode-based approaches have the flexibility to find different brain configurations during task processing but often do not relate BOLD signal back to original task timings.

The approach by Cherkaoui et al. [2019] derives modes that comprise of neural activation time courses and spatial maps. In contrast to mode approaches that regularise modes with respect to spatial characteristics, Cherkaoui et al. [2019] focuses on the regularisation of estimated neural activation time courses. Similarly to the TA approach, Cherkaoui et al. [2019] uses piece-wise linear constraining on neural activation time courses but computes modes instead of the parcel-wise deconvolution performed in the TA approach.

7.1.3 Proposed solution

In this chapter, a new mode decomposition of such kind, called Haemodynamic Matrix Factorisation (HMF), is proposed that computes modes using an auto-encoding matrix factorisation framework. Each of these modes comprises of a neural activation time course and a corresponding spatial map. Two variants of HMF are proposed in which neural activation is either convolved with the canonical HRF or a subject-specific pre-determined HRFs to relate the observed BOLD time courses to neural activation time courses. Similarly as in de Pierrefeu et al. [2017], the spatial maps of such modes are regularised by l1 sparsity and TV. The neural activation time courses are also regularised by TV which is more flexible than the discussed piece-wise constant restriction on time courses [Karahanoğlu et al., 2013a, Cherkaoui et al., 2019].

HMF was applied to the Midnight Scan Club (MSC) open source data[1], which comprises of ten healthy adult subjects with five hours of task-based fMRI experiments including motor, incidental memory, spatial coherence discrimination and verbal discrimination task. Furthermore, HMF was applied to the Brainomics task data[2], which includes various stimuli to map the eloquent cortex. The proposed HMF approach, blind to the original stimulus timings, recovered modes whose neural activation time course matched timings and duration of the corresponding task stimuli. Hereby, HMF revealed individual subjects whose task participation differed from anticipated experiment participation. In addition, neural activation time courses of default mode networks (DMNs) presented with an anti-correlated behaviour to the task timings in MSC and Brainomics tasks.

Lastly, HMF modes were compared to modes produced by sICA, showing that BOLD time courses of HMF modes had greater correlation with the generic task design than time courses produced by sICA. With respect to spatial estimates, HMF showed greater spatial reproducibility than sICA among the ten sessions of the MSC data.

7.2 Methods

The proposed generative model is concerned with BOLD time courses of length T, measured at V voxels: $\mathbf{Y} \in \mathbb{R}^{T \times V}$. The observed BOLD signal change is assumed to be driven by C latent modes. The cost function of the generic version of the proposed HMF model is given by

$$\underset{\{N_i\},\{F_i\}}{\arg\min} \frac{1}{2} \|\mathbf{M} \odot \left(\sum_{i=0}^{C} F_i N_i H_i \right) - \mathbf{Y}\|_2^2, \tag{7.1}$$

in which $F_i \in \mathbb{R}^{T \times T}$ is a Toeplitz matrix of filter f_i with length L for mode i, $N_i \in \mathbb{R}^{T \times 1}$ is a neural activation time course, $H_i \in \mathbb{R}^{1 \times V}$ is a spatial map, and $\mathbf{M} \in \mathbb{R}^{1 \times V}$ is a vector

---

[1] `https://openfmri.org/dataset/ds000224/`

[2] `http://brainomics.cea.fr/localizer`

that weighs the importance of each voxel using grey matter probabilities.

The following will discuss special cases of this HMF model. Firstly, HMF is only optimised with respect to N_i assuming HRFs $\{f_1,...,f_C\}$ are fixed. Secondly, an algorithm for the alternating optimisation of N_i and F_i is discussed.

7.2.1 HMF with the canonical HRF

Given the assumption that all filter $\{f_1,...,f_C\}$ equal the canonical HRF f, neural activation time courses of all modes can be aggregated in matrix $\mathbf{N} \in \mathbb{R}^{T\times C}$. These neural activation time courses are convolved with the canonical HRF f by multiplying the Toeplitz matrix $\mathbf{F} \in \mathbb{R}^{T\times T}$ of f with $\mathbf{N}$ as depicted in Equation 7.2.

$$\mathbf{FN} = \begin{pmatrix} f_1 & 0 & \cdots & 0 & 0 \\ f_2 & f_1 & \ldots & \vdots & \vdots \\ f_3 & f_2 & \ldots & 0 & 0 \\ \vdots & f_3 & \ldots & f_1 & 0 \\ f_{L-1} & \vdots & \cdots & f_2 & f_1 \\ f_L & f_{L-1} & \vdots & \vdots & f_2 \\ 0 & f_L & \ldots & f_{L-2} & \vdots \\ 0 & 0 & \cdots & f_{L-1} & f_{L-2} \\ \vdots & \vdots & \vdots & f_L & f_{L-1} \\ 0 & 0 & 0 & \cdots & f_L \end{pmatrix} \begin{pmatrix} n_{1,1} & n_{1,2} & \cdots & n_{1,C} \\ n_{2,1} & n_{2,2} & \cdots & \vdots \\ \vdots & \vdots & \ldots & \vdots \\ \vdots & \vdots & n_{T-1,C-1} & n_{T-1,C} \\ n_{T,1} & \cdots & n_{T,C-1} & n_{T,C} \end{pmatrix} \tag{7.2}$$

The data $\mathbf{Y}$ can thus be decomposed by a matrix factorisation $\mathbf{FNH}$ where matrix $\mathbf{N} \in \mathbb{R}^{T*S\times C}$ contains neural activation time courses per subject $\mathbf{N_s} \in \mathbb{R}^{T\times C}$ and matrix $\mathbf{H} \in \mathbb{R}_+^{C\times V}$ contains a set of spatial maps shared among all S subjects. Neural activation time courses $\mathbf{N}$ in this matrix factorisation are optimised by minimising the l2 loss between original and reconstructed fMRI data as given by

$$\arg\min_{\mathbf{N}} \frac{1}{2} \|\mathbf{M} \odot (\mathbf{FNH} - \mathbf{Y})\|_2^2 = \arg\min_{\mathbf{N}} \frac{1}{2} \|\mathbf{M} \odot \Big(\mathbf{FN}\sigma((\mathbf{FN})^\top \mathbf{Y}) - \mathbf{Y}\Big)\|_2^2, \tag{7.3}$$

where spatial map matrix $\mathbf{H}$ is obtained by $\sigma((\mathbf{FN})^\top \mathbf{Y})$ and vector $\mathbf{M} \in \mathbb{R}^{1\times V}$ weighs the importance of each voxel using grey matter probabilities. The neural activation time course parameters $\mathbf{N}$ are initialised with a random Xavier initialisation [Glorot and Bengio, 2010]. The corresponding gradient of Equation 7.3 is given by

$$\begin{aligned} \frac{\partial J}{\partial \mathbf{N}} =& \mathbf{F}^\top (\mathbf{M} \odot (\mathbf{FN}\sigma((\mathbf{FN})^\top \mathbf{Y}) - \mathbf{Y}) \odot \mathbf{M}) \sigma(\mathbf{Y}^\top \mathbf{FN}) + \\ & \mathbf{F}^\top \mathbf{Y}(((\mathbf{M}^\top \odot (\sigma(\mathbf{Y}^\top \mathbf{FN})\mathbf{N}^\top \mathbf{F}^\top - \mathbf{Y}^\top) \odot \mathbf{M}^\top)\mathbf{FN}) \odot \sigma(\mathrm{sign}(\mathbf{Y}^\top \mathbf{FN}))) \end{aligned} \tag{7.4}$$

The limited memory Broyden-Fletcher-Goldfarb-Shanno (L-BFGS) is used for finding the optimal **N**. This model is referred to as canonical HMF.

7.2.2 HMF with predetermined subject-specific HRFs

To model each subject with a predetermined HRF in HMF, the Toeplitz matrix **F** in Equation 7.3 is composed of individual HRFs changing along the diagonal as depicted in Figure 7.1. Cost function and gradient remain the same as in canonical HMF. The model is referred to as subject-specific HMF.

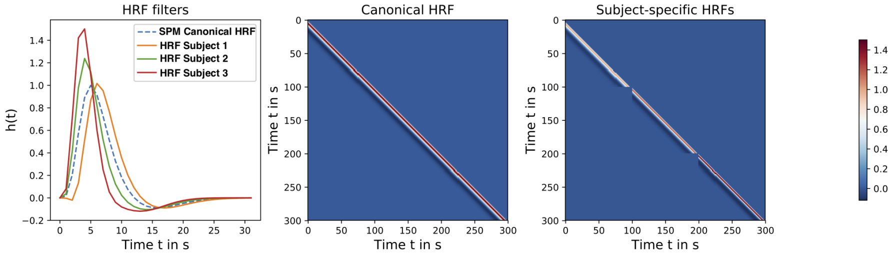

Figure 7.1: The canonical HRF and three subject-specific HRFs with distinct height and width (left). The Toeplitz matrix modelling three subjects concatenated in time with the canonical HRF (middle). The Toeplitz matrix modelling each of the three subjects concatenated in time with its own HRF (right). In this example, each scan has a length of 100s.

7.2.3 HMF with HRF parameter fitting

In contrast to using predetermined HRFs, it is possible to derive the gradient of Equation 7.3 with respect to Toeplitz matrix **F** as given by

$$\begin{aligned}\frac{\partial J}{\partial \mathbf{F}} =& (\mathbf{M} \odot (\mathbf{F}\mathbf{N}\sigma((\mathbf{F}\mathbf{N})^\top \mathbf{Y}) - \mathbf{Y}) \odot \mathbf{M})\sigma(\mathbf{Y}^\top \mathbf{F}\mathbf{N})\mathbf{N}^\top + \\ & \mathbf{Y}(((\mathbf{M}^\top \odot (\sigma(\mathbf{Y}^\top \mathbf{F}\mathbf{N})\mathbf{N}^\top \mathbf{F}^\top - \mathbf{Y}^\top) \odot \mathbf{M}^\top)\mathbf{F}\mathbf{N}) \odot \sigma(\text{sign}(\mathbf{Y}^\top \mathbf{F}\mathbf{N})))\mathbf{N}^\top\end{aligned} \tag{7.5}$$

Optimising for neural activation **N** and haemodynamic filters **F** in Equation 7.3 is possible by alternating between gradient computation in Equation 7.4 and 7.5.

However, degenerate results are produced with optimisation being stuck in poor parameter spaces of **N** and **F** when poor initialisations of HRFs and neural activation time courses are provided.

7.2.4 Regularisation of spatial maps and neural activation

The regularisation terms R_H and R_N for spatial map matrix and neural activation matrix, respectively, are introduced in the following.

7.2.4.1 Spatial regularisation

The regularisation term $R_H = \beta_1 R_{H_{TV}} + \beta_2 R_{H_S}$ comprises of a total variation and sparsity term. To compute the total variation term, the spatial map matrix **H** is reshaped into a 4D volume $\mathbf{H^{(4D)}}$ to obtain the following regularisation cost $R_{H_{TV}}$:

$$\begin{aligned} R_{H_{TV}} = \sum_{c,i,j,k} & \left|\mathbf{H^{(4D)}}_{c,i+1,j,k} - \mathbf{H^{(4D)}}_{c,i,j,k}\right| + \\ & \left|\mathbf{H^{(4D)}}_{c,i,j+1,k} - \mathbf{H^{(4D)}}_{c,i,j,k}\right| + \left|\mathbf{H^{(4D)}}_{c,i,j,k+1} - \mathbf{H^{(4D)}}_{c,i,j,k}\right| \end{aligned} \tag{7.6}$$

To compute spatial total variation with efficient matrix multiplications, the product of $\mathbf{H} = \sigma((\mathbf{FN})^\top \mathbf{Y})$ is rewritten element-wise as

$$\begin{bmatrix} \\ \sigma((\mathbf{FN})^\top y_1) & \sigma((\mathbf{FN})^\top y_2) & \dots & \sigma((\mathbf{FN})^\top y_V) \\ \\ \end{bmatrix}, \tag{7.7}$$

where $\sigma((\mathbf{FN})^\top y_v)$ constitutes a column vector for voxel v. All column vectors taken together form the spatial maps $\mathbf{H}$ as depicted in Equation 7.7. The original data $\mathbf{Y}$ is rearranged into individual matrices along either dimension $V1$, $V2$ or $V3$ of the three-dimensional Euclidean space. An approximation of Equation 7.6 is computed with the following term

$$\begin{aligned} R_{H_{TV}} = & \beta_1 \sum_i^{V2} \sum_j^{V3} \|\sigma((\mathbf{FN})^\top \mathbf{Y_{ij}^{(1)}})\mathbf{D_1}^\top\|_1 + \\ & \sum_i^{V1} \sum_j^{V3} \|\sigma((\mathbf{FN})^\top \mathbf{Y_{ij}^{(2)}})\mathbf{D_2}^\top\|_1 + \sum_i^{V1} \sum_j^{V2} \|\sigma((\mathbf{FN})^\top \mathbf{Y_{ij}^{(3)}})\mathbf{D_3}^\top\|_1 \end{aligned} \tag{7.8}$$

where $\mathbf{Y_{ij}^{(1)}} \in \mathbb{R}^{T \times V1}$, $\mathbf{Y_{ij}^{(2)}} \in \mathbb{R}^{T \times V2}$, $\mathbf{Y_{ij}^{(3)}} \in \mathbb{R}^{T \times V3}$, $\mathbf{D_1} \in \mathbb{R}^{(V1-1) \times V1}$, $\mathbf{D_2} \in \mathbb{R}^{(V2-1) \times V2}$ and $\mathbf{D_3} \in \mathbb{R}^{(V3-1) \times V3}$. An example of the difference operator matrix $\mathbf{D_i}$ is given in Equation 7.9.

$$\mathbf{D_i} = \begin{pmatrix} -1 & 1 & & & & \\ & -1 & 1 & & & \\ & & -1 & 1 & & \\ & & & \ddots & & \\ & & & -1 & 1 & \\ & & & & -1 & 1 \end{pmatrix} \tag{7.9}$$

The gradient for the proposed regularisation term in Equation 7.7 is given by:

$$\begin{aligned}\frac{\partial R_{tv}}{\partial \mathbf{N}} = & \sum_{i}^{V2}\sum_{j}^{V3}\mathbf{Y}^{(\mathbf{1})}_{\mathbf{ij}}((\mathbf{D_1}\operatorname{sign}\left(\mathbf{D_1}^{\top}\sigma((\mathbf{FN})^{\top}\mathbf{Y}^{(\mathbf{1})}_{\mathbf{ij}})^{\top}\right)\odot\sigma'((\mathbf{FN})^{\top}\mathbf{Y}^{(\mathbf{1})}_{\mathbf{ij}})^{\top}))+ \\ & \sum_{i}^{V1}\sum_{j}^{V3}\mathbf{Y}^{(\mathbf{2})}_{\mathbf{ij}}((\mathbf{D_2}\operatorname{sign}\left(\mathbf{D_2}^{\top}\sigma((\mathbf{FN})^{\top}\mathbf{Y}^{(\mathbf{2})}_{\mathbf{ij}})^{\top}\right)\odot\sigma'((\mathbf{FN})^{\top}\mathbf{Y}^{(\mathbf{2})}_{\mathbf{ij}})^{\top}))+ \\ & \sum_{i}^{V1}\sum_{j}^{V2}\mathbf{Y}^{(\mathbf{3})}_{\mathbf{ij}}((\mathbf{D_3}\operatorname{sign}\left(\mathbf{D_3}^{\top}\sigma((\mathbf{FN})^{\top}\mathbf{Y}^{(\mathbf{3})}_{\mathbf{ij}})^{\top}\right)\odot\sigma'((\mathbf{FN})^{\top}\mathbf{Y}^{(\mathbf{3})}_{\mathbf{ij}})^{\top}))\end{aligned} \tag{7.10}$$

In addition to the total variation term, the Kullback-Leibler divergence between two exponential distributions was used as regularisation term for spatial sparsity. It is given by $\Delta(\lambda||\widehat{\lambda}_c) = \log(\lambda) - \log(\hat{\lambda}_c) + \frac{\hat{\lambda}_c}{\lambda} - 1$ between a desired exponential distribution p with rate λ and an exponential distribution p_c of spatial map values $H_c \in \mathbb{R}^{1\times V}$ with estimated rate parameter $\hat{\lambda}_c$ resulting in the following loss term

$$R_{H_S} = \frac{1}{C}\sum_{c=1}^{C}\Delta(\lambda||\widehat{\lambda}_c). \tag{7.11}$$

The definition of the exponential value distribution p, the derivation of KL $\Delta(\lambda||\widehat{\lambda}_c)$ and the estimate used for $\hat{\lambda}_c$ are provided in the following.
The exponential distribution is given by

$$p_\lambda(x) = \begin{cases} \lambda e^{-\lambda x} & x \geq 0 \\ 0 & x < 0 \end{cases} \tag{7.12}$$

The Kullback-Leibler divergence between the desired rate parameter λ and the estimated rate parameter $\widehat{\lambda}_c$ in mode c is derived as follows:

$$\begin{aligned}\Delta\left(\lambda||\widehat{\lambda}_c\right) &= \mathbb{E}_\lambda\left(\log\frac{p_\lambda(x)}{p_{\widehat{\lambda}_c}(x)}\right) \\ &= \mathbb{E}_\lambda\left(\log\frac{\lambda e^{-\lambda x}}{\widehat{\lambda}_c e^{-\widehat{\lambda}_c x}}\right) \\ &= \log(\lambda) - \log(\widehat{\lambda}_c) - \left(\lambda - \widehat{\lambda}_c\right)E_\lambda(x) \\ &= \log(\lambda) - \log(\widehat{\lambda}_c) + \frac{\widehat{\lambda}_c}{\lambda} - 1\end{aligned} \tag{7.13}$$

The maximum likelihood estimate for the rate parameter $\widehat{\lambda}_c$ of mode c is

$$\widehat{\lambda}_c = \frac{1}{\bar{x}} = \frac{n}{\sum_i x_i}. \tag{7.14}$$

7.2.4.2 Temporal regularisation

The neural activation time courses are regularised by combining l1, l2 and total variation. The l2 regularisation term prevents biologically non-plausible large magnitude signal change at individual time points. The total variation and l1 regularisation approximate biologically efficient neural activation organisation by preferring BOLD responses produced by the most sparse and energy efficient neural activation pattern. Total variation of the neural time course matrix $\mathbf{N}$ is implemented by using a difference operator matrix similar to spatial regularisation in Equation 7.9. The complete temporal regularisation term is given by

$$R_N = \alpha_1 \|\mathbf{N}\mathbf{D_4}\|_1 + \alpha_2 \|\mathbf{N}\|_1 + \alpha_3 \|\mathbf{N}\|_2, \tag{7.15}$$

where $\mathbf{D_4} \in \mathbb{R}^{(T*S-1)\times(T*S)}$.

7.2.5 Ensemble averaging framework

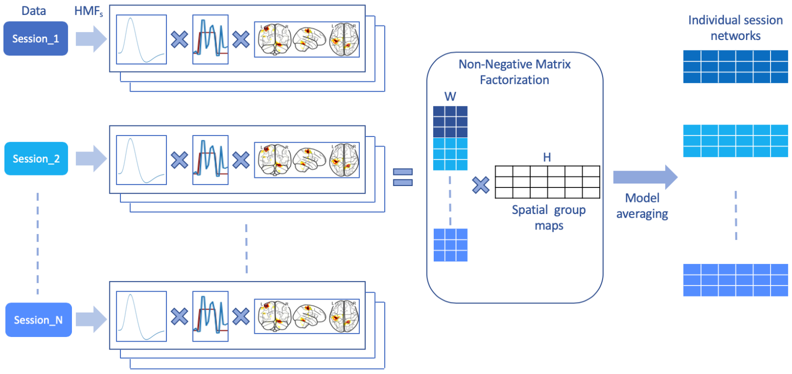

Figure 7.2: Summary of ensemble averaging of individual haemodynamic matrix factorisations to obtain individual session modes in the MSC tasks. First, 10 decompositions are obtained for each task for each of the 10 sessions. All concatenated spatial maps of estimated modes are decomposed into two matrices with NMF. An association matrix and a corresponding matrix of spatial maps. The spatial maps obtained by NMF are the average of the spatial maps of all modes for a respective task. Similarly, the association matrix is used to obtain averages of neural activation time courses in the corresponding sessions.

The HMF approach is a non-convex optimisation problem because of the non-linear activation function σ. Each neural activation time course is normalised by the l2 norm to address the scale ambiguity between neural activation time courses $\mathbf{N}$ and spatial maps $\mathbf{H}$. A non-optimal solution may be obtained with only one random initialisation. Therefore, several HMFs are obtained from random initialisations of $\mathbf{N}$. Their outputs are combined with an ensemble averaging framework as depicted in Figure 7.2. An ensemble average of these HMFs across all sessions is found such that $\mathbf{\Omega}_{opt} = \sum_{n=1}^{N}\sum_{c=1}^{C} \alpha_{n,c}\mathbf{\Omega}_{n,c}$. A fast coordinate descent non-negative matrix factorisation (CD-NMF) [Hsieh and Dhillon, 2011] is used on the concatenated spatial maps $\mathbf{H}_{ALL} = \{\mathbf{H}_{ns} \in \mathbb{R}^{C\times V}, s = 1\cdots S, n = 1\cdots N\}$ to obtain a set of group maps H shared across all sessions by solving for the following loss function

$$\frac{1}{2}\|\mathbf{A}\mathbf{H}_{group} - \mathbf{H}_{ALL}\|_2^2 \tag{7.16}$$

A non-negative double singular value initialisation (NNDSVD) Boutsidis and Gallopoulos [2008] is used for $\mathbf{A} \in \mathbb{R}^{(C*N*S)\times C}$ and $\mathbf{H}_{group} \in \mathbb{R}^{C\times V}$ to speed up convergence and to guarantee deterministic behaviour of the ensemble averaging process. No regularisation term is applied in the CD-NMF.

7.3 Materials

This section introduces simulated and real imaging data used with HMF.

7.3.1 Simulated data

In addition to HMF evaluation, simulated data is used to tune HMF hyper-parameters. More specifically, the simulated data is split into a training and test set, to tune the hyper-parameters of HMF and to report HMF performance, respectively.

The characteristics of HMF modes are determined by six hyper-parameters: three for spatial smoothness and sparsity $\beta = \{\beta_1, \beta_2, \lambda\}$, and three for total variation, l1 and l2 regularisation $\alpha = \{\alpha_1, \alpha_2, \alpha_3\}$ to determine the temporal characteristics of the neural activation time courses.

To tune these hyper-parameters for multiple task experiments, two types of simulated fMRI data are computed. The first type resembles fast spike-like neural activation change, while the second type resembles slow block-wise neural activation. In the following, these two types are referred to as simulated event-type and block-type fMRI data, respectively.

The simulated event-type fMRI data consists of 5 brain modes modulated by short event-type binary neural activation, and 9 brain modes modulated by random neural activation drawn from a half normal distribution. Simulated block-type fMRI data consists of 5 brain modes modulated by a binary block-type neural activation, and 9 task-free modes as in the event-type data. The 14 spatial maps for these brain modes are taken from Shirer et al. [2012]. Twenty training and twenty test simulated fMRI scans are generated for each type of data. Each scan is created with the generative model

$$\mathbf{Y} = \mathbf{F}\mathbf{N}\mathbf{H} + \mathbf{E} \tag{7.17}$$

in which $\mathbf{H} \in \mathbb{R}_+^{C\times V}$ is the set of 14 spatial maps, $\mathbf{N} \in \mathbb{R}^{T\times C}$ is a matrix with either 5 event- or 5 block-type and 9 random neural activation time courses, $\mathbf{F} \in \mathbb{R}^{T\times T}$ is the Töplitz matrix of the individual HRF used for each subject, and $\mathbf{E} \in \mathbb{R}^{T \times V}$ is a Gaussian noise contribution. The original spatial maps, the subject-specific HRFs and an example of the block-type, event-type and random neural activation are depicted in Figure 7.3.

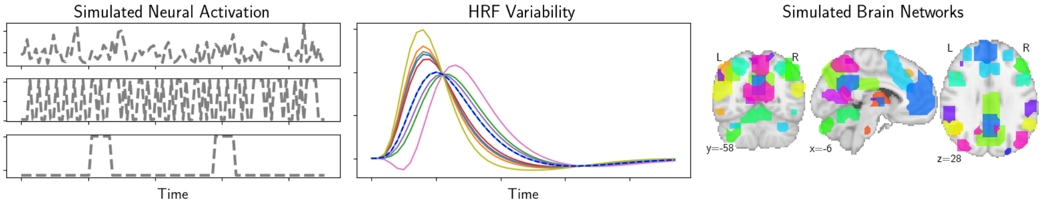

Figure 7.3: A simulated random, event and block neural activation time course depicted from top to bottom (left). Variability among the simulated HRF filters (middle). Ground truth spatial maps (right).

7.3.1.1 Experiments on simulated data

HMF is tested in two scenarios. In the first scenario, canonical HMF is applied to the simulated data assuming that the true HRF in each subject is unknown. In the second scenario, the true HRF in each subject is known by HMF, thus, subject-specific HMF is applied to the simulated data. The error in neural activation estimation is subsequently compared between the two scenarios.

Fourteen HMF modes are estimated in accordance with the original number of simulated brain networks. For the hyper-parameter tuning, a grid-search based approach is utilised. The search cost function maximises median correlation between original and estimated neural activation time courses. The cost function balances the quality of estimation in random-, event- and block-type neural activation patterns. Results obtained with canonical and subject-specific HMF are then evaluated on the test set.

7.3.2 Imaging data

The following introduces the two examined fMRI data cohorts analysed with HMF, the preprocessing applied to the imaging data and, finally, the conducted experiments to evaluate HMF.

7.3.2.1 Data

Two cohorts are used to evaluate HMF: the Midnight Scan Club (MSC) [Gordon et al., 2017] and the Brainomics cohort [Pinel et al., 2007, 2012, Orfanos et al., 2017]. The MSC data comprises of functional and anatomical T1 images. Structural MRI was conducted across two separate days. In total, four T1-weighted images (sagittal, 224 slices, 0.8mm isotropic resolution, TE 3.74ms, TR 2400ms, TI 1000ms, flip angle 8 degrees), four T2-weighted images (sagittal, 224 slices, 0.8mm isotropic resolution, TE 479ms, TR 3200ms) [Gordon et al., 2017]. All functional imaging was performed using a gradient-echo EPI sequence (TR 2200ms, TE 27ms, flip angle 90 degrees, voxel size $4 \times 4 \times 4\text{mm}^3$, 36 slices) [Gordon et al., 2017].

The subjects of the MSC data were scanned in ten repetitive sessions. Each session consists of two motor task runs, two spatial discrimination task runs, two verbal discrimination task runs, and three incidental memory task runs (word discrimination, scene discrimination, face discrimination). The MSC motor task timings consist of five distinct task blocks. Each task block appears twice throughout the task. In each of these five task blocks, the subject continuously moves either left or right foot, left or right hand, or tongue. Further details about the MSC task experiments can be found in Gordon et al. [2017].

The Brainomics data comprises of functional and anatomical T1 images. Functional images were acquired on a 3T Brucker scanner using an EPI sequence (TR 2400ms, TE 30ms, matrix size 64×64, FOV 24×24cm, voxel size $3 \times 3 \times 3$mm). Each volume consisted of 34 slices of 4mm thickness. Anatomical T1 images were acquired with a spatial resolution of $1 \times 1 \times 1.2$mm [Pinel et al., 2007]. The Brainomics cohort comprises of 94 subjects scanned with a very short and sparse task paradigm of 5 minutes to localise several areas of the eloquent cortex. These tasks comprised of auditory and visual perception, sensory motor actions, reading, language comprehension, and mental calculation stimuli [Pinel et al., 2007, 2012, Orfanos et al., 2017].

7.3.2.2 Image preparation

Volumes of the fMRI scan of each subject are realigned to the first volume of the scan to correct for head motion. The first volume is registered to its corresponding bias-corrected T1-weighted anatomical scan (affine registration). The intra-subject affine registration and non-linear inter-subject registration to the Montreal Neurological Institute (MNI) template are combined to map all fMRI volumes with one re-sampling into the MNI space. Results included in this manuscript come from pre-processing performed using FMRIPREP version 1.3.1 [Esteban et al., 2019]. The analysis of the Brainomics data is conducted on 90 subjects because of failure of FMRIPREP in four of the original subjects. Time courses of voxels within a brain mask are extracted. Time courses are high-pass filtered (0.01Hz cut-off) to remove signal drifts from scanner instabilities. Time courses are centred and variance-normalised. The functional 4D volume set of each scan is reshaped into a matrix $\mathbf{Y} \in \mathbb{R}^{T \times V}$.

7.3.2.3 Experiments on imaging data

The optimal hyper-parameter setting of the simulation experiments is used to compute canonical and subject-specific HMF on real imaging data. Decompositions into 40 modes are computed as motivated by empirical observations detailed in Varoquaux et al. [2010]. In addition to canonical and subject-specific HMF, sICA is also applied to the imaging data. Similarly as for HMF, the grey matter segmentation in MNI space is used to weigh the importance of each voxel in sICA [Beckmann and Smith, 2004]. For the Brainomics task, all subject scans are concatenated in time. One decomposition into 40 modes is computed with canonical HMF, subject-specific HMF and sICA. For each MSC task, all subject scans are concatenated in time for each session. Hence, a decomposition into 40 modes for canonical HMF, subject-specific HMF and sICA is obtained for each task in each session. The association matrix obtained with CD-NMF described in the ensemble averaging framework outlined in Figure 7.2 is used to relate modes across individual sessions of the MSC data.

Comparison of HMF modes to task timings in all considered tasks

Canonical HMF is applied to MSC tasks and Brainomics task. Several combinations of task timings are compared to neural activation estimates of the HMF modes. In the motor task, task timings for all visual cues, all foot, all hand, left hand, right hand, left foot, right foot and tongue movement are compared against neural activation time courses of HMF modes. In incidental memory tasks, and spatial and verbal discrimination task, task timings of the two visual cue types and their combination are compared against neural activation time courses of HMF modes. And last, in the Brainomics task, task timings are grouped into audio, video, vertical checkerboard, horizontal checkerboard, left hand, right hand, phrases and calculus and are compared to neural activation time courses. The HMF mode with the highest correlation between task timing and neural activation is determined and in the following referred to as “most task-relevant mode”.

Comparison of subject-specific HMF with canonical HMF

HRF estimates are obtained by using a three basis function (canonical HRF + first and second derivative) GLM. In the MSC cohort, voxel-wise GLM estimates are obtained with task timings of all stimuli cues from incidental memory tasks. In the Brainomics cohort, voxel-wise GLM estimates are obtained with video stimuli cue timings. In both data sets, a second level analysis on subject GLM estimates produces a spatial map, which is z-transformed and thresholded at 3 standard deviations. The thresholded spatial map is used to obtain an average HRF estimate per subject. The correlation of neural activation time course and task timings of the most task-relevant mode is compared between canonical and subject-specific HMF.

Comparison of sICA with canonical HMF

To compare sICA with canonical HMF, task timings are convolved with the canonical HRF to derive a generic task design. The ICs with the highest correlation between generic task design and time course of the IC are compared to the most task-relevant mode of canonical HMF.

Additionally, the reproducibility of spatial map estimates of the most task-relevant IC and canonical HMF mode is compared across the ten sessions of the MSC data. The reproducibility of spatial maps is obtained by computing the correlation between all pairs of spatial maps associated with the corresponding group average spatial map of the most task-relevant IC or canonical HMF mode.

7.4 Results

The most task-relevant modes were compared between canonical HMF, subject-specific HMF and sICA in motor, discrimination, incidental memory and Brainomics task. Firstly, the correlation between task timings and neural activation time course was compared between canonical and subject-specific HMF. Secondly, the correlation between BOLD time course and task design of the corresponding stimuli was compared between canonical HMF and sICA. And lastly, the spatial reproducibility of the most task-relevant modes across the 10 sessions of the MSC cohort were compared between canonical HMF and sICA. Summary statistics of the average correlation are provided for individual stimulus types in each task.

7.4.1 Simulated data

Canonical HMF and subject-specific HMF recovered all 14 simulated brain networks. The median correlation between original and estimated neural activation obtained with canonical HMF was 0.78, 0.76, and 0.95 for random-, event-, and block-type stimulus, respectively. The median correlation between original and estimated BOLD time courses was 0.98, 0.97, and 0.99 for random-, event-, and block-type stimulus, respectively. Discontinuous neural activation change in block- or event-type neural activation was less well recovered than continuous change in random neural activation by HMF as depicted in Figure 7.4. Using subject-specific HMF instead of canonical HRF, the median correlation between original and estimated neural activation increased to 0.87, 0.89, and 0.98 for random-, event- and block-type neural activation, respectively. The median correlation between original and estimated BOLD time courses increased to 0.99, 0.98, and 0.99 for random-, event- and block-type neural activation, respectively. The median correlation difference between canonical and

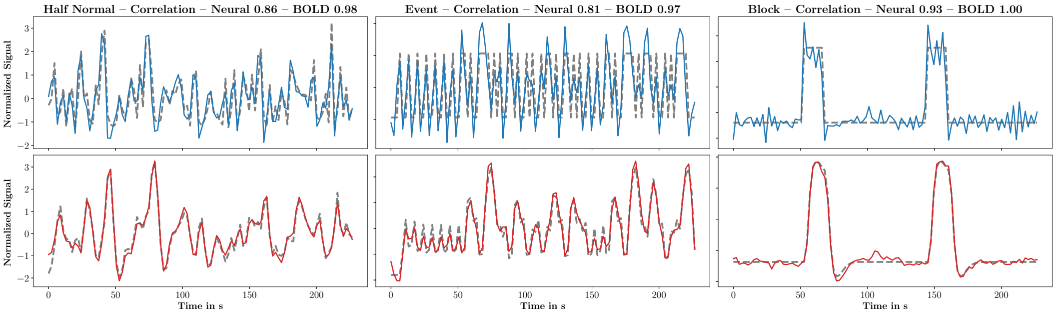

Figure 7.4: Original and estimated neural activation (top row) and corresponding BOLD time courses (bottom row) obtained by canonical HMF for random- (left), event- (middle) and block-type (right) neural activations. Estimated and original neural activation time courses were normalised to zero mean and unit standard deviation for presentation.

subject-specific HMF was caused by a mismatch between canonical and actual HRF in each subject. This HRF mismatch translated into a mismatch between original and estimated neural activation, which resulted in low correlation depicted in Figure 7.5 in subjects whose HRF largely deviated from the canonical HRF. The more mismatch there was in the time-to-peak delay between actual and canonical HRF, the lower the observed correlation between estimated and actual neural activation time course. In contrast, the effect on BOLD time course estimation was marginal. Only a small improvement in the correlation between original and estimated BOLD time courses was observed when comparing subject-specific with canonical HMF.

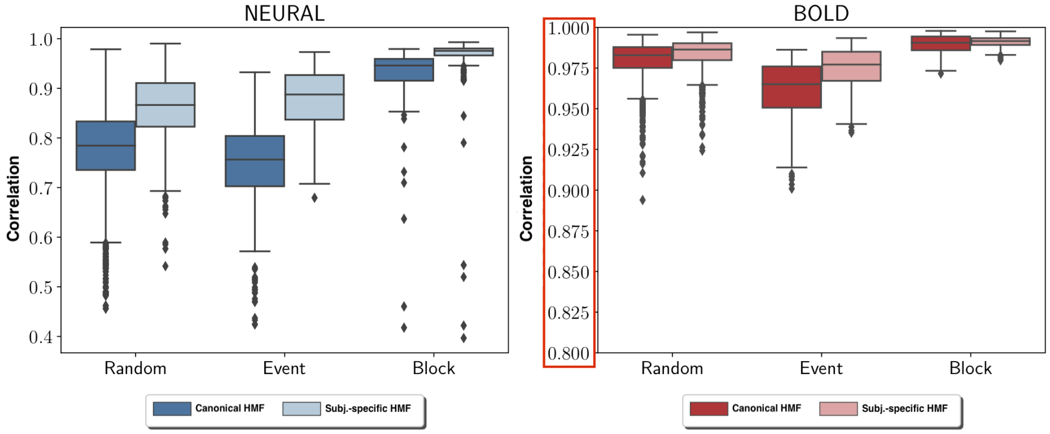

Figure 7.5: The distribution of correlation between original and estimated neural activation time courses (left) as well as the distribution of correlation between original and estimated BOLD time courses (right) for random-, event-, and block-type activation, respectively, using either canonical HMF or subject-specific HMF.

7.4.2 Imaging data

To determine how well HMF recovers neural activation time courses in task scenarios ranging from block to fast random task designs, HMF was applied to tasks of the MSC and Brainomics cohort.

The following examines the alignment between canonical HMF modes and task timings in each individual task. Then, the alignment to task timings is compared between modes from subject-specific HMF and canonical HMF. Finally, spatial maps and BOLD time courses of modes from canonical HMF are compared to corresponding ICs of sICA.

7.4.2.1 Motor task

Figure 7.6 shows the spatial maps and the neural activation time course obtained by canonical HMF on the motor task along with the timing blocks for the first six subjects of session one. More specifically, each row depicts the following movements: foot, left and right hand, and tongue (from top to bottom). The obtained neural activation followed individual task timings in subjects 1,2, and 5. On the other hand, in subjects 3, 4 and 6, the neural

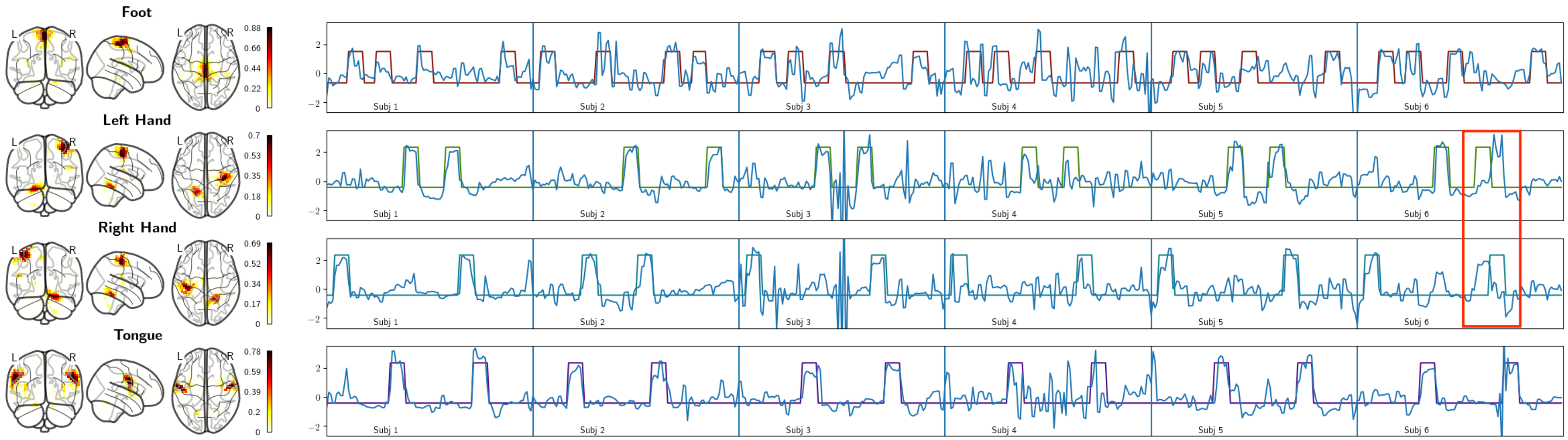

Figure 7.6: Each row depicts task blocks (lines in four distinct colours in row one to four) of either foot, left hand, right hand or tongue movement, respectively. The neural activation time course of the mode with the highest correlation to a particular movement type is depicted as continuous blue line superimposed on the individual block movement timings.

activation only partially followed task timings.

Hand

However, most importantly, HMF exposed that subject 6 confused moving left with right hand in one task block as highlighted by the red bounding box.

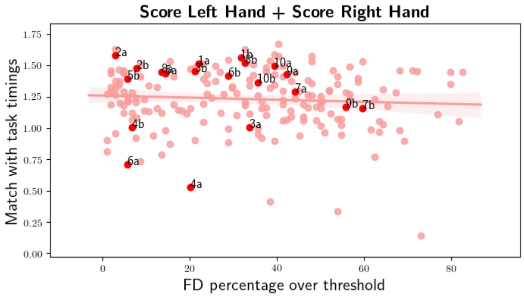

Figure 7.7: Total correlation score plotted against the percentage of time points over frame-wise displacement (FD) threshold in the MSC motor task. The labelled data points correspond to the first and second scan of session one of subject one to ten. The y-axis depicts total correlation score (TCS), defined as the sum of the correlations computed for the left and right hand task timings. The x-axis depicts the percentage of time points over the frame-wise displacement threshold.

The correlation between task timings and neural activation time course of the most task-relevant mode is computed to find more scans in which the subject confuses instructions in the motor task. Since for hand movement there are two correlation scores, a total correlation score (TCS) is defined as the sum of the correlations computed for the left and right hand task timings. Figure 7.7 shows TCS computed for the first and second scan of all subjects and across all sessions plotted against the percentage of time points over frame-wise displacement (FD) threshold in the MSC motor task. In the figure, only the points corresponding to the first session are labelled with na or nb where $n = (1...10)$ indicates the subject, and a and b indicate the first and second scan, respectively.

Estimated neural activation time course and task timings showed high accordance in task runs $1a$, $1b$, $2a$, $2b$, $5a$ and $5b$ as seen in Figure 7.6, which translated into corresponding high correlation scores in Figure 7.7. In contrast, task runs $3a$, $4a$ and $6a$ had lower scores given their worse alignment with task timings. However, the second task runs $3b$, $4b$ and $6b$ of these subjects had better alignment with task timings (similarly high correlation values as in subject 1, 2, and 5) with similarly experienced head motion. A small negative correlation (≈ -0.1) was observed between FD and TCS.

Figure 7.7 shows that low TCS values only occur in one of the many scans for one subject. This suggests that HMF did not under-perform in these scans but subjects did potentially not comply with the given task as shown for subject 6 in Figure 7.6. More specifically, scans of subjects with TCS below 0.75 provide evidence for non-compliant task behaviour. The average correlation of the neural activation time course of the most task-related mode to the left hand task timings was 0.64. The average correlation of the neural activation time course of most task-related mode to the right hand task timings was 0.67. Spatial maps comprised of clusters in premotor cortex, primary somatosensory cortex and several clusters in the cerebellum.

Tongue

The spatial map of the most task-related mode comprised of activation clusters in the primary somatosensory cortex. The average correlation between neural activation time course and task timings for tongue movements was 0.68.

Foot

The spatial maps of the most task-related mode showed clusters in premotor cortex, primary motor cortex and cerebellum. The average correlation between neural activation time course and task timings of foot movements was 0.36 and thus substantially lower than for hand movements and tongue.

Visual cues

The spatial map of the most task-relevant mode for visual cues in task blocks comprised of the primary visual cortex. The corresponding neural activation time course peaked approximately when visual cues were presented to the subject. The average correlation between neural activation time course and task timings was 0.27.

All task blocks

The spatial map of the most task-relevant mode for all task blocks comprised of operculum and supplementary motor area. The average correlation between neural activation time course and task timings was 0.32.

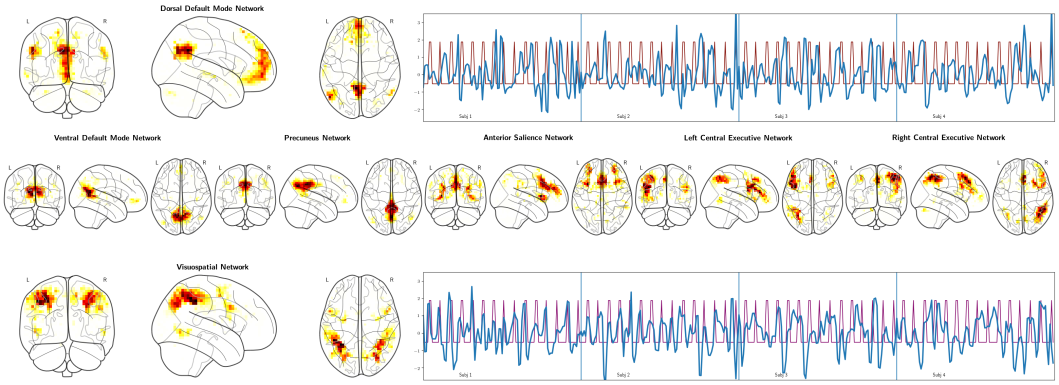

Figure 7.8: The first and third row depict spatial map and neural activation time course of modes that resembled the dorsal dDMN and VSN, respectively. The neural activation time course (blue line) is superimposed on task timings of the visual motor task cues (red line). The median correlation between visual cue task timings and estimated neural activation time course is −0.23 and 0.28, for dDMN and VSN, respectively (averaged over all sessions and subjects). The second row depicts vDMN, PN, ANS, LCEN, RCEN. The corresponding median correlations for these modes are −0.02, −0.07, 0.06, 0.08 and 0.24, respectively.

Resting-state modes

In addition to modes mapping the eloquent cortex, HMF also produced several modes including dorsal and ventral default mode network (dDMN and vDMN), precuneus network (PREC), left and right central executive network (LCEN and RCEN), visuospatial network (VSN), and anterior salience network (ASN) that resembled commonly found resting-state networks. The dDMN presented with an antagonistic behaviour to visual cues as, for example, depicted in Figure 7.8 for task run 1 of subject 1 to 4 in the first session of the MSC motor task.

The first row depicts the spatial map and neural activation time course (blue line) superimposed on corresponding task timings of visual cues (red line) for the dDMN. The dDMN showed the strongest negative correlation (-0.23) to visual cue task timings. The second row depicts the spatial maps of vDMN, PREC, ASN, LCEN, and RCEN. Their corresponding average correlation with visual cue task timings (median and MAD of correlations) is depicted in Table 7.1. The third row depicts the spatial map and neural activation time courses of the VSN superimposed on the task timings of visual cues in subject 1-4. The VSN showed the strongest positive correlation (0.28) to visual cue task timings. Table 7.1 shows the average correlation between neural activation time course and individual task timings for each of these modes. Correlations with absolute value higher or equal than 0.2 are highlighted in bold. Overall, default mode networks presented with a negative correlation to timings of the motor task, most pronounced in correlation between neural activation time course of the dDMN and motor task cue timings (-0.2). The opposite trend was observed in the RCEN and VSN, which showed an on average positive correlation (> 0.2) between neural activation time course and corresponding task timings. Figure 7.9 depicts the average of pairwise correlation between neural activation time courses of the 7 resting-state modes. Most strikingly, there is an opposing behaviour between the default mode networks (dDMN, vDMN, PREC) and ASN, LCEN, RCEN and VSN.

Stimuli Type	dDMN	vDMN	PREC	ASN	LCEN	RCEN	VSN
Foot	0.07	-0.03	-0.03	0.05	0.0	-0.02	-0.03
Hand	-0.12	-0.08	-0.06	0.03	0.05	-0.0	0.17
Left Foot	0.03	0.03	-0.01	-0.01	-0.04	-0.04	-0.04
Right Foot	0.03	-0.05	-0.04	0.02	-0.01	0.02	0.02
Left Hand	-0.05	-0.04	-0.06	-0.04	-0.0	0.01	0.09
Right Hand	-0.09	-0.05	-0.04	0.05	0.08	0.03	0.13
Tongue	-0.12	-0.06	0.03	0.19	0.08	0.19	0.14
Block	-0.15	-0.14	-0.1	0.07	0.09	0.1	0.18
Motor Cue	**-0.23**	-0.05	-0.12	0.11	0.04	**0.2**	**0.26**
All Cue	**-0.23**	-0.02	-0.07	0.06	0.08	**0.24**	**0.28**
Rest Cue	0.01	0.08	0.02	-0.02	0.09	0.06	0.03

Table 7.1: The median correlation between the neural activation time course and corresponding task timings of seven resting-state modes in the MSC motor task (among 40 estimated modes). Values over 0.2 are highlighted in bold.

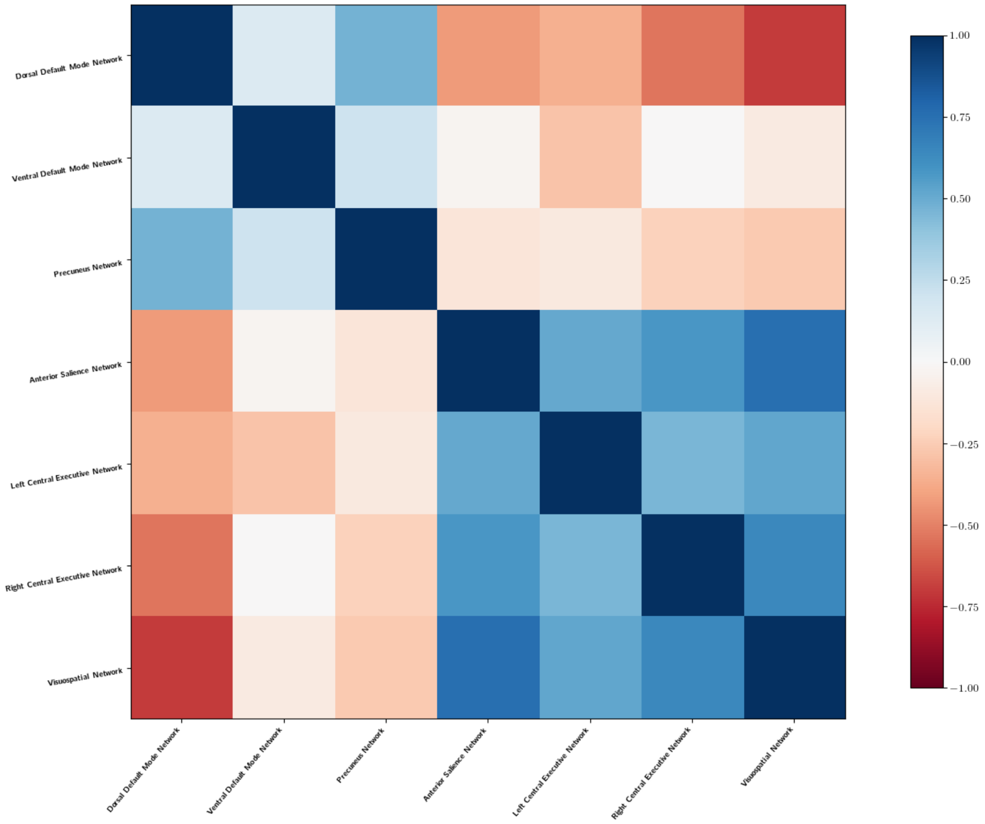

Figure 7.9: Average of the functional connectivity matrix (average of pairwise correlation between neural activation time courses) between dDMN, vDMN, PN, ASN, LCEN, RCEN and VSN in the MSC motor task runs.

7.4.2.2 Spatial and verbal discrimination task

Spatial discrimination task

Three groups of task timings were analysed in the spatial discrimination task: timings for spatial coherent stimuli, timings for incoherent stimuli, and timings for both stimuli combined. There was no coherent stimuli or incoherent stimuli specific mode obtained with canonical HMF. Instead, the most task-related mode was the same for all three groupings but showed the strongest correlation to task timings of both stimuli types combined. The spatial map of the most task-related mode comprised of the visual cortex. The average correlation between neural activation time course and task timings was 0.42. The spatial map and neural activation time course of the corresponding mode of session one is depicted in Figure 7.10 (first row). The estimated neural activation time course (blue line) is superimposed on the

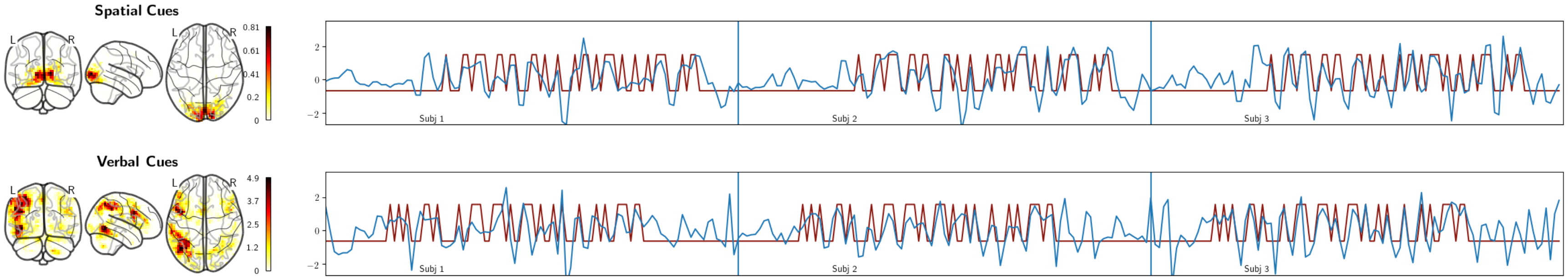

Figure 7.10: The task timings of coherent and incoherent stimuli combined (dark red line) for the spatial discrimination task (first row) and noun and verbal stimuli for the verbal discrimination task (second row). The spatial map and neural activation time course estimate (blue line) of the most task-relevant mode for either spatial disc. (first row) and verbal disc. (second row) task obtained with canonical HMF.

task timings (dark red) of combined spatial coherent and incoherent stimuli for the scans of the first three subjects in session one.

Verbal discrimination task

Timings for the verb stimuli, timings for the noun task stimuli, and timings for verb and noun stimuli combined were analysed in the verbal discrimination task. Similar to spatial discrimination task, the most task-related mode was the same for all three task groupings and showed the strongest correlation to the task timings of verb and noun stimuli combined. The spatial map of the most task-related mode comprised of brain areas that are involved in lexical decision making including para-cingulate gyrus, pre-central gyrus, middle frontal and inferior gyrus, lateral occipital cortex, angular and supra-marginal gyrus and small areas such as Broca's area 44 and 45 [Heim et al., 2005]. The average correlation between neural activation time course and task timings was 0.26. The spatial map and neural activation time course of the corresponding mode of session one is depicted in Figure 7.10 (second row). The estimated neural activation time course (blue line) is superimposed on the task timings (dark red) of combined verbal and noun stimuli for the scans of the first three subjects in session one.

7.4.2.3 Incidental memory tasks

The incidental memory tasks comprised of the most densely packed visual stimuli compared to the motor, spatial and verbal discrimination task.

The most task-relevant mode for abstract word stimuli task timings, concrete word stimuli task timings, and task timings for abstract and concrete word stimuli combined were examined in the incidental memory word task.

The most task-relevant mode for male stimuli task timings, female task timings, and task timings for both stimuli combined were examined in the incidental memory face task.

Lastly, the most task-relevant mode for indoor stimuli task timings, outdoor stimuli task timings, and task timings of both stimuli combined were examined in the incidental memory scene task.

Similar to spatial and verbal discrimination task, the most task-relevant mode found by canonical HMF in each of the three incidental memory tasks is a mode that showed the greatest correlation to both stimuli combined. The average correlation between neural activation time course and task timings of combined stimuli in incidental memory word, faces and scenes task was 0.38, 0.41 and 0.45, respectively. Figure 7.11 depicts spatial map and neural activation time course of the mode for the first three subject scans of session one in incidental memory words, faces and scenes task. The spatial map of these modes comprised of areas in the visual cortex.

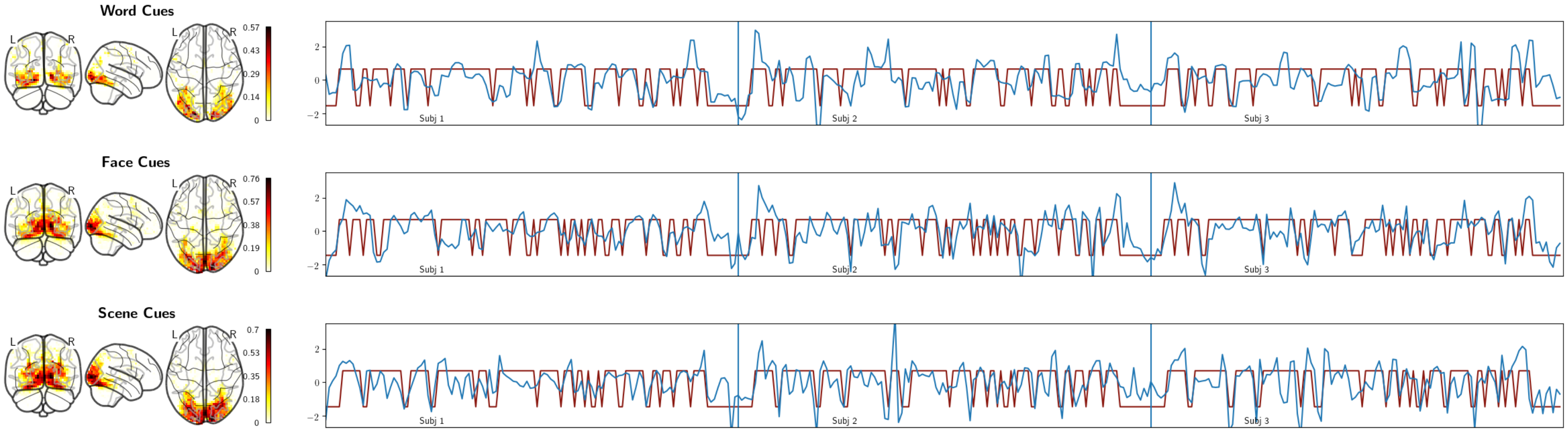

Figure 7.11: All task stimuli combined for either word (first row), face (second row) and scene incidental memory task (third row). Spatial map and neural activation time course estimate of the most task-relevant mode for the respective incidental memory task obtained with canonical HMF.

7.4.2.4 Brainomics task

In order to demonstrate that the proposed approach can recover neural activation in tasks with short but also sparse stimulus presentation with the same hyper-parameter setting, HMF was also applied to the Brainomics data. The neural activation times courses of the obtained modes followed visual, auditory, motor, and higher cognitive function processing stimulus timings. Figure 7.12 depicts the spatial map and neural activation time courses of the obtained modes among the individual stimulus timings. Also for this cohort, neural activation time courses followed task timings of individual stimulus types. However, there was no exact one to one relationship in all modes between neural activation time course and task stimuli. One mode activated only for auditory stimuli (row 1) whereas the mode with the highest correlation to video stimuli (row 3) activated also for horizontal and vertical checkerboard stimuli (rows 2 and 4) as indicated by the dashed red arrows.

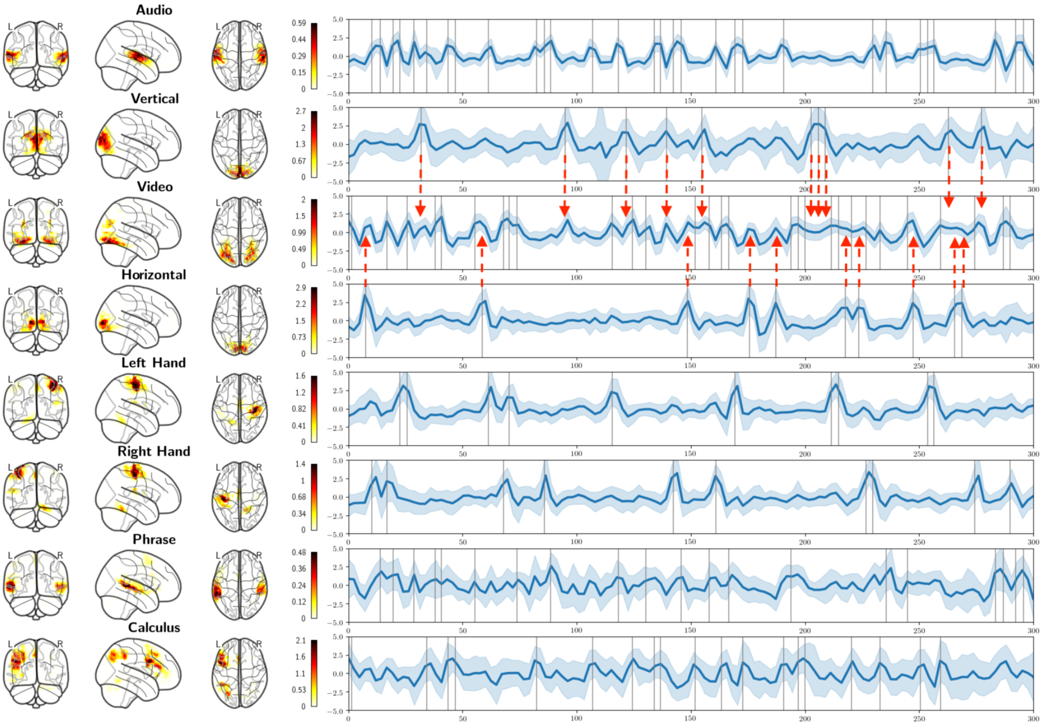

Figure 7.12: The mean (dark blue line) and standard deviation (light blue interval) of 90 Brainomics subjects of HMF modes whose neural activation time course correlates most with either left button click, right button click, auditory, visual, horizontal checkerboard, vertical checkerboard, calculus, and sentence stimuli (grey vertical lines). Modes for vertical and horizontal checkerboard stimuli co-activate with the mode for video processing (red dashed errors).

The neural activation time courses of the mode associated with auditory stimuli had the lowest standard deviation across subjects followed by modes for video, horizontal checkerboard, left and right hand (rows 5 and 6), and vertical checkerboard stimuli. The HMF modes associated with all phrases or calculus stimuli (rows 7 and 8) showed the highest standard deviation in neural activation time courses across subjects. Figure 7.13 depicts several computed contrasts for the Brainomics data. The following compares the spatial maps of obtained maps with canonical HMF and these contrast maps.

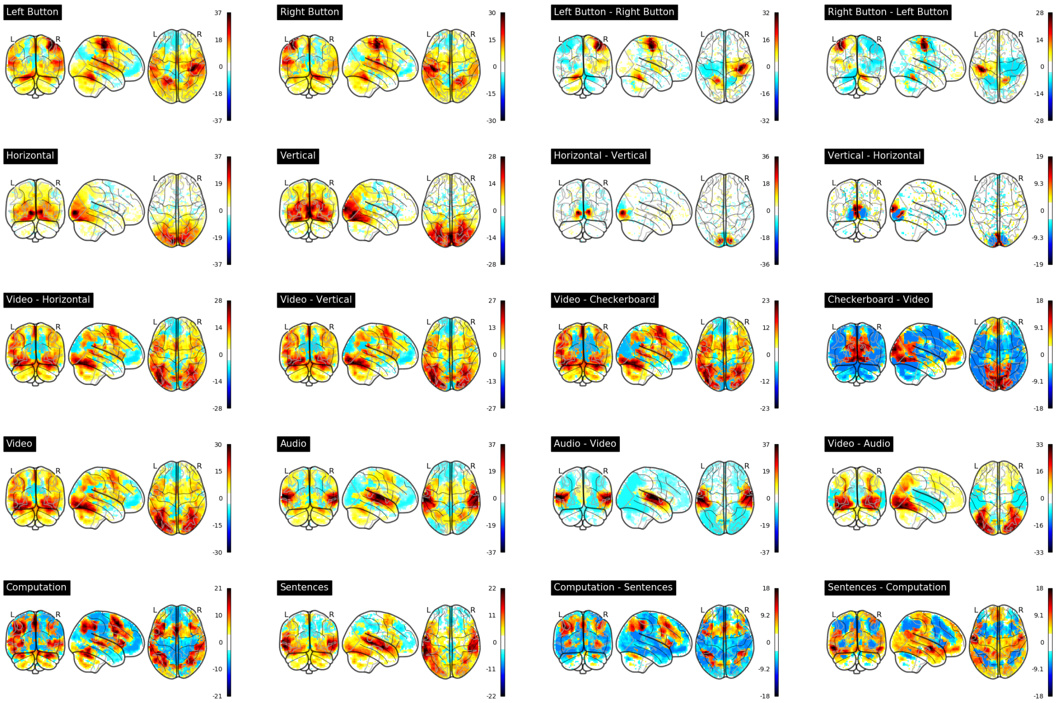

Figure 7.13: The spatial maps (z-values) of 20 computed contrasts obtained with a second level GLM analysis on the Brainomics task data.

Audio

The spatial map of the mode with the highest correlation (0.27) between neural activation time course and task timings of audio stimuli overlapped to a large extent with the primary auditory cortex. The map showed strong spatial similarity to the contrast Audio-Video.

Checkerboard

The spatial map of the mode with the highest correlation (0.22) between neural activation time course and task timings of vertical stimuli showed a strong correspondence to contrast Vertical-Horizontal. Accordingly, the mode with the strongest correlation (0.17) between neural activation time course and horizontal task timings showed high spatial similarity to contrast Horizontal-Vertical. The spatial maps of both of these modes overlap with the areas for horizontal or vertical pattern recognition in the visual cortex.

Video

The spatial map of the mode with the highest correlation (0.18) between neural activation time course and task timings of all video stimuli showed an overlap with parts of the visual cortex different to the spatial maps found for vertical and horizontal stimulus patterns. However, this mode also activates for horizontal and vertical stimuli as seen in the neural activation time course depicted in Figure 7.12 (red arrows).

Button Press

The spatial maps for right and left button press stimuli comprised of areas in the primary motor cortex, primary somatosensory cortex, and premotor cortex. These spatial maps showed a high similarity to contrast Right Button-Left Button and Left Button- Right Button. The average correlation between neural activation time course and button press task stimuli was 0.28 for right button press and 0.25 for left button press.

Phrases

The spatial map of the mode with the highest correlation (0.12) between neural activation time course and phrase task stimuli comprised of areas such as BA45, Middle Temporal Gyrus, Supramarginal Gyrus, and Superior Temporal Gyrus posterior division.

Calculation

The spatial map of the mode with the highest correlation (0.15) between neural activation time course and phrase task stimuli comprised of areas such as Superior Parietal Lobule, Supramarginal Gyrus, and Angular Gyrus. The modes for phrases and calculation task stimuli showed the least correspondence between neural activation time course and task timings compared to modes mapping visual, auditory or sensory-motor function.

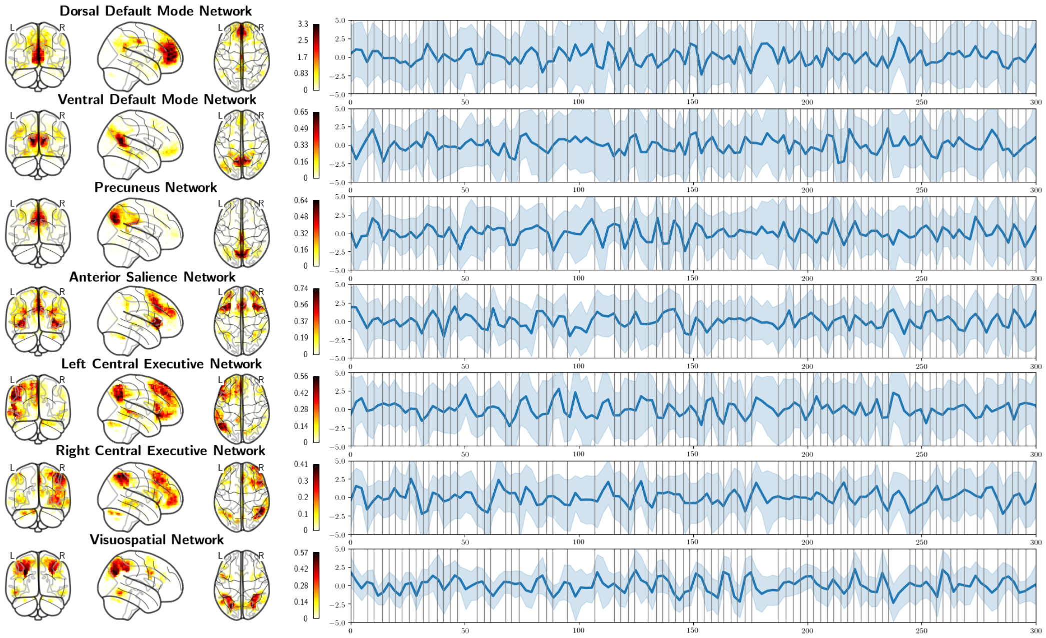

Figure 7.14: The spatial map and corresponding mean and standard deviation time course for the dDMN, vDMN, PREC, ASN, LCEN, RCEN, and VSN mode.

Resting-state modes

The seven resting-state modes reported for the MSC motor task were also found among modes in the Brainomics task. The spatial maps, mean and standard deviation of neural activation time courses of dDMN, vDMN, PREC, LCEN, RCEN, ASN and VSN are depicted Figure 7.14.

Stimuli Type	dDMN	vDMN	PREC	LCEN	RCEN	ASN	VSN
Audio	-0.07	-0.07	-0.09	**0.27**	-0.12	-0.01	-0.14
Video	**-0.27**	**-0.27**	-0.08	**0.21**	-0.18	-0.06	0.15
Vertical	0.02	0.02	0.06	-0.14	0.05	-0.03	0.01
Horizontal	0.01	0.07	0.16	-0.07	-0.01	-0.08	-0.02
Left Hand	-0.19	-0.09	-0.09	0.17	-0.08	-0.06	-0.06
Right Hand	-0.1	0.01	0.1	0.13	-0.1	-0.12	-0.08
Phrase	0.06	0.01	**-0.23**	-0.02	0.08	-0.07	-0.19
Calculus	**-0.22**	**-0.32**	0.0	**0.34**	**-0.28**	0.13	**0.27**

Table 7.2: The median correlation between the neural activation time course and corresponding task timings of seven resting-state modes in the Brainomics data (among 40 estimated modes). Values over 0.2 are highlighted in bold.

Table 7.2 shows the pair-wise correlation between mean average neural activation time course of each resting-state mode to the task timings of the Brainomics task. For the default mode networks, there was no consistent negative correlation between the neural activation time course and task timings. The neural activation time course of the dDMN and vDMN had a negative correlation with Video (0.27 in both) and Calculus task timings (-0.22 and -0.32, respectively). The neural activation time course of the PREC presented with a negative correlation (-0.23) to the Phrase task timings.

Similarly, the modes for LCEN, RCEN, ASN, and VSN networks presented with no consistent negative or positive correlation pattern between neural activation time courses and task timings. For example, the LCEN showed a negative correlation of -0.27 to vertical stimuli but positive correlations 0.3 and 0.32 for Audio stimuli and Calculus stimuli, respectively. However, the time-dependent standard deviation of neural activation time courses of these modes is much larger than for modes of visual, auditory or sensory-motor function.

7.4.2.5 Subject-specific HMF outperforms canonical HMF in neural activation estimation

In order to determine if using subject-specific HRFs instead of the canonical HRF in HMF would result in modes whose neural activation time courses align better with task timings, subject-specific HRFs were obtained with GLM analysis and replaced the canonical HRF in the Toeplitz matrix of HMF. The obtained HRF mean and standard deviation of all 10 subjects of the MSC data are depicted in Figure 7.15. Figure 7.16 depicts the difference in the neural activation of the mode estimated with canonical and subject-specific HMF in the first three subjects of the MSC motor task in session one. Both modes correspond to areas of the visual cortex activated by visual cues presented during the motor task. As highlighted in the increased view for subject one, the neural activation time course (light blue line) obtained by subject-specific HMF had a better alignment to task timings (red dashed

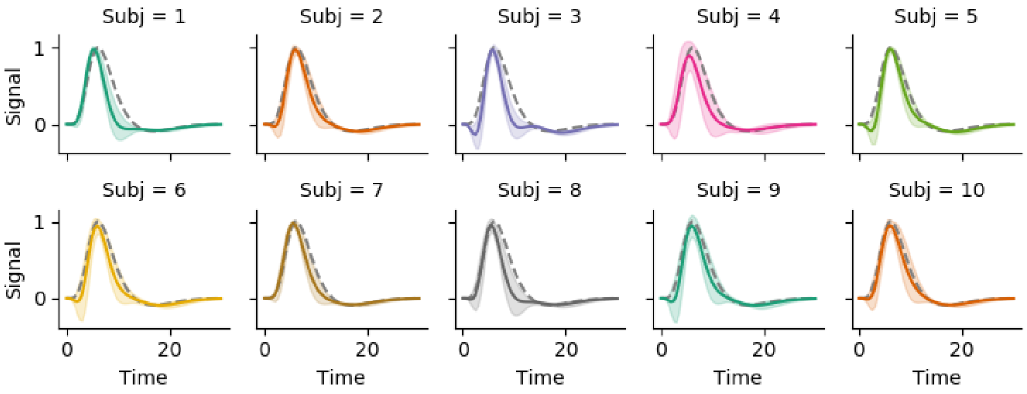

Figure 7.15: The average HRF (mean and standard deviation) for subject 1-10 of the MSC cohort estimated from the incidental memory tasks.

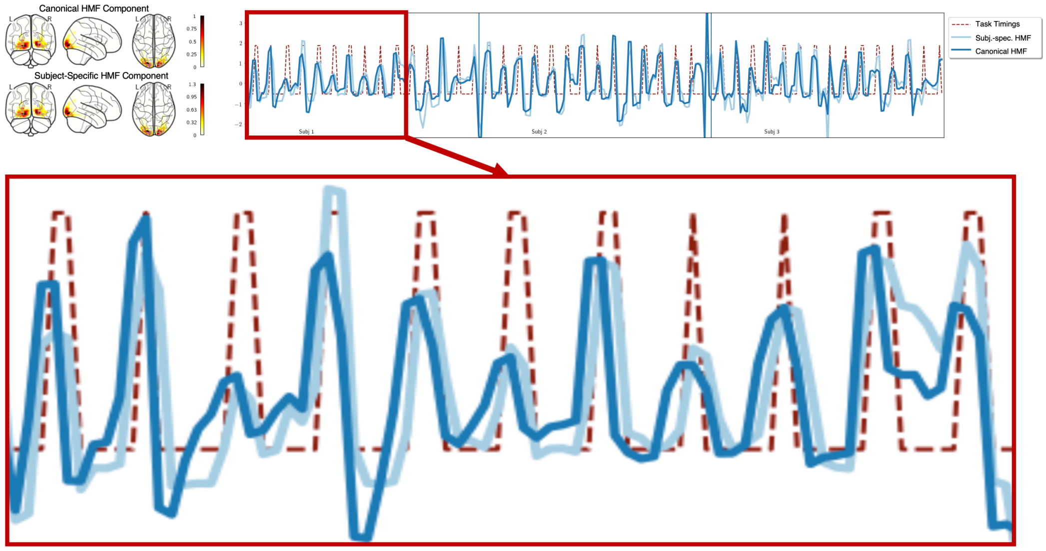

Figure 7.16: The neural activation time courses and spatial maps of the most correlated canonical and subject-specific HMF mode in motor task session one. The enlarged view of neural activation time courses of subject 1 show a small delay between the neural activation time course of canonical and subject-specific HMF mode. The canonical HRF takes a longer time to peak than the subject-specific HRF in subject 1 depicted in Figure 7.15. The neural activation time course of the corresponding canonical HMF mode therefore peaks earlier than the neural activation time course of the subject-specific HMF mode. Ultimately, modes using the subject-specific HRF resulted in a better alignment with task timings (red dashed line) compared to modes using the canonical HRF.

line) than the neural activation time course (dark blue line) obtained by canonical HMF. Table 7.3 shows median and median absolute deviation (MAD) of the most task-relevant mode for each stimulus type in MSC tasks and Brainomics task. Subject-specific HMF achieved a greater median correlation to the original task timing than canonical HMF in all MSC tasks, and a greater median correlation in six of eight task timings of the Brainomics task. The superscript † indicates significantly better ($p\text{-}value < 0.05$) as obtained with a non-parametric Wilcoxon rank test between paired samples of the most task-relevant mode of subject-specific HMF and canonical HMF. Subject-specific HMF was statistically better than canonical HMF in ten out nineteen of the examined task timings for both MSC and Brainomics tasks, while for nine task timings there was no statistical difference between the two approaches.

7.4.2.6 ICA produced more noisy mode estimates than HMF

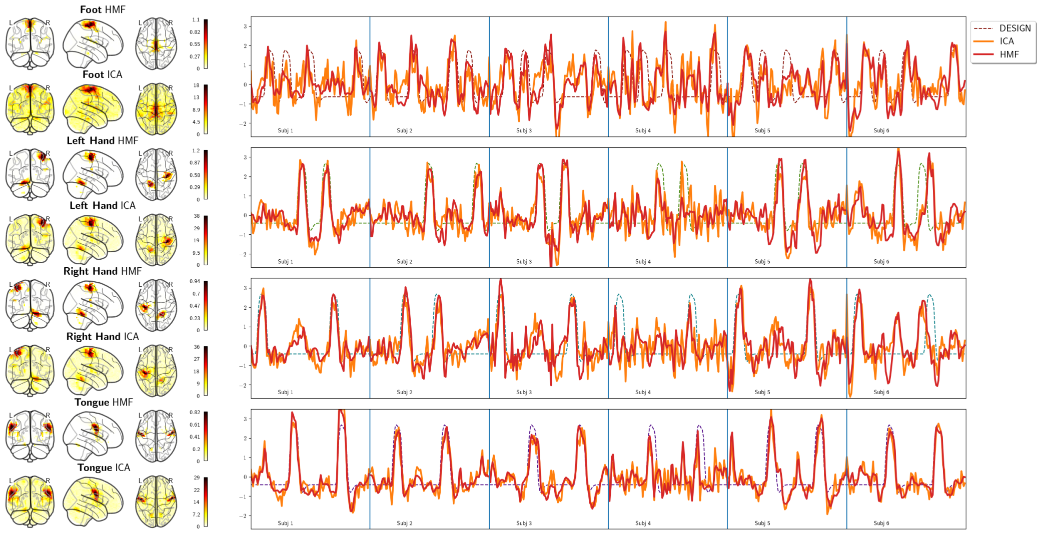

Figure 7.17: The juxtaposition of spatial maps and BOLD time courses of ICs and canonical HMF modes, which were the most task-relevant for foot, left and right hand, and tongue movements. The task design corresponds to the individual task timings and BOLD time courses correspond to neural activation time courses in Figure 7.6.

Figure 7.17 shows spatial maps and BOLD time courses of modes found by canonical HMF and sICA for the first session of the MSC motor task. The confusion between right and left hand movement seen in the neural activation time course of subject six in Figure 7.6 was also evident in the BOLD time course produced by canonical HMF and sICA as depicted in Figure 7.17. As the figure shows, the modes found by sICA and canonical HMF had highly similar spatial maps and BOLD time courses, but modes produced by canonical HMF were spatially and temporally smoother than their sICA counterparts. The same holds also for the other MSC and Brainomics tasks as seen in the median correlations summarised in Table 7.4 and 7.5. Table 7.4 summarises median and MAD of correlation between task design and

	Motor						Incidental Memory			Glass	
	Foot	Left Hand	Right Hand	Tongue	Block	Motor Cue	Faces	Scenes	Words	Spatial	Verbal
Canonical HMF	0.36±0.18	0.63±0.14	0.65±0.16	0.68±0.1	0.32±0.13	0.27±0.1	0.41±0.11	0.45±0.08	0.38±0.13	0.42±0.1	0.26±0.1
Subject-specific HMF	**0.48±0.19**†	**0.64±0.13**	**0.67±0.16**†	**0.7±0.08**†	**0.4±0.16**†	**0.31±0.13**	**0.46±0.13**	**0.51±0.07**†	**0.43±0.12**†	**0.5±0.09**†	**0.27±0.11**

	Brainomics							
	Audio	Video	Vertical	Horizontal	Left Hand	Right Hand	Phrase	Calculus
Canonical HMF	0.23±0.07	0.18±0.06	**0.22±0.08**	0.17±0.08	0.25±0.09	0.28±0.1	0.12±0.06	**0.15±0.08**†
Subject-specific HMF	**0.27±0.06**†	**0.21±0.07**†	0.21±0.08	**0.18±0.07**†	**0.29±0.09**	**0.3±0.08**	**0.13±0.07**	0.14±0.08

Table 7.3: Median ± MAD of the correlation between task timings and neural activation estimates for the most task-relevant mode for either canonical or subject-specific HMF. The best approach with respect to the median correlation is highlighted with bold font, the superscript † represents significantly greater correlation (*p-value*< 0.05).

		Motor						Incidental Memory			Glass	
		Foot	Left Hand	Right Hand	Tongue	Block	Cues	Faces	Scenes	Words	Spatial	Verbal
BOLD	Canonical HMF	**0.51±0.21**†	**0.75±0.10**†	**0.78±0.14**†	**0.78±0.08**†	**0.44±0.16**†	**0.34±0.12**	**0.52±0.11**	0.54±0.09	**0.49±0.14**†	**0.46±0.12**†	**0.32±0.13**
	sICA	0.33±0.17	0.69±0.10	0.68±0.16	0.73±0.10	0.38±0.16	0.33±0.12	0.51±0.07	**0.57±0.06**	0.44±0.10	0.38±0.11	0.31±0.13

		Brainomics							
		Audio	Video	Vertical	Horizontal	Left Hand	Right Hand	Phrase	Calculus
BOLD	Canonical HMF	**0.59±0.08**	**0.47±0.12**	**0.35±0.10**	**0.41±0.15**	0.41±0.20	0.38±0.09	**0.36±0.10**	**0.31±0.13**
	sICA	0.58±0.08	0.40±0.11	0.32±0.09	0.37±0.11	**0.49±0.14**	**0.41±0.11**	0.33±0.11	0.30±0.15

Table 7.4: Median ± MAD of canonical HMF and sICA of the correlation between task timings convolved with canonical HRF and BOLD time course estimates. The best method with respect to the median correlation is highlighted with bold font, the superscript † represents significantly greater correlation (p-$value < 0.05$).

BOLD time course of the most task-relevant mode for MSC and Brainomics task stimuli. A greater correlation for modes obtained by canonical HMF than modes by sICA was observed in seventeen out of nineteen task designs. Regarding the spatial reproducibility, canonical HMF obtained higher values compared to sICA in all nineteen MSC task-related spatial maps as shown in Table 7.5. HMF produced modes characterised by statistically higher median values of spatial reproducibility compared to sICA in eight out of eleven tasks.

7.5 Discussion

This paper proposed a novel matrix factorisation technique called HMF, which decomposes fMRI data into modes. Each mode is composed of a neural activation time course, a BOLD time course and a spatial map. Task timings were not provided to HMF but were retrospectively matched with neural activation time courses of estimated modes to evaluate how well these task timings were recovered.

For stimuli causing increased neural activation in the visual, auditory and motor areas of the eloquent cortex, HMF obtained modes whose neural activation time courses followed corresponding task timings with high correlation.

For the MSC motor task, HMF produced modes whose neural activation time courses corresponded with the experiment block design. Moreover, HMF also produced modes whose neural activation time courses followed sparse event-type task timings in MSC incidental memory, MSC spatial and verbal discrimination, and in the Brainomics task.

To further improve the correlation between neural activation time course and task timings in these modes, subject-specific HRF estimates were obtained by means of GLM analysis and used within HMF estimation. The obtained subject-specific HMF modes showed a statistically significant increase in correlation between neural activation estimates and task timings when compared to canonical HMF.

HMF tries to bridge the gap between hypothesis and data-driven analysis techniques in fMRI. The fMRI task experiment relies on two basic assumptions. Firstly, a task stimuli of certain duration causes an equally long period of increased neural activation in an on/off manner. Secondly, the translation of neural activation increase into BOLD response can be approximated by a haemodynamic forward model based on linear filter theory. Similarly to GLM analysis, HMF relies on both of these assumptions but, since it does not need task timings of the experiment to reveal involved areas in brain processing, it can be applied to a much wider range of tasks where these two assumptions might not hold, such as in intrinsic brain activity.

Moreover, HMF can reveal individual task scans where subjects did not comply with task instruction. This is a strong advantage over GLM analysis because unexpected subject behaviour will lead to the derivation of wrong spatial activation maps. Tools such as HMF are

		Motor						**Incidental Memory**			**Glass**	
		Foot	Left Hand	Right Hand	Tongue	Block	Cues	Faces	Scenes	Words	Spatial	Verbal
Spatial Repr.	Canonical HMF	**0.92±0.05**†	**0.95±0.07**†	**0.95±0.17**	**0.97±0.01**†	**0.81±0.17**†	**0.89±0.12**	**0.91±0.09**†	**0.94±0.03**†	**0.90±0.22**†	**0.92±0.12**†	**0.86±0.12**
	sICA	0.65±0.13	0.89±0.06	0.87±0.22	0.90±0.09	0.58±0.2	0.79±0.19	0.81±0.02	0.84±0.06	0.78±0.04	0.82±0.02	0.79±0.06

Table 7.5: Median ± MAD of the reproducibility of the spatial maps obtained by canonical HMF and sICA. The best approach is in bold, the superscript † represents statistically significant better/worse results when compared to sICA (*p-value*< 0.05).

therefore needed to retrospectively check task participation. For example, in circumstances in which task fMRI is currently in use for surgery planning [Karahanoğlu et al., 2013b, Lopes et al., 2012], or in task experiments for newborns, which cannot be asked about their task performance or experienced intensity of a presented stimulus.

HMF is therefore proposed as a validation tool that enables reconstruction of task timings in fMRI task experiments. As shown in the experiments, inferred neural activation time courses matched task timings of foot, hand and tongue movements as well as visual cues in the MSC motor task. Accordingly, inferred neural activation time courses matched sparse task timings of auditory, video, horizontal and vertical checkerboard, and hand movements in the Brainomics task.

Furthermore, HMF provided insights of neural activation in task-free networks. For example, the dDMN was found to deactivate during visual stimuli presentation in the MSC motor task. HMF shares this ability with other BSS techniques, such as sICA, proposed to study brain networks in which ‘activation is difficult to predict‘ [McKeown et al., 1998]. sICA [Beckmann and Smith, 2004] became one of the most prominent of such tools for analysing task-unrelated brain networks in both task and resting-state fMRI experiments. Nonetheless, one of the problems of sICA is that it does not take into account the order of time points and spatial relationships of adjacent voxels. On the contrary, HMF leverages such intrinsic topological properties by using TV in the estimation process of spatial maps and time courses. Although obtained ICs are characterised by high spatial and temporal similarity with HMF modes, HMF produced modes with higher correlation with task design and greater spatial reproducibility when compared to sICA due to explicit spatial and temporal regularisation.

Studies have shown intra-subject HRF variability to be lower than inter-subject variability [Aguirre et al., 1998, Handwerker et al., 2012]. Therefore, subject-specific HRFs were chosen as an extension of HMF in this work, which resulted in a better alignment with task timings.

Other studies have hypothesised that the entire brain might respond to an extrinsic task by translating task stimulus into BOLD signal with varying HRFs across the brain [Gonzalez-Castillo et al., 2012]. However, although the evidence for this assumption is low given the reported HRF magnitudes in Gonzalez-Castillo et al. [2012], varying HRFs across the cortex has not be conducted in this work but could be explored by having an individual Toeplitz matrix for each HMF mode.

Another limitation of the proposed approach is that subject-specific HRFs used with HMF were predetermined with GLM analysis. The gradient of the cost function was derived with respect to neural activation time courses $\mathbf{N}$. However, the gradient can also be derived with respect to Toeplitz matrix $\mathbf{F}$. Constraining neural activation to piece-wise constant time courses such as proposed in Karahanoğlu et al. [2013a] or Cherkaoui et al. [2019] might enable an alternating or simultaneous derivation of neural activation time courses and haemodynamic filters.

Furthermore, hyper-parameters of HMF were optimised for an entire set of different task settings. Performance on individual tasks is expected to improve by task-specific hyper-parameter tuning. The comparison between HMF and ICA was limited to real imaging data. Therefore, a comprehensive comparison of the performance of HMF and ICA on commonly used fMRI simulation toolboxes [Welvaert and Rosseel, 2014, Erhardt et al., 2012] will be necessary in future work.

The proposed HMF approach is currently limited to spatial group maps. Nevertheless, many approaches have been proposed that include subject-specific spatial estimates [Varoquaux et al., 2011, Harrison et al., 2015, 2019]. Therefore, a possible future extension of the proposed HMF model could include subject-specific instead of spatial group maps.

Finally, task experiments that recruit higher cognitive function might evoke neural activation that strongly deviates from the simple assumptions of the haemodynamic forward model. Thus, one of the limitations of the proposed HMF model, shared with GLM analysis, is the assumption that the haemodynamic forward model holds for the entire cortex. However, the question to what degree higher cognitive function behaves in accordance with the haemodynamic forward model is beyond the scope of this paper and remains a challenging problem for future research.

7.6 Conclusion

A novel BSS technique called HMF has been proposed to obtain mode configurations of the brain while engaged in task processing. HMF recovered modes whose neural activation time course correlated well with corresponding stimulus timings in each task as shown in retrospective analysis in this work. Using the same haemodynamic forward model, HMF also recovered modes whose neural activation time courses reflected ongoing intrinsic neural activation during task processing. fMRI research in the last decades has either focused on estimating the spatial extent of areas involved in task processing with GLM analysis or studied intrinsic brain activity of brain networks obtained by BSS techniques such as sICA. Recent years have shown this division is closing and a novel class of techniques has emerged modelling fMRI data in its entirety by combing analysis of networks engaged in task processing and networks of ongoing intrinsic brain activity. The proposed HMF model is a step towards unification of resting-state and task fMRI analysis.

Chapter 8

Conclusions and Perspectives

8.1 Summary of contributions

This thesis presented novel approaches for fMRI pre-processing and analysis of two challenging resting-state fMRI cohorts of pathological subjects. In addition, these approaches were evaluated on publicly available fMRI cohorts that comprised of task and resting-state experiments in healthy subjects.

8.1.1 The EPICure cohort

The EPICure cohort comprised of resting-state fMRI data of approximately 10 minutes of term- and preterm-born adults. The fMRI scans were acquired with a low TR of 3 seconds. Therefore, physiological motion artefacts were caused by aliasing effects of the heart rate contributing to these fMRI time courses. The heart rate was recorded during resting-state scanning with a pulse plethysmography. However, these physiological recordings were impacted by body motion and were substantially corrupted in several time periods. A specific feature of the EPICure cohort was that pre-term born adults coherently presented with dilated ventricles compared to their term-born peers.

Extracting robust heart rate variability estimates with Multi-Task Gaussian Processes

The problem of the corrupted physiological recordings was addressed in Chapter 3 by training a MTGP model that jointly learned the correlation between the heart rate obtained from the pulse plethysmography recording and the heart rate obtained from an average signal extracted in a slice-wise fashion from the fMRI data. The MTGP model successfully produced heart rate estimates for the corrupted time periods of the pulse plethysmography recordings.

Classification of ICs using heart rate variability

The obtained heart rate variability estimates by the MTGP model were used in the CAMR-SVM pre-processing pipeline in Chapter 4. Firstly, CAMR applied spatial ICA to individual fMRI scans to find physiological motion artefacts among obtained ICs in the MPI7T cohort using physiological recordings. An IC was labelled as physiological motion if its SWS explained a significant amount of variance in the physiological recording. These labelled ICs were subsequently used for training the CAMR-SVM model on temporal characteristics of time courses of such ICs.

CAMR and CAMR-SVM resulted in a substantial reduction of cardiac aliasing frequencies in fMRI time courses in the EPICure and MPI cohort.

Functional mapping and connectivity in pre-term born adults

Chapter 5 showed how these pre-processed fMRI scans of the EPICure cohort were used to examine functional connectivity within and between individual brain areas in the pre-term born adult. This analysis established common resting-state networks in the extremely-preterm 19 year old brain and compared these to those present in a cohort of term-born peers. A small cluster with greater functional connectivity in term- than in preterm-born adults was obtained in the right anterior intra-parietal sulcus of the DAN but did not survive correction for multiple comparison.

In contrast, VN3 of the four obtained visual networks showed a significant larger *core strength* in term-born adults even after correction for multiple comparison. It is well known that preterm cohorts are more susceptible to visual impairment, and these results may represent a neuroimaging manifestation of this impairment. This is believed to be more than a retinal pathology and extend to the visual processing regions of the cortex. Future work will bridge the gap between network-based neuroimaging and objective functional impairment in this cohort by obtaining measurements in tasks assessing visual processing.

8.1.2 The YOAD cohort

The YOAD cohort comprised of subjects whose resting-state fMRI data only lasted for approximately 5 minutes. This presented a significant challenge for the computation of robust single subject spatial maps and their subsequent comparison across disease groups.

Ensemble averaging of matrix factorisations

The challenge of the short fMRI acquisition was addressed by the development of a novel image processing technique in Chapter 6 that used ensemble averaging of several matrix factorisations to obtain reproducible spatial map estimates in each individual. A comparison of these spatial maps between YOAD and healthy elderly controls resulted in differences in the precuneus cortex in the DMN. In addition, small differences were found in clusters of left and right hippocampus in the DMN with greater functional connectivity in healthy controls. The obtained group differences were compared to results obtained with ICA and DR. While results of both approaches spatially overlapped in the anatomical region of the precuneus cortex in the DMN, only the EMF approach was able to detect small but significant differences in left and right hippocampus.

8.1.3 MSC and Brainomics task experiment data

Reproducibility of fMRI analyses requires and will improve due to the vast open source data efforts, among them OpenNeuro[1], the Human Connectome Project[2] and Biobank [3] to name the most important.

The proposed approaches gained more credibility because the additional validation on publicly available data showed that these approaches also work for different task and acquisition types different to resting-state data of YOAD and EPICure cohort. Similar to how approaches presented in this thesis have profited from the MSC and Brainomics publicly available data, ongoing efforts will produce extraordinary insights of brain function in the coming years while also enabling research groups with small financial budgets to contribute to the field of neuroimaging analysis.

Haemodynamic matrix factorisation

The MSC and Brainomics cohort provided ideal task experiment data to evaluate the HMF approach presented in Chapter 7. The inclusion of a haemodynamic filter within the EMF model allowed for obtaining modes that consisted of spatial maps and neural activation time courses. The neural activation time courses of these modes matched with original task timings of the examined task experiments in both cohorts. The obtained modes showed that in some task experiment scans the participant confused the experiment instruction as for example depicted in the motor task experiment in Figure 8.1 in which subject 6 moved left hand instead of following the instruction to move the right hand.

The replacement of canonical HRF with a subject-specific HRF in the HMF model resulted in an improvement of the temporal alignment between neural activation time courses of modes and corresponding stimulus timings in MSC and Brainomics tasks.

Therefore, the HMF model will provide the fMRI community with an evaluation tool to falsify task experiment designs.

8.2 Directions for future research

In addition to these presented techniques, emerging developments in the fMRI community will derive new insights from fMRI imaging. These are acceleration of the fMRI image acquisition with multi-band imaging, the push towards fMRI-specific analysis techniques that leverage open source data and encourage methods sharing, and lastly, surface-based fMRI analysis which is superior to the still most commonly used voxel-based analysis.

---

[1] `https://openneuro.org/`

[2] `http://www.humanconnectomeproject.org`

[3] `https://www.ukbiobank.ac.uk/`

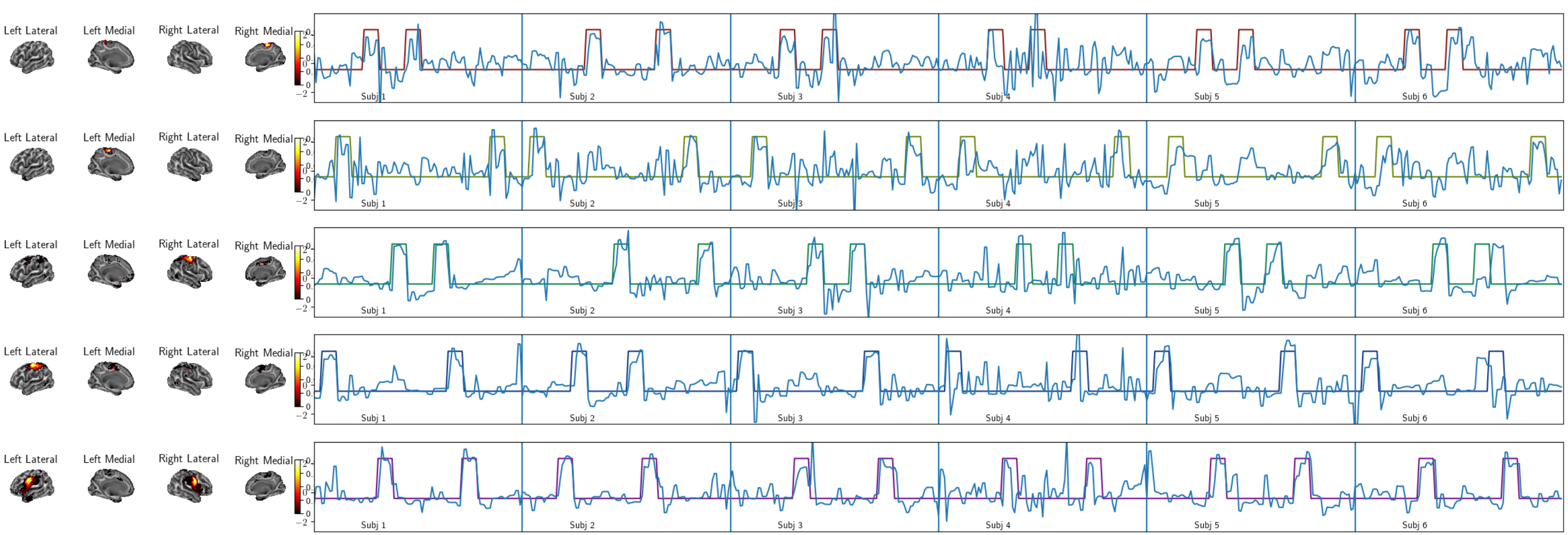

Figure 8.1: The cortical areas activated by execution of individual MSC motor tasks (as compared to the voxel-wise analysis presented in Chapter 7 Figure 7.6). Each row depicts task blocks of either foot, left hand, right hand or tongue movement (top to bottom). The neural activation time course of the mode with the highest correlation to a particular movement type is depicted as continuous blue line superimposed on individual task blocks.

Image acquisition

The prevalence of multi-band EPI [Moeller et al., 2010, Feinberg and Setsompop, 2013, Todd et al., 2016] will enable higher spatially resolved volumes as well as much faster volume sampling. The haemodynamic response has a temporal smoothness that lies in between 0.01 and 0.1Hz [Cordes et al., 2014], whereas average heart (1Hz) and respiration rate (0.3Hz) belong to higher frequency bands. In theory, a bandpass filter could thus be applied to remove unwanted frequency contributions. However, the fastest acquisition rate currently achieved in large cohort setups is 0.72s (HCP). It would require acquisition rates below 0.33s to fully capture the entire frequency spectrum of the heart rate (up to 1.5Hz were observed in physiological recordings of the EPICure cohort). Nevertheless, the rapid advances in fMRI acquisition techniques will render physiological noise models redundant in the future. In addition to the reduced acquisition time, field strengths higher than 3T will allow better resolution, improve sensitivity and specificity, and result in the dissemination of functional activations from individual cortical layers [Hendriks et al., 2020, Huber et al., 2020, Finn et al., 2019].

Image analysis

Furthermore, this work added to the vast model zoo of hypothesis- and data-driven model approaches for the study of functional connectivity of the human brain.

The beginning of fMRI experiments focused on designing tasks for the localisation of brain function with hypothesis-driven models [Poldrack, 2012, Rosen and Savoy, 2012]. The most prominent and still the most used among them is the GLM. A good task experiment puts the brain in a controlled state. Areas engaged in task processing are directly obtained with GLM analysis and can be compared among subjects with statistical testing. In contrast, data-driven models such as spatial ICA require the computation of a set of shared features (brain networks) prior to comparison of subject-specific spatial maps.

The disadvantage of the GLM and the spatial ICA approach is that both do not leverage the inherent spatial correlation in fMRI data directly[4]. One could permute the order of individual voxels without an effect on the actual parameter estimates of GLM or ICA. In the case of ICA, one could even permute the temporal order of time points without an effect on subsequent spatial estimates. Therefore, ICA has come of age and more fMRI-specific models that incorporate intrinsic temporal and spatial characteristics, as for example by Harrison et al. [2015], will shape the field of fMRI in the future.

Surface-based analysis

fMRI analyses are still most commonly performed in 3D space. However, the majority of brain activity arises from cortical GM. Therefore, surface mapping and registration tech-

---

[4] The spatial correlation among time courses is only exploited via spatial smoothing but not by the analysis technique itself.

niques were developed that enable fMRI analysis on the cortical surface [Fischl, 2012, Saad and Reynolds, 2012, Tucholka et al., 2012, Tustison et al., 2014].

In surface-based fMRI analysis, a triangulated mesh is fitted to the cortical surface of the brain maintaining certain topological properties. As a result, a mapped spherical space can be obtained, which allows for inter-patient comparison while also increasing statistical power compared to traditional approaches in 3D voxel space.

Chapter 7 showed the application of HMF to several task experiments in 3D voxel space. HMF assumed that the observed fMRI signal in each voxel is only driven by the BOLD effect. Therefore, each of the obtained mode estimates is restricted by the assumed sparsity of neural activation and the smoothness-inducing haemodynamic filter.

However, modes whose spatial maps comprised of areas in WM and GM were also obtained with HMF. These spatial maps resembled commonly observed spatial fMRI noise patterns for which the haemodynamic forward model is not applicable.

This disadvantage is circumvented by applying HMF as surface-based analysis technique as depicted in Figure 8.1. However, future work is required to evaluate and compare the performance of HMF on the cortical surface to other techniques.

Prospective head motion correction

The most confounding effect for task or resting-state fMRI is head motion. Substantial alterations of group analysis results, especially in developmental cohorts [Power et al., 2012, Van Dijk et al., 2012], have been found and pose a caveat to drawing valid conclusions from conducted experiments.

Before considering any form of retrospective correction for head motion, it is of tremendous importance to instruct patients about the impact of even small head motion on scan quality. Behavioural compliance in combination with soft head constraint via padding is one of the best ways to achieve good quality fMRI data. However, certain patient populations exist, such as the examined YOAD cohort, in which low participant compliance is unavoidable. The often occurring subject motion in these cohorts during scanning causes signal dropout due to the spin history effect. A large variety of retrospective approaches have been proposed (see Murphy et al. [2013] or Esteban et al. [2019] for a review), which have been extensively discussed throughout this work.

However, prospective head motion correction approaches are a promising alternative although less prevalent due to availability of hardware and novel scanning sequences (see Maknojia et al. [2019] for a review).

In contrast to standard fMRI protocols that reconstruct images in a coordinate system static with respect to the MRI coordinate system, acquired images are reconstructed with respect to a reference coordinate system of the head. Therefore, these prospective approaches require additional technical equipment to track translations and rotations of the head, and a way of making spatial encoding during acquisition dependent on head position.

Several implementations have been proposed including MRI-sensitive fiducial markers to measure the described rigid body head motion. For example, van Niekerk et al. [2019] is achieving sub-millimetre accuracy with such fiducial MRI devices. However, the majority of the field is using optical sensors due to their high temporal resolution and intrinsic MRI compatibility. These approaches fix fiducial markers to the head, which are then tracked by optical cameras during scanning [Todd et al., 2015, Maclaren et al., 2018, 2012]. These approaches achieve tracking errors below 100 micrometer, which by far exceeds MRI-based approaches [Maknojia et al., 2019]. Although these approaches come with their own challenges including initial calibration time and errors, movement of the skin, or high cost for MRI-compatible camera equipment, they are a promising alternative to currently applied retrospective motion correction and will potentially replace these in the future.

Future applications

These outlined developments will certainly result in the wider adaptation of fMRI in clinical practice (see Rosen and Savoy [2012] or Bullmore [2012] for a review).

Currently, the most prominent clinical translation of fMRI are task experiments for the planning of neurosurgery of intracranial lesions. These experiments are conducted prior to surgery aiming to avoid damage on areas of the eloquent cortex.

However, the recent years have seen a convergence of brain networks found in task and resting-state experiment analysis [Mennes et al., 2010, Cole et al., 2014, 2016, Tavor et al., 2016, Gratton et al., 2018]. The resting-state experiment has advantages compared to task experimentation in the clinical setting. As shown in this work, spatial parametric mappings of cortical areas depend on the correct participation of the subject; especially when task experiments are challenging to perform or do not translate into the expected BOLD signal change predicted by the researcher.

In contrast, the resting-state experiment allows studying brain function in individuals that potentially could forget or do not comply with given task instructions.

8.2.1 Final conclusions

The computation of matrix decomposition models with auto-encoding architectures provides a powerful and flexible approach to fMRI image analysis. The two variants of this approach presented in this work have resulted in more reproducible spatial map estimates in the individual subject as well as a novel signal information in form of surrogate neural activation time courses.

fMRI-specific mode approaches, as proposed in this work, leverage the intrinsic spatial and temporal correlation among adjacent time points in order to obtain compact representations of brain configurations during task processing and resting-state. These are superior to clustering approaches because the brain constitutes a dynamical system that changes its spatial configuration dependent on the task at hand.

Analysis of task and resting-state fMRI experiments have provided tremendous insights into the understanding of the eloquent cortex and higher cognitive function processing. However, the obtained spatial parametric mapping depends on the precise execution of task instructions. The wider adaptation into clinical practice is therefore hampered if subject task execution is not monitored or validated retrospectively. Future research into the validity of fMRI task experiments is necessary to enable the transition of the fMRI experiment into routine clinical practice.

Bibliography

A. Abraham, E. Dohmatob, B. Thirion, D. Samaras, and G. Varoquaux. Extracting brain regions from rest fmri with total-variation constrained dictionary learning. In *International Conference on Medical Image Computing and Computer-Assisted Intervention*, pages 607–615. Springer, 2013.

F. Agosta, M. Pievani, C. Geroldi, M. Copetti, G. B. Frisoni, and M. Filippi. Resting state fmri in alzheimer's disease: beyond the default mode network. *Neurobiology of aging*, 33 (8):1564–1578, 2012.

G. K. Aguirre, E. Zarahn, and M. D'esposito. The variability of human, bold hemodynamic responses. *Neuroimage*, 8(4):360–369, 1998.

D. G. Albrecht and D. B. Hamilton. Striate cortex of monkey and cat: contrast response function. *Journal of neurophysiology*, 48(1):217–237, 1982.

G. Allen, H. Barnard, R. McColl, A. L. Hester, J. A. Fields, M. F. Weiner, W. K. Ringe, A. M. Lipton, M. Brooker, E. McDonald, et al. Reduced hippocampal functional connectivity in alzheimer disease. *Archives of neurology*, 64(10):1482–1487, 2007.

J. S. Anderson, T. J. Druzgal, M. Lopez-Larson, E.-K. Jeong, K. Desai, and D. Yurgelun-Todd. Network anticorrelations, global regression, and phase-shifted soft tissue correction. *Human brain mapping*, 32(6):919–934, 2011.

A. Anticevic, D. L. Dierker, S. K. Gillespie, G. Repovs, J. G. Csernansky, D. C. Van Essen, and D. M. Barch. Comparing surface-based and volume-based analyses of functional neuroimaging data in patients with schizophrenia. *Neuroimage*, 41(3):835–848, 2008.

T. Arichi, G. Fagiolo, M. Varela, A. Melendez-Calderon, A. Allievi, N. Merchant, N. Tusor, S. J. Counsell, E. Burdet, C. F. Beckmann, et al. Development of bold signal hemodynamic responses in the human brain. *Neuroimage*, 63(2):663–673, 2012.

T. Arichi, K. Whitehead, G. Barone, R. Pressler, F. Padormo, A. D. Edwards, and L. Fabrizi. Localization of spontaneous bursting neuronal activity in the preterm human brain with simultaneous eeg-fmri. *Elife*, 6:e27814, 2017.

T. Ash, J. Suckling, M. Walter, C. Ooi, C. Tempelmann, A. Carpenter, and G. Williams. Detection of physiological noise in resting state fmri using machine learning. *Human brain mapping*, 34(4):985–998, 2013.

S. Aslan, L. Hocke, N. Schwarz, and B. Frederick. Extraction of the cardiac waveform from simultaneous multislice fmri data using slice sorted averaging and a deep learning reconstruction filter. *Neuroimage*, 198:303–316, 2019.

B. B. Avants, C. L. Epstein, M. Grossman, and J. C. Gee. Symmetric diffeomorphic image registration with cross-correlation: evaluating automated labeling of elderly and neurodegenerative brain. *Medical image analysis*, 12(1):26–41, 2008.

A. Badhwar, A. Tam, C. Dansereau, P. Orban, F. Hoffstaedter, and P. Bellec. Resting-state network dysfunction in alzheimer's disease: a systematic review and meta-analysis. *Alzheimer's & Dementia: Diagnosis, Assessment & Disease Monitoring*, 8:73–85, 2017.

G. Ball, P. Aljabar, T. Arichi, N. Tusor, D. Cox, N. Merchant, P. Nongena, J. V. Hajnal, A. D. Edwards, and S. J. Counsell. Machine-learning to characterise neonatal functional connectivity in the preterm brain. *Neuroimage*, 124:267–275, 2016.

P. A. Bandettini. Twenty years of functional mri: the science and the stories. *Neuroimage*, 62(2):575–588, 2012.

P. A. Bandettini, A. Jesmanowicz, E. C. Wong, and J. S. Hyde. Processing strategies for time-course data sets in functional mri of the human brain. *Magnetic resonance in medicine*, 30(2):161–173, 1993.

M. Bastiani, J. L. Andersson, L. Cordero-Grande, M. Murgasova, J. Hutter, A. N. Price, A. Makropoulos, S. P. Fitzgibbon, E. Hughes, D. Rueckert, et al. Automated processing pipeline for neonatal diffusion mri in the developing human connectome project. *NeuroImage*, 185:750–763, 2019.

E. B. Beall. Adaptive cyclic physiologic noise modeling and correction in functional mri. *Journal of neuroscience methods*, 187(2):216–228, 2010.

E. B. Beall and M. J. Lowe. Isolating physiologic noise sources with independently determined spatial measures. *Neuroimage*, 37(4):1286–1300, 2007.

E. B. Beall and M. J. Lowe. Simpace: generating simulated motion corrupted bold data with synthetic-navigated acquisition for the development and evaluation of slomoco: a new, highly effective slicewise motion correction. *Neuroimage*, 101:21–34, 2014.

C. F. Beckmann and S. M. Smith. Probabilistic independent component analysis for functional magnetic resonance imaging. *IEEE transactions on medical imaging*, 23(2):137–152, 2004.

C. F. Beckmann, C. E. Mackay, N. Filippini, and S. M. Smith. Group comparison of resting-state fmri data using multi-subject ica and dual regression. *Neuroimage*, 47(Suppl 1):S148, 2009.

Y. Behzadi, K. Restom, J. Liau, and T. T. Liu. A component based noise correction method (compcor) for bold and perfusion based fmri. *Neuroimage*, 37(1):90–101, 2007.

A. J. Bell and T. J. Sejnowski. An information-maximization approach to blind separation and blind deconvolution. *Neural computation*, 7(6):1129–1159, 1995.

G. G. Berntson, J. Thomas Bigger Jr, D. L. Eckberg, P. Grossman, P. G. Kaufmann, M. Malik, H. N. Nagaraja, S. W. Porges, J. P. Saul, P. H. Stone, et al. Heart rate variability: origins, methods, and interpretive caveats. *Psychophysiology*, 34(6):623–648, 1997.

K. Bhaganagarapu, G. D. Jackson, and D. F. Abbott. An automated method for identifying artifact in independent component analysis of resting-state fmri. *Frontiers in human neuroscience*, 7:343, 2013.

M. Bianciardi, M. Fukunaga, P. van Gelderen, S. G. Horovitz, J. A. de Zwart, K. Shmueli, and J. H. Duyn. Sources of functional magnetic resonance imaging signal fluctuations in the human brain at rest: a 7 t study. *Magnetic resonance imaging*, 27(8):1019–1029, 2009.

M. A. Binnewijzend, M. M. Schoonheim, E. Sanz-Arigita, A. M. Wink, W. M. van der Flier, N. Tolboom, S. M. Adriaanse, J. S. Damoiseaux, P. Scheltens, B. N. van Berckel, et al. Resting-state fmri changes in alzheimer's disease and mild cognitive impairment. *Neurobiology of aging*, 33(9):2018–2028, 2012.

R. M. Birn, P. A. Bandettini, R. W. Cox, A. Jesmanowicz, and R. Shaker. Magnetic field changes in the human brain due to swallowing or speaking. *Magnetic Resonance in Medicine*, 40(1):55–60, 1998.

R. M. Birn, R. W. Cox, and P. A. Bandettini. Experimental designs and processing strategies for fmri studies involving overt verbal responses. *Neuroimage*, 23(3):1046–1058, 2004.

R. M. Birn, J. B. Diamond, M. A. Smith, and P. A. Bandettini. Separating respiratory-variation-related fluctuations from neuronal-activity-related fluctuations in fmri. *Neuroimage*, 31(4):1536–1548, 2006.

R. M. Birn, M. A. Smith, T. B. Jones, and P. A. Bandettini. The respiration response function: the temporal dynamics of fmri signal fluctuations related to changes in respiration. *Neuroimage*, 40(2):644–654, 2008.

B. Biswal, F. Zerrin Yetkin, V. M. Haughton, and J. S. Hyde. Functional connectivity in the motor cortex of resting human brain using echo-planar mri. *Magnetic resonance in medicine*, 34(4):537–541, 1995.

H. Blencowe, J. E. Lawn, T. Vazquez, A. Fielder, and C. Gilbert. Preterm-associated visual impairment and estimates of retinopathy of prematurity at regional and global levels for 2010. *Pediatric research*, 74(S1):35–49, 2013.

Z. Boukouvalas, Y. Levin-Schwartz, V. D. Calhoun, and T. Adalı. Sparsity and independence: Balancing two objectives in optimization for source separation with application to fmri analysis. *Journal of the Franklin Institute*, 355(4):1873–1887, 2018.

C. Boutsidis and E. Gallopoulos. Svd based initialization: A head start for nonnegative matrix factorization. *Pattern Recognition*, 41(4):1350–1362, 2008.

G. M. Boynton, S. A. Engel, G. H. Glover, and D. J. Heeger. Linear systems analysis of functional magnetic resonance imaging in human v1. *Journal of Neuroscience*, 16(13): 4207–4221, 1996.

G. M. Boynton, S. A. Engel, and D. J. Heeger. Linear systems analysis of the fmri signal. *NeuroImage*, 62(2):975–984, 2012.

M. G. Bright and K. Murphy. Removing motion and physiological artifacts from intrinsic bold fluctuations using short echo data. *Neuroimage*, 64:526–537, 2013.

E. Bullmore. The future of functional mri in clinical medicine. *Neuroimage*, 62(2):1267–1271, 2012.

K. S. Button. Double-dipping revisited. *Nature neuroscience*, 22(5):688–690, 2019.

R. B. Buxton, K. Uludağ, D. J. Dubowitz, and T. T. Liu. Modeling the hemodynamic response to brain activation. *Neuroimage*, 23:S220–S233, 2004.

C. Caballero-Gaudes and R. C. Reynolds. Methods for cleaning the bold fmri signal. *Neuroimage*, 154:128–149, 2017.

C. Caballero Gaudes, N. Petridou, S. T. Francis, I. L. Dryden, and P. A. Gowland. Paradigm free mapping with sparse regression automatically detects single-trial functional magnetic resonance imaging blood oxygenation level dependent responses. *Human brain mapping*, 34(3):501–518, 2013.

V. D. Calhoun and T. Adali. Multisubject independent component analysis of fmri: a decade of intrinsic networks, default mode, and neurodiagnostic discovery. *Biomedical Engineering, IEEE Reviews in*, 5:60–73, 2012.

V. D. Calhoun, R. F. Silva, T. Adalı, and S. Rachakonda. Comparison of pca approaches for very large group ica. *NeuroImage*, 118:662–666, 2015.

M. J. Cardoso, M. Modat, R. Wolz, A. Melbourne, D. Cash, D. Rueckert, and S. Ourselin. Geodesic information flows: spatially-variant graphs and their application to segmentation and fusion. *IEEE transactions on medical imaging*, 34(9):1976–1988, 2015.

L. Chaari, T. Vincent, F. Forbes, M. Dojat, and P. Ciuciu. Fast joint detection-estimation of evoked brain activity in event-related fmri using a variational approach. *IEEE transactions on Medical Imaging*, 32(5):821–837, 2013.

C. Chang and G. H. Glover. Relationship between respiration, end-tidal co 2, and bold signals in resting-state fmri. *Neuroimage*, 47(4):1381–1393, 2009a.

C. Chang and G. H. Glover. Effects of model-based physiological noise correction on default mode network anti-correlations and correlations. *NeuroImage*, 47(4):1448–59, 2009b. ISSN 1095-9572.

C. Chang and G. H. Glover. Time–frequency dynamics of resting-state brain connectivity measured with fmri. *Neuroimage*, 50(1):81–98, 2010.

C. Chang, J. P. Cunningham, and G. H. Glover. Influence of heart rate on the bold signal: the cardiac response function. *Neuroimage*, 44(3):857–869, 2009.

C. Chang, C. D. Metzger, G. H. Glover, J. H. Duyn, H.-J. Heinze, and M. Walter. Association between heart rate variability and fluctuations in resting-state functional connectivity. *Neuroimage*, 68:93–104, 2013.

C. Chang, E. P. Raven, and J. H. Duyn. Brain–heart interactions: challenges and opportunities with functional magnetic resonance imaging at ultra-high field. *Philosophical Transactions of the Royal Society A: Mathematical, Physical and Engineering Sciences*, 374(2067):20150188, 2016.

H. Cherkaoui, T. Moreau, A. Halimi, and P. Ciuciu. fmri bold signal decomposition using a multivariate low-rank model. In *2019 27th European Signal Processing Conference (EUSIPCO)*, pages 1–5. IEEE, 2019.

M. Christ, A. W. Kempa-Liehr, and M. Feindt. Distributed and parallel time series feature extraction for industrial big data applications. *arXiv preprint arXiv:1610.07717*, 2016.

P. Ciuciu, J.-B. Poline, G. Marrelec, J. Idier, C. Pallier, and H. Benali. Unsupervised robust nonparametric estimation of the hemodynamic response function for any fmri experiment. *IEEE Transactions on medical imaging*, 22(10):1235–1251, 2003.

D. M. Cole, S. M. Smith, and C. F. Beckmann. Advances and pitfalls in the analysis and interpretation of resting-state fmri data. *Frontiers in systems neuroscience*, 4:8, 2010.

M. W. Cole, D. S. Bassett, J. D. Power, T. S. Braver, and S. E. Petersen. Intrinsic and task-evoked network architectures of the human brain. *Neuron*, 83(1):238–251, 2014.

M. W. Cole, T. Ito, D. S. Bassett, and D. H. Schultz. Activity flow over resting-state networks shapes cognitive task activations. *Nature neuroscience*, 19(12):1718–1726, 2016.

D. Cordes, R. R. Nandy, S. Schafer, and T. D. Wager. Characterization and reduction of cardiac-and respiratory-induced noise as a function of the sampling rate (tr) in fmri. *NeuroImage*, 89:314–330, 2014.

R. W. Cox. Afni: software for analysis and visualization of functional magnetic resonance neuroimages. *Computers and Biomedical research*, 29(3):162–173, 1996.

H. Critchley and A. Seth. Will studies of macaque insula reveal the neural mechanisms of self-awareness? *Neuron*, 74(3):423–426, 2012.

H. D. Critchley, J. Eccles, and S. N. Garfinkel. Interaction between cognition, emotion, and the autonomic nervous system. In *Handbook of clinical neurology*, volume 117, pages 59–77. Elsevier, 2013.

C. Crump, E. A. Howell, A. Stroustrup, M. A. McLaughlin, J. Sundquist, and K. Sundquist. Association of preterm birth with risk of ischemic heart disease in adulthood. *JAMA pediatrics*, 173(8):736–743, 2019.

C. Crump, A. Groves, J. Sundquist, and K. Sundquist. Association of preterm birth with long-term risk of heart failure into adulthood. *JAMA pediatrics*, 2021.

K. Dadi, M. Rahim, A. Abraham, D. Chyzhyk, M. Milham, B. Thirion, G. Varoquaux, A. D. N. Initiative, et al. Benchmarking functional connectome-based predictive models for resting-state fmri. *NeuroImage*, 192:115–134, 2019.

K. Dadi, G. Varoquaux, A. Machlouzarides-Shalit, K. J. Gorgolewski, D. Wassermann, B. Thirion, and A. Mensch. Fine-grain atlases of functional modes for fmri analysis. *NeuroImage*, 221:117126, 2020.

M. S. Dagli, J. E. Ingeholm, and J. V. Haxby. Localization of cardiac-induced signal change in fmri. *Neuroimage*, 9(4):407–415, 1999.

E. Damaraju, J. Phillips, J. R. Lowe, R. Ohls, V. D. Calhoun, and A. Caprihan. Resting-state functional connectivity differences in premature children. *Frontiers in systems neuroscience*, 4:23, 2010.

J. S. Damoiseaux, K. E. Prater, B. L. Miller, and M. D. Greicius. Functional connectivity tracks clinical deterioration in alzheimer's disease. *Neurobiology of aging*, 33(4):828–e19, 2012.

I. Daubechies, E. Roussos, S. Takerkart, M. Benharrosh, C. Golden, K. D'ardenne, W. Richter, J. Cohen, and J. Haxby. Independent component analysis for brain fmri does not select for independence. *Proceedings of the National Academy of Sciences*, 106 (26):10415–10422, 2009.

F. de la Cruz, A. Schumann, S. Köhler, K.-J. Bär, and G. Wagner. Impact of the heart rate on the shape of the cardiac response function. *Neuroimage*, 162:214–225, 2017.

F. de la Cruz, A. Schumann, S. Köhler, J. R. Reichenbach, G. Wagner, and K.-J. Bär. The relationship between heart rate and functional connectivity of brain regions involved in autonomic control. *Neuroimage*, 196:318–328, 2019.

A. de Pierrefeu, T. Löfstedt, F. Hadj-Selem, M. Dubois, R. Jardri, T. Fovet, P. Ciuciu, V. Frouin, and E. Duchesnay. Structured sparse principal components analysis with the TV-elastic net penalty. *IEEE transactions on medical imaging*, 37(2):396–407, 2017.

X. Ding, J.-H. Lee, and S.-W. Lee. Performance evaluation of nonnegative matrix factorization algorithms to estimate task-related neuronal activities from fmri data. *Magnetic resonance imaging*, 31(3):466–476, 2013.

V. Doria, C. F. Beckmann, T. Arichi, N. Merchant, M. Groppo, F. E. Turkheimer, S. J. Counsell, M. Murgasova, P. Aljabar, R. G. Nunes, et al. Emergence of resting state networks in the preterm human brain. *Proceedings of the National Academy of Sciences*, 107(46):20015–20020, 2010.

J. Dubois, G. Dehaene-Lambertz, S. Kulikova, C. Poupon, P. S. Hüppi, and L. Hertz-Pannier. The early development of brain white matter: a review of imaging studies in fetuses, newborns and infants. *Neuroscience*, 276:48–71, 2014.

G. Durantin, J.-F. Gagnon, S. Tremblay, and F. Dehais. Using near infrared spectroscopy and heart rate variability to detect mental overload. *Behavioural brain research*, 259: 16–23, 2014.

R. Dürichen, M. A. Pimentel, L. Clifton, A. Schweikard, and D. A. Clifton. Multitask gaussian processes for multivariate physiological time-series analysis. *IEEE Transactions on Biomedical Engineering*, 62(1):314–322, 2014.

D. Duvenaud. *Automatic model construction with Gaussian processes.* PhD thesis, University of Cambridge, 2014.

V. Edward, C. Windischberger, R. Cunnington, M. Erdler, R. Lanzenberger, D. Mayer, W. Endl, and R. Beisteiner. Quantification of fmri artifact reduction by a novel plaster cast head holder. *Human brain mapping*, 11(3):207–213, 2000.

S. B. Eickhoff, R. T. Constable, and B. T. Yeo. Topographic organization of the cerebral cortex and brain cartography. *Neuroimage*, 170:332–347, 2018.

A. J. Elliot, V. Payen, J. Brisswalter, F. Cury, and J. F. Thayer. A subtle threat cue, heart rate variability, and cognitive performance. *Psychophysiology*, 48(10):1340–1345, 2011.

E. B. Erhardt, S. Rachakonda, E. J. Bedrick, E. A. Allen, T. Adali, and V. D. Calhoun. Comparison of multi-subject ica methods for analysis of fmri data. *Human brain mapping*, 32(12):2075–2095, 2011.

E. B. Erhardt, E. A. Allen, Y. Wei, T. Eichele, and V. D. Calhoun. Simtb, a simulation toolbox for fmri data under a model of spatiotemporal separability. *Neuroimage*, 59(4): 4160–4167, 2012.

O. Esteban, C. J. Markiewicz, R. W. Blair, C. A. Moodie, A. I. Isik, A. Erramuzpe, J. D. Kent, M. Goncalves, E. DuPre, M. Snyder, et al. fmriprep: a robust preprocessing pipeline for functional mri. *Nature methods*, 16(1):111–116, 2019.

M. Ewers, G. B. Frisoni, S. J. Teipel, L. T. Grinberg, E. Amaro Jr, H. Heinsen, P. M. Thompson, and H. Hampel. Staging alzheimer's disease progression with multimodality neuroimaging. *Progress in neurobiology*, 95(4):535–546, 2011.

M. Eyre, S. P. Fitzgibbon, J. Ciarrusta, L. Cordero-Grande, A. N. Price, T. Poppe, A. Schuh, E. Hughes, C. O'Keeffe, J. Brandon, et al. The developing human connectome project: typical and disrupted perinatal functional connectivity. *BioRxiv*, 2020.

Y. Farouj, F. I. Karahanoğlu, and D. Van De Ville. Regularized spatiotemporal deconvolution of fmri data using gray-matter constrained total variation. In *Biomedical Imaging (ISBI 2017), 2017 IEEE 14th International Symposium on*, pages 472–475. Ieee, 2017.

D. A. Feinberg and K. Setsompop. Ultra-fast mri of the human brain with simultaneous multi-slice imaging. *Journal of magnetic resonance*, 229:90–100, 2013.

E. S. Finn, L. Huber, D. C. Jangraw, P. J. Molfese, and P. A. Bandettini. Layer-dependent activity in human prefrontal cortex during working memory. *Nature neuroscience*, 22(10): 1687–1695, 2019.

B. Fischl. Freesurfer. *Neuroimage*, 62(2):774–781, 2012.

S. P. Fitzgibbon, S. J. Harrison, M. Jenkinson, L. Baxter, E. C. Robinson, M. Bastiani, J. Bozek, V. Karolis, L. C. Grande, A. N. Price, et al. The developing human connectome project (dhcp) automated resting-state functional processing framework for newborn infants. *NeuroImage*, 223:117303, 2020.

V. S. Fonov, A. C. Evans, R. C. McKinstry, C. Almli, and D. Collins. Unbiased nonlinear average age-appropriate brain templates from birth to adulthood. *NeuroImage*, page S102, 2009.

A. Fotopoulou and M. Tsakiris. Mentalizing homeostasis: The social origins of interoceptive inference. *Neuropsychoanalysis*, 19(1):3–28, 2017.

M. D. Fox and M. E. Raichle. Spontaneous fluctuations in brain activity observed with functional magnetic resonance imaging. *Nature reviews neuroscience*, 8(9):700, 2007.

P. Fransson, U. Åden, M. Blennow, and H. Lagercrantz. The functional architecture of the infant brain as revealed by resting-state fmri. *Cerebral cortex*, 21(1):145–154, 2011.

C. A. Fredericks, J. A. Brown, J. Deng, A. Kramer, R. Ossenkoppele, K. Rankin, J. H. Kramer, B. L. Miller, G. D. Rabinovici, and W. W. Seeley. Intrinsic connectivity networks in posterior cortical atrophy: A role for the pulvinar? *NeuroImage: Clinical*, 21:101628, 2019.

G. B. Frisoni, N. C. Fox, C. R. Jack, P. Scheltens, and P. M. Thompson. The clinical use of structural mri in alzheimer disease. *Nature Reviews Neurology*, 6(2):67–77, 2010.

K. J. Friston. Modes or models: a critique on independent component analysis for fmri. *Trends in cognitive sciences*, 2(10):373–375, 1998.

K. J. Friston and C. J. Price. Dynamic representations and generative models of brain function. *Brain research bulletin*, 54(3):275–285, 2001.

K. J. Friston, A. P. Holmes, K. J. Worsley, J.-P. Poline, C. D. Frith, and R. S. Frackowiak. Statistical parametric maps in functional imaging: a general linear approach. *Human brain mapping*, 2(4):189–210, 1994.

K. J. Friston, C. D. Frith, R. Turner, and R. S. Frackowiak. Characterizing evoked hemodynamics with fmri. *Neuroimage*, 2(2):157–165, 1995.

K. J. Friston, S. Williams, R. Howard, R. S. Frackowiak, and R. Turner. Movement-related effects in fmri time-series. *Magnetic resonance in medicine*, 35(3):346–355, 1996.

K. J. Friston, O. Josephs, G. Rees, and R. Turner. Nonlinear event-related responses in fmri. *Magnetic resonance in medicine*, 39(1):41–52, 1998.

M. A. Frost and R. Goebel. Measuring structural–functional correspondence: spatial variability of specialized brain regions after macro-anatomical alignment. *Neuroimage*, 59(2): 1369–1381, 2012.

W. Gao, S. Alcauter, A. Elton, C. R. Hernandez-Castillo, J. K. Smith, J. Ramirez, and W. Lin. Functional network development during the first year: relative sequence and socioeconomic correlations. *Cerebral cortex*, 25(9):2919–2928, 2015a.

W. Gao, S. Alcauter, J. K. Smith, J. H. Gilmore, and W. Lin. Development of human brain cortical network architecture during infancy. *Brain Structure and Function*, 220(2): 1173–1186, 2015b.

C. C. Gaudes, N. Petridou, I. L. Dryden, L. Bai, S. T. Francis, and P. A. Gowland. Detection and characterization of single-trial fmri bold responses: Paradigm free mapping. *Human brain mapping*, 32(9):1400–1418, 2011.

B. L. Gillie, M. W. Vasey, and J. F. Thayer. Heart rate variability predicts control over memory retrieval. *Psychological Science*, 25(2):458–465, 2014.

J. H. Gilmore, R. C. Knickmeyer, and W. Gao. Imaging structural and functional brain development in early childhood. *Nature Reviews Neuroscience*, 19(3):123–137, 2018.

D. R. Gitelman, W. D. Penny, J. Ashburner, and K. J. Friston. Modeling regional and psychophysiologic interactions in fmri: the importance of hemodynamic deconvolution. *Neuroimage*, 19(1):200–207, 2003.

M. F. Glasser, S. N. Sotiropoulos, J. A. Wilson, T. S. Coalson, B. Fischl, J. L. Andersson, J. Xu, S. Jbabdi, M. Webster, J. R. Polimeni, et al. The minimal preprocessing pipelines for the human connectome project. *Neuroimage*, 80:105–124, 2013.

M. F. Glasser, T. S. Coalson, E. C. Robinson, C. D. Hacker, J. Harwell, E. Yacoub, K. Ugurbil, J. Andersson, C. F. Beckmann, M. Jenkinson, et al. A multi-modal parcellation of human cerebral cortex. *Nature*, 536(7615):171–178, 2016.

X. Glorot and Y. Bengio. Understanding the difficulty of training deep feedforward neural networks. In *Proceedings of the Thirteenth International Conference on Artificial Intelligence and Statistics*, pages 249–256, 2010.

G. H. Glover. Deconvolution of impulse response in event-related bold fmri1. *Neuroimage*, 9(4):416–429, 1999.

G. H. Glover, T. Q. Li, and D. Ress. Image-based method for retrospective correction of physiological motion effects in fMRI: RETROICOR. *Magn. Reson. Med.*, 44(1):162–7, 2000. ISSN 0740-3194.

J. Gonzalez-Castillo, Z. S. Saad, D. A. Handwerker, S. J. Inati, N. Brenowitz, and P. A. Bandettini. Whole-brain, time-locked activation with simple tasks revealed using massive averaging and model-free analysis. *Proceedings of the National Academy of Sciences*, 109 (14):5487–5492, 2012.

K. Gopinath, B. Crosson, K. McGregor, K. K. Peck, Y.-L. Chang, A. Moore, M. Sherod, C. Cavanagh, A. Wabnitz, C. Wierenga, et al. Selective detrending method for reducing task-correlated motion artifact during speech in event-related fmri. *Human brain mapping*, 30(4):1105–1119, 2009.

E. M. Gordon, T. O. Laumann, A. W. Gilmore, D. J. Newbold, D. J. Greene, J. J. Berg, M. Ortega, C. Hoyt-Drazen, C. Gratton, H. Sun, et al. Precision functional mapping of individual human brains. *Neuron*, 95(4):791–807, 2017.

K. Gorgolewski, C. D. Burns, C. Madison, D. Clark, Y. O. Halchenko, M. L. Waskom, and S. S. Ghosh. Nipype: a flexible, lightweight and extensible neuroimaging data processing framework in python. *Frontiers in neuroinformatics*, 5:13, 2011.

K. J. Gorgolewski, N. Mendes, D. Wilfling, E. Wladimirow, C. J. Gauthier, T. Bonnen, F. J. Ruby, R. Trampel, P.-L. Bazin, R. Cozatl, et al. A high resolution 7-tesla resting-state fmri test-retest dataset with cognitive and physiological measures. *Scientific data*, 2, 2015.

C. Goutte, F. A. Nielsen, and K. Hansen. Modeling the hemodynamic response in fmri using smooth fir filters. *IEEE transactions on medical imaging*, 19(12):1188–1201, 2000.

A. Gramfort, B. Thirion, and G. Varoquaux. Identifying predictive regions from fmri with tv-l1 prior. In *2013 International Workshop on Pattern Recognition in Neuroimaging*, pages 17–20. IEEE, 2013.

C. Gratton, T. O. Laumann, A. N. Nielsen, D. J. Greene, E. M. Gordon, A. W. Gilmore, S. M. Nelson, R. S. Coalson, A. Z. Snyder, B. L. Schlaggar, et al. Functional brain networks are dominated by stable group and individual factors, not cognitive or daily variation. *Neuron*, 98(2):439–452, 2018.

M. A. Gray, L. Minati, N. A. Harrison, P. J. Gianaros, V. Napadow, and H. D. Critchley. Physiological recordings: basic concepts and implementation during functional magnetic resonance imaging. *Neuroimage*, 47(3):1105–1115, 2009.

M. D. Greicius, G. Srivastava, A. L. Reiss, and V. Menon. Default-mode network activity distinguishes alzheimer's disease from healthy aging: evidence from functional mri. *Proceedings of the National Academy of Sciences*, 101(13):4637–4642, 2004.

D. N. Greve and B. Fischl. Accurate and robust brain image alignment using boundary-based registration. *Neuroimage*, 48(1):63–72, 2009.

L. Griffanti, G. Salimi-Khorshidi, C. F. Beckmann, E. J. Auerbach, G. Douaud, C. E. Sexton, E. Zsoldos, K. P. Ebmeier, N. Filippini, C. E. Mackay, et al. Ica-based artefact removal and accelerated fmri acquisition for improved resting state network imaging. *Neuroimage*, 95:232–247, 2014.

L. Griffanti, G. Douaud, J. Bijsterbosch, S. Evangelisti, F. Alfaro-Almagro, M. F. Glasser, E. P. Duff, S. Fitzgibbon, R. Westphal, D. Carone, et al. Hand classification of fmri ica noise components. *Neuroimage*, 154:188–205, 2017.

D. A. Gusnard and M. E. Raichle. Searching for a baseline: functional imaging and the resting human brain. *Nature reviews neuroscience*, 2(10):685, 2001.

C. D. Hacker, A. Z. Snyder, M. Pahwa, M. Corbetta, and E. C. Leuthardt. Frequency-specific electrophysiologic correlates of resting state fmri networks. *NeuroImage*, 149: 446–457, 2017.

D. A. Handwerker, J. M. Ollinger, and M. D'Esposito. Variation of bold hemodynamic responses across subjects and brain regions and their effects on statistical analyses. *Neuroimage*, 21(4):1639–1651, 2004.

D. A. Handwerker, J. Gonzalez-Castillo, M. D'esposito, and P. A. Bandettini. The continuing challenge of understanding and modeling hemodynamic variation in fmri. *Neuroimage*, 62 (2):1017–1023, 2012.

A. L. Hansen, B. H. Johnsen, and J. F. Thayer. Relationship between heart rate variability and cognitive function during threat of shock. *Anxiety, Stress, & Coping*, 22(1):77–89, 2009.

S. J. Harrison, M. W. Woolrich, E. C. Robinson, M. F. Glasser, C. F. Beckmann, M. Jenkinson, and S. M. Smith. Large-scale probabilistic functional modes from resting state fmri. *NeuroImage*, 109:217–231, 2015.

S. J. Harrison, J. D. Bijsterbosch, A. R. Segerdahl, S. P. Fitzgibbon, E. Duff, S. M. Smith, and M. W. Woolrich. Modelling subject variability in the spatial and temporal characteristics of functional modes. *bioRxiv*, page 544817, 2019.

B. J. He, A. Z. Snyder, J. M. Zempel, M. D. Smyth, and M. E. Raichle. Electrophysiological correlates of the brain's intrinsic large-scale functional architecture. *Proceedings of the National Academy of Sciences*, 105(41):16039–16044, 2008.

S. Heim, K. Alter, A. K. Ischebeck, K. Amunts, S. B. Eickhoff, H. Mohlberg, K. Zilles, D. Y. von Cramon, and A. D. Friederici. The role of the left brodmann's areas 44 and 45 in reading words and pseudowords. *Cognitive Brain Research*, 25(3):982–993, 2005.

A. D. Hendriks, F. D'Agata, L. Raimondo, T. Schakel, L. Geerts, P. R. Luijten, D. W. Klomp, and N. Petridou. Pushing functional mri spatial and temporal resolution further: High-density receive arrays combined with shot-selective 2d caipirinha for 3d echo-planar imaging at 7 t. *NMR in Biomedicine*, 33(5):e4281, 2020.

R. Henson, M. D. Rugg, K. J. Friston, et al. The choice of basis functions in event-related fmri. *NeuroImage*, 13(6):149–149, 2001.

L. Hernandez-Garcia and M. O. Ulfarsson. Neuronal event detection in fmri time series using iterative deconvolution techniques. *Magnetic resonance imaging*, 29(3):353–364, 2011.

L. M. Hocke and B. B. Frederick. Post-hoc physiological waveform extraction from motion estimation in simultaneous multislice (sms) functional mri using separate stack processing. *Magnetic Resonance in Medicine*, 85(1):309–315, 2021.

C.-J. Hsieh and I. S. Dhillon. Fast coordinate descent methods with variable selection for non-negative matrix factorization. In *Proceedings of the 17th ACM SIGKDD international conference on Knowledge discovery and data mining*, pages 1064–1072. ACM, 2011.

L. Huber, E. S. Finn, D. A. Handwerker, M. Bönstrup, D. R. Glen, S. Kashyap, D. Ivanov, N. Petridou, S. Marrett, J. Goense, et al. Sub-millimeter fmri reveals multiple topographical digit representations that form action maps in human motor cortex. *Neuroimage*, 208: 116463, 2020.

A. Hyvarinen. Fast and robust fixed-point algorithms for independent component analysis. *IEEE transactions on Neural Networks*, 10(3):626–634, 1999.

A. Hyvärinen and E. Oja. A fast fixed-point algorithm for independent component analysis. *Neural computation*, 9(7):1483–1492, 1997.

C. Iadecola. The neurovascular unit coming of age: a journey through neurovascular coupling in health and disease. *Neuron*, 96(1):17–42, 2017.

H. Irzan, E. Molteni, M. Hütel, S. Ourselin, N. Marlow, and A. Melbourne. White matter analysis of the extremely preterm born adult brain. *NeuroImage*, 237:118112, 2021.

M. Jenkinson, P. Bannister, M. Brady, and S. Smith. Improved optimization for the robust and accurate linear registration and motion correction of brain images. *Neuroimage*, 17 (2):825–841, 2002.

M. Jenkinson, C. F. Beckmann, T. E. Behrens, M. W. Woolrich, and S. M. Smith. Fsl. *Neuroimage*, 62(2):782–790, 2012.

J. R. Jennings, L. K. Sheu, D. C.-H. Kuan, S. B. Manuck, and P. J. Gianaros. Resting state connectivity of the medial prefrontal cortex covaries with individual differences in high-frequency heart rate variability. *Psychophysiology*, 53(4):444–454, 2016.

J. L. Ji, M. Spronk, K. Kulkarni, G. Repovš, A. Anticevic, and M. W. Cole. Mapping the human brain's cortical-subcortical functional network organization. *Neuroimage*, 185: 35–57, 2019.

H. J. Jo, Z. S. Saad, W. K. Simmons, L. A. Milbury, and R. W. Cox. Mapping sources of correlation in resting state fmri, with artifact detection and removal. *Neuroimage*, 52(2): 571–582, 2010.

T. Johnstone, K. S. Ores Walsh, L. L. Greischar, A. L. Alexander, A. S. Fox, R. J. Davidson, and T. R. Oakes. Motion correction and the use of motion covariates in multiple-subject fmri analysis. *Human brain mapping*, 27(10):779–788, 2006.

T. B. Jones, P. A. Bandettini, and R. M. Birn. Integration of motion correction and physiological noise regression in fmri. *Neuroimage*, 42(2):582–590, 2008.

J. Jovicich, L. Minati, M. Marizzoni, R. Marchitelli, R. Sala-Llonch, D. Bartrés-Faz, J. Arnold, J. Benninghoff, U. Fiedler, L. Roccatagliata, et al. Longitudinal reproducibility of default-mode network connectivity in healthy elderly participants: a multicentric resting-state fmri study. *Neuroimage*, 124:442–454, 2016.

F. I. Karahanoğlu, C. Caballero-Gaudes, F. Lazeyras, and D. Van De Ville. Total activation: fmri deconvolution through spatio-temporal regularization. *Neuroimage*, 73:121–134, 2013a.

F. I. Karahanoğlu, F. Grouiller, C. C. Gaudes, M. Seeck, S. Vulliemoz, and D. Van De Ville. Spatial mapping of interictal epileptic discharges in fmri with total activation. In *Biomedical Imaging (ISBI), 2013 IEEE 10th International Symposium on*, pages 1500–1503. Ieee, 2013b.

R. Karvonen, M. Sipola, A. Kiviniemi, M. Tikanmäki, M.-R. Järvelin, J. G. Eriksson, M. Tulppo, M. Vääräsmäki, and E. Kajantie. Cardiac autonomic function in adults born preterm. *The Journal of pediatrics*, 208:96–103, 2019.

R. E. Kelly Jr, G. S. Alexopoulos, Z. subsection, F. M. Gunning, C. F. Murphy, S. S. Morimoto, D. Kanellopoulos, Z. Jia, K. O. Lim, and M. J. Hoptman. Visual inspection of independent components: defining a procedure for artifact removal from fmri data. *Journal of neuroscience methods*, 189(2):233–245, 2010.

I. Khalidov, J. Fadili, F. Lazeyras, D. Van De Ville, and M. Unser. Activelets: Wavelets for sparse representation of hemodynamic responses. *Signal Processing*, 91(12):2810–2821, 2011.

S.-G. Kim and S. Ogawa. Biophysical and physiological origins of blood oxygenation level-dependent fmri signals. *Journal of Cerebral Blood Flow & Metabolism*, 32(7):1188–1206, 2012.

B. L. Klaassens, J. van Gerven, J. van der Grond, F. de Vos, C. Möller, and S. A. Rombouts. Diminished posterior precuneus connectivity with the default mode network differentiates normal aging from alzheimer's disease. *Frontiers in aging neuroscience*, 9:97, 2017.

N. Kriegeskorte, W. K. Simmons, P. S. Bellgowan, and C. I. Baker. Circular analysis in systems neuroscience: the dangers of double dipping. *Nature neuroscience*, 12(5):535–540, 2009.

F. Kruggel, C. J. Wiggins, C. S. Herrmann, and D. Y. von Cramon. Recording of the event-related potentials during functional mri at 3.0 tesla field strength. *Magnetic Resonance in Medicine: An Official Journal of the International Society for Magnetic Resonance in Medicine*, 44(2):277–282, 2000.

A. Kucyi, J. Schrouff, S. Bickel, B. L. Foster, J. M. Shine, and J. Parvizi. Intracranial electrophysiology reveals reproducible intrinsic functional connectivity within human brain networks. *Journal of Neuroscience*, 38(17):4230–4242, 2018.

P. Kundu, S. J. Inati, J. W. Evans, W.-M. Luh, and P. A. Bandettini. Differentiating bold and non-bold signals in fmri time series using multi-echo epi. *Neuroimage*, 60(3): 1759–1770, 2012.

C. A. Lane, T. D. Parker, D. M. Cash, K. Macpherson, E. Donnachie, H. Murray-Smith, A. Barnes, S. Barker, D. G. Beasley, J. Bras, et al. Study protocol: Insight 46–a neuroscience sub-study of the mrc national survey of health and development. *BMC neurology*, 17(1):75, 2017.

M. Lehmann, C. Madison, P. M. Ghosh, Z. A. Miller, M. D. Greicius, J. H. Kramer, G. Coppola, B. L. Miller, W. J. Jagust, M. L. Gorno-Tempini, et al. Loss of functional connectivity is greater outside the default mode network in nonfamilial early-onset alzheimer's disease variants. *Neurobiology of aging*, 36(10):2678–2686, 2015.

D. A. Leopold and A. Maier. Ongoing physiological processes in the cerebral cortex. *Neuroimage*, 62(4):2190–2200, 2012.

M. A. Lindquist and T. D. Wager. Validity and power in hemodynamic response modeling: a comparison study and a new approach. *Human brain mapping*, 28(8):764–784, 2007.

M. A. Lindquist, J. M. Loh, L. Y. Atlas, and T. D. Wager. Modeling the hemodynamic response function in fmri: efficiency, bias and mis-modeling. *Neuroimage*, 45(1):S187–S198, 2009.

C. Liu, J. JaJa, and L. Pessoa. Leica: Laplacian eigenmaps for group ica decomposition of fmri data. *NeuroImage*, 169:363–373, 2018.

T. T. Liu. Noise contributions to the fmri signal: An overview. *NeuroImage*, 143:141–151, 2016.

N. K. Logothetis. What we can do and what we cannot do with fmri. *Nature*, 453(7197): 869–878, 2008a.

N. K. Logothetis. What we can do and what we cannot do with fmri. *Nature*, 453(7197): 869–878, 2008b.

N. K. Logothetis and B. A. Wandell. Interpreting the bold signal. *Annu. Rev. Physiol.*, 66: 735–769, 2004.

N. K. Logothetis, J. Pauls, M. Augath, T. Trinath, and A. Oeltermann. Neurophysiological investigation of the basis of the fmri signal. *Nature*, 412(6843):150–157, 2001.

R. Lopes, J.-M. Lina, F. Fahoum, and J. Gotman. Detection of epileptic activity in fmri without recording the eeg. *Neuroimage*, 60(3):1867–1879, 2012.

T. E. Lund, M. D. Nørgaard, E. Rostrup, J. B. Rowe, and O. B. Paulson. Motion or activity: their role in intra-and inter-subject variation in fmri. *Neuroimage*, 26(3):960–964, 2005.

T. E. Lund, K. H. Madsen, K. Sidaros, W.-L. Luo, and T. E. Nichols. Non-white noise in fmri: does modelling have an impact? *Neuroimage*, 29(1):54–66, 2006.

J. Maclaren, B. S. Armstrong, R. T. Barrows, K. Danishad, T. Ernst, C. L. Foster, K. Gumus, M. Herbst, I. Y. Kadashevich, T. P. Kusik, et al. Measurement and correction of microscopic head motion during magnetic resonance imaging of the brain. *PloS one*, 7 (11):e48088, 2012.

J. Maclaren, M. Aksoy, M. B. Ooi, B. Zahneisen, and R. Bammer. Prospective motion correction using coil-mounted cameras: cross-calibration considerations. *Magnetic resonance in medicine*, 79(4):1911–1921, 2018.

S. U. Maier and T. A. Hare. Higher heart-rate variability is associated with ventromedial prefrontal cortex activity and increased resistance to temptation in dietary self-control challenges. *Journal of Neuroscience*, 37(2):446–455, 2017.

S. Makni, P. Ciuciu, J. Idier, and J.-B. Poline. Joint detection-estimation of brain activity in functional mri: a multichannel deconvolution solution. *IEEE Transactions on Signal Processing*, 53(9):3488–3502, 2005.

S. Makni, C. Beckmann, S. Smith, and M. Woolrich. Bayesian deconvolution fmri data using bilinear dynamical systems. *Neuroimage*, 42(4):1381–1396, 2008.

S. Maknojia, N. W. Churchill, T. A. Schweizer, and S. Graham. Resting state fmri: Going through the motions. *Frontiers in neuroscience*, 13:825, 2019.

A. Makropoulos, E. C. Robinson, A. Schuh, R. Wright, S. Fitzgibbon, J. Bozek, S. J. Counsell, J. Steinweg, K. Vecchiato, J. Passerat-Palmbach, et al. The developing human connectome project: A minimal processing pipeline for neonatal cortical surface reconstruction. *Neuroimage*, 173:88–112, 2018.

K. Mandrick, V. Peysakhovich, F. Rémy, E. Lepron, and M. Causse. Neural and psychophysiological correlates of human performance under stress and high mental workload. *Biological psychology*, 121:62–73, 2016.

N. Marlow, D. Wolke, M. A. Bracewell, and M. Samara. Neurologic and developmental disability at six years of age after extremely preterm birth. *New England journal of medicine*, 352(1):9–19, 2005.

G. Marrelec, H. Benali, P. Ciuciu, M. Pélégrini-Issac, and J.-B. Poline. Robust bayesian estimation of the hemodynamic response function in event-related bold fmri using basic physiological information. *Human Brain Mapping*, 19(1):1–17, 2003.

R. McCraty and F. Shaffer. Heart rate variability: new perspectives on physiological mechanisms, assessment of self-regulatory capacity, and health risk. *Global advances in health and medicine*, 4(1):46–61, 2015.

M. J. McKeown, S. Makeig, G. G. Brown, T.-P. Jung, S. S. Kindermann, A. J. Bell, and T. J. Sejnowski. Analysis of fmri data by blind separation into independent spatial components. *Human brain mapping*, 6(3):160–188, 1998.

D. G. McLaren, M. L. Ries, G. Xu, and S. C. Johnson. A generalized form of context-dependent psychophysiological interactions (gppi): a comparison to standard approaches. *Neuroimage*, 61(4):1277–1286, 2012.

M. Mennes, C. Kelly, X.-N. Zuo, A. Di Martino, B. B. Biswal, F. X. Castellanos, and M. P. Milham. Inter-individual differences in resting-state functional connectivity predict task-induced bold activity. *Neuroimage*, 50(4):1690–1701, 2010.

A. Mensch, J. Mairal, B. Thirion, and G. Varoquaux. Extracting representations of cognition across neuroimaging studies improves brain decoding. *PLoS computational biology*, 17(5): e1008795, 2021.

V. Michel, A. Gramfort, G. Varoquaux, E. Eger, and B. Thirion. Total variation regularization for fmri-based prediction of behavior. *IEEE transactions on medical imaging*, 30 (7):1328–1340, 2011.

F. M. Miezin, L. Maccotta, J. Ollinger, S. Petersen, and R. Buckner. Characterizing the hemodynamic response: effects of presentation rate, sampling procedure, and the possibility of ordering brain activity based on relative timing. *Neuroimage*, 11(6):735–759, 2000.

R. Migliaccio, C. Gallea, A. Kas, V. Perlbarg, D. Samri, L. Trotta, A. Michon, L. Lacomblez, B. Dubois, S. Lehericy, et al. Functional connectivity of ventral and dorsal visual streams in posterior cortical atrophy. *Journal of Alzheimer's Disease*, 51(4):1119–1130, 2016.

M. Milh, A. Kaminska, C. Huon, A. Lapillonne, Y. Ben-Ari, and R. Khazipov. Rapid cortical oscillations and early motor activity in premature human neonate. *Cerebral cortex*, 17(7): 1582–1594, 2007.

S. Moeller, E. Yacoub, C. A. Olman, E. Auerbach, J. Strupp, N. Harel, and K. Uğurbil. Multiband multislice ge-epi at 7 tesla, with 16-fold acceleration using partial parallel imaging with application to high spatial and temporal whole-brain fmri. *Magnetic Resonance in Medicine*, 63(5):1144–1153, 2010.

J. S. Mulcahy, D. E. Larsson, S. N. Garfinkel, and H. D. Critchley. Heart rate variability as a biomarker in health and affective disorders: A perspective on neuroimaging studies. *Neuroimage*, 202:116072, 2019.

K. Murphy, J. Bodurka, and P. A. Bandettini. How long to scan? the relationship between fmri temporal signal to noise ratio and necessary scan duration. *Neuroimage*, 34(2):565–574, 2007.

K. Murphy, R. M. Birn, and P. a. Bandettini. Resting-state fMRI confounds and cleanup. *NeuroImage*, 80:349–59, 2013. ISSN 1095-9572. doi: 10.1016/j.neuroimage.2013.04.001.

L. D. Nickerson, S. M. Smith, D. Öngür, and C. F. Beckmann. Using dual regression to investigate network shape and amplitude in functional connectivity analyses. *Frontiers in neuroscience*, 11:115, 2017.

C. Nosarti, K. W. Nam, M. Walshe, R. M. Murray, M. Cuddy, L. Rifkin, and M. P. Allin. Preterm birth and structural brain alterations in early adulthood. *NeuroImage: Clinical*, 6:180–191, 2014.

T. R. Oakes, A. S. Fox, T. Johnstone, M. K. Chung, N. Kalin, and R. J. Davidson. Integrating vbm into the general linear model with voxelwise anatomical covariates. *Neuroimage*, 34(2):500–508, 2007.

S. Ogawa and T.-M. Lee. Magnetic resonance imaging of blood vessels at high fields: in vivo and in vitro measurements and image simulation. *Magnetic resonance in medicine*, 16(1):9–18, 1990.

S. Ogawa, T.-M. Lee, A. R. Kay, and D. W. Tank. Brain magnetic resonance imaging with contrast dependent on blood oxygenation. *Proceedings of the National Academy of Sciences*, 87(24):9868–9872, 1990a.

S. Ogawa, T.-M. Lee, A. S. Nayak, and P. Glynn. Oxygenation-sensitive contrast in magnetic resonance image of rodent brain at high magnetic fields. *Magnetic resonance in medicine*, 14(1):68–78, 1990b.

H. O'Reilly, S. Johnson, Y. Ni, D. Wolke, and N. Marlow. Neuropsychological outcomes at 19 years of age following extremely preterm birth. *Pediatrics*, 145(2), 2020.

D. P. Orfanos, V. Michel, Y. Schwartz, P. Pinel, A. Moreno, D. Le Bihan, and V. Frouin. The brainomics/localizer database. *NeuroImage*, 144:309–314, 2017.

J. Oster and G. D. Clifford. Acquisition of electrocardiogram signals during magnetic resonance imaging. *Physiological measurement*, 38(7):R119, 2017.

H.-D. Park, S. Correia, A. Ducorps, and C. Tallon-Baudry. Spontaneous fluctuations in neural responses to heartbeats predict visual detection. *Nature neuroscience*, 17(4):612–618, 2014.

T. D. Parker, C. F. Slattery, J. Zhang, J. M. Nicholas, R. W. Paterson, A. J. Foulkes, I. B. Malone, D. L. Thomas, M. Modat, D. M. Cash, et al. Cortical microstructure in young onset alzheimer's disease using neurite orientation dispersion and density imaging. *Human brain mapping*, 39(7):3005–3017, 2018.

T. D. Parker, C. F. Slattery, K. X. Yong, J. M. Nicholas, R. W. Paterson, A. J. Foulkes, I. B. Malone, D. L. Thomas, D. M. Cash, S. J. Crutch, et al. Differences in hippocampal subfield volume are seen in phenotypic variants of early onset alzheimer's disease. *NeuroImage: Clinical*, 21:101632, 2019.

F. Pedregosa, M. Eickenberg, P. Ciuciu, B. Thirion, and A. Gramfort. Data-driven hrf estimation for encoding and decoding models. *NeuroImage*, 104:209–220, 2015.

V. Perlbarg, P. Bellec, J.-L. Anton, M. Pélégrini-Issac, J. Doyon, and H. Benali. Corsica: correction of structured noise in fmri by automatic identification of ica components. *Magnetic resonance imaging*, 25(1):35–46, 2007.

S. E. Petersen and O. Sporns. Brain networks and cognitive architectures. *Neuron*, 88(1): 207–219, 2015.

P. Pinel, B. Thirion, S. Meriaux, A. Jobert, J. Serres, D. Le Bihan, J.-B. Poline, and S. Dehaene. Fast reproducible identification and large-scale databasing of individual functional cognitive networks. *BMC neuroscience*, 8(1):91, 2007.

P. Pinel, F. Fauchereau, A. Moreno, A. Barbot, M. Lathrop, D. Zelenika, D. Le Bihan, J.-B. Poline, T. Bourgeron, and S. Dehaene. Genetic variants of foxp2 and kiaa0319/ttrap/them2 locus are associated with altered brain activation in distinct language-related regions. *Journal of Neuroscience*, 32(3):817–825, 2012.

R. A. Poldrack. The future of fmri in cognitive neuroscience. *Neuroimage*, 62(2):1216–1220, 2012.

J.-B. Poline and M. Brett. The general linear model and fmri: does love last forever? *Neuroimage*, 62(2):871–880, 2012.

J. D. Power, K. A. Barnes, A. Z. Snyder, B. L. Schlaggar, and S. E. Petersen. Spurious but systematic correlations in functional connectivity mri networks arise from subject motion. *Neuroimage*, 59(3):2142–2154, 2012.

J. D. Power, A. Mitra, T. O. Laumann, A. Z. Snyder, B. L. Schlaggar, and S. E. Petersen. Methods to detect, characterize, and remove motion artifact in resting state fmri. *Neuroimage*, 84:320–341, 2014.

R. H. Pruim, M. Mennes, D. van Rooij, A. Llera, J. K. Buitelaar, and C. F. Beckmann. Ica-aroma: A robust ica-based strategy for removing motion artifacts from fmri data. *Neuroimage*, 112:267–277, 2015.

M. E. Raichle, A. M. MacLeod, A. Z. Snyder, W. J. Powers, D. A. Gusnard, and G. L. Shulman. A default mode of brain function. *Proceedings of the National Academy of Sciences*, 98(2):676–682, 2001.

D. Rangaprakash, G.-R. Wu, D. Marinazzo, X. Hu, and G. Deshpande. Hemodynamic response function (hrf) variability confounds resting-state fmri functional connectivity. *Magnetic resonance in medicine*, 80(4):1697–1713, 2018.

C. E. Rasmussen and C. K. I. Williams. *Gaussian processes for machine learning.* Adaptive computation and machine learning. MIT Press, 2006. ISBN 026218253X.

S. Rathore, M. Habes, M. A. Iftikhar, A. Shacklett, and C. Davatzikos. A review on neuroimaging-based classification studies and associated feature extraction methods for alzheimer's disease and its prodromal stages. *NeuroImage*, 155:530–548, 2017.

W. Richter and M. Richter. The shape of the fmri bold response in children and adults changes systematically with age. *NeuroImage*, 20(2):1122–1131, 2003.

N. Roche-Labarbe, F. Wallois, E. Ponchel, G. Kongolo, and R. Grebe. Coupled oxygenation oscillation measured by nirs and intermittent cerebral activation on eeg in premature infants. *Neuroimage*, 36(3):718–727, 2007.

B. R. Rosen and R. L. Savoy. fmri at 20: Has it changed the world? *Neuroimage*, 62(2): 1316–1324, 2012.

Z. S. Saad and R. C. Reynolds. Suma. *Neuroimage*, 62(2):768–773, 2012.

M. Sakaki, H. J. Yoo, L. Nga, T.-H. Lee, J. F. Thayer, and M. Mather. Heart rate variability is associated with amygdala functional connectivity with mpfc across younger and older adults. *Neuroimage*, 139:44–52, 2016.

J. A. Salas, R. G. Bayrak, Y. Huo, and C. Chang. Reconstruction of respiratory variation signals from fmri data. *NeuroImage*, 225:117459, 2021.

G. Salimi-Khorshidi, G. Douaud, C. F. Beckmann, M. F. Glasser, L. Griffanti, and S. M. Smith. Automatic denoising of functional mri data: combining independent component analysis and hierarchical fusion of classifiers. *Neuroimage*, 90:449–468, 2014.

T. D. Satterthwaite, D. H. Wolf, J. Loughead, K. Ruparel, M. A. Elliott, H. Hakonarson, R. C. Gur, and R. E. Gur. Impact of in-scanner head motion on multiple measures of functional connectivity: relevance for studies of neurodevelopment in youth. *Neuroimage*, 2012.

T. D. Satterthwaite, D. H. Wolf, K. Ruparel, G. Erus, M. A. Elliott, S. B. Eickhoff, E. D. Gennatas, C. Jackson, K. Prabhakaran, A. Smith, et al. Heterogeneous impact of motion on fundamental patterns of developmental changes in functional connectivity during youth. *Neuroimage*, 83:45–57, 2013.

A. Schaefer, R. Kong, E. M. Gordon, T. O. Laumann, X.-N. Zuo, A. J. Holmes, S. B. Eickhoff, and B. T. Yeo. Local-global parcellation of the human cerebral cortex from intrinsic functional connectivity mri. *Cerebral Cortex*, 28(9):3095–3114, 2017.

A. Schäfer and J. Vagedes. How accurate is pulse rate variability as an estimate of heart rate variability?: A review on studies comparing photoplethysmographic technology with an electrocardiogram. *International journal of cardiology*, 166(1):15–29, 2013.

S. M. Schulz. Neural correlates of heart-focused interoception: a functional magnetic resonance imaging meta-analysis. *Philosophical Transactions of the Royal Society B: Biological Sciences*, 371(1708):20160018, 2016.

W. Shirer, S. Ryali, E. Rykhlevskaia, V. Menon, and M. D. Greicius. Decoding subject-driven cognitive states with whole-brain connectivity patterns. *Cerebral cortex*, 22(1): 158–165, 2012.

A. Shmuel, M. Augath, A. Oeltermann, and N. K. Logothetis. Negative functional mri response correlates with decreases in neuronal activity in monkey visual area v1. *Nature neuroscience*, 9(4):569, 2006.

K. Shmueli, P. van Gelderen, J. a. de Zwart, S. G. Horovitz, M. Fukunaga, J. M. Jansma, and J. H. Duyn. Low-frequency fluctuations in the cardiac rate as a source of variance in the resting-state fMRI BOLD signal. *NeuroImage*, 38:306–320, 2007. ISSN 10538119. doi: 10.1016/j.neuroimage.2007.07.037.

C. F. Slattery, J. Zhang, R. W. Paterson, A. J. Foulkes, A. Carton, K. Macpherson, L. Mancini, D. L. Thomas, M. Modat, N. Toussaint, et al. Apoe influences regional white-matter axonal density loss in alzheimer's disease. *Neurobiology of aging*, 57:8–17, 2017.

S. M. Smith, M. Jenkinson, M. W. Woolrich, C. F. Beckmann, T. E. Behrens, H. Johansen-Berg, P. R. Bannister, M. De Luca, I. Drobnjak, D. E. Flitney, et al. Advances in functional and structural mr image analysis and implementation as fsl. *Neuroimage*, 23:S208–S219, 2004.

S. M. Smith, P. T. Fox, K. L. Miller, D. C. Glahn, P. M. Fox, C. E. Mackay, N. Filippini, K. E. Watkins, R. Toro, A. R. Laird, et al. Correspondence of the brain's functional architecture during activation and rest. *Proceedings of the National Academy of Sciences*, 106(31):13040–13045, 2009.

S. M. Smith, K. L. Miller, G. Salimi-Khorshidi, M. Webster, C. F. Beckmann, T. E. Nichols, J. D. Ramsey, and M. W. Woolrich. Network modelling methods for fmri. *Neuroimage*, 54(2):875–891, 2011.

S. M. Smith, K. L. Miller, S. Moeller, J. Xu, E. J. Auerbach, M. W. Woolrich, C. F. Beckmann, M. Jenkinson, J. Andersson, M. F. Glasser, et al. Temporally-independent functional modes of spontaneous brain activity. *Proceedings of the National Academy of Sciences*, 109(8):3131–3136, 2012.

S. M. Smith, A. Hyvärinen, G. Varoquaux, K. L. Miller, and C. F. Beckmann. Group-pca for very large fmri datasets. *NeuroImage*, 101:738–749, 2014.

C. D. Smyser, T. E. Inder, J. S. Shimony, J. E. Hill, A. J. Degnan, A. Z. Snyder, and J. J. Neil. Longitudinal analysis of neural network development in preterm infants. *Cerebral cortex*, 20(12):2852–2862, 2010.

C. D. Smyser, A. Z. Snyder, J. S. Shimony, A. Mitra, T. E. Inder, and J. J. Neil. Resting-state network complexity and magnitude are reduced in prematurely born infants. *Cerebral cortex*, 26(1):322–333, 2016.

V. Sochat, K. Supekar, J. Bustillo, V. Calhoun, J. A. Turner, and D. L. Rubin. A robust classifier to distinguish noise from fmri independent components. *PloS one*, 9(4):e95493, 2014.

J. V. Stone. *Independent component analysis*. Wiley Online Library, 2004.

K. Supekar, V. Menon, D. Rubin, M. Musen, and M. D. Greicius. Network analysis of intrinsic functional brain connectivity in alzheimer's disease. *PLoS Comput Biol*, 4(6): e1000100, 2008.

I. Tavor, O. P. Jones, R. Mars, S. Smith, T. Behrens, and S. Jbabdi. Task-free mri predicts individual differences in brain activity during task performance. *Science*, 352(6282):216–220, 2016.

J. F. Thayer, F. Åhs, M. Fredrikson, J. J. Sollers, and T. D. Wager. A meta-analysis of heart rate variability and neuroimaging studies: implications for heart rate variability as a marker of stress and health. *Neuroscience & Biobehavioral Reviews*, 36(2):747–756, 2012.

C. G. Thomas, R. A. Harshman, and R. S. Menon. Noise reduction in bold-based fmri using component analysis. *Neuroimage*, 17(3):1521–1537, 2002.

M. E. Thomason, D. Scheinost, J. H. Manning, L. E. Grove, J. Hect, N. Marshall, E. Hernandez-Andrade, S. Berman, A. Pappas, L. Yeo, et al. Weak functional connectivity in the human fetal brain prior to preterm birth. *Scientific reports*, 7(1):1–10, 2017.

N. Todd, O. Josephs, M. F. Callaghan, A. Lutti, and N. Weiskopf. Prospective motion correction of 3d echo-planar imaging data for functional mri using optical tracking. *NeuroImage*, 113:1–12, 2015.

N. Todd, S. Moeller, E. J. Auerbach, E. Yacoub, G. Flandin, and N. Weiskopf. Evaluation of 2d multiband epi imaging for high-resolution, whole-brain, task-based fmri studies at 3t: Sensitivity and slice leakage artifacts. *NeuroImage*, 124:32–42, 2016.

J. Tohka, K. Foerde, A. R. Aron, S. M. Tom, A. W. Toga, and R. A. Poldrack. Automatic independent component labeling for artifact removal in fmri. *Neuroimage*, 39(3):1227–1245, 2008.

H. Toulmin, C. F. Beckmann, J. O'Muircheartaigh, G. Ball, P. Nongena, A. Makropoulos, A. Ederies, S. J. Counsell, N. Kennea, T. Arichi, et al. Specialization and integration of functional thalamocortical connectivity in the human infant. *Proceedings of the National Academy of Sciences*, 112(20):6485–6490, 2015.

A. Tucholka, V. Fritsch, J.-B. Poline, and B. Thirion. An empirical comparison of surface-based and volume-based group studies in neuroimaging. *Neuroimage*, 63(3):1443–1453, 2012.

N. J. Tustison, B. B. Avants, P. A. Cook, Y. Zheng, A. Egan, P. A. Yushkevich, and J. C. Gee. N4itk: improved n3 bias correction. *IEEE transactions on medical imaging*, 29(6): 1310–1320, 2010.

N. J. Tustison, P. A. Cook, A. Klein, G. Song, S. R. Das, J. T. Duda, B. M. Kandel, N. van Strien, J. R. Stone, J. C. Gee, et al. Large-scale evaluation of ants and freesurfer cortical thickness measurements. *Neuroimage*, 99:166–179, 2014.

A. V. Utevsky, D. V. Smith, and S. A. Huettel. Precuneus is a functional core of the default-mode network. *Journal of Neuroscience*, 34(3):932–940, 2014.

K. R. Van Dijk, M. R. Sabuncu, and R. L. Buckner. The influence of head motion on intrinsic functional connectivity mri. *Neuroimage*, 59(1):431–438, 2012.

D. C. Van Essen, K. Ugurbil, E. Auerbach, D. Barch, T. E. Behrens, R. Bucholz, A. Chang, L. Chen, M. Corbetta, S. W. Curtiss, et al. The human connectome project: a data acquisition perspective. *Neuroimage*, 62(4):2222–2231, 2012.

D. C. Van Essen, S. M. Smith, D. M. Barch, T. E. Behrens, E. Yacoub, K. Ugurbil, W.-M. H. Consortium, et al. The wu-minn human connectome project: an overview. *Neuroimage*, 80:62–79, 2013.

A. van Niekerk, E. Meintjes, and A. van der Kouwe. A wireless radio frequency triggered acquisition device (wrad) for self-synchronised measurements of the rate of change of the mri gradient vector field for motion tracking. *IEEE transactions on medical imaging*, 38 (7):1610–1621, 2019.

G. Varoquaux, S. Sadaghiani, P. Pinel, A. Kleinschmidt, J.-B. Poline, and B. Thirion. A group model for stable multi-subject ica on fmri datasets. *Neuroimage*, 51(1):288–299, 2010.

G. Varoquaux, A. Gramfort, F. Pedregosa, V. Michel, and B. Thirion. Multi-subject dictionary learning to segment an atlas of brain spontaneous activity. In *Biennial International Conference on information processing in medical imaging*, pages 562–573. Springer, 2011.

T. D. Verstynen and V. Deshpande. Using pulse oximetry to account for high and low frequency physiological artifacts in the BOLD signal. *NeuroImage*, 55(4):1633–1644, 2011. ISSN 10538119. doi: 10.1016/j.neuroimage.2010.11.090.

T. Vincent, L. Risser, and P. Ciuciu. Spatially adaptive mixture modeling for analysis of fmri time series. *IEEE transactions on medical imaging*, 29(4):1059–1074, 2010.

M. E. Wagshul, P. K. Eide, and J. R. Madsen. The pulsating brain: A review of experimental and clinical studies of intracranial pulsatility. *Fluids Barriers CNS*, 8(1):5, 2011. ISSN 2045-8118. doi: 10.1186/2045-8118-8-5.

D. Wang, R. L. Buckner, M. D. Fox, D. J. Holt, A. J. Holmes, S. Stoecklein, G. Langs, R. Pan, T. Qian, K. Li, et al. Parcellating cortical functional networks in individuals. *Nature neuroscience*, 18(12):1853, 2015.

L. Wang, Y. Zang, Y. He, M. Liang, X. Zhang, L. Tian, T. Wu, T. Jiang, and K. Li. Changes in hippocampal connectivity in the early stages of alzheimer's disease: evidence from resting state fmri. *Neuroimage*, 31(2):496–504, 2006.

A. B. Watson et al. Temporal sensitivity. *Handbook of perception and human performance*, 1:6–1, 1986.

M. W. Weiner, D. P. Veitch, P. S. Aisen, L. A. Beckett, N. J. Cairns, R. C. Green, D. Harvey, C. R. Jack, W. Jagust, E. Liu, et al. The alzheimer's disease neuroimaging initiative: a review of papers published since its inception. *Alzheimer's & Dementia*, 9(5):e111–e194, 2013.

A. Weissenbacher, C. Kasess, F. Gerstl, R. Lanzenberger, E. Moser, and C. Windischberger. Correlations and anticorrelations in resting-state functional connectivity mri: a quantitative comparison of preprocessing strategies. *Neuroimage*, 47(4):1408–1416, 2009.

M. Welvaert and Y. Rosseel. A review of fmri simulation studies. *PLoS One*, 9(7):e101953, 2014.

T. P. White, I. Symington, N. P. Castellanos, P. J. Brittain, S. F. Walsh, K.-W. Nam, J. R. Sato, M. P. Allin, S. S. Shergill, R. M. Murray, et al. Dysconnectivity of neurocognitive networks at rest in very-preterm born adults. *NeuroImage: Clinical*, 4:352–365, 2014.

D. P. Williams, C. Cash, C. Rankin, A. Bernardi, J. Koenig, and J. F. Thayer. Resting heart rate variability predicts self-reported difficulties in emotion regulation: a focus on different facets of emotion regulation. *Frontiers in psychology*, 6:261, 2015.

A. M. Winkler, G. R. Ridgway, M. A. Webster, S. M. Smith, and T. E. Nichols. Permutation inference for the general linear model. *Neuroimage*, 92:381–397, 2014.

M. W. Woolrich, S. Jbabdi, B. Patenaude, M. Chappell, S. Makni, T. Behrens, C. Beckmann, M. Jenkinson, and S. M. Smith. Bayesian analysis of neuroimaging data in fsl. *Neuroimage*, 45(1):S173–S186, 2009.

E. Zarahn. Testing for neural responses during temporal components of trials with bold fmri. *Neuroimage*, 11(6):783–796, 2000.

J. Zhou, M. D. Greicius, E. D. Gennatas, M. E. Growdon, J. Y. Jang, G. D. Rabinovici, J. H. Kramer, M. Weiner, B. L. Miller, and W. W. Seeley. Divergent network connectivity changes in behavioural variant frontotemporal dementia and alzheimer's disease. *Brain*, 133(5):1352–1367, 2010.

D. M. Zöller, T. A. Bolton, F. I. Karahanoğlu, S. Eliez, M. Schaer, and D. Van De Ville. Robust recovery of temporal overlap between network activity using transient-informed spatio-temporal regression. *IEEE transactions on medical imaging*, 38(1):291–302, 2019.